Karlsruher Institut für Technologie

Development of Rheo-IR: Combination of a Strain-Controlled Rheometer with an IR Spectrometer for in-situ Mechanical and Chemical Analysis of Cement Paste

---

Zur Erlangung des akademischen Grades eines
DOKTORS DER NATURWISSENSCHAFTEN
(Dr. rer. nat.)
von der KIT-Fakultät für Chemie und Biowissenschaften
des Karlsruher Instituts für Technologie (KIT)

genehmigte

DISSERTATION

von

M.Sc. Nonkululeko Winnie Radebe

aus Johannesburg, Südafrika

Betreuer	Prof. Dr. Manfred Wilhelm
Dekan	Prof. Dr. Hans-Achim Wagenknecht
Korreferent	Prof. Dr.-Ing. Michael Haist
Tag der mündlichen Prüfung	17 Dezember 2021

Die Arbeiten in dieser Arbeit wurden im Zeitraum von April 2018 bis Dezember 2021 am Institut für Technische Chemie und Polymerchemie (ITCP) des Karlsruher Instituts für Technologie (KIT) unter der Betreuung von Prof. Dr. Manfred Wilhem durchgeführt.

Hiermit versichere ich, dass ich die vorgelegte Arbeit selbstständig verfasst habe, dass ich die verwendeten Quellen und Hilfsmittel sowie die Arbeitsstellen vollständig angegeben habe, die anderen Arbeiten sind im Wortlaut oder Sinn übernommen, entsprechend gekennzeichnet.

Nonkululeko Winnie Radebe
Karlsruhe, den 07 March 2022

Dedicated to my late grandmother
Nkgono Nomsa Diana Chabeli ♡

'There is no shame in not knowing. The shame lies in not finding out'

ABSTRACT

Fourier-transform infrared (FTIR) spectroscopy is a common tool for determining the chemical composition of a material in the solid, liquid, or gas phases, both qualitatively and quantitatively. It is also employed as a technique for monitoring the rate of chemical changes as a function of time, concentration, temperature etc. These chemical changes can have rheological implications, such as polymerization kinetics, rubber crosslinking, or epoxy curing, to name a few. In this thesis, a unique set-up that is able to simultaneously measure rheology and IR spectra with an improved sensitivity, to correlate mechanical behavior with microstructural changes, was developed. The stepwise development of chemically and mechanically sensitive Rheo-IR set-up is presented. This includes the design of an IR transparent upper-plate rheological geometry used as an attenuated total reflectance (ATR) sampling tool and a description of the technical and methodological adaption of the ATR crystal into an ARES G2 rheometer. In this new set-up, a strain-controlled rheometer is combined in a novel configuration with an ATR crystal and the IR beam is guided through two off-axis parabolic mirrors to the quasi-static upper plate of the rheometer to gain maximum IR sensitivity. Thereby online and directly correlated real-time FTIR spectra can be acquired whilst simultaneously conducting rheological measurements. This allows for 'in-situ' correlation of macroscopic rheological properties with microscopic, molecular chemical changes. These experiments are conducted for a material under controlled conditions having exactly the same sample time evolution for the simultaneous measurement. In addition, this set-up allows to study the effect of shear under steady state and oscillatory shear conditions, both in the linear (SAOS) and nonlinear regime (steady shear and LAOS).

As a proof of concept and to demonstrate its potential, this newly developed method was applied to correlate the polymer network formation for a free radical co-polymerization of acrylic acid and methylenebis(acrylamide) as a crosslinking agent via IR spectroscopy and the respective mechanical time evolution, in a dilute water-based solution. In addition, the newly developed Rheo-IR technique was applied to cement paste hydration and structural build-up. The IR results were compared to those from offline FTIR. Along with the Rheo-IR and FTIR measurements other rheological techniques, including FT-Rheology, Rheo-NMR and Rheo-Dielectrics were applied to study early cement paste hydration and structural build-up. The strain deformation and flow of fresh cement paste on the basis of microscale processes during early hydration was of interest. Applying FT-rheology, the intensity at mechanical higher harmonics are quantified and normalized to the fundamental intensity. A model with a quadratic scaling in the strain amplitude is used to predict two critical strains, that can be associated with the solid ($\gamma_{cs} \sim 0.1\%$) and mobile ($\gamma_{cm} \sim 0.01\%$) parts of cement paste. Interestingly, the effect of hydration time has minimal relevance on these critical strains. The influence of the microstructure seen through the mechanical evolution is attributed to the formation of hydrates, as determined spectroscopically through FTIR. Although, the hydration products (i.e. ettringite) do form within the first hour of hydration, the relative amount seems not to be the main contributing factor to structural build up. The structural build-up as a function of applied strain as investigated by Rheo-NMR, shows

that although a relatively large strain for cement ($\gamma_c = 0.3\%$) is applied, the molecular mobility is the same as that of a lower strain ($\gamma_c = 0.01\%$), within the first hour of hydration. Through Rheo-Dielectrics, a similar trend is observed for the dc-conductivity. However, after 2 to 5 hours a 100 to 1000 times decrease in conductivity is seen, due to setting. The sample exposed to a higher strain, sets faster. Based on the observations from the Rheo-combined methods as a well as FT-Rheology the assumption is that physical interactions such as colloidal interactions could be more dominant than chemical bond formation for structural build-up in the first few minutes to the first hour of cement paste hydration.

ZUSAMMENFASSUNG

Die Fourier-Transformations-Infrarot-Spektroskopie (FTIR) ist ein gängiges Instrument zur qualitativen und quantitativen Bestimmung der chemischen Zusammensetzung eines Materials in der festen, flüssigen oder gasförmigen Phase. Sie wird auch als Technik zur Überwachung der Geschwindigkeit chemischer Veränderungen in Abhängigkeit von Zeit, Konzentration, Temperatur usw. eingesetzt. Diese chemischen Veränderungen können rheologische Auswirkungen haben, z.B. auf die Kinetik der Polymerisation, die Vernetzung von Gummi oder die Aushärtung von Epoxidharzen, um nur einige Beispiele zu nennen. In dieser Arbeit wurde ein einzigartiger Aufbau entwickelt, der die gleichzeitige Messung von Rheologie und IR-Spektren mit einer verbesserten Empfindlichkeit ermöglicht, um das mechanische Verhalten mit mikrostrukturellen Veränderungen zu korrelieren. Die schrittweise Entwicklung eines chemisch und mechanisch empfindlichen Rheo-IR-Aufbaus wird vorgestellt. Dies umfasst die Entwicklung einer IR-transparenten rheologischen Oberplattengeometrie, die als ATR-Probenahmegerät (abgeschwächte Totalreflexion) verwendet wird, und eine Beschreibung der technischen und methodischen Anpassung des ATR-Kristalls an ein ARES G2-Rheometer. In diesem neuen Aufbau wird ein dehnungsgesteuertes Rheometer in einer neuartigen Konfiguration mit einem ATR-Kristall kombiniert, und der IR-Strahl wird über zwei außeraxiale Parabolspiegel auf die quasistatische obere Platte des Rheometers geleitet, um eine maximale IR-Empfindlichkeit zu erreichen. Auf diese Weise können online und direkt korrelierte Echtzeit-FTIR-Spektren erfasst und gleichzeitig rheologische Messungen durchgeführt werden. Dies ermöglicht eine "in-situ"-Korrelation makroskopischer rheologischer Eigenschaften mit mikroskopischen, molekularen chemischen Veränderungen. Diese Experimente werden für ein Material unter kontrollierten Bedingungen durchgeführt, wobei die zeitliche Entwicklung der Probe für die gleichzeitige Messung exakt gleich ist. Außerdem kann mit diesem Aufbau die Wirkung der Scherung unter stationären und oszillierenden Scherungsbedingungen untersucht werden, und zwar sowohl im linearen (SAOS) als auch im nichtlinearen Bereich (stationäre Scherung und LAOS).

Zum Nachweis des Konzepts und zur Demonstration seines Potenzials wurde diese neu entwickelte Methode angewandt, um die Bildung von Polymernetzwerken bei einer radikalischen Copolymerisation von Acrylsäure und Methylenbis(acrylamid) als Vernetzungsmittel mittels IR-Spektroskopie und der entsprechenden mechanischen Zeitentwicklung in einer verdünnten wässrigen Lösung zu korrelieren. Darüber hinaus wurde die neu entwickelte Rheo-IR-Technik auf die Hydratation und den Gefügeaufbau von Zementleim angewendet. Die IR-Ergebnisse wurden mit denen der Offline-FTIR verglichen. Neben den Rheo-IR- und FTIR-Messungen wurden auch andere rheologische Verfahren wie FT-Rheologie, Rheo-NMR und Rheo-Dielektrik zur Untersuchung der frühen Zementleimhydratation und des Gefügeaufbaus eingesetzt. Die Verformung und das Fließen von frischem Zementleim auf der Grundlage von mikroskaligen Prozessen während der frühen Hydratation waren von Interesse. Unter Anwendung der FT-Rheologie wird die Intensität der mechanischen höheren harmonischen quantifiziert und auf die Grundintensität normiert. Ein Modell mit einer quadratischen Skalierung in der Dehnungsamplitude wird verwendet, um zwei

kritische Dehnungen vorherzusagen, die mit den festen ($\gamma_{cs} \sim 0.1\%$) und beweglichen ($\gamma_{cm} \sim 0.01\%$) Teilen des Zementleims in Verbindung gebracht werden können. Interessanterweise ist der Einfluss der Hydratationszeit auf diese kritischen Dehnungen minimal. Der Einfluss der Mikrostruktur, der sich in der mechanischen Entwicklung zeigt, wird auf die Bildung von Hydraten zurückgeführt, die spektroskopisch mittels FTIR bestimmt wurden. Obwohl sich die Hydratationsprodukte (d. h. Ettringit) innerhalb der ersten Stunde der Hydratation bilden, scheint die relative Menge nicht der Hauptfaktor für den Strukturaufbau zu sein. Die mit Rheo-NMR untersuchte Strukturbildung in Abhängigkeit von der angewendeten Dehnung zeigt, dass trotz einer für Zement relativ großen Dehnung ($\gamma_c = 0,3\%$) die molekulare Mobilität innerhalb der ersten Stunde der Hydratation die gleiche ist wie bei einer geringeren Dehnung ($\gamma_c = 0,01\%$). Mit Hilfe der Rheo-Dielektrik wird ein ähnlicher Trend für die Leitfähigkeit beobachtet. Nach 2 bis 5 Stunden ist jedoch ein 100- bis 1000-facher Rückgang der Leitfähigkeit zu beobachten, der auf das Aushärten zurückzuführen ist. Die Probe, die einer höheren Belastung ausgesetzt ist, härtet schneller aus. Auf der Grundlage der Beobachtungen aus den kombinierten Rheo-Methoden und der FT-Rheologie wird davon ausgegangen, dass physikalische Wechselwirkungen, wie z.B. kolloidale Wechselwirkungen, für den Strukturaufbau in den ersten Minuten bis zur ersten Stunde der Zementleimhydratation dominanter sein könnten als die Formation von direkten, kovalenten Bindungen.

Contents

Nomenclature

Acronyms

$\frac{S/N}{\sqrt{t}}$	Time independent signal-to-noise ratio
DP	Depth of penetration
S/N	Signal-to-noise ratio
ATR	Attenuated total reflection
CPMG	Carr-Purcell-Meiboom-Gill
DC	Degree of crosslinking
DSS	Dynamic strain sweep
DTS	Dynamic time sweep
EMR	Electromagnetic radiation
FIR	Far Infrared
FTIR	Fourier Transform Infrared spectroscopy
IRE	Internal reflection element
LAOS	Large amplitude oscillatory shear
LVE	Linear viscoelastic (region)
MCT	Mercury-cadmium-telluride
MIR	Mid Infrared
MSE	Magic-sandwich-echo
NIR	Near Infrared
NMR	Nuclear Magnetic Resonance
NVE	Nonlinear viscoelastic (region)
OAP	Off-axis parabolic mirrors

OPC	Ordinary Portland cement
OPD	Optical path difference
Rheo-Dielectrics	Rheology combined with Dielectric spectroscopy
Rheo-IR	Rheology combined with Infrared spectroscopy
Rheo-NMR	Rheology combined with Nuclear Magnetic Resonance spectroscopy or relaxometry
RSC	Reference single channel
SAOS	Small amplitude oscillatory shear
SCS	Single channel spectrum

Cement Chemsitry Notation

C_2S	Dricalcium silicate, Ca_2SiO_4
C_3S	Tricalcium silicate, Ca_3SiO_5
CH	Calcium Hydroxide, $Ca(OH)_2$, portlandite
C-S-H	Calcium silcate hydrate, $\underbrace{CaO}_{C} \cdot \underbrace{SiO_2}_{S} \cdot \underbrace{H_2O}_{H}$

Greek Symbols

δ	phase angle
$\dot{\gamma}$	rate of shear deformation
η	viscosity
γ	strain amplitude in shear
γ_0	applied strain amplitude
γ_{cm}	large strain amplitude/strain amplitude associated with mobile part of cement paste
γ_{cs}	small strain amplitude/strain amplitude associated with solid part of cement paste
γ_c	critital strain amplitude
λ	wavelength
ω	angular frequency, $2\pi v = \omega$
Φ	photon flux
ϕ	solid volume fraction

Φ_{rel}	relative photon flux
σ	shear stress
σ^*	complex dielectrics conductivity
σ''	imaginary part of the complex conductivity function
σ'	real part of the complex conductivity function
σ_0	dc-conductivity
θ_c	critical angle
θ_{IR}	normalized intergral of IR peak
θ_{rheo}	normalized storage modulus
ε	molar extinction coefficient
ε^*	complex dielectric permittivity
ε''	imaginary part of the complex permittivity function
ε'	real part of the complex permittivity function
$\widetilde{\nu}$	wavenumber

Roman symbols

A	absorbance
B_0	external magnetic field
c	speed of light, $2.997 \times 10^8 ms^{-1}$
E	electromagnetic field
G''	loss modulus
G'	storage modulus
h	Plancks constant, $6.63 \times\ 10^{-34} m^2 kg/s$
n_c	refractive index of the crystal
n_s	refractive index of the sample
t_{cross}	G', G'' crossover time in time-dependent rheological measurement
t_{gel}	gelation time
V	interaction/potential energy
v	frequency, $2\pi v = \omega$

V_A	Van der Waals attraction energy
V_R	electrostatic replusion energy
$I_{n/1}$	intensity of higher mechanical harmonic at a given frequency (n) relative to the intensity of the fundemental harmonic, I_1
d	distance between particles

Chapter 1

Introduction

The introductory chapter provides a background into the different material parameters that are given by both rheological and spectroscopic techniques. In addition, the concept and importance of combining rheological measurements and a second molecular characterization method, in situ, is introduced. These techniques (i.e. Rheo-NMR and Rheo-Dielectrics) are used in addressing some of the characterization challenges that are intrinsic in complex materials. There is a special focus on cement paste as one of the complex materials, for this reason, a brief introduction open questions about material is presented. Combined techniques provide unique information about molecular dynamics and structure in time or as a result of strain or shear. The development of the Rheo-IR method, using a strain-controlled rheometer, is a worldwide unique and developed within our research group. The development of the technique and implementation on complex materials forms the body of this thesis.

1.1 Background

Rheological properties, such as the viscosity, oscillatory shear moduli or phase angle represent the macroscopic behavior and mechanical response of materials including polymeric materials, gels, low and high concentration dispersions and solids[1–3]. The origin of these macroscopic mechanical properties can be attributed to and originate from the molecular structure. Mechanical deformation, both in the linear and nonlinear regime, induce changes in the microstructure e.g. shear induced crystallization[4,5], phase separation or macroscopic ordering. In the linear viscoelastic regime, where the applied stress/strain or stress/strain rate does not change or affect the materials response, time and temperature are the common parameter to induce structural changes e.g via molecular mobility or induction of chemical reactions. Therefore, in-situ molecular characterization is beneficial in understanding the relation between rheological response of a material and the respective molecular origin. This can be done through the simultaneous detection of local microscopic molecular dynamics as well as macroscopic mechanical information. These general relationships have been studied in the past using combined rheology and spectroscopic

techniques which includes Fourier-transform Infrared (FTIR) spectroscopy[4,5], Raman spectroscopy[6–8], optical spectroscopy[4], dielectric spectroscopy[9–12], small angle X-ray scattering (SAXS)[13,14], or nuclear magnetic resonance spectroscopy (NMR)[15–18]. In Rheo-optics, a mechanical test is combined with optical measurements (e.g. birefringence or dichroism[19,20]) and the relation between stress, strain and the simultaneously measured optical quantity respective physical changes (e.g. orientation) are established. Rheo-SAXS is used to correlate mechanical non-linearities with structural ordering[21], while Rheo-Dielectrics is able to measure correlation times of molecular dipoles typically over a wide range of $10^{-6} - 10^{2}$ s at a single temperature. Rheo-Dielectrics can also measure the molecular dynamics on the length scale of the end-to-end vector of a polymer material which correlate with the relaxation times and distribution[22] for 'Stockmayer type-A' polymers[23,24]. Differential scanning calorimetry (DSC) has also been integrated into a stress-controlled shear rheometer to study, for example, the chemical and macroscopic changes during the cure of a thermosetting epoxy-amine system and the flow-induced crystallization of syndiotactic polypropylene[25].

1.2 Motivation For This Study

Spectroscopic parameters can be and have been related to chemical composition, conformation, crystallization and orientation can be monitored on-line and simultaneously as a function of deformation, stress relaxation, and time. Therefore, the material can be investigated over very small strains, and time scales. Since rheometers alone, cannot directly provide material information related to chemical origin of macroscopic mechanical properties, a second characterization technique is necessary. To bridge this gap, an in-situ rheology-Fourier transform infrared spectroscopy (Rheo-IR) technique is designed and used, in this thesis. The Rheo-IR combined technique is a new method and consequently can be applied in several different kinds of systems. The temperature effects on rubber curing by monitoring the formation of crosslinks[26] whilst simultaneously measuring the storage and loss moduli would be one such system or epoxy curing by monitoring the ether bond formation resulting from homopolymerization[27] as well as the resulting viscosity. A strain-controlled rheological measurement uniquely coupled with attenuated reflectance infrared spectroscopy, will allow for FT-Rheology, LAOS and mechanical non-linear rheo-optical correlation. The time dependent development of the intensity of the higher harmonics will allow for the quantification and prediction of material orientation and fatigue.

1.2.1 Challenges in Characterizing Complex Materials: Case Study - Cement Paste

Cement and concrete consumption

Concrete construction contributes significantly to global carbon emissions. The majority of it is due to the use of cement as a binder in concrete. Cement alone accounts for about 10% of global carbon emissions[28,29]. Each ton of cement generates 600–900 kg CO_2, primarily

due to calcium carbonate ($CaCO_3$) decomposition according to Equation 1.2.1 but also due to energy requirements, processing, and grinding[28,30].

$$CaCO_3 \rightarrow CaO + CO_2 \tag{1.2.1}$$

Even though current cement manufacturing plants are highly efficient, carbon emissions from the typical Portland cement clinker sintering process are unavoidable and can only be decreased by reducing clinker volume in concrete. Cement clinker is a solid material used as an intermediate product in the production of Portland cement. Clinker appears as lumps or nodules with a diameter ranging from 3 mm to 25 mm. Tricalcium silicate, dicalcium silicate, tricalcium aluminate, and calcium aluminoferrite are the main constituents. It is made up of a mix of raw materials that usually includes limestone, clay, sand, iron ore, and other components (e.g. fly ash) in definite proportions.[31]). Other carbon emissions in concrete technology come from the processing, transporting, and energy consumption of the concrete itself while casting on site, in addition to the cement contribution. Concrete is the only material on the planet that has enough supply to meet the global demand for building materials. Cementitious material usage is currently around 8.5 times higher than total worldwide wood production and 1.5 times more than total global steel production, by mass[28]. As a result, concrete is used in far greater quantities for structural elements than any other construction material, and it will continue to be utilized because other construction materials, with the exception of non-cement-stabilized compressed earth, have higher embodied carbon and energy[29,32]. Thus, the high carbon emissions from concrete in comparison to other materials are primarily due to its massive demand and consumption. This necessitates more efficient use of concrete in the future in order to reduce cross sections, as well as structural dimensioning that aids in reducing overall material consumption[1]. However, a precondition for reducing cement consumption and replacing it with other supplementary cementitious materials, is understanding the working mechanisms behind hydration and structuration. By gaining knowledge of the material at a molecular level, some important properties are understood and can be transferred to other materials or at least understood relative to the supplementary cementitious materials.

Multiscale Characterization Approach

When the microstructure of a material is understood, its properties and performance can be understood and predicted. However, cementitious materials are particularly challenging to characterize. The first challenge is the importance of length scales. The important length scales extend from nanometers (nm) to the meter (m) scale. A second consideration is the influence of water on the microstructure, whether it be the water added or water being removed in order to fully study the structure at a specific hydration time. Although cement has been used as building material for thousands of years (i.e. the Pantheon in Rome which is approximately 2500 years old), only in the past few decades has there been significant progress in making microstructural analytical techniques more quantitative. However,

[1] Cement and concrete are not synonymous. Cement, a powdered limestone and clay mixture, is one of the ingredients in concrete, along with water, sand, and gravel.

in order to fully understand the mechanisms of hydration of cementitious materials it is valuable to know the relationship between the microscopic changes and the mechanical properties. These properties are influenced by time[33–35] temperature[36,37], water to cement ratio[38,39], addition of admixtures[40], aggregates type and size[41,42], cement powder size distribution, mix designs[43] and many other factors. The abovementioned factors influence the rheology and the microstructural build up. These are changes that can be observed at two different length scales, *mm* and *nm*, respectively.

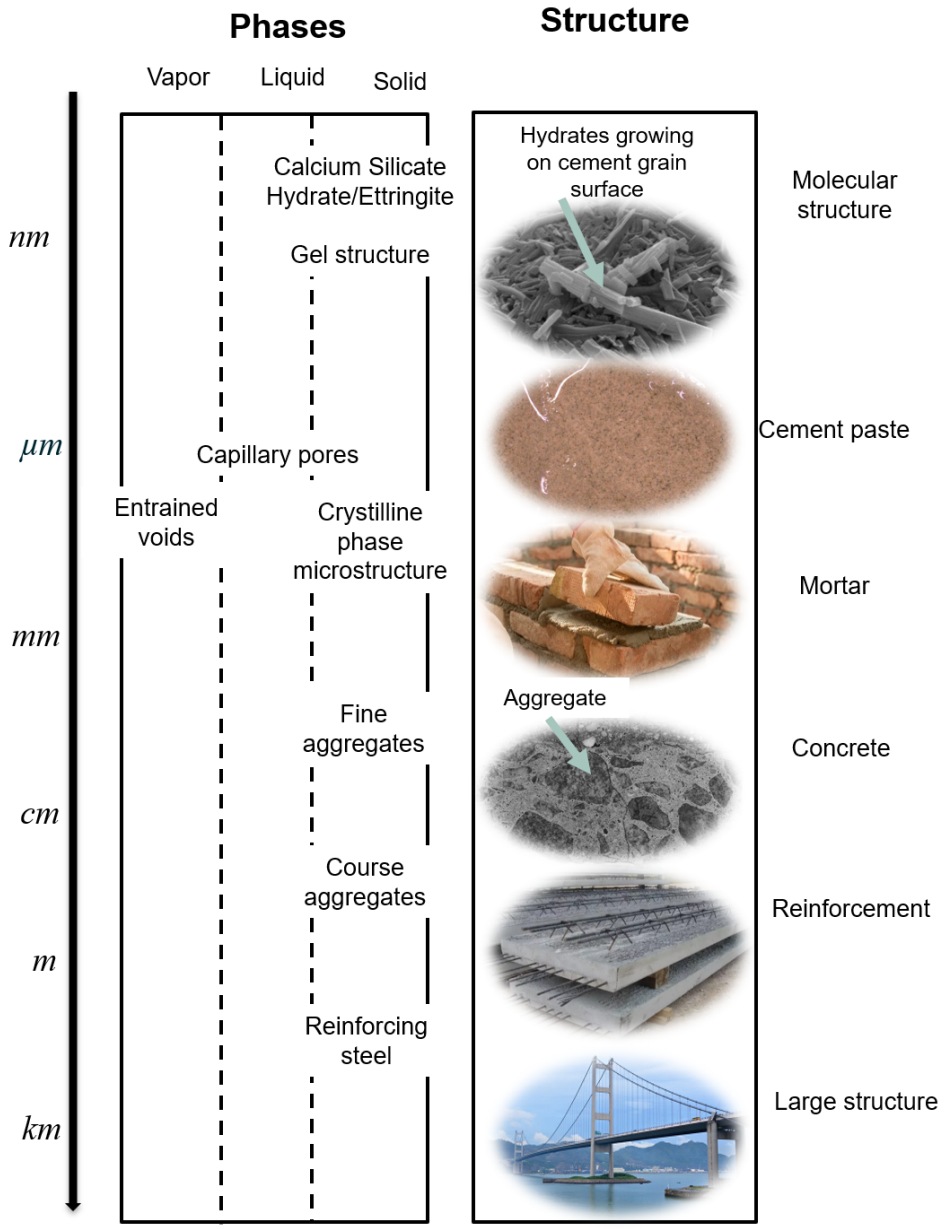

Figure 1.1: A schematic overview of the different length scales that cement is found as well as the different phases and structures that are associated with each length scale.

In general, cement paste is studied at various time and length scales, ranging from molecular structure in *nm* to huge structures, such as steel reinforced structures, in the *m* even *km* range as seen in Figure 1.1. It is therefore valuable to know whether these changes

occurring on different lengths scales are a function of each other, and if they are, to what extent. Additionally, it is important to consider that many of the aesthetic and physical failures that are seen a few months after a structure erected, can directly be linked to the microstructure, which starts to form immediately when water is added to the cement powder. Some of these failures can be seen in Figure 1.2. These failures can range anywhere between a few centimeters to a few meters. For example, if the coarse aggregates seen in Figure 1.2d are $\sim 10\ mm$ in diameter, then the damage spans over 100 mm. This is likely to be an underestimation because the coarse aggregates could be even larger (ca. 30 mm for walls and 90 mm for road construction[44]).

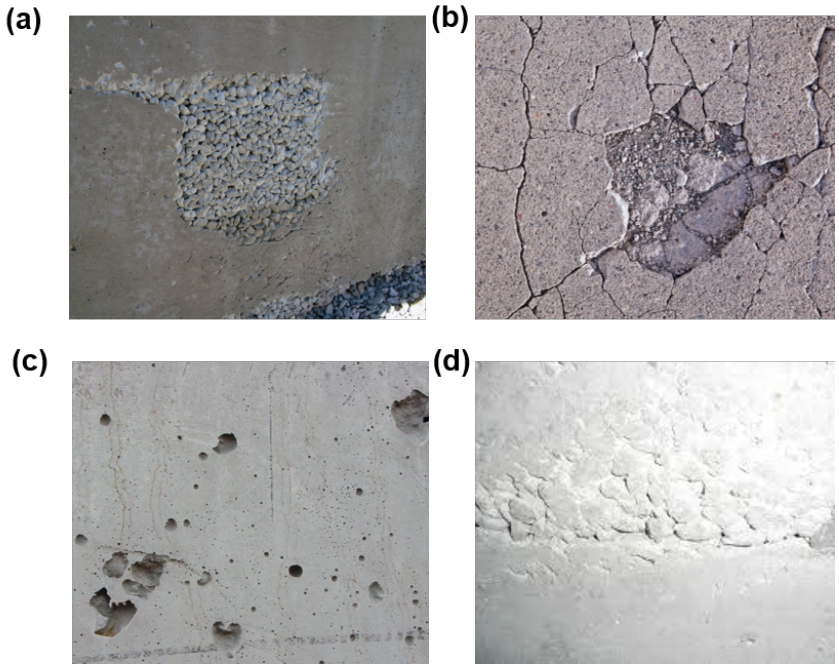

Figure 1.2: Physical faluires that are orginate from the microsctrure of cement paste seen as **(a)** consolidation related surface blemishes, **(b)** cracking, **(c)** porosity and **(d)** segregation.

1.2.2 Importance of Combined Methods in Answering Some Open Questions in Cement Chemistry

As mentioned, the performance of a cement of a given composition is controlled by factors such as mixing, time, temperature and additives. Furthermore, the microstructural formation governed by thermodynamics and kinetics determines the rheological, hardening and durability properties (performance measures). Considering this, some open questions in cement chemistry can be addressed using combined rheological-spectroscopic techniques, which include:

- How does the microsctructure formation affect rheological properties?
- Are hydrates completely or partially destroyed during shearing?
- How does ion migration affect rheological properties of hydrating cement?

Table 1.1: A summary of different parameters that are measured with rheological (macroscopic aspects) and spectroscopic methods (molecular aspects).

parameter	macroscopic aspect	molecular aspect
time scale	0.01 – 100 Hz	100 Hz – 10 MHz
length scales	0.1 – 100 mm	1 nm – 500 nm
material characteristics	elasticity, viscosity, glass transition	chemistry, particle diffusion, relaxation time, orientation and order phenomena

Rheo-combined techniques provide unique correlated information about a materials mechanical and molecular behavior can be deduced. The different physical parameters and material characteristics that are covered by both rheological and spectroscopic measurements are highlighted in Table 1.1. In Figure 1.3, a schemaitic overview of the rheological and spectroscopic materials properties that are measured with Rheo-NMR, Rheo-Dielectrics, and Rheo-IR. Rheo-NMR and Rheo-Dielectrics, were used and will be described in the context of studying molecular fluctuations in porous media (i.e. cement paste).

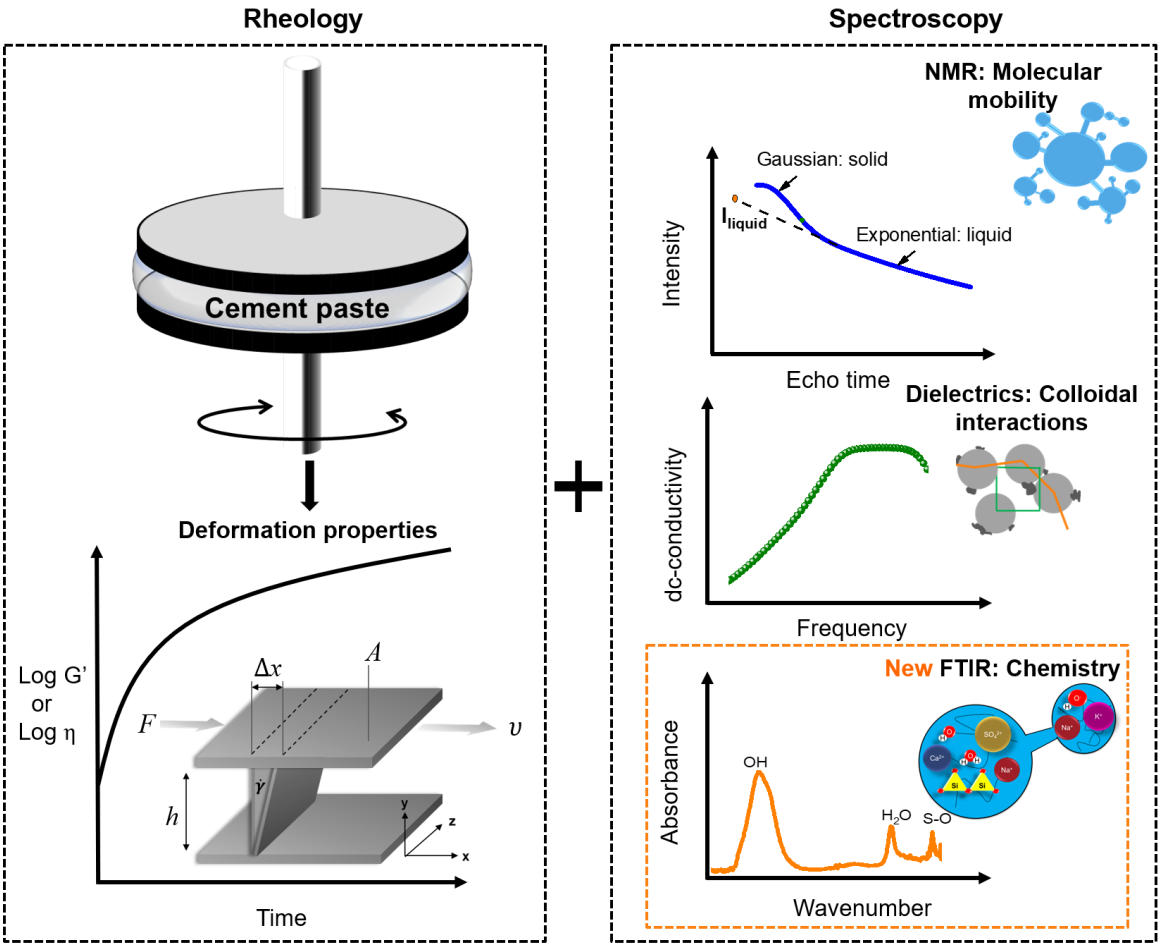

Figure 1.3: A schematic overview of the rheological and spectroscopic information deduced when using Rheo-NMR, Rheo-Dielectrics and Rheo-IR.

1.3 Research Objectives and Thesis Outline

Within the framework of the Rheo-IR technique development, three main objectives were prioritized:

- the development of the Rheo-IR experimental device, i.e. design, construction and implementation of an IR spectrometer (a highly sensitive chemical detector) to a strain-controlled rheometer,
- the application of the Rheo-IR combined technique to study two complex materials with, namely polyacrylic acid and cement paste,
- study of the result of deformation ($G'(t, \omega, \gamma_0)$, $G''(t, \omega, \gamma_0)$ of fresh cement paste using FT-rheology and different combined techniques: Rheo-IR, Rheo-NMR and Rheo-dielectrics.

Following the theory of Rheology, Rheo-combined methods and IR spectroscopy in **Chapters 2** and **3**, the results and discussion are outlined in the following way:

1. Design and construct a transparent attenuated total reflectance (ATR) crystal as the rheological geometry through which the FTIR spectra are sampled and the rheology is measured in **Chapter 4**.
2. Use off-axis parabolic mirrors to focus the IR light beam onto the sample, thus improving the signal to noise ratio in **Chapter 4**.
3. Signal to noise ratio improvement and optimization through physical changes in the system or mathematical enhancements in **Chapter 4**.
4. Testing the combined technique on simple and known materials that do not when a spectra is taken at room temperature in an open atmosphere (e.g. poly(methyl methacrylate) (PMMA)) as done in **Chapter 4.**
5. Apply the newly developed Rheo-IR set-up to monitor the network formation in a free radical acrylic acid copolymerization, in an aqueous solution as a proof of concept. By monitoring the polymerization kinetics through the appearance of a CH_2 ($\widetilde{\nu} = 2983 - 2880\ cm^{-1}$) stretching bond[45–47] and rheological development of the elastic and the storage moduli, a gel point is determined. This was done in **Chapter 5.**
6. Apply the newly developed Rheo-IR as well as Rheo-NMR and Rheo-diectrics to cement paste as a function of strain and water to cement ratio as done in **Chapter 6.**

Chapter 2

Principles of Rheology and Rheo-combined techniques

The basic theory of rheology is presented in this chapter. For this, some phenomenological models for viscous and elastic behavior based on rotational and oscillatory shear rheometry are described. The concept of Fourier transform (FT) rheology is introduced to the reader. The experimental details (i.e. instrumental specifications, test parameters, sample preparation) are given in the individual chapters together with the results and discussion sections. An overview the rheology of cement paste and the physical parameters that govern the rheology of this thixotropic and time dependent complex materials, is discussed. This is the main material of interest, the results of which will be discussed in Chapter 6. The fundamental theory, working principles and application examples of the three in-situ Rheo-combined methods used in this work, are presented in this chapter. These methods include Rheo-NMR and Rheo-Dielectrics. Since Rheo-IR was developed in this thesis, it will be discussed in the method development section in Chapter 4 and the theory of infrared spectroscopy is presented in Chapter 3.

2.1 Introduction

Rheology is an independent branch of the natural sciences and is commonly described as the science of flow and deformation of matter. The word 'rheology' is deduced from the Greek words *rheo* meaning "flow" and *logia* meaning "study of". Interestingly, spell check on most writing software often correct 'rheology' to 'theology' and it turns out that there is, in fact, a theological connection between the two. Markus Reiner, one of the founding people of rheology, proposed the Deborah Number[48] at the meeting of the 'Third Plasticity Symposium', on April 29th 1929[49]. It is named after the prophetess Deborah. The line "The mountains flowed before the Lord"[50] appears in Deborah's song in the Old Testament Book of Judges, which Reiner attributes to Deborah's understanding of material deformation properties. To begin with, everything flows, including mountains, but there is also an observation timescale associated with this. The mountains are solid for

humans during our relatively brief lifetime, but the mountains flow for the Lord, who has an infinite observation time.

Rheology uses a combination of theoretical concepts from fluid and solid mechanics with observed flow phenomena to describe a range of mostly soft materials such as simple liquids, emulsions, suspensions, polymers, solutions, or gel forms that show both fluid and solid-like character. These are called viscoelastic materials. Rheology is also important in understanding more solid-like material behavior. The above-mentioned list of examples can easily be extended to include examples from specific industries like shampoo from pharmaceuticals, dough from food science and blood from anatomy. In general, these materials exhibit a complex superimposition of liquid and solid properties which strongly influence their flow behavior. Unravelling the structural behavior properties in relation to mechanical process is of high importance in both processing engineering and in product development. In the following chapter sections, some fundamental basics with regards to viscoelastic properties of material are introduced. A description of the types of rheological measurements that are possible and used in this work to describe complex material behavior based on work by Dealy 2006[51], Dealy 2013[52], Larson 1999[2], Mewis 2012[53], Shaw 2012[54], Tadros 2010[55] is shown. Additionally, the rheological behavior of concentrated non-spherical suspensions (i.e. cement paste) is presented, as this is a material of particular interest, in Chapter 6.

2.2 Fundamentals of Rheology

Flow and deformation of matter can be described by fluid and solid mechanics, which rely on the conservation of mass, momentum, and energy. The main goal in rheological experiments is to obtain information on the material properties under defined flow and deformation conditions in shear or elongation[52]. From the classical works of Sir Isaac Newton and Robert Hooke, the formal mathematical representations describing liquids and solids were modeled. Newton[1] reflected upon the resistance of a liquid to a cylinder rotating in a vessel. It was later converted and formulated in a more accurate general law of liquid-like behavior in the following relationship:

$$\frac{F}{A} = \ \sigma = \eta(\frac{v}{h}) = \ \eta\dot{\gamma}, \tag{2.2.1}$$

where F is the applied force over a specific area, A, resulting in a shear stress, σ. The viscosity is η and the rate of deformation, $\dot{\gamma}$, is the velocity, v, over a distance, x. This is illustrated in Figure 2.1 for two parallel plates where the top plate is applied with a force over a displacement Δx.

$$\frac{F}{A} = \sigma \quad [Pa]$$

$$\gamma = \frac{\Delta x}{h}$$

$$\dot{\gamma} = \frac{d\gamma}{dt} = \frac{\upsilon}{h} \quad [s^{-1}]$$

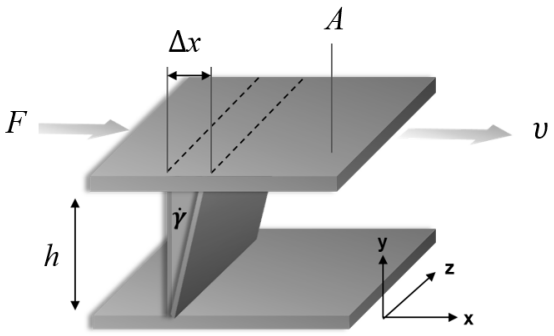

Figure 2.1: Illustration showing a sample (i.e. between two parallel plates) applied with a force, F, and shear profile generated across the gap, h and the shear rate derivation.

2.2.1 Viscoelasticity through linear phenomenological models based on spring and dashpot

In rheology, there are two limiting material behaviors, namely elasticity and viscosity[1]. A material is considered to behave purely elastically (i.e. solid) if it returns to its original size after a mechanical load has been applied then is removed. The viscoelastic behavior of materials can be tested using several different rheological techniques. These include creep testing, stress relaxation, steady shear and dynamic oscillatory shear testing. Before using the rheological testing methods, we will first describe commonly used linear phenomenological models that are based on the spring and dashpot analogies. These mathematical models detail a linear relation between the stress and the strain/strain rate. The elastic modulus (G, described later) and the η are constant.

Elastic behavior: Hooke spring model

When a structured fluid is at equilibrium (i.e. rest state), it has a minimum energy associated with the microstructure. Examples of this can be the inter-entangled chains in a polymer solution, randomly ordered particles in a suspension, jammed droplets in an emulsion. By applying a force or a deformation to a structured fluid, the material will shift from its equilibrium minimum state which will create an elastic force. The elastic force will try to restore the materials microstructure to its initial state. This behavior is analogous to a spring that is stretched and then returns to its unstretched (unformed) state as illustrated in Figure 2.2.

A spring represents a linear elastic solid that obeys Hooke's law[56]. This means that the applied stress (i.e. force per area), is proportional to the resultant strain (i.e. displacement) providing that the elastic limit is not exceeded. The elastic solid will return to its initial form when the same stress is removed as shown in Figure 2.2. If the elastic limit is exceeded, the spring/elastic solid will be distorted permanently. These principles also apply to a shear deformation similar to Figure 2.1, if the parallel plates were replaced with an ideal solid. The constant of proportionality in a simple elastic deformation is the elastic modulus (also known as the shear modulus of elasticity), G. The modulus is the measure of resistance to

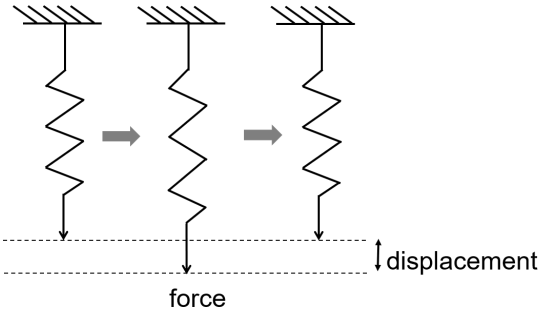

Figure 2.2: Hooke spring analogy: the response of an ideal solid (spring) to an applied and subsequently removed strain inducing force.

deformation, similarly to how the viscosity is the measure of resistance to flow. When a stress is applied to a purely elastic material, the observed strain is immediate (also works in reverse). When the stress is removed, the strain disappears immediately, meaning that there is no time dependence. This ideal elastic behavior is described by Hooke's law of elasticity:

$$\gamma = \frac{G}{\sigma}. \tag{2.2.2}$$

Viscous behavior: Newton dashpot model

Similarly to how a spring represents a linear elastic solid that obeys Hooke's law, a dashpot can be used to model a viscous material which obeys Newton's law. A dashpot is mechanical device, used in many applications to dampen shock or vibration. It consists of a plunger moving through a viscous Newtonian fluid (defined in Section 2.3.1). Once a stress/force is applied to a dashpot, the dashpot immediately starts to deform and continues deforming at a constant rate (i.e. strain rate) until the stress is removed as seen in Figure 2.3.

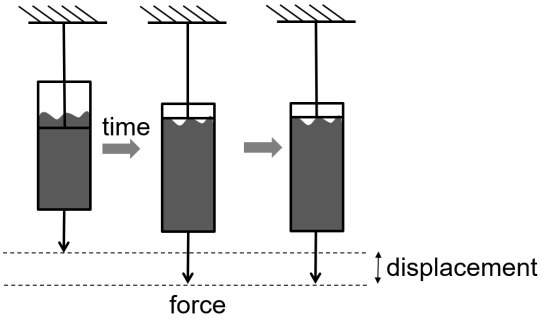

Figure 2.3: Newton dashpot analogy: the response of an ideal liquid (dashpot) to an applied and subsequently removed strain inducing force.

The energy required for deformation or displacement dissipated in the fluid, usually as heat, and the strain is permanent. The strain in an ideal liquid is expressed as follows:

$$\gamma = \frac{\sigma t}{\eta}. \tag{2.2.3}$$

Viscoelastic behavior

The rheological behavior of most materials can be classified in the region somewhere between liquid and solid and thus are classed as viscoelastic materials. As a result, it is possible to model or describe actual viscoelastic material behavior by combining springs and dashpots. The Maxwell model is the simplest representation of a viscoelastic fluid. It consists of a spring and a dashpot connected in series. The Kelvin-Voigt model, which uses the same set of elements but connects in parallel, can be used to describe a viscoelastic solid (see Figure 2.4).

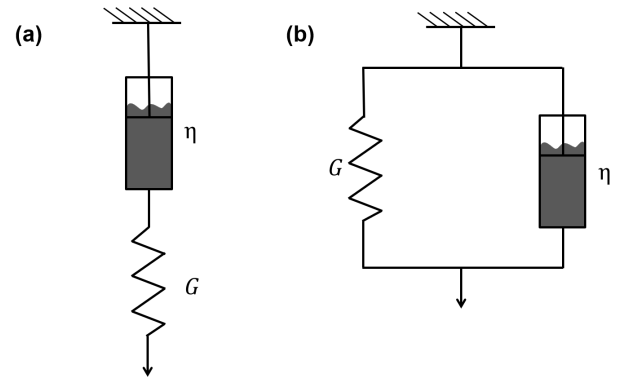

Figure 2.4: (a) Maxwell model: representative of a simple viscoelastic liquid; (b) Kelvin-Voigt model- representative of a simple viscoelastic solid. G and η are the shear modulus and viscosity, respectively.

When a stress is applied to a Maxwell model, the response is predominantly elastic and governed by G at very short times, but viscous behavior prevails at much longer times and is governed by η. The following expression can be used to define the strain evolution in a Maxwell model:

$$\gamma = \sigma(\frac{1}{G} + \frac{\sigma t}{\eta}). \tag{2.2.4}$$

When a stress is applied to a Kelvin-Voigt model, the strain takes time to develop because the dashpot retards the spring's response. Initially, the system behaves like a viscous liquid, but as the spring is extended, it behaves elastically over longer time scales. The relaxation process in a specfic time scale at which this transition takes place (i.e 1 s for polymer melts) is determined by the retardation time r, given by η/G. This is defined as the time required for the strain to reach approximately 63% of its final asymptotic value[2]. The following expression can be used to define strain evolution in a Kelvin-Voigt model.

$$\gamma = \frac{\sigma}{G}\left(1 - e^{-t/r}\right) \tag{2.2.5}$$

To accurately describe the overall behavior of a system under a given set of loading conditions, the standard linear solid model (see Figure 2.5a) combines aspects of the Maxwell and Kelvin–Voigt models. The response of a material when subjected to an instantaneous stress is shown to have an instantaneous component. As expected, the

instantaneous release of a stress causes a discontinuous decrease in strain. Depending on how the model is loaded, the shape of the time-dependent strain curve is true to the type of equation that characterizes the behavior of the model over time. The Burgers model, as shown in Figure 2.5b, which is basically a Maxwell and Kelvin-Voigt model linked in sequence, is the model that describes the viscoelastic behavior of real systems in response to an applied stress.

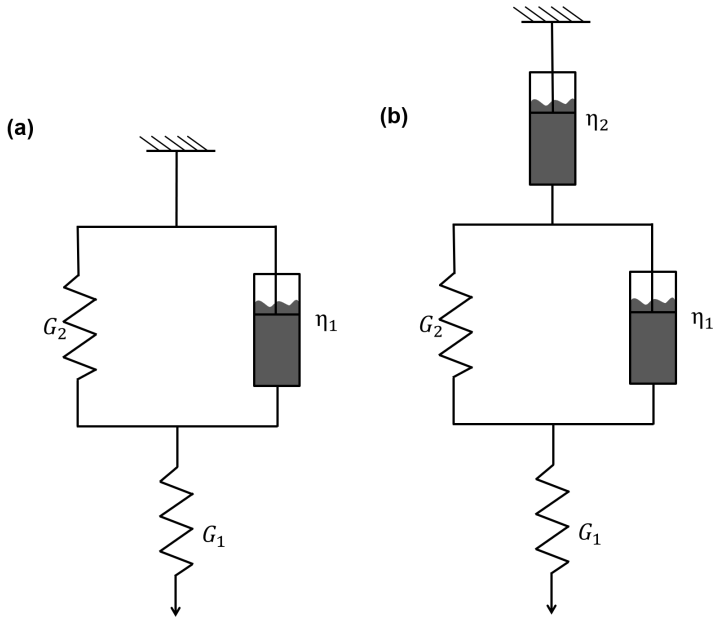

Figure 2.5: **(a)** Standard linear solid model. **(b)** Burgers model: the combined Kelvin-Voigt and Maxwell elements in series.

Combining both mathematical expressions (Equation 2.2.4 and 2.2.5) yields the following equation, which represents the strain dependency of a Burgers model[57]:

$$\gamma = \sigma(\frac{1}{G_1} + \frac{1}{G_2}\left(1 - e^{-t/r}\right) + \frac{t}{\eta_2}). \tag{2.2.6}$$

In the following sections, two rheological measurements are introduced, namely steady shear and dynamic shear rheometry.

2.3 Steady Shear Rheometry

In steady shear rheometry, the measurement takes place under steady state conditions where a shear rate is applied.

2.3.1 Shear flow

Shear flow can be visualized as layers of a fluid sliding over each other, with each layer flowing faster than the one underneath it. The top layer has the fastest maximum velocity, while the bottom layer is stagnant (see Figure 2.1). A shear force must act on the fluid in order for shear flow to occur. This external force takes the form of a shear stress (σ), which is defined as the force (F) acting over a unit area (A). The upper layer will travel x distance in response to this force, while the bottom layer will remain stationary. As a result, we have a displacement gradient (x/h) through the sample, which is the shear strain (γ). For a solid that acts as a single block of material, the pressure for an applied stress would be finite – no flow is achievable. However, for a fluid in which the constituent components will shift relative to one another, shear strain can begin to increase throughout the applied stress period. This results in a velocity gradient known as the shear rate or strain rate ($\dot{\gamma}$), which is the rate of change of strain over time ($d\gamma/dt$). As a shear stress is applied to a fluid, a momentum is transmitted; the shear stress is proportional to the momentum flux or rate of momentum transfer to the fluid's upper layer. Collisions and interactions with other fluid materials shift this momentum across the layers of fluid, resulting in a decrease in fluid velocity and kinetic energy. The shear viscosity or dynamic viscosity (η in Pa.s), which is a quantitative measure of internal fluid friction and correlated with damping or loss of kinetic energy in the system, is known as the coefficient of proportionality between the shear stress and shear rate (Equation 2.3.1):

$$\eta = \frac{\sigma}{\dot{\gamma}}. \tag{2.3.1}$$

Newtonian fluids have a shear stress that is proportional to the shear rate, and therefore its viscosity is unaffected by shear rate or shear stress. Air, basic hydrocarbons, and dilute colloidal dispersions are examples of Newtonian fluids. The viscosity of non-Newtonian fluids varies as a function of the applied shear rate or shear stress. It is worth noting that fluid viscosity is affected by both pressure and temperature, with viscosity increasing with higher pressure and declining with lower temperature. In this case, temperature is more important than pressure, with higher viscosity fluids like asphalt or bitumen which are much more temperature sensitive than low viscosity fluids like water.

The sample is filled between the plates at a known gap (h) as shown in Figure 2.6a, to measure shear viscosity with a stress or strain-controlled rheometer with parallel plate measuring systems. Rheometers with a stationary transducer and a moving motor can operate in either stress/strain controlled or stress/strain rate controlled mode, which means either a torque is applied and the rotational speed is measures, or a rotational speed is applied and a torque response is measures. In stress-controlled mode, a torque response

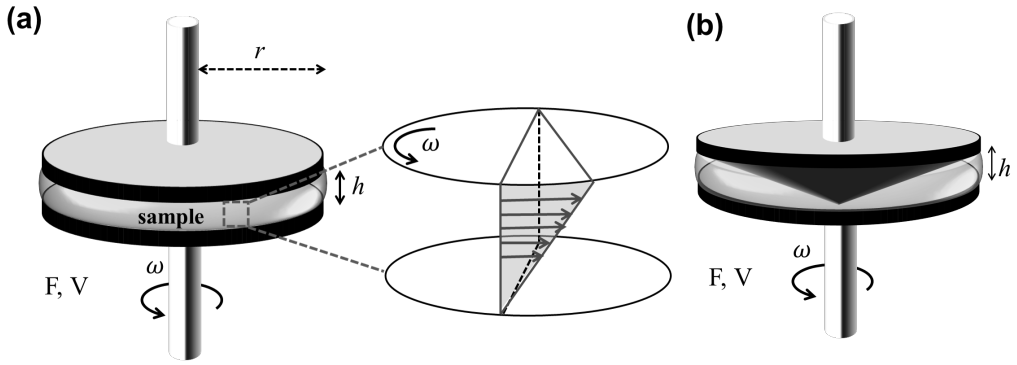

Figure 2.6: Illustration showing a sample loaded between **(a)** parallel plate flow geometry and shear profile generated across the gap, **(b)** cone-and-plate geometry in steady shear (geometries can also be used in oscillation), where V = $r\omega$ and F is force.

is required from the motor, which translates to a force (F) acting over the surface area of the plate (A), resulting in shear stress (F/A). A liquid-like sample can flow at a shear rate determined by its viscosity in response to applied shear stress. Since V = $r\omega$, the shear rate (V/h) can be calculated using the upper plate's measured angular velocity (ω), which is estimated by high precision location sensors, and its radius (r). Other viscosity measurement devices, such as cone-plate (Figure 2.6b) and concentric cylinders, are widely used, with cone-plate being favoured because the shear rate is constant through the sample. In a cone-plate geometry, the r increases linearly to compensate for the increase in strain, therefore the strain rate is equal throughout. The sample type and viscosity determine the type of measurement device and its dimensions. When working with large particle suspensions, for example, a cone-plate measurement geometry is not suitable. As a rule of thumb, a measuring gap 10 times larger than the particle aggregates, should be maintained in order to reduce overestimation of rheological behavior. Unlike a plate-plate geometry, a cone-plate geometry allows for a uniform shear profile throughout the sample. The main disadvantage of both cone-plate and plate-plate geometries is the tendency low viscosity and low surface tension liquids, like oils, due to the tendency of these fluids to leak out of the gap.

2.3.2 Shear Thinning and Shear Thickening

For some fluids/materials, the relationship between the shear stress and the strain rate is nonlinear. These are referred to as non-Newtonian fluids and there are two main types, which are shear thinning and and shear thickening fluids. Shear thinning, also known as pseudoplastic flow, is when a fluids viscosity decreases under a shear/strain rate. A commonly used example of a shear thinning fluid is ketchup, which when shaken in a bottle, becomes less viscous and subsequently flows out of the bottlet. Similarly, for materials such as paint, lotions and cement paste, an increase in the shear/strain rate results in a 'thinner' fluid. The behavior cement is slighlty more complex as it depends on several parameter such as solid content, admixtures, temperature e.t.c and will be further discussed in Section 2.5. Shear thickening or dilant fluids show an increase in the apparent viscosity as the strain/shear rate increases.

2.3.3 Steady Shear Rheometry Geometries

In some, rheological measurements, steady shear is placed on a sample is often refereed to as rotational geometry, (but can also be used for oscillatory measurements). The rheological characteristics of materials may be determined using rotational instruments in a steady simple shear flow with a uniform deformation regime. Imposition of constant rotational speed or constant torque, corresponding to controlled shear rate and controlled shear stress, respectively, are the two basic deformation regimes. Furthermore, several rotational rheometers can measure viscoelastic material characteristics using harmonic oscillations. In current rotational rheometry, three types of measurement methods are typically used: concentric cylinder (see Figure 2.7), cone-and-plate, and parallel-plate (see Figure 2.6). Rotational rheometers can measure shear rates that are typically between 10^{-3} and 10^{3} s. A cylinder measurement system, as illustrated in Figure 2.7, consists of an outer cylinder (cup) and an inner cylinder (bob). Depending on whether the cup or the bob is rotating, there are two ways of functioning. The Searle technique uses a rotating bob and a stationary cup, whereas the Couette technique uses a moving cup and a fixed bob. The disadvantage of the Searle system is that the sample is static whereas the measuring unit rotates, which may result in Taylor vortices at high shear rates[58]. The gap between the two concentric cylinders should be small enough to maintain a consistent shear rate for the sample confined in the gap. When the ratio of the outer to inner cylinder radius is more than 0.97, this criteria is met, and the gap is characterized as "narrow".

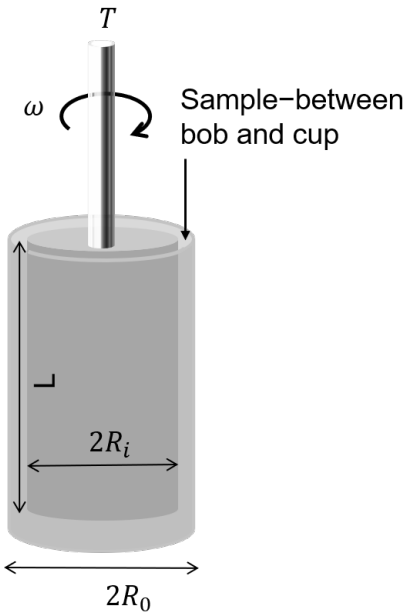

Figure 2.7: Schematic representation of a steady shear concentric cylinder, where R_0 is the radius of the cup and R_i is the radius of bob (geometry can also be used in oscillation).

On the other hand, when analyzing suspensions of relatively large particles, small gap concentric cylinder measurement devices are not useful. For this, wider gap viscometers are more desirable. However, wide gap viscometers present a different challenge, in that the shear rate varies and thus introduces inaccuracies. For a sample flowing within the

enclosed gap between the cup, with radius R_0 and the bob with a radius R_i where the bob is rotating with an angular velocity ω, then the shear rate is defined as follows:

$$\dot{\gamma} = 2\omega \frac{R_0}{R_0 R_i} \tag{2.3.2}$$

If the torque measured on the bob is T, then the shear stress is given by:

$$\sigma = \frac{T}{2\pi \times L \times R_i^2} \tag{2.3.3}$$

where L is the length of the bob that has been immersed into the cup.

2.4 Dynamic Oscillatory Shear Rheometry

Dynamic oscillatory testing the most commonly used rheological measurement method to investigate the linear viscoelastic behavior of a fluid. Oscillatory rheometry is sensitive to the microstructural changes, is relatively easy to use and has a strong mathematical foundation. When a viscoelastic material is subjected to oscillatory shear strain it is deformed sinusoidally by a deformation $\gamma(t)$ with amplitude γ_0 and a specific angular frequency (ω_1):

$$\gamma(t) = \gamma_0 \sin(\omega_1 t) \tag{2.4.1}$$

where t is time. Therefore, the shear rate is expressed as the time derivative of the shear strain as follows:

$$\dot{\gamma}(t) = \frac{d\gamma(t)}{dt} = \gamma_0 \omega_1 cos(\omega t) \tag{2.4.2}$$

When the strain amplitude is sufficiently small, the response is linear, and the corresponding stress of the viscoelastic material is:

$$\sigma(t) = \sigma_0 sin(\omega t + \delta) \tag{2.4.3}$$

where the shear stress is $\sigma(t)$ with amplitude σ_0 and angular frequency ω. The phase is shifted by an angle δ (mechanical loss angle).

2.4.1 Linear Oscillatory Rheometry

In order to probe into the linear (unperturbed) material properties, small amplitude oscillatory shear (SAOS) testing is used. The results from SAOS are usually reported in terms of the storage modulus, which characterizes to the elastic portion of the viscoelastic behavior, and loss modulus, which corresponds to the viscous portion of the viscoelastic behavior as follows:

$$\sigma(t) = \gamma_0 [\, G'(\omega) sin\omega t + G''(\omega) cos\omega t]. \tag{2.4.4}$$

Here, $G'(\omega)$ is the storage (elastic) modulus, which is a measure of the energy that can be used to partially recover the deformation (i.e. the reversible stored energy). The loss (viscous) modulus is $G''(\omega)$ and is a measure of the lost energy dissipated as heat through internal friction. The ratio of $G''(\omega)$ to $G'(\omega)$ is the tangent delta which is a damping factor:

$$tan\delta = \frac{G''(\omega)}{G'(\omega)} \tag{2.4.5}$$

For an ideally elastic material behavior, there is no viscous part ($G'' = 0$) therefore, $\delta = 0$ and $tan\delta = 0$. The other extreme is the ideally viscous materials ($G' = 0$) for which $\delta = 90°$ and $tan\delta$ approaches infinity. Depending on the time scale and temperature, viscoelastic materials show a loss tangent between the two extremes. When the elastic modulus equals

the loss modulus (delta = 45° or tanδ = 1), the material goes through a phase transition from liquid to solid or vice versa. An example is during thermoset curing at the sol/gel transition, the material transitions from liquid (tan$\delta > 1$, as G″ > G′) to solid (tan$\delta < 1$, as G″ < G′), after gelation.

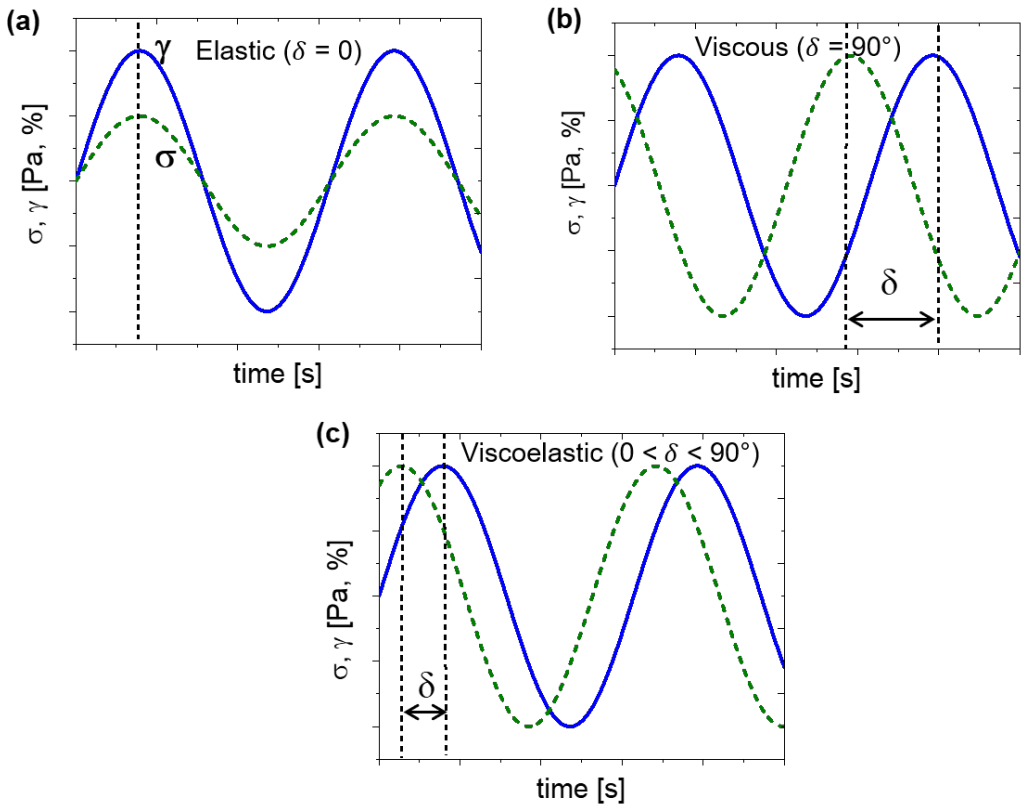

Figure 2.8: Stress and strain wave relationships for **(a)** purely elastic, **(b)** purely viscous and **(c)** viscoelastic material.

In terms of the stress-strain relationship, a purely elastic material where the stress is proportional to strain, the maximum stress occurs at maximum strain. Here, the deformation is greatest and both stress and strain are in phase, as seen in Figure 2.8a. For a purely viscous material where the stress is proportional to strain rate, the maximum stress occurs when the strain rate is maximum. The flow rate, at this point is greatest and the stress and strain are out of phase by 90° or $\pi/2$ radians, as seen in Figure 2.8b. For a viscoelastic material the phase difference between stress and strain will fall somewhere between the two extremes (see Figure 2.8c).

Another important material function used to characterize viscoelastic materials in SAOS is the complex viscosity:

$$|\eta^*| = \frac{|G^*|}{\omega} = \frac{(\sqrt{G'^2 + G''^2})}{\omega} \tag{2.4.6}$$

where $|\eta^*|$ and $|G^*|$are the absolute complex viscosity and complex modulus. For Newtonian fluids or inelastic materials, $|\eta^*| = \eta$, the shear viscosity.

Dynamic Strain Sweep (DSS)

It is critical to quantify the viscoelastic properties previously described in the linear viscoelastic regime of the material, where stress and strain are proportional. Microstructural properties are determined in the linear viscoelastic regime (LVE) when applied stresses are insufficient to induce structural failure (i.e. yielding) of the structure.

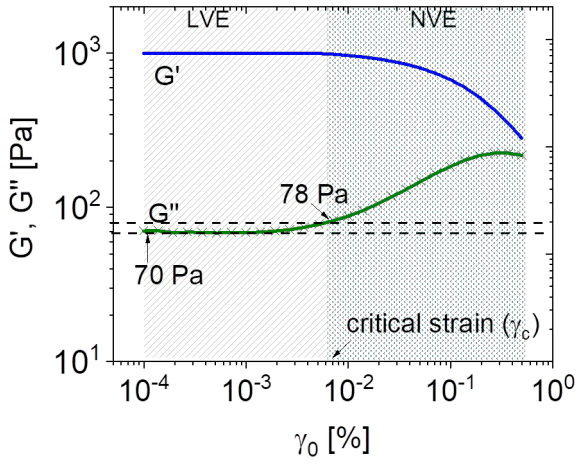

Figure 2.9: Strain-sweep test of a predominantly elastic material (i.e. ultrasound gel). The linear and nonlinear viscoelastic regimes are separated by a critical strain, γ_c.

Nonlinearities arise as applied stresses surpass yield stress, and measured results are no longer readily associated with microstructural properties. The LVE is described as the regime where the moduli (e.g. the storage shear modulus, G′, and the loss shear moduli, G″) are independent of the strain amplitude, γ_0. Whereas in the nonlinear viscoelastic regime (NVE), the moduli are changing as a function of γ_0. Generally, a distinction between the LVE and NVE region is not clear because the change between the storage and loss modulus is asymptotic. The criteria set to determine the end of the LVE region, for polymeric materials, is when there is a 10 % deviation from the plateau values of G′ and G″, the materials is no longer behaving in a linear fashion[1]. The LVE and NVE are seen in Figure 2.9, for an ultrasound gel (non-Newtonian liquid), where the inital G″ was 70 Pa then deviated to 77 Pa and higher in the NVE region. Furthermore, the strain amplitude at whcih this deviation occurs, is commonly refered to as the critical strain (γ_c).

Dynamic Frequency Sweep (DFS)

Since viscoelastic materials are time dependent, G′ and G″ are not material constants. Time dependency may be measured in an oscillatory test by changing the frequency of the applied stress or pressure, with high frequencies corresponding to short time scales and low frequencies corresponding to longer time scales, since $\omega = 1/t$, in s^{-1} or $\omega = 2\pi v$ in

rad/s. A frequency sweep on a viscoelastic liquid (representing Maxwell type behavior) yields a plot of the type seen in Figure 2.10 since G′ and G″ differ with angular frequency according to the following expressions for a Maxwell model (Figure 2.4a):

$$G' = \frac{G(\omega\tau)^2}{1+(\omega\tau)^2} \tag{2.4.7}$$

$$G'' = G\frac{\omega\tau}{1+(\omega\tau)^2} \tag{2.4.8}$$

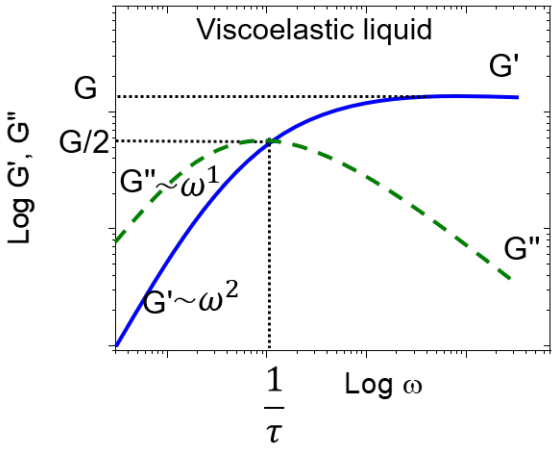

Figure 2.10: Frequency-dependent test of a sample that shows a viscoelastic liquid behavior, for the Maxwell model.

Generally, at high frequencies, G′ is larger than G″ and thus solid behavior predominates ($\delta < 45°$), while at lower frequencies, G″ is larger than G′ and thus liquid behavior predominates ($\delta > 45°$). The frequency at which G′ and G″ cross ($\delta = 45°$) is equal to $1/\tau$, and the relaxation time τ, or time for the elastic stress to decay by 50% of its original value. This is known as stress relaxation which is why such plots are also referred to as relaxation spectrums – stored elastic stresses are relaxed and transferred to viscous stresses by microstructure rearrangement. Knowing a material's longest relaxation time (real materials will have a range of relaxation times) can help predict the viscoelastic response of a material strained for a certain period of time. This can be evaluated using the Deborah number D_e. The D_e is the ratio of the relaxation time (τ) to the test time (t), or time over which stress is applied. Subsequently a $D_e > 1$ is indicative of a solid-like behavior while $D_e < 1$ indicates liquid-like behavior. When a frequency sweep is performed on a viscoelastic material, G′ is equal to the modulus of the spring, G, and frequency independent. The G″ is equal to $\eta\omega$ and dependent on frequency. Thus, at low frequencies, G′ is constant and dominates at low frequencies, whereas G″ decays with decreasing frequency but dominates at high frequencies. This behavior is common for glass-like materials. For a gel like material, the G′ and G″ are parallel and $0 < \delta < 45°$. Using the Maxwell model, with the spring in parallel, the gel-like behavior can be well described[2]. Since any associated structure

[2]The Maxwell model has infinite extendability, whcih is not characteristic of real polymers. It is used for simplicity.

(represented by single springs in their respective models) must be disrupted for macroscopic flow to occur, all viscoelastic solid and gel-like structures exhibit yield stress behavior.

2.4.2 Nonlinear Oscillatory Rheometry

In section 2.4.1, SAOS was discussed and in this section we introduce the concept of large amplitude oscillatory shear (LAOS). The region between SAOS and LAOS (transition region) is often referred to as the medium amplitude oscillatory shear (MAOS) regime[59]. When large amplitudes are applied, complex and nonlinear shear stress responses arise in many viscoelastic materials including polymers and suspensions. The material stress response, for a strain deformation input is considered to be nonlinear when the viscoelastic moduli, $G'(\omega, \gamma_0)$ or $G''(\omega, \gamma_0)$, begins to vary in γ_0 or when the output stress response is a non-sinusoidal waveform as seen in Figure 2.11a. Therefore, G' and G'' are no longer mathematically or physically definitive in this nonlinear region[60,61]. These waveforms are quantified in one of two ways; (1) Through geometric analysis by Lissajous-Bowditch (L-B) curves as shown in Figure 2.11b, where the stress σ is plotted vs. the strain γ (or strain rate $\dot{\gamma}(t)$)[60] or (2) through stress composition method using Chebychev polynomials by Ewoldt and McKinley[60] and the Fourier transform (FT) rheology method by Wilhelm et al.[61–63], as shown in 2.11c as a harmonic spectrum.

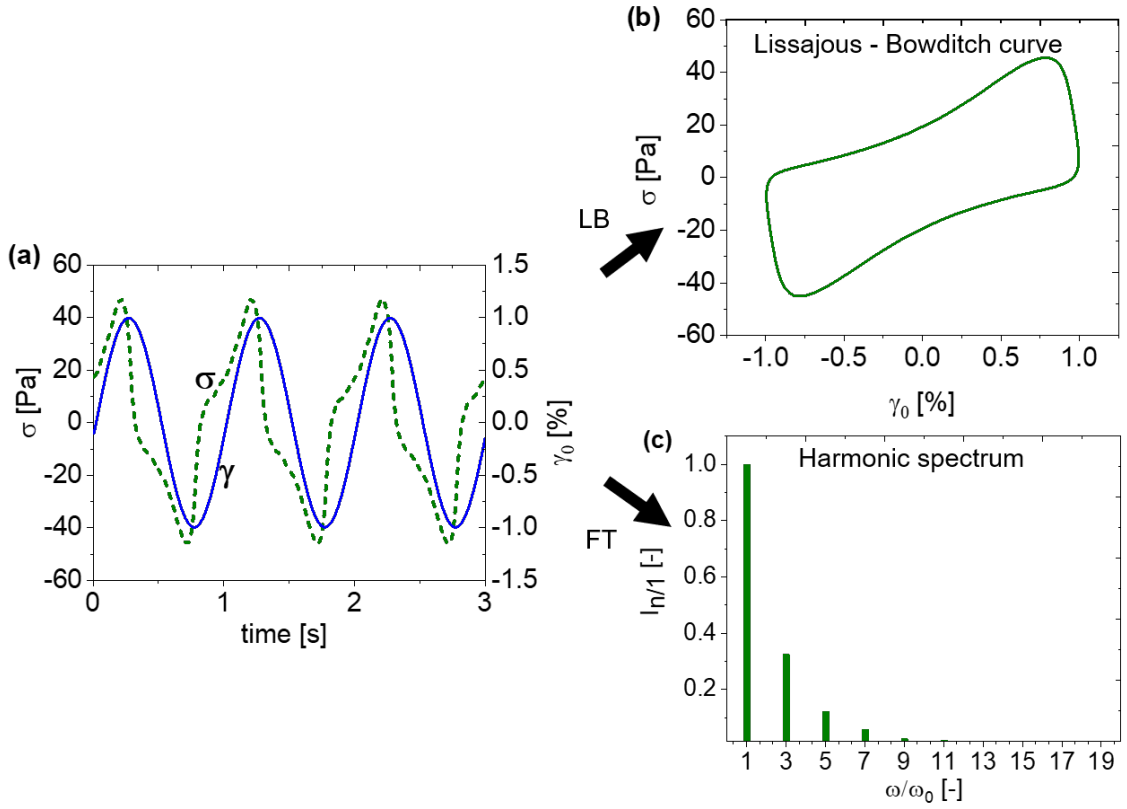

Figure 2.11: **(a)** Non-sinusoidal stress (σ) response at a given strain, **(b)** L-B curve of γ_0 and a function of σ, **(c)** higher harmonic spectrum of the Fourier transformed stress response.

Fourier Transform (FT)-Rheology

Lissajous-Bowditch figures provide a physical picture of nonlinear viscoelastic responses, however they do not provide any quantitative value to describe the geometric shapes of the responses. For this reason, Fourier transform (FT) rheology provides a more sophisticated approach for quantifying nonlinear responses[63]. As explained, when a sinusoidal strain amplitude is applied on a material, and the stress response is also sinusoidal with a phase lag of, δ, the materials is within the LVE regime. The stress response signal to the applied sinusoidal strain during the test, $\sigma(t)$, is recorded for Fourier transformation. If the $\sigma(t)$ is sinusoidal, the material is responding linearly. The periodic stress response, $\sigma(t)$, can then be expressed in the following complex notation[64]:

$$\sigma(t) = G_0\gamma_0 e^{i(\omega_1 t+\delta)} \tag{2.4.9}$$

Where G_0 is the absolute moduli at the basic excitation frequency, $\omega_1/2\pi$. Once the material falls into the NVE regime, the structure of the materials changes as a result of the applied deformation, thus the stress response is no longer pure sinusoidal (nonlinear response). To describe this nonlinear behavior of the module in Equation 2.4.9 , G_0 can be expressed by Taylor expansion with even exponents[63]:

$$\sigma(t) = G_0\gamma_0^1 e^{i(\omega_1 t+\delta)} + G_3\gamma_0^3 e^{i(\omega_1 t+\delta)} + G_5\gamma_0^5 e^{i(\omega_1 t+\delta)} + ... \tag{2.4.10}$$

The moduli $G_1, G_3, G_5\ldots$ are the prefactors and $\delta_1, \delta_3, \delta_5\ldots$ are the phase angles of the related Tayler series at the excitation frequency, the 3rd higher harmonic, the 5th higher harmonics and so forth. Through Fourier transformation (FT) of the output stress signal and subsequent qunatification of the relative intensity of higher harmonics[61,62], the influence of a small change in strain on the macrostructural build-up can be better understood. This FT-rheology technique has been used to study the origins of the nonlinearity for polymers and its filled systems[62], such as polymer melts[65], plastic[66] and filled rubber vulcanizate[64,67]. Typically, the intensities of the odd harmonics ($I_{(\omega_1)}$, $I_{(3\omega_1)}, I_{(5\omega_1)}, I_{(7\omega_1)}$ etc.) are of interest. Theoretically, even harmonics are neglected due to symmetry arguments[33]. The experimental variances must be minimised in order to compare the output stress signals from multiple samples (i.e., different solid fractions, or a sample at different time evolutions). This is done by comparing the intensity at higher harmonics that are normalized to the fundamental intensity I_1 giving the relative intensities,

$$I_{(n\omega_1)}/I_{(1\omega_1)} = I_{\ n/1}(i.e.\ I_{3/1} \ \equiv \ I_{3\omega_1}/I_{1\omega_1} \ = \ G_3\gamma_0^3/\ G_1\gamma_0) \tag{2.4.11}$$

where $n = 1, 2, 3, 4...$ and $I_{3/1}$ is expected to be directly proportional to γ_0^2.

By using the Fourier transformation, the rheological higher harmonics can further aid in making a more accurate assumption about the end of the LVE and the determination of the strain associated with it (i.e. the critical strain, γ_c).

2.5 Rheology of Concentrated Suspensions: Cementitious Materials

Understanding the rheological behavior of suspensions and dispersions requires a thorough knowledge of their microstructure and particle-fluid interactions. The rheology of a concentrated non-spherical yield stress/thixotropic suspension (i.e. cement paste) is discussed next. The rheology of cement and/or concrete is affected by the mixing regime[68], solid volume fraction[69], pumping[70], casting[71] etc. before and after hardening. Thus, precise understanding physical and chemical factors that affect the above-mentioned factors is vital. In this section, an introduction to methods and techniques for standard rheological tests and characterization of the yield stress, plastic viscosity, and structural build-up of cement paste, is given. With regards to the effects of colloidal interactions on these phenomena, the role of the solid fraction on the rheology of chemically changing suspensions and the thixotropic behaviors will be discussed. These materials are investigated further by the newly developed Rheo-IR (Chapters 4), Rheo-NMR and Rheo-Dielectrics in the results of Chapter 6 in order to correlate the mechanical behavior to the microstructural behavior.

2.5.1 Introduction to Cement Paste Mechanisms of 'Early' Hydration and the Influence on Rheological Behavior

Fresh cement paste is a mixture of cement powder and water. It has varying consistencies depending on the water to cement ratio, but generally is a plastic mass before it begins to harden. The hardening paste consists of hydrates of various compounds ($Ca^{2+}, Fe^{2-}, OH^{-}, SiO_4, SO_4^{2-}$), unhydrated cement particles, and water within minutes of water addition. The cement grains then dissolve ions from their surface into the water. The ions from the cement grain surfaces pass into the liquid phase/aqueous phase of the cement paste. The liquid phase becomes oversaturated, which causes precipitation of new combinations leading to undersaturation of the liquid phase. This leads to further dissolution of ions from the surafce of the cement grains into the liquid phase, then the process repeats itself. These combinations precipitate into hydrates. Theses hydrates are solids and gradually occupy a higher volume than the cement grains. They hold the grains together and form a rigid solid structure. Non-hydrated areas that contain water or air remain and are known as pores. Tricalcium silicate (Ca_3SiO_5 commonly named C_3S) hydrates relatively quickly, controlling the setting and hardening of cement to a great extent. It is responsible for early strength development (first 7 days) and typically 70% of C_3S reacts in 28 days and nearly all of it in a year[72]. C_3S and C_2S (dicalcium silicate, Ca_2SiO_4) reacts with water, principally generating a poorly crystalline calcium silicate hydrate ($Ca_3Si_2O_7 \cdot 3H_2O$ or *C-S-H*) gel and significant amounts of calcium hydroxide ($Ca(OH)_2$, also called portlandite or CH in cement chemistry nomenclature, not be be confused with a carbon-hydrogen bond in chemistry) as a secondary hydration product[73] (see Equations 2.5.1, 2.5.2 and 2.5.3). Equation 2.5.2 is the main and most dominant calcium silcate reaction between the cement paste and water, during early hydration[74].

$$CaO + H_2O \rightarrow Ca(OH)_2 \tag{2.5.1}$$

$$2Ca_3SiO_5 + 6H_2O \rightarrow Ca_3Si_2O_7 \cdot 3H_2O + 3Ca(OH)_2 \tag{2.5.2}$$

$$2Ca_2SiO_4 + 4H_2O \rightarrow Ca_3Si_2O_7 \cdot 3H_2O + Ca(OH)_2 \tag{2.5.3}$$

In addition to the above mentioned hydrates, the reaction between sulfate ions (which is added to cemnet as a set retarder) and the calcium aluminate phases in cement produces ettringite ($[Ca_3Al(OH)_6]_2 \cdot (SO_4)_3 \cdot 26H_2O$), or hydrated calcium aluminum sulfate hydroxide as shown by Equation 2.5.4[75].

$$Ca_3Al_2O_6 + 3CaSO_4 \cdot 2H_2O + 26H_2O \rightarrow [Ca_3Al(OH)_6]_2 \cdot (SO_4)_3 \cdot 26H_2O \tag{2.5.4}$$

Carbonation (Equation 2.5.5) occurs when carbon dioxide in the atmosphere reacts with calcium hydroxide in cement paste. Calcium carbonate is formed as a result of this reaction, which lowers the pH to roughly 9. The protective oxide layer covering the reinforcing steel breaks down at this temperature, allowing corrosion to occur. Carbon dioxide and calcium hydroxide can only react in solution, in the presence of water and CO_2, hence carbonation will be delayed in very dry concrete/cement.

$$Ca(OH)_2 + CO_2 \rightarrow CaCO_3 + H_2O \tag{2.5.5}$$

In this work, we investigate 'early' hydration as chemical and physical phenomenon that occur between the moment when cement makes contact with water and before setting (typically 3 hours, if no admixtures are added). Figure 2.12a shows an isothermal (20 °C) calorimetry heat flow curve of a Portland cement containing an initial solid volume fraction (ϕ) of 0.42[76]. The cement used here is the same one used in the rheological and spectroscopic investigation in Chapter 6, page 97. This time period is usually described as the initial dissolution and the induction period, highlighted in grey in Figure 2.12a. In the initial dissolution period, the rapid initial reaction (15 mins) occurs. Here hydrolysis of C_3S results in the release of Ca^{2+}, OH^-, K^+, Na^+ and SO_4^{2+} ions from the surface of C_3S grains, as shown schematically in Figure 2.12b. Initially the dissociation reaction is very fast, up to $10^{-5} mol \cdot (m^2 \cdot s)^{-1}$[77]. However, this hydrolysis slows down quickly but continues throughout the induction period. The induction period typically lasts up to approximately 1-2 hours, after which time a very small amount of C_3S has reacted, $< 1\%$[78].

Whilst there is general agreement on the framework of hydration, the fundamental mechanisms governing the slowing down of the reactions seen in the induction period (Figure 2.12a) 'are not yet fully understood'. For example reasons for the C_3S induction period beginning and ending is subject to several theories[79], including:

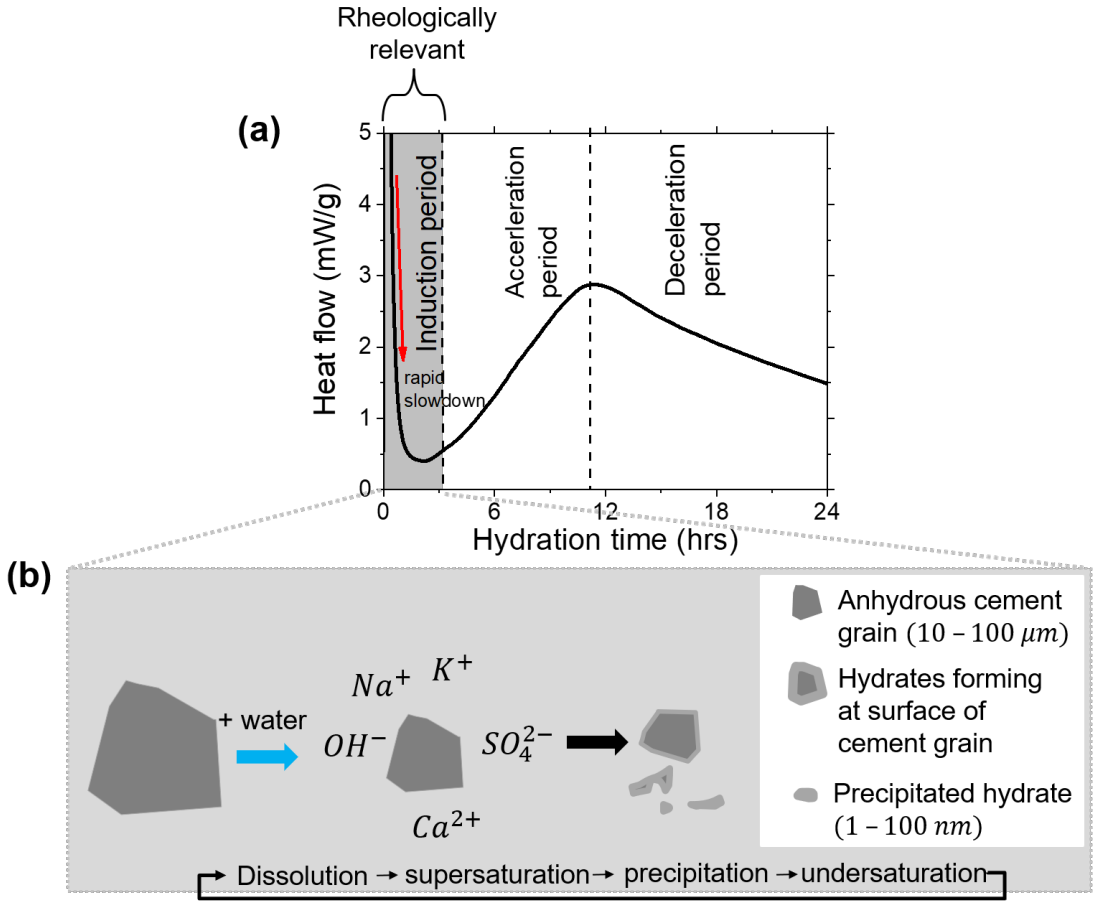

Figure 2.12: **(a)** Calorimetry curve of cement paste with $\phi = 0.42$ at a temperature of 20 °C where 3 main hydration periods are highlighted, namely the induction period, the acceleration period and deceleration period. Adapted from Figure 12 in Lu et al.[76]. In this work, the induction period is of interest and the other periods will not be discussed beyond this figure. Acceleration period: the hydration proceeds $(3-12$ hours), hydration products, including calcium hydroxide $(Ca(OH)_2)$ are precipitated from the saturated solution and bridge the gap between the neighboring cement grains, allowing the past to stiffen. Deceleration period: further hydration $(12-24$ hours) involving some complex form of diffusion process results in further deposition of the cement gel at the expense of the unhydrated cement and capillary pore water. **(b)** A schematic representation of the state of cement particles immediately when dispersed in an aqueous solution, is the first few minutes $(0-5$ mins) of hydration where the reaction rate is rapid and the calcium silicate hydrate (C-S-H) and ettringite is believed to be forming at the surface of the cement grains.

1. Dissolution as a function of undersaturation, see Figure 20 and 21 in Juilland et al.[80]. When the level of undersaturation falls below what is required to provide enough energy for the nucleation, the rate of dissolution slows. This theory implies that the dissolution mechanism depends on the solution concentrations and thus the degree of saturation[79].

2. The initial products form a protective layer over the C_3S particles in the form of a of a continuous but thin metastable layer of C–S–H, which when destroyed by osmotic pressure[81] or nucleation and growth[82], becomes more permeable. At this point, the induction period ends.

3. A nucleation and growth mechanism of C-S-H production controls the reaction rate

in the induction and acceleratory periods. The induction period ends when growth begins[83–85].

4. SiO_2 poisoning of the CH nuclei causes the induction period, if nucleation of CH is rate determining. It ends when the level of supersaturation is enough to overcome this and the CH products crystallize[86].

Bullard and Flatt[78] simulated the hypothesized mechanisms in theories 1 and 2, and found that both mechanisms lead to changes in solution composition that are consistent with those reported in the literature for C_3S hydration. All theories in which nucleation is the rate determining factor (theories 3 and 4) for the end of the induction period fail to address the issue of the reaction's rapid slowdown in the first few minutes, indicated with a red arrow in Figure 2.12a

The amount of unhydrated cement left in the paste reduces as time passes, while the hydrates of the different compounds increase. Part of the mixing water is taken up in the chemical reaction, some water fills the gel-pores, and the rest stays in the mixture. After a sufficiently long period of time (e.g. 28 days), the hydrated paste can be found to be composed of approximately 85 to 90 % hydrates of the different compounds and 10 to 15% unhydrated cement. The chemical reactions use some of the mixing water. Some of it fills the gel-pores, and the remaining water, which is not required for hydration or filling the gel-pores, creates capillary cavities. Depending on the age and the atmospheric temperature and humidity conditions, these capillary cavities may be completely filled with water, partially filled with water, or completely empty.

The above description, merely describes the approximate hardening process of cement paste and does not consider other influences that aid or prevent the hardening and hydration process. In the following section, we focus on the rheological properties of the cement paste that are directly related to the hardening process. For this we consider that cement paste is a thixotropic, yield stress material that simultaneously undergoes structural build-up.

Forces acting on particles in cement paste

In flowing suspensions, three types of forces coexist to varying degrees. These are namely, colloidal interactions such as electrostatic and steric interaction, Brownian motion and viscous forces. Colloidal forces originate from the interactions between particles. These forces are controlled by fluid properties such as polarizability and results in an overall attraction or repulsion between particles. Attraction arises from the Van der Waals attraction present between particles, or electrostatic attraction that is governed by the differently charged parts/surfaces of the particles. The repulsive forces can arise from electrostatic charges or from entropic repulsion of polymeric (i.e. superplasticizers) material that is present on the particle surface. Depending on whether the net results of forces is attractive or repulsive, the particles will tend to flocculate or disperse, respectively. The stability of colloidal suspension is determined by the equilibrium between the van der Waals attraction

forces (V_A) and the electrostatic repulsion (V_R) that occurs between the electric double layers, according to the classic DVLO theory (named after Derjaguin, Landau, Verwey, and Overbeck)[87]. The changes of these forces as a function of the distance between colloid particles is shown in Figure 2.13.

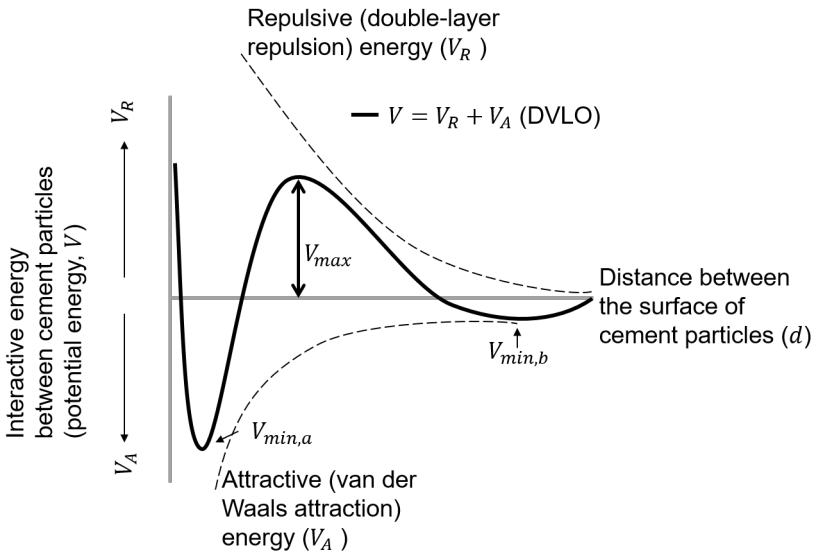

Figure 2.13: DLVO potential energy (V) of two particles as function of the particle distance (d), adapted from[88,89].

The total interaction/potential energy, V depends on the distance (d) between particles and is defined as the sum of the electrostatic repulsion, V_R, and the Van der Waals attraction, V_A, as shown by Equation 2.5.6:

$$V(d) = V_R(d) + V_A(d). \tag{2.5.6}$$

The repulsion forces are directly proportional to the product of charges of both particles and decreases with the second power of the distance between them, as shown below in Equation 2.5.7[89,90]:

$$V_R \approx \frac{q_1 q_2}{\epsilon d^2}, \tag{2.5.7}$$

where q_1 and q_2 is the charge of atom 1 and atom 2, respectively and ϵ is the permittivity constant of the system. The van der Waals attractive forces result from the appearance and disappearance of instantaneous dipoles in the particles. These dipoles originate from the movement of atom components following Equation 2.5.8:

$$V_A \sim \frac{1}{d^n} \tag{2.5.8}$$

Coagulation (irreversible) occurs when particles approach each other at the distance, d, corresponding to the first minimum energy ($V_{min,a}$), or the second minimum energy ($V_{min,b}$ in Figure 2.13), corresponding to flocculation. The energy barrier (V_{max}), which depends on particle size and surface charge, impedes particle approach towards $V_{min,a}$.

A colloidal suspension is considered stable when V_R is higher than V_A. In the case of large particles, the potential energy curve reveals a second, significant minimum, which can result in flocculation (reversible). In the presence of superplasticizers (i.e. water reducers), the zeta potential becomes more negative, and they also produce the steric effect, which counteracts particle approach[89]. The zeta potential is an electrical potential at the interface which separates mobile fluid from fluid, the so called shear plane, that remains attached to the surface of the particle[90]. Basically, the zeta potential causes adsorption of superplasticizers, but also of ions, thus, zeta potentials in cementitious systems are low ($\sim$ +2 and -4 mV)[91,92], which is not enough to cause electrostatic repulsion, but enough to cause superplasticizer adsorption. The changes of electrolyte concentration (mixing water plus the dissolving anions and cations from the cement grains) cause the changes of surface charge and consequently the thickness of diffuse layer. The reduction of this layer favors the coagulation. However, the surface of cement grains are continuously reacting with water and, as a result, are releasing different ions into the liquid phase thus the zeta potential varies all the time[89]. Furthermore, the DLVO is limited to low surface potentials (i.e., low surface charges) and monovalent counter-ions. However, the high pH (ca. 10) and reactivity of cementitious suspensions, results in the divalence of the calcium ions, and subsequently an attractive electrostatic contribution to the steric repulsion[93].

In addition to the abovementioned forces, particles of all shapes (including non-spherical particles) are influenced by Brownian motion that is described as a randomization radial distribution function, which is the spatial arrangement of surrounding particles as seen from the centre of any one of the particles. Brownian motion loses its influence depending upon size. For particles below 1 μm it has a strong influence, whereas above this size its influence dramatically reduces. This force ensures that the particles are in constant motion and any description of the spatial distribution of these particles is a time average. Lastly, viscous forces are the forces that are proportional to the difference in local velocity between a particle and the surround liquid (i.e viscosity).

From this, it is clear that although rheology measures at a macroscopic scale, a materials mechanical response is highly dependent on these microstructural properties. For example, a particle suspension containing a high concentration of particles, is more resistant to flow because the particles are required to move from each other's way to allow for flow. The effect of particles (solid) fraction in a suspension will be discussed in subsequent sections.

2.5.2 Viscosity of Cement Paste

Yield stress and thixotropy of hydration cement paste

The existence of a network structure provides cement with largely solid-like properties associated with elasticity, the strength of which is directly related to the intermolecular or interparticle binding forces that keep the network together, which is linked to the yield stress. If an external stress less than the yield stress is applied, the material deforms elastically. When the external stress reaches the yield stress, the network structure collapses

and the material begins to flow like a liquid. Thixotropy on the other hand is a time-dependent phenomenon that is best described as the material fluidifying under (high) shear and stiffening at rest (or at low shear rates)[94]. Thixotropic behavior is reversible by definition. Thixotropy has the effect of making rheological parameters (yield stress, plastic viscosity, etc.) dependent on the applied shear, or time of applied shear. Workability loss is mostly caused by the hydration reaction of cement during the dormant phase, as opposed to thixotropy, which is mostly caused by the consequence of coagulation and dispersion of small cementitious particles[43]. The reduction in shear stress at constant shear rate also contribute to structural breakdown of initial connections between cement particles owing to hydration[95,96]. As cement-based materials transition from a liquid to a solid material, the rheological (i.e. storage modulus) characteristics will increase with passed time. Chemical admixtures as well as the physical and chemical properties of cement can dramatically influence rheological qualities such as thixotropy, structural breakdown, and workability loss. In most cases, the yield stress and thixotropic behavior of cement-based materials can be described by means of the Bingham model[95,97,98] (see Equation 2.5.9). Here, σ_y is the yield stress and η_p is the plastic viscosity.

$$\sigma = \sigma_y + \eta_p \dot{\gamma}. \tag{2.5.9}$$

In an interlaboartory study[3] by Haist et al.[99], the rheological properties of cement paste using a variety of different geometries was studied, where silicon oil and ultrasound gel were used as a reference material. Figure 2.14 shows a stress-shear curve for ultrasound gel where the Bingham regression fits between a shear rate of $\dot{\gamma} = 21$ and 84 ($^1/_s$). A boxplot is used as a statistical representation of the data, where the blue rectangle represents the interquartile range (25-75%) and the horizontal line is the median value. The upper and lower qualities are the horizonal top and bottom line between the vertical line, respectively. This plot shows the limitation of the Bingham model at lower shear rates.

Even though the Bingham model is commonly used for cement-based materials, non-linear rheological behavior has been reported for some special/different cementitious materials[100–103] (i.e. self compacting concrete and highly plasticized concrete mixtures). As a result of the high shear rates applied coupled with a low water content in the mixes, the material tends to show a shear-thickening behavior[102]. Therefore, the application of the Bingham model for these cases, leads to an inaccurate value of the yield stress. By incorporating a third parameter, which is a power function, n, the Herschel–Bulkley model (Equation 2.5.10) is formed, where K is the consistency factor. However, the Herschel–Bulkley model does not perfectly describe the non-linear rheological behavior either[36,104,105]. Yahia et al.[104] have demonstrated that in shear-thinning materials, the Herschel–Bulkley model often yields the lowest yield stress (when compared to other models applied to the same set of data), but in shear-thickening materials, the converse is true.

[3]This was work done as a collaborative study that the thesis author was a part of, along with several other authors from different institutions in Germany. The project was funded by the Deutsche Forschungsgemeinschaft (German Research Foundation), priority program 2005.

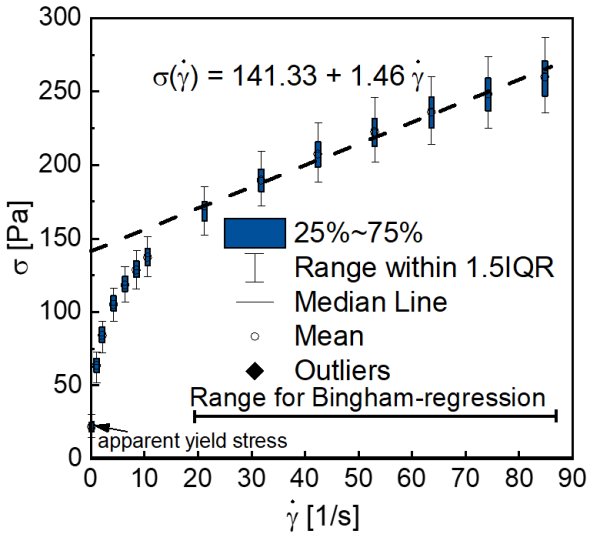

Figure 2.14: Boxplot shear-stress flow curve shown as of ultrasound gel. A Bingham fit is used between the range of $\dot{\gamma} = 21\ ^1/_s$ and $84\ ^1/_s$ to obtain a yield stress σ and reference plastic viscosity η_p. Reprinted, with permission, from Haist et al.[99].

If $n < 1$ (shear thinning), the zero shear viscosity (inclination of the rheological curve at zero shear rate) is always infinite, and if $n > 1$, it is always zero (shear thickening).

$$\sigma = \sigma_y + K\dot{\gamma}^n \tag{2.5.10}$$

Therefore, the modified Bingham model (Equation 2.5.11), where a linear term in the rheological equation is added, was proposed[104]. This model describes the nonlinear behavior for a material that is not highly shear-thickening. Here c is a coefficient, for which, when $c = 0$, Bingham behavior is observed.

$$\sigma = \sigma_y + \eta_p\dot{\gamma} + c\dot{\gamma}^2 \tag{2.5.11}$$

Effect of solid volume fraction (ϕ) on yield stress and thixotropy

At high concentrations, dispersions will act like solids, requiring a finite amount of stress to deform the structural network and allow the fluid to flow. Since the colloidal interactions that control the microstructure have a limited range and decrease with increasing inter-particle separation, the microstructure deformed under stress normally does not recover immediately from large strains. Particles form various structures depending on whether colloidal interactions are attractive or repulsive, which determines the material's rheological behavior. When attractive particle interactions occur, loose flocs with fractal structures may form, immobilizing a portion of the continuous phase and resulting in a higher effective particle volume fraction and, as a result, a higher viscosity. A network, spanning throughout the sample, forms above a critical volume fraction, resulting in extremely elastic, gel-like behavior and an apparent yield stress. For Bingham fluids (e.g. cement and ultrasound gel), where the yield stress is indefinite, an apparent yield stress can be defined by extrapolation

from the linear shear rate of the flow curve to the shear stress axis[1,106,107] (see Figure 2.14). Thixotropic behavior is caused by shear-induced floc structure breakup and recovery. At particle concentrations lower than the maximum packing fraction, electrostatic or steric repulsion between particles defines an excluded volume that is not accessible by another particle, resulting in a crystalline or gel-like state.

2.5.3 SAOS of cement paste

An understudied measure of thixotropy is determining the structural build up at rest. The rheological properties of dispersions are complex and highly dependent on the applied forces, particularly at high solid material. However, to understand the intrinsic material properties, that material should remain unperturbed. The procedures mentioned above (applied constant shear) are limited in that they are destructive, and this is not suitable if the chemical reactivity of a system has to be considered. For this reason, a non-destructive system may be considered like ultrasound spectroscopy or oscillation rheometry.

For cementitious materials, unlike polymeric materials, the critical strain (γ_c) cannot be related to the yield stress of the materials because this is not a true measurement of the onset of flow [108]. Therefore, there usually inconsistencies with the γ_c value fro materials that have networks of interaction particles [109–111], including cement paste. The change in shear modulus observed in oscillatory rheometry is thought to be the result of small changes in particle/particle contacts. Breakage of an interparticle bond with a range of a few nm with respect to particles on the order of 10 μm, for example, would result in a critical deformation of a few hundredths of percent. However, this is not indicative of the system flowing. A higher value (few percent), in contrast, is associated with large structural changes that corresponding to reorganization of the particle network at flow onset (i.e. yield stress)[108].

Structural Build-up

For cement paste, when the strain is limited to small strains (i.e <0.05%)[34,112,113], the particles remain in close contact with each other and respond elastically to the applied strain. Therefore, the microstructure is disturbed and the paste behaves as a solid. However, the range of the 'very low' strain amplitude is tested by applying a low to high strain sweep on the sample, and monitoring, the point at which the G' and the G'' deviate more than e.g 10% from the plateau (a criteria commonly used for polymeric materials). The strain at which the G' and the G'' deviate from the plateau is called the critical strain (γ_c). This estimation works if the materials is not changing as a function of time and strain ($G'(t,\gamma)$ and $G''(t,\gamma)$), as cement does. By using Fourier transform (FT) rheology, the evolution of the higher harmonics as a function of strain and time. As we have learnt in previous sections, if the applied strain has an output stress that is not sinusiodal, the material microstructure is affected, and higher order harmonics come into play. FT-rheology of cement paste, during early hydration (first 1 hour) is explored in deatail in Section 6.1, page 97.

Effect of solid volume fraction (ϕ) on structural build-up

The critial strain is the same for for cement pastes with water to cement (w/c) ratios in the range 0.40 and 0.45 (ϕ = 0.44 and 0.41, respectively). At w/c ratios above 0.45 or below 0.40, the critical strain either decreases or increases, respectively[113]. In general, the storage modulus increases as the volume fraction of solid particles increases[113]. Higher solid fractions allow for a faster formation of the elastic percolated network reflected by lower percolation time (t_{perc} in s)[34,114]. The t_{perc} is described as the resting period needed for colloidal particles to reach their favorable and equilibrium positions[115]. The formation of a sample-spanning connectivity between the structural elements describes the phenomenon of percolation[53]. An additional structural build-up index called G_{rigid} [Pa/s] was introduced by Mostafa et al.[114] to describe the linear increase in the G' after the formation of the percolated network, during the dormant period. This rigidification rate can also define the contribution of chemical hydration of the cement paste on the structral build-up/rigidification at rest (under a very small strain amplitude). The influence of cement fineness and content, alkali sulfate content, and suspension temperature on the t_{perc} and G_{rigid} of neat cement suspensions was investigated using non-destructive dynamic rheometry[34]. The resultant microstructural changes in cement suspension were investigated using zeta potential, calorimetric, and spectrometric techniques. The results indicated that the frequency of Brownian collisions, the distance between dispersed particles, and the level of cohesion between cement particles all influence the t_{perc}. Increase the number of contact points per unit volume of paste, the nucleation rate of cement hydrates, and the intensity of interparticle cohesion to achieve a high G_{rigid}.

In the following section, combined rheology techniques will be discussed. Since these methods provide both mechanical and molecular information, the processes that occur at a microscale that govern macroscale processes can be better understood.

2.6 Rheo-NMR

2.6.1 Principles of Nuclear Magnetic Resonance Spectroscopy

In this section a brief introduction into nuclear magnetic resonance (NMR) will be given followed by a section on nuclear magnetic relaxation, which is used in this work as method to study cementitious materials. Detailed literature on NMR spectroscopy, particularly on the quantification and qualification of structure, dynamics, and orientation in polymers is covered by Slichter 1978[116], Abragam 1961[117], Ernst 1987[118], Harris 1983[119], Blumich 2018[120] as well as Schmidt-Rohr 1994[121].

As all spectroscopic methods, NMR relies on the interaction of matter with electromagnetic radiation, specifically radio frequency energy. The frequency of radiation required for energy absorption is determined by three factors.

1. The type of nucleus (e.g., ^{1}H or ^{13}C).
2. The chemical environment of the nucleus (e.g., the methyl and hydroxyl protons found in methanol absorb at different frequencies).
3. The spatial location in the magnetic field if the field is not uniform.

Energy quanta are absorbed and/or emitted (no spontaneous emission is observable) resulting from discrete energy state transitions as per the Bohr frequency relation:

$$\Delta E = hv, \tag{2.6.1}$$

where ΔE is the difference in energy between the final and initial state, h is Plancks constant and v is the frequency of electro-magnetic radiation. The quantum mechanical property called spin, is the phenomenon from which nuclear magnetic resonance arises. The spin confers a spin angular momentum $\hat{I}$ to some nuclei. As a nucleus spins, so does its charge, resulting in a macroscopic nuclear magnetic moment $\tilde{\mu}$, which is directly proportional to the spin angular momentum as follows:

$$\vec{\mu} \; = \; \gamma\hbar\hat{I}, (\hbar = {}^{h}/_{2\pi}), \tag{2.6.2}$$

where γ is referred to as the gyromagnetic ratio (not to be confused with γ used for strain amplitude in rheology) and is the nucleus-specific proportionality constant. There are two interdependent spin quantum numbers associated with the angular momentum operator $\hat{I}$, these are namely the nuclear spin I and the magnetic spin quantum number m_I, used to determine the magnitude $\hat{I}^2 \; = \; I(I+1)$ as well as the z-component ($I_z \; = \; m_I \; = \; I, \; I-1, ..., -I+1, \; -I$) of the spin angular momentum, respectively. The spins, abundance, gyromagnetic ratio and sensitivity relative to ^{1}H of common nuclei like ^{13}C and ^{15}N can be found in literature[120]. The spin quantum number (I) for ^{1}H is $\frac{1}{2}$ and the magnetogyric ratio $\gamma/2\pi$ [MHz/T] is 42.6, which is the highest amongst common nuclei. Nuclei that contain both an even number of protons and neutrons (i.e ^{12}C and ^{14}N) have zero spin and are therefore 'NMR inactive'.

Magnetic resonance and the Laemor equation

NMR spectroscopy uses the fact that the magnetic moment $\vec{\mu}$ is able to interact with an applied, external magnetic field, B_0. The energy of the interation is as follows:

$$E = -\mu_z B_0 = -\gamma \hbar m_I B_0, \tag{2.6.3}$$

given that the direction of the external static magnetic field is along the z-axis. When a static magnetic filed is present, the degenerate $2I + 1$ nuclear spin energy levels split, accoring to their quantum number m_I, termed the Zeeman interaction. As a consequence, there are two energy states for a nucleus with spin = -$\frac{1}{2}$ called (1) the α-state with an energy $+\frac{1}{2}\gamma\hbar B_0$ (spin-up) and (2) β-state with energy $-\frac{1}{2}\gamma\hbar B_0$ (spin-down) as seen in Figure 2.15a. Therefore, the energy differnce between the two spin states is proportional to the magnetic field strength and the gyromagnetic ratio.

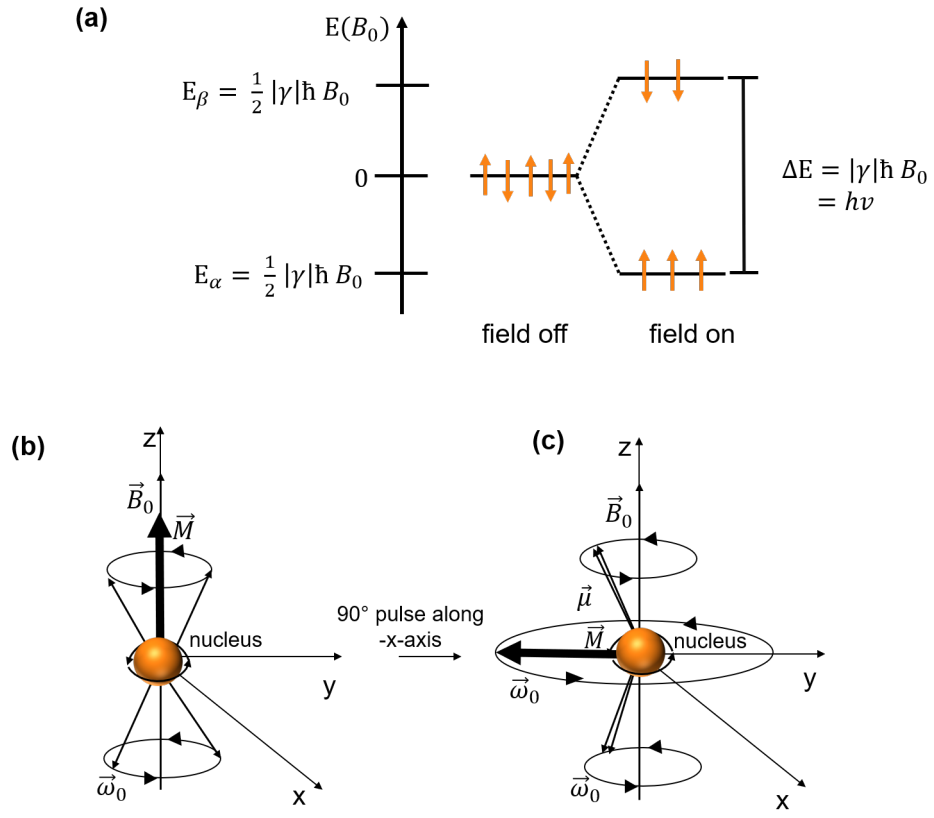

Figure 2.15: **(a)** Nuclear spin energy levels with and without an applied static magntic field B_0,**(b)** net magnitization, $\vec{M}$, and the precession and orientation of nuclear magnetic moments, $\vec{\mu}$, in thermal equilibrium and **(c)** coherent precession of the magnetic moments after a 90° pulse is applied along the x-axis leading to a rotation of the $\vec{M}$ in the x,y-plane, reffered to as transverse magnitization, at a Larmor frequency $\vec{\omega_0}$.

As the nucleus is spinning, the magnetic dipole does not completely align with the magnetic field, but encounters a torque that gives rise to a rotational motion (i.e. precession) about the direction of the magnetic field B_0 at Larmor frequency ω_0:

$$\omega_0 = -\gamma B_0 = \frac{\Delta E}{\hbar}. \tag{2.6.4}$$

More spins orient in parallel than anti-parallel to the static magnetic field because the energy of the α-state is lower than that of the β-state. The nuclear magnetic moments sum up to a net magnetization $\vec{M}$ in the direction of the static magnetic field as the longitudinal magnetization. Contrarily, $\vec{M}_x$ and $\vec{M}_y$, transverse magnetization, average out as the individual spins precess in a random fashion about B_0 as seen in Figure 2.15b.

2.6.2 NMR Relaxometry: The Bloch Equations and Relaxation Times

Thus far, the interaction between the spins and their environment have not been taken into account because only isolated spins were explained. However, a sample made up of matter needs both internal magnetic and electric field to be considered. Additional motion of magnetization can be caused by these fields, which is known as relaxation. Bloch[122] was the first to solve the problem of evolving magnetization under the influence of the sum of the constant, and a rotating field with simultaneous relaxation. He proposed the following equations to describe the evolution of the macroscopic magnetization:

$$\frac{dM_z}{dt} = \frac{M_0 - M_x}{T_1} + \gamma(M \times B)_z \tag{2.6.5}$$

$$\frac{dM_x}{dt} = \gamma(M \times B)_x - \frac{M_x}{T_2}, \tag{2.6.6}$$

$$\frac{dM_y}{dt} = \gamma(M \times B)_y - \frac{M_y}{T_2}. \tag{2.6.7}$$

Here, B is $B_0 + B_1$[4]. Additionally, two times have been introduced T_1 and T_2 which are the longitudinal and transverse relaxation time, respectively. The longitudinal relaxation, T_1, is also known as the spin-lattice relaxation, as it results from an exchange of energy between the spin system and the lattice. The lattice can be described as the assembly of the sample molecules considered as a reservoir of thermal energy as determined by the motion of molecules. The evolution of the transverse magnetization, T_2, is influenced by quantum transitions, using a transfer of energy between spins. Hence, it is also called the spin-spin relaxation.

Free induction decay (FID) and spin echoes

When a sample is exposed to a high magnetic field for an extended period of time, the protons within the sample will tend to align themselves along the direction of the external magnetic field. This forms a nuclear magnetization of the sample. However, if the magnetization is perturbed from the alignment with the field using a 90° pulse, precession of the resulting magnetization will occur. Gradually, the magnetization will

[4]The z-direction is that of the constant field with strength B_0 and the x-direction that of the radio-frequency field with angular frequency ω and amplitude $2B_1$ so that the total external field vector B has the components, $B_x = 2B_1 cos\omega t$; $B_y = 0$ and $B_z = B_0$[122].

dephase resulting in a loss of coherence of the precessing magnetization. Due to the dephasing of the transverse magnetization, a gradual decrease of the signal induced by the RF (radio frequency) coil will be observed. This decaying NMR signal, is the free induction decay (FID).

In the year 1950, Hahn[123] subjected samples to two RF pulses, thereby showing that a echo of the MR signal could be forced. By first applying a $\pi/2$ pulse (90° pulse) to a sample, an FID that follows a turn-off of a pulse is observed. A spread in the precession frequencies is caused by inhomogeneities, therefore some of the spins go out-of-phase with respect to the others. As a result of dephasing, the signal decays with time in the order of $1/\gamma\Delta B$, where ΔB describes the spread in the magnetic field over the sample. However, if a second 90° or 180° pulse is applied after a time τ, a reappearance of another signal at a time 2τ after the initial pulse, is observed. This was named the *spin echo* by Hahn. Hahn later showed the existence of echoes using Bloch's equations. If τ is varied, the solution shows that the echo diminishes exponentially with a time constant T_2. Figure 2.15c shows a pictorial description of the echo formation when a 90°-τ-90° pulse sequence is used.

Following the excitation pulse, the precessing magnetization induces a signal in a detector coil of wire wound around the sample in the form of an a.c. electric current at the resonance frequency. Detection and excitation are usually done with the same coil. M_0, the signal's intensity, is proportional to the total amount of protons in the sample. The signal M normally decays exponentially with time, t, as follows:

$$M(t) = M_0 \exp(-t/T_2) \tag{2.6.8}$$

As discussed in the next sections, the signal lifetime, T_2 is used to determine how mobile or confined the protons are (i.e of water in cement). The most basic NMR experiment is the application of a single pulse excitation and measurement of a FID. Figure 2.16 depicts it schematically.

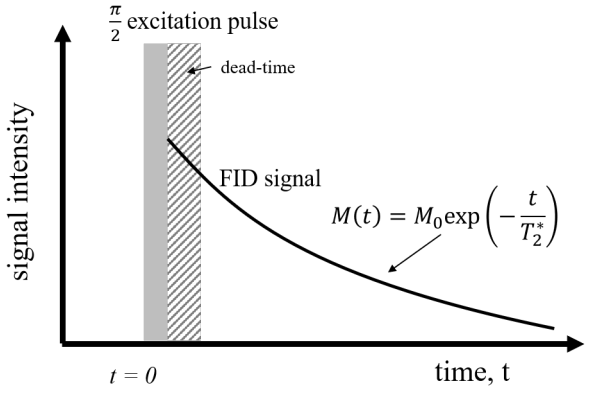

Figure 2.16: A basic one-pulse excitation, free induction decay (FID) experiment is shown schematically. In practice, the observed signal decays more quickly than expected due to magnet inhomogeneity, with a time constant T_2^* rather than T_2. Adapted from the 'Good Practice Guide No. 144' by McDonald et al.[124].

It is not possible to repeat the experiment once the signal has fully decayed. The rotating magnetization's precessing nuclei all rotate at the same time at first. However, due to magnetic interactions between nuclei, each nucleus has a slightly different magnetic field than its neighbors. As a result, each nucleus precesses at a slightly different frequency. They lose coherence and de-phase as a result. The signal amplitude decreases as the net magnetization, which is the vector sum of the individual nuclear moments in the sample, decreases. This is the origin of T_2 relaxation. When all of the nuclei in the transverse plane point in opposite directions, no net current is created in the detector coil, and no signal is seen. The nuclei, however, remain on the $x - y$ plane. They are still not in equilibrium alignment with the applied field along the z axis, as they were when they started. This second exponential relaxation process has a characteristic relaxation time T_1. It is always the case that $T_1 \geq T_2$.

Nuclear spin relaxation times: T_1, T_2 and T_2^*

The FID decays with a time constant T_2 due to magnetic interactions between nuclei that cause fluctuations in the local magnetic field from one nucleus to the next, as indicated in the previous section. Because all experiments are imperfect, the FID decays with a time constant $T_2^* < T_2$ in practice. The additional differences in local magnetic field encountered by various nuclei that cause de-phasing and signal loss on this shorter timescale have a variety of causes, including magnet inhomogeneity, internuclear interactions, electron-nuclear interactions and/or magnetic susceptibility. Magnetic field inhomogeneity occurs when the applied magnetic field varies with across the sample, causing nuclei in various regions to precess at different rates. The degree of field inhomogeneity is a function of the magnet quality and is hence not a measure of the sample. The associated decay time, $T_2^{\Delta B}$, is, often shorter than the true sample T_2. Internuclear interactions are magnetic dipolar interactions between neighboring nuclei cause variations in the local field. Interactions can occur between like nuclei (e.g., $^1H - ^1H$) or unlike nuclei (e.g., $^1H - ^{29}Si$, heteronuclear dipole interactions), with the former being more important for ^1H in water. True T_2 decay results from these interactions. Electron-nuclear interactions are particularly relevant to cement. T_2 decay is also aided by magnetic dipolar interactions between nuclei, such as ^1H, and unpaired electrons on paramagnetic impurity ions, such as Fe^{3+}. Because an electron's magnetic moment is approximately 6×10^2 times greater than that of a hydrogen ^1H, paramagnetic relaxation has a strong effect even when the electrons are "dilute". Local field fluctuations can be caused by spatial variations in magnetic susceptibility inside the material, such as porosity or paramagnetic contaminants. Susceptibility variations distort the applied field in the same way as a lens distorts light. Whether or not this is considered an inherent effect that contributes to T_2 or an extrinsic effect that contributes to $T_2^{\Delta B}$ is subjective. The observed signal decay rate is the rate at which the signal decays and defined as the sum of all intrinsic and extrinsic rates as follows:

$$\frac{1}{T_2^*} = \frac{1}{T_2^{\Delta B}} + \frac{1}{T_2}. \tag{2.6.9}$$

T_1 relaxation is caused by the same nuclear–nuclear and electron–nuclear interactions that cause T_2 relaxation. T_1 relaxation, on the other hand, is only affected by dynamic features of the local field, but T_2 relaxation is substantially influenced by both static and dynamic aspects. As a result, it is always a slower process. Thus, magnetic field inhomogeneity has no effect on T_1 relaxation[124].

2.6.3 Relaxation in Different Water Environments: Bulk water, Solids, Small Pores (ca. 1 - 10 nm)

The local magnetic field experienced by each one ^1H due to its close neighbors is temporally averaged to zero in pure bulk liquids due to rapid molecule tumbling. All nuclei have the same average local field, which is approximately B_0. As a result, the T_2 relaxation rate is slow and the relaxation period is long – a few seconds at room temperature for bulk water. The effective local fields grow steadily as molecular mobility is inhibited, for example by reducing the temperature or increasing the fluid viscosity. Therefore, T_2 becomes shorter and shorter. By adding paramagnetic materials, the T_2 can be further shortened. These ideas were discussed quantitatively in the late 1940s by Bloembergen, Purcell and Pound[125].

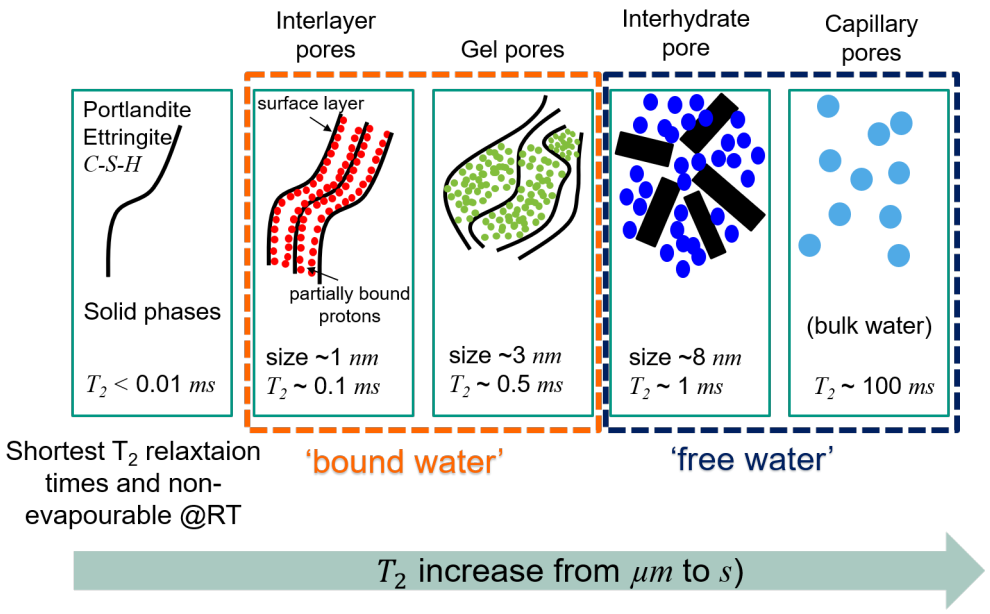

Figure 2.17: A schematic overview of the different T_2 and pore sizes[126–129] for ^1H environments found in cement paste. Pore schemes adapted from Muller et al.[128].

In solids, reduced molecular mobility is the extreme of liquids. The static distribution of local inter-nuclear magnetic dipole–dipole field dominates T_2 relaxation in this case. The rate of relaxation is extremely fast, on the order of a few microseconds. $T_2 \ll T_2^{\Delta B}$ almost always stays true in solids since this is quick enough. In solids, the decay cannot always be regarded exponential, as shown by a the one-pulse FID experiment. The decrease is more Gaussian-like for powdery crystals made up of pairs of static ^1H, such as calcium hydroxide, $Ca(OH)_2$ (portlandite). Figure 2.17 shows are schematic representation of the

different T_2 relaxation environments found in cement paste and is separated three fractions: solid water (from the hydrates, as discussed above), bound water-water near the pore surface layer- and free water-water in the bulk of the pore. The water in the pore's bulk behaves similarly to "free" water. It has a long T_2 relaxation period, which is usually in the seconds range. In general, the water in the near surface layer has a lesser mobility. Therefore, the relaxation time is substantially shorter, possibly as little as microseconds. As a result, the relaxation time dispersion should have two components. This is true in sufficiently bigger pores, except that the bulk water fraction completely outnumbers the surface layer fraction. In small pores, however, this is not always the case. In the timeframe of relaxation, diffusion provides a rapid exchange of bulk and surface layer water molecules. Thus, all of the water in the smaller pores has a single averaged relaxation rate.

T_2 relaxation differs from T_1 relaxation in that T_2 relies on both the low and high frequency elements of the function, whereas T_1 relies solely on the high frequency part. As a consequence, T_1 reaches a minimum as motion decreases, whereas T_2 continues to drop monotonically. As a result, separating free water from solids based on T_1 can be challenging because both have long relaxation durations. T_2, on the other hand, is simple since solids have short relaxation times whereas liquids have longer relaxation times. Hence why, it is not common to measure T_1 times for cement paste NMR relaxometry experiments. In this work we focus on the T_2 times and will therefore not expand on the discussion on T_1 further. The T_2 values associated with the different environments will be further discussed in Chapter 6, Section 6.3.

MSE-CPMG pulse sequence: Experiment to measure T_2 relaxation in cementitious materials

There are several experiments that are used to measure T_1 and T_2 relaxation times in cementitious materials such as the Hahn echo experiments, saturation and inversion recovery experiments. However in this work we focus on the mixed magic-sandwich echo (MSE) combined with the Carr-Purcell-Meiboom-Gill (CPMG)[130–132] experiment (specifically, T_2) as it was used to measure and separate evaporable water in different structural environments in cement.
Because a major portion of the rigid-part signal, which normally decays within 20 μs, vanishes during the dead time, direct crystallinity or hard/soft composition information is not easily obtained. Using specialized equipment with a very small dead time on the order of $1-2$ μs is the most elegant way for obtaining more quantitative real-time information[133]. If special probes are not available then an MSE can be used to focused on the first part of the FID and produce near-quantitative rigid fractions on almost any sort of equipment. As shown in Figure 2.18, an MSE can be used to tackle the NMR's dead time problem[132]. In cement, the CPMG experiment is used to separate evaporable water in various structural environments. In this experiment, a train of 180° refocusing pulses, following the initial NMR sequence, is utilized to generate a train of echoes from which the relaxation time T_2 is determined, as illustrated in Figure 2.18.

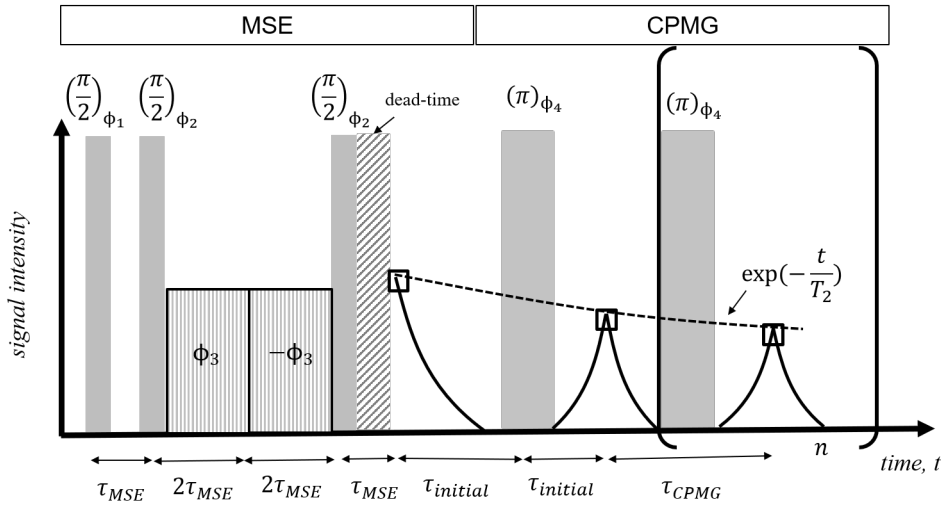

Figure 2.18: A combined MSE-CPMG pulse sequence to refocus the signal of a homonuclear dipolar coupled spin system, and to differentiate between more rigid and more mobile protons. CPMG:A series of echoes are formed by a series of 180° refocusing pulses. They decay in amplitude according to true T_2 relaxation. Adapted from Maus et al.[132].

NMR Relaxometry examples as Applied to Cementitious Materials

NMR relaxometry is a non-destructive and non-invasive method for pore water analysis. Mobile water within a less confined space will have slow relaxation times and more confined water will have faster relaxation times. In 1978, Blinc et al.[134] reported the first known NMR measurements of evaporable water in cement pastes. From 10 minutes after mixing to 28 days following hydration, these researchers measured the ^1H T_1 and T_2 relaxation durations of water in cement pastes. Several stages of hydration were discovered. However, the authors did not divide the signals into components according to different microstructural settings. It was Halperin et al.[126] who performed experiments that were the first ones to link measured relaxation times to cement pore size and specific surface area using the fast exchange theory[135] and idea of surface relaxation[136]. Because it is a more straightforward experiment and because chemically combined water in crystalline solids can be separated more easily from large pores, T_2 became the preferred method of measurement for most authors over T_1.

More recently, NMR diffusion and relaxation studies were used to investigate the post-curing of hardening cement pastes as a result of addition of alginate (98% water)[137]. By comparing samples with and without aliginate, the pore size distribution in the micropore region was unchanged. In another study, NMR sensors were emmbeded into drying Portland cement mortars[138] to study the evaporable water loss during hydration. The results were comparable to those done using gravimetric methods. Wyrzykowski et al.[139] used ^{1}H NMR relaxometry to study the effect of mechanical loading on microdiffusion in cement paste. The authors noted that under compression, the NMR signals related to the gel pore water decreased whereas the signal to unbound water, interhydrate water and capillary pore water increased. These changes were attributed to microstructural rearrangement.

2.6.4 Rheo-NMR Set-up: Mechanical Properties and Proton Mobility

Rheo-NMR is a unique tool that simultaneously measures the mechanical behavior, using a strain-controlled rheometer, and the relaxation properties with a low-field NMR spectrometer as shown by Ratzsch et al.[17].

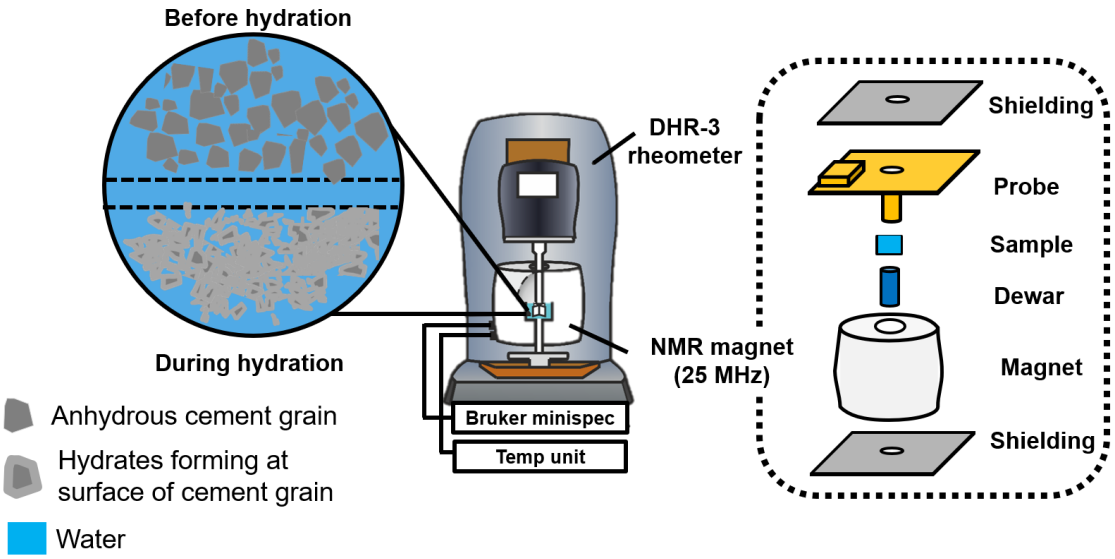

Figure 2.19: Low field (25 MHz) Rheo-NMR set-up attached to a DHR-3 TA Instruments rheometer.

Figure 2.19 shows the Rheo-NMR set-up adaped to a DHR-3 stress-controlled rheometer, however it can and has been used on a G2 ARES strain-controlled rheometer[17]. The rheology corresponds to macromolecular properties at a timescale of seconds and the molecular mobility in the form of ^{1}H transverse relaxation time takes place at a timescale that is between 50 μs and several hundred ms. This unique combination leads to new insights into the relationship between macroscopic rheometric observables and microscopic molecular dynamics. With this Rheo-NMR combination, Räntzsch et al.[140] characterized and quantified the crystallization of iPP at different temperatures which showed that there is a physical gelation process that occurs during polymer crystallization, that is mediated by the interaction of growing superstructures at volume fractions of 10–15%. This Rheo-NMR combined technique has also been used to characterize hydrating cement paste of different water to cement ratios[38] and shows that there is a partial dependence of the proton mobility of the increase in the storage modulus. The authors concluded that a process of percolation is also dominant in leading to rigidification/structuration. Recently, the combined technique has been used to investigate fat crystallization under shear[141]. It was seen that, applying a smaller shear rate results in a stronger crystal network.

2.7 Rheo-Dielectrics

2.7.1 Principles of Broadband Dielectric Spectroscopy (BDS)

The fundamental mathematics behind BDS are readily available in several books[22,142–144] and will serve as a basis for the derivations presented here. Broadband dielectric spectroscopy is based on the interaction of an external field with the electric dipole moment of the sample. By using this technique, the molecular dynamics in a very broad frequency (10^{-6} to 10^{11} Hz) and temperature range can be studied[145]. The changes of local electrical fields are measured, and are connected to the dynamics on a molecular scale. A dielectric measurement is performed by placing a sample between two metallic electrodes, which form a capacitor. The sample capacitance, C, is expressed as:

$$C = \frac{\varepsilon\ d}{A} \tag{2.7.1}$$

where ε is the dielectric permittivity of the sample, A is the sample surface area, and d its thickness. The properties of the material are characterized by the complex dielectric permittivity function, ε^*, defined as:

$$\varepsilon^*(\omega) = \varepsilon'(\omega) - i\varepsilon''(\omega) = \frac{C^*(\omega)}{C_0} \tag{2.7.2}$$

where C^* is the capacitor filled with the material under study and C_0 is the capacitance of the free space. The angular frequency is defined by $\omega = 2\pi v$, where v is the frequency in Hz. The real part is described by $\varepsilon'(\omega)$ and the imaginary part is $\varepsilon''(\omega)$ of the complex dielectric function. The dielectric function $\varepsilon^*(\omega)$ describes the material's dielectric behavior and contains information about molecular transport and relaxation processes by monitoring the charged ions and electric dipoles present in the molecule. Generally, transport processes in solids, particularly complex structured polymers, are influenced by internal morphology as well as important physical properties. Temperature, frequency, molecular mobility within the material, macroscopic orientation of the polymer chains, electromagnetic fields, and applied mechanical loads, including pressure and tensile stresses, all influence the dielectric function $\varepsilon^*(\omega)$[145].

Dielectric data is also often presented in terms of the complex conductivity function:

$$\sigma^*(\omega, T) = i\varepsilon_0\omega\varepsilon^*(\omega, T), \tag{2.7.3}$$

implying that

$$\sigma''(\omega, T) = \varepsilon_0\omega\varepsilon' \tag{2.7.4}$$

and

$$\sigma'(\omega, T) = \varepsilon_0\omega\varepsilon'' \tag{2.7.5}$$

ε_0 being the vacuum and σ_0 (T) is dc-conductivity. The connectivity of the pore system has been related to the conductivity of the cement paste. In this work, the rheological storage modulus, is correlated to the dc-conductivity of hydration cement, in a non-destructive way (i.e in SAOS).

2.7.2 Molecular Transport and Relaxation Processes in Water found in Cementitious Materials

Broadband dielectric spectroscopy (BDS) is a suitable technique to investigate water motion on different time scales (due to its large frequency range) and to obtain information about how the water molecules moves depending on the pore size[146–151]. This method has already been widely applied to the study of water dynamics in the porous network of nano-alumina[152], *C-S-H* gel[148,150], cements[151] as well as in other silica-based systems such as mineral clays[153]. Curing in a high relative humidity environment results in high dc-conductivity values, particularly during the early stages of hardening on cement-based materials[147]. In this case, the contribution of conductivity masks all dielectric relaxation mechanisms at low frequencies. The dc-conductivity is caused by ion motion in percolative pore channels within the *C-S-H* gel phase. Water, structural, chemically bound, physically absorbed, or free water, has been attributed to dielectric dispersion in the high-frequency range ($10^5 - 10^9$ Hz)[154–156]. Various relaxation models, such as the Debye relaxation[157][5], Cole–Cole (C–C) relaxation[158] (Equation 2.7.6), Cole-Davidson (C-D) relaxation[159], and Havriliak–Negami (H–N) relaxation[160] (Equation 2.7.7), characterize the mode of the relaxation processes in the complex plane or in a frequency dependency plot.

$$\varepsilon^*(\omega) \ = \varepsilon_\infty + \frac{\Delta\varepsilon}{1 + (i\omega\tau)^z} \tag{2.7.6}$$

$$\varepsilon^*(\omega) \ = \varepsilon_\infty + \frac{\Delta\varepsilon}{(1 + (i\omega\tau)^z)^k} \tag{2.7.7}$$

Here $\Delta\varepsilon$ is the dielectric strength ($\Delta\varepsilon = \varepsilon_s - \varepsilon_\infty$ and ε_s are the unrelaxed and relaxed values of the dielectric constant respectively), τ is the relaxation time, z $(0 < z)$ and $k(k \ \leq 1)$ are the stretching parameter and ω is the angular frequency. Research on the dielectric response of cement-based materials in the medium to high frequency range ($10^3 - 10^9$ Hz), from the initial mixing to several weeks of cure, has been conducted[146] at room temperature. The results are fit to a Cole-Davidson relaxation model:

$$\varepsilon^*(\omega) \ = \varepsilon_\infty + \frac{\Delta\epsilon}{(1 + (i\omega\tau))^k} \tag{2.7.8}$$

1. a low relaxation near 10^6 Hz, which grows initially and then decreases as curing advances;

2. a Debye relaxation near 10^8 Hz, which grows initially and then decreases with an advancing cure;

[5]The dielectric relaxation response of an ideal, noninteracting population of dipoles to an alternating external electric field is known as Debye relaxation[22].

3. a free-water relaxation near 10^9 Hz, which decreases with an advancing cure; and

4. an ion conductivity and electrode polarization, which decreases with progression in the curing process[146].

By comparing tricalcium silicate paste and tricalcium silicate with various ionic strengths, the source of the low relaxation was determined. When additional salts are present, the low relaxation is considerably reduced in C_3S compared to OPC, although the amplitude is identical. The authors hypothesize that the low relaxation is due to bulk polarization of ions accumulating on the gel surface, whereas the medium relaxation is due to water connecting to growing microstructure and acquiring a relaxation different from bulk water[146].

Additionally, studies on cement mortars were conducted in the low-frequency range ($10^{-2} - 10^6$ Hz)[147,148] at room temperature or lower. The dc-conductivity effects were found to be prominent at room temperature during the first week of hardening. During the first days, one dominant dielectric relaxation mechanism occurred at frequencies greater than 1MHz, but as the hardening time progressed, it progressively moved to lower frequencies. Two distinct relaxation mechanisms existed in the frequency spectrum, in $\varepsilon^*(\omega)$ and tan $\delta(\omega)$ formalisms, after a week. Both relaxation mechanisms shifted to lower frequencies with time. The dielectric strength of the low-frequency mechanism increased over time, while the dielectric strength of the high-frequency relaxation mechanism decreased. It was also determined that depolarization currents are strong during the early days of hardening and subsequently decrease as hardening progresses[147]. At low temperatures ($110 - 250$ K), dielectric spectra revealed three different relaxation processes related to water in 39 day hydrated C_3S samples. Each process showed its own dynamical characteristics and two slowest relaxation processes originated in different populations of water molecules[148]. A study was also conducted to investigate the rotational dynamics of hydration water confined in *C-S-H* gel over a broad temperature ($110 - 300$ K) and frequency ($10^{-1} - 10^8$ Hz) ranges[150]. Here, an apparent crossover in the temperature dependence was seen. It was attributed to the fact that the analysis is performed in a very limited frequency intervals, which masked the merging between the main water relaxation and a faster relaxation process. This hypothesis is consistent with recent literature data[161–163] on other systems.

2.7.3 Applications of Rheo-Dielectrics

Several approaches can be used to identify and characterize molecular structures under flow. For example, in the case of neutron scattering, birefringence detects an average orientation of the chemical bonds in the molecules, dichroism detects the orientation of a specific bond, and static scattering resolves a spatial distribution of the scattering elements that can be contrasted with isotopes[164,165]. The Rheo-optical and rheo-scattering measurements offer information about the non-equilibrium stationary structure of soft matter under constant flow[164,165]. If a small-amplitude oscillatory velocity field is added, for example, optical/scattering signals oscillating with time are superimposed on the steady signals, and analysis of the frequency dependence of the oscillatory signals can provide

us with information for the molecular dynamics under steady flow. Those oscillating signals, however, detect only a restricted part of the dynamics, the isochronal anisotropy and/or scattering point distribution that originate from the oscillatory flow and relax through molecular motion under steady flow, as with any observable signal. As a result, a supplementary approach to detect a non-isochronal component of the dynamics is required. This is when the dielectric approach comes in handy. The dielectric relaxation detects the correlation of microscopic polarization at two different periods and so specifies the non-isochronal component of the motion of molecules bearing electrical dipoles (and/or net charges) by definition[22,24]. Furthermore, even when the dipole-carrying molecules are flow-oriented, the flow does not differentiate between the head and tail of the dipoles (plus and minus charges), resulting in no constant electrical output. Because of the lack of a consistent signal, we can readily detect the dielectric signal for a weak electric field even when the flow is fast. Rheo-dielectric measurements have been conducted on a wide variety of soft matters[12,24,166–171] polymers, liquid crystals, and composites, under steady shear flow.

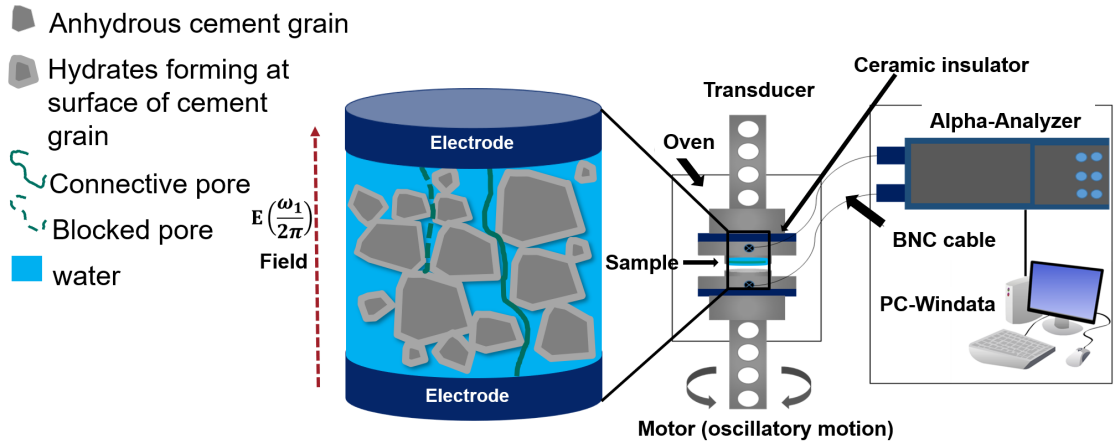

Figure 2.20: Schematic representation of the Rheo-Dielectrics set-up and the of connectivity of capillary pores that is deduced from the dc-conductivity.

The Rheo-dielectric data was acquired by applying an electric field in the shear gradient direction are merged with the rheological data to reveal interesting dynamics (and structure) of the component molecules in those materials. The instrumental parameters are presented in Chapter 6 and the instrumental set-up is seen in Figure 2.20 where the heating unit of the rheometer is an oven. Using cement paste an example, an electric field is applied to the material that is between two electrodes that also serve as rheological geometries. Depending on the connectedness/structural arrangement of the cement paste, the dc-conductivity at a specfic frequency will either decrease or increase, either due to hydration or percolation.

Chapter 3

Principles of Infrared Spectroscopy

Electromagnetic radiation, the wavelength of light and frequency are some of the few and important paramters that govern infrared spectroscopy. Although dielectric and nuclear magnetic resonance spectroscopy form part of the electromagnetic spectrum, the origins of electromagnetic absorption are briefly discussed as a backdrop for understanding the frequency, wavelength and wavenumbers that are associated with molecular transitions seen in infrared spectroscopy. The instrumentation used to produce the infrared spectrum of materials, the sampling methods used and the parameters used to diagnose the quality of the spectra are highlighted. These include, the resolution, the measurement time and most importantly the signal-to-noise ratio. Lastly examples of the use of FTIR to charaterize cementitious materials are given.

3.1 Electromagnetic Spectrum and Fundamentals of IR Spectroscopy

One of the ways that energy travels through space is through electromagnetic radiation. As defined by Maxwell's classical theory of electro and magneto dynamics, electromagnetic radiation is considered as perpendicular electric and magnetic fields that oscillate in a single plane at right angles to each other[172,173]. Spectroscopy is defined as the interaction of electromagnetic waves with matter, where light in this context, is the broad spectrum of continuous energy referred to as the electromagnetic spectrum. The different spectral regions of the electromagnetic spectrum are seen in Figure 3.1.

Electromagnetic radiation travels at the speed of light, ($c = 2.997 \times 10^8\ ms^{-1}$), in a vacuum. When one complete wave travels a fixed distance, the velocity of this wave is the product of the wavelength, λ, which is the distance between adjacent peaks, the frequency, v, is the number of cycles per unit time. Additionally, the wavenumber, $\widetilde{\nu}$, is the number of waves per unit length and has an inverse relationship to the wavelength as seen in Equation 3.1.1[174].

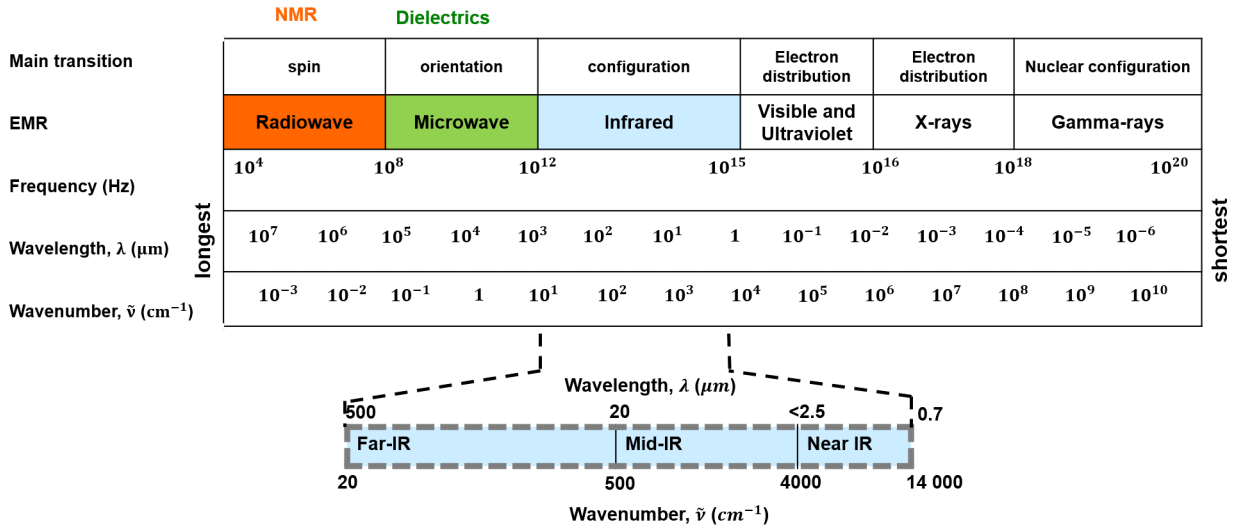

Figure 3.1: Spectral regions of electromagnetic radiation (EMR), with an expansion of the IR region (near, mid and far)., Adapted from Derrick et al.[175].

$$\widetilde{\nu} = \frac{1}{\lambda} = \frac{v}{c}. \tag{3.1.1}$$

The interaction of light with the electrical dipoles within the molecules is the basis of IR spectroscopy[176]. When materials are radiated with and absorb IR light, the absorbed energy causes vibrations of the nuclei along the atomic bonds and generates their IR spectrum. The absorbed energy, E, is directly proportional to the wavenumber as follows:

$$E = hc\widetilde{\nu}. \tag{3.1.2}$$

The parameters, E and h, represent energy in Joules and Planck's constant which has a value of $6.63 \times 10^{-34}\ Js$. Different atomic groups absorb at different wavenumbers and this can be used to identify the structure of those groups. The IR spectrum can be divided into three spectral areas, in relation to the visible region:

- near infrared (NIR), near the visible region, excites overtone or higher harmonic vibrations—range: $\sim 13000 - 4000\ cm^{-1}$ $(\lambda : 0.77 - 2.5\ \mu m)$,
- mid infrared (MIR) excites mainly fundamental vibrations—range: $4000 - 400\ cm^{-1}$ $(\lambda : 2.5 - 25\ \mu m)$,
- far infrared (FIR) excites lattice vibrations and below $300\ cm^{-1}$ it can be used for rotational spectroscopy—range: $400 - 10\ cm^{-1} (\lambda : 25 - 1000\ \mu m)$.

A large number of FTIR studies use the are within the MIR region, including in this work, but the NIR and FIR regions can also provide important information[177].

Infrared (IR) Spectroscopy: Molecular Vibrations as related to a simple Harmonic Oscillator

The characteristics of an atomic stretching vibration can be approximated by a mechanical model that consists of two masses connected with a spring. A movement of one of these two masses along the axis of the spring results in a vibration, called a simple harmonic oscillator[178].

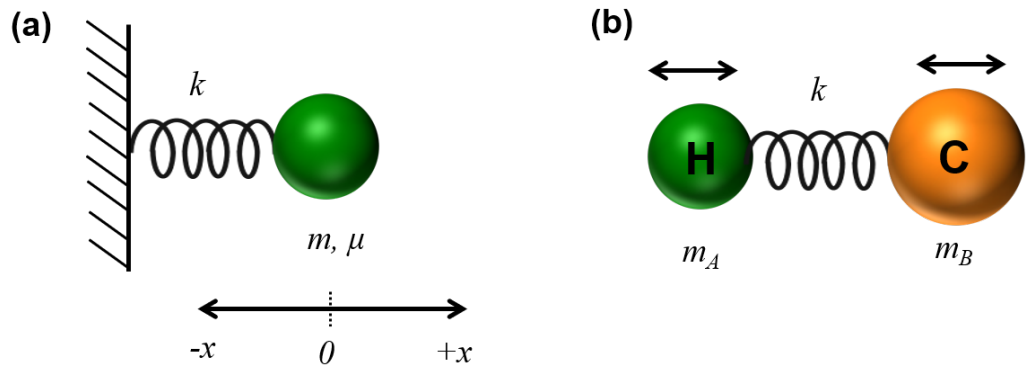

Figure 3.2: Harmonic oscillator**(a)** of a one-particle system with the reduced mass, m or a reduced mass μ and **(b)** two-particle (hydrogen and carbon) system with masses, m_A and m_B related to the hydrogen and carbon atoms, respectively.

First the vibration of a single mass (m or μ) attached to a spring connected to an immovable object (e.g. a wall) (see Figure 3.2a) is considered. If this mass is displaced by a distance x from its equilibrium position ($x = 0$) by applying a force, f, along the axis of the spring, the restoring force is proportional to the displacement, as per Hooke's law as shown in Equation 3.1.3:

$$f = -kx, \tag{3.1.3}$$

where k is the force constant in N/m, which depends on the stiffness of the spring. The negative sign is indicative of f being a restoring force, meaning that the direction of the force is opposite to the direction of the displacement. Therefore, the force tends to restore the mass to its original position[178].The potential energy, V, of the mass and spring can be arbitrarily assigned a value of zero when the mass is at equilibrium or rest position ($x = 0$). However, as the spring is compressed or stretched, the potential energy of the system increases by an amount equal to the work required to displace the mass. For example, if the mass is moved from position x to $x + dx$, the work and thus the potential energy dV is the product of the force, f, and the distance dx as follows:

$$dV = -f dx \tag{3.1.4}$$

Integrating between the rest position ($x = 0$) and x gives:

$$V = \frac{1}{2}kx^2 \tag{3.1.5}$$

Equation 3.1.5 results in a parabolic potential energy-displacement curve, for a simple harmonic oscillator[178].

Peak Positions and Absorbance

Peak positions are a result of the frequency of light that a molecule will absorb when excited by light as follows:

$$v = \frac{1}{2\pi}\sqrt{\frac{k}{\mu}}, \tag{3.1.6}$$

where v is the frequency in Hz, and μ is the reduced mass in kg. Reduced mass is defined as

$$\mu = \frac{m_A m_B}{m_A + m_B}, \tag{3.1.7}$$

where m_A and m_B are the respective masses of atoms A and B in kg (see Figure 3.2b). The wavenumber at which a molecule absorbs infrared light is determined by the reduced mass and the force constant, while the dipole moment and polarizability of the bond determine the relative intensity of absorption. Chemical substances typically do not have exactly the same ratio of force constants (typically 500 N/m for a single bond) and atomic masses. If the reduced mass of H and C is 1.5×10^{-27} kg and the bond strength is 500 N/m then the frequency, v, according to Equation 3.1.6 is 9.2×10^{13} Hz. By applying Equation 3.1.1, the wavenumber, $\widetilde{\nu}$, for the $C-H$ vibration is ca. 3062 $cm^{-}1$. Experimentally, the $C-H$ stretching band vibration is found in the region of $2800-3100$ cm^{-1}.

Furthermore, the different atoms have a certain degree of freedom with respect to relative motion within the molecule, resulting in a wide range of vibrations or torsional motion. As a result, the infrared spectrum of each chemical substance is distinct. An IR spectrum is a plot of the wavenumber against the measured IR absorbance[176]. As seen in Equation 3.1.8, the absorbance (A) values of spectral bands are described as the negative logarithm of the ratio between the intensity of light transmitted through a sample, I, and the intensity of light reaching the sample before it is transmitted, I_0. According to the Bouguer–Lambert–Beer law, the absorbance, A, is proportional to the sample concentration[177,179], where ε is the molar extinction coefficient, l is the length of the light passing a cuvette, and c is the molar sample concentration (mole), see Equation 3.1.9.

$$-log\frac{I}{I_0} = A \tag{3.1.8}$$

and

$$A = \varepsilon lc. \tag{3.1.9}$$

The responses of molecules with greater electrical dipole moments are stronger than those of molecules with smaller induced dipole moments. Dipole moments results from the charge distribution around molecule. Groups with strong dipole moments, such as $-NH$ and $-OH$, typically have strong absorption bands[176].

3.2 FTIR Instrumentation

3.2.1 Interferometer

At the core of every FTIR instrument is an optical device called an interferometer[174,177,180,181]. The oldest and most common interferometer is the Michelson Interferometer.

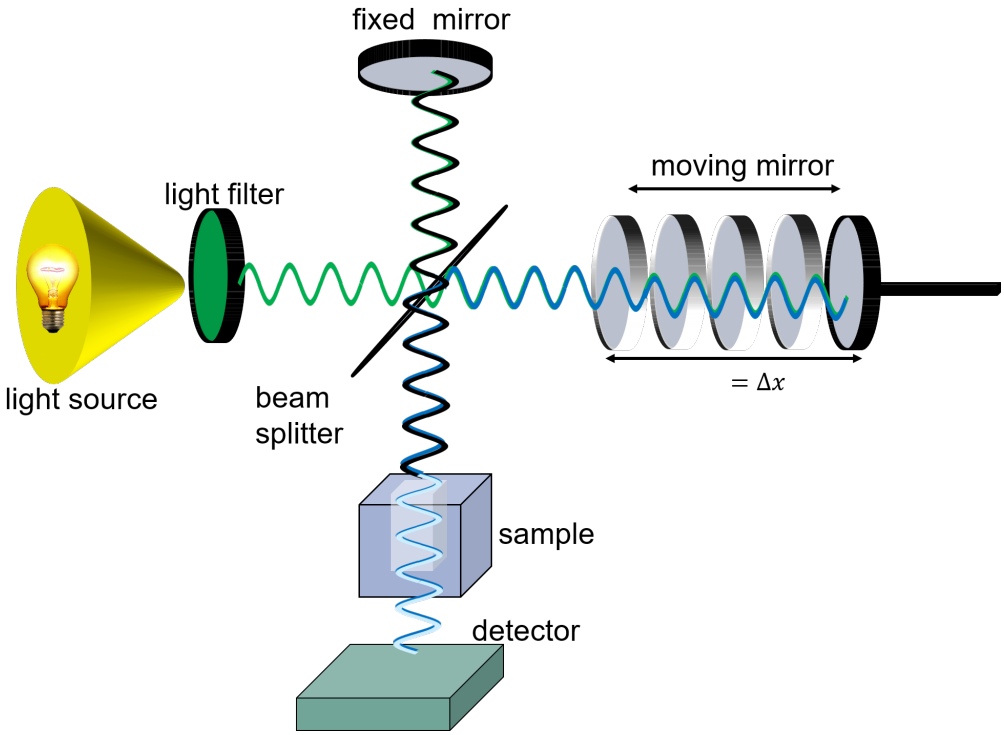

Figure 3.3: Schematic representation of the FTIR – Michelson Interferometer[177].

It consists of a beam splitter, a mirror that moves back and forth, a fixed mirror and an infrared source. The beam splitter is designed such that it transmits incident light and reflects some of the light incident upon it. Once the radiation source strikes the beam splitter it separates into two beams. One light beam is transmitted through the beam splitter to the fixed mirror and the second is reflected off the beam splitter to the moving mirror[174,176]. Thereafter, the light beams recombine and again, half of the reflected radiation is transmitted and, half is reflected at the beam splitter. This results in one beam passing to the detector and the second back to the source. Due to the effect of interference, the intensity of each beam, one passing to the detector and the other returning to the source, depends on the difference of path lengths (i.e optical path difference, OPD) in the two arms of the interferometer. This principle is illustrated in Figure 3.3. The path difference between the two beams varies as the moving mirror scans a defined distance (Δx), which is called optical retardation and is two times the distance traveled by the moving mirror ($2\Delta x$). A plot of light intensity as function of OPD is called an interferogram.

Interferograms recorded by the interferometer are a results of a phase-dependent interference of light with variable optical retardation. By first assuming that the source has only a

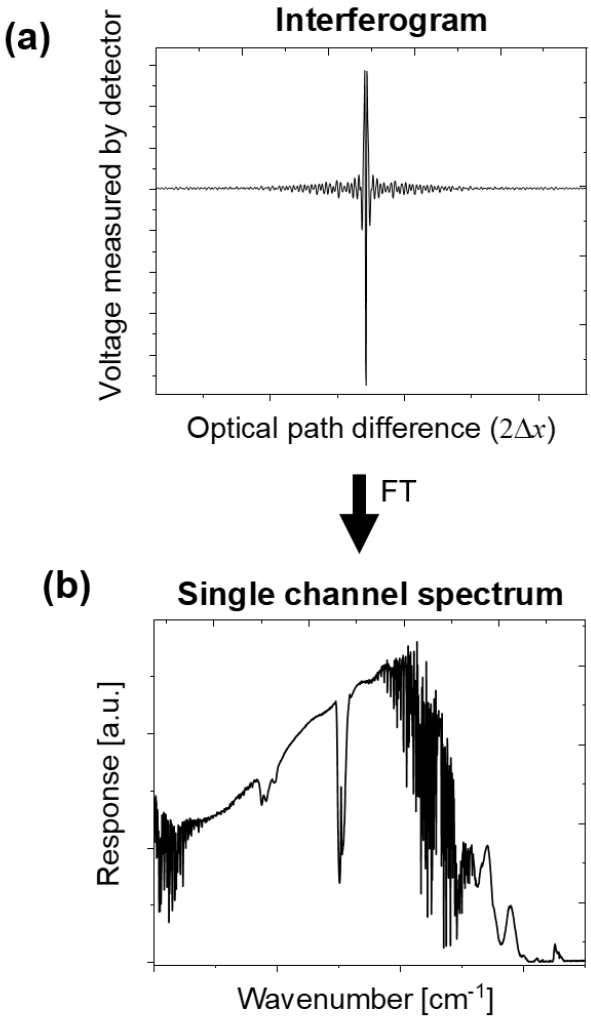

Figure 3.4: **(a)** The signal measured by the detector (i.e interferogram).**(b)** An example of a single channel spectrum after Fourier transformation (i.e. a background spectrum at atmospheric conditions).

single monochromatic wavelength, λ, the operating principle may be easily defined. When the moving mirror's position in relation to the beamsplitter is identical to that of the fixed mirror, the optical retardation is zero (zero path difference, ZPD, aslo known as the centerburst), and the two beams combine in-phase at the beamsplitter, resulting in constructive interference for the beam passing through to the detector. When the optical retardation is an integral number $(0, \lambda, 2\lambda)$ of wavelengths, the detector response reaches a maximum. Destructive interference at optical retardation values with intervals of $\lambda/2(\lambda/2, 3\lambda/2...)$ will also result in a minimum detector response. As the mirror scans at a constant velocity, the two beams will move in and out of phase, resulting in a simple sine wave. The Fourier transform of the sinusoidal interferogram yields a single band with the frequency and intensity of the monochromatic source. When a polychromatic source is used, the interferogram will be a sum of all the different cosine functions that correspond to all of the wavelengths and intensities in the source. Only when the path difference is zero are all the wavelengths in-phase. Consequently, the resulting interferogram in FTIR spectra has a very strong centerburst and rapidly damped intensity in the interferogram's

wings as seen in Figure 3.4a. In order to precisely determine the optical path differences in the interferometer, a helium neon (He-Ne) laser, $\lambda = 632.8\ nm$ ($\widetilde{\nu} = 15,800 cm^{-1}$) is used[174,180].

After Fourier transformation (FT) of the time domain signal, $I(t)$, the interferogram yields a frequency domain, $I(\nu)$, spectrum (see Figure 3.4b) according to

$$I(\nu) = \int_{-\infty}^{+\infty} I(t) e^{-2\pi i \nu t} dx. \tag{3.2.1}$$

An infrared spectrum contains two critical pieces of information: light (IR) intensity and frequency. Because of multiplexing, fast recording, and averaging, the FT technique has several advantages for infrared spectroscopy, including a significantly improved signal to noise ratio (S/N)[176]. The FTIR technique can measure molecular absorbances in short time intervals (e.g. < 1 s). Therefore, FTIR can be used to perform kinetic studies on polymerization reactions[182,183].The chemical changes in a sample stored in a temperature controlled environment can be monitored very sensitively and with a high time resolution using the rapid scanning capacity of FTIR. Thus, conversion curves for each species involved in a polymerization or curing process can be generated as a function of time and/or temperature[184]. However it is also important to mention that since absorbed radiation frequencies are unique for each molecule, bond strengths, atom number, material condition (state, interference/contamination, concentration, temperature, etc.), and the multiplicity of bending and stretching vibration modes, IR spectra can be quite complicated. In such cases, where possible, samples are separated and studied in their elemental form.

3.2.2 Detectors

In an optimized IR measurement (high spectral quality) for a given application, the spectrometer specifications should be carefully considered and be selected based on specific system components such as the source, optics, electronics, interferometer, beamsplitter and detector. Of the mentioned components, the detector selection is key as performance of a detector can be matched uniquely to specific applications. The choice of detector for spectral measurement is dependent upon but not limited to the following factors: (1) optical throughput (percent of IR beam reaching the detector), (2) spectral range of the measurement, (3) temporal resolution of the data collection, and (4) spectral resolution response time.

There are two main types of detectors used in mid-infrared spectroscopy, namely pyroelectric and quantum detectors. The IR Cube spectrometer can incorporate one of either a pyroelectric detector of deuterated L-alanine doped triglycerol sulfate (DLaTGS) or a quantum mercuric cadmium telluride (MCT) detector as standard detectors. The DLaTGS can be used from 250 cm^{-1} to 12000 cm^{-1} and the MCT can be used in the spectral range of 600 cm^{-1} to 12000 cm^{-1}[185]. Static measurements with a high throughput ($> 20\%$ of the IR beam reached the detector) are usually conducted using a DLaTGS detector because it is stable in high flux environments. However, the application of DLaGS detectors

is limited by low sensitivity, mainly due to thermal noise, and slow response time. The specific detectivity of the detector is described by Equation 3.2.2[174], as follows:

$$D^* = \frac{\sqrt{\Delta} f \times V_s}{V_n \times E_s \times \sqrt{A}}, \tag{3.2.2}$$

where Δf is bandwidth, V_s is detector signal, V_n is the root mean square (rms) detector noise, E_s is energy flux at the detector, and A is detector area. From Equation 3.2.2, it is clear that D^* is proportional to the signal from the detector relative to the energy flux reaching the detector. Therefore, a detector with a higher D^* can provide a higher response in a low energy flux environment. The detectivity of a DLaTGS detector (as given by the manufacturer) is with $D^* > 4 \times 10^8 cm\sqrt{Hz}/\ W$ and a maximum usable mirror speed of 10 kHz (this depends on the frequency of the He-Ne reference laser). Contrarily, a quantum detector such as one made from mercury-cadmium telluride (MCT) semiconductor material has a detectivity of $D^* > 6.4 \times 10^{10} cm\sqrt{Hz}/\ W$ and has mirror speeds up to 160 kHz. Thus, quantum detectors are about 100 times more sensitive than pyroelectric detectors. Although an MCT detector element has to be cooled with approximately $0.3 - 0.7\ L$ of liquid nitrogen (-196 °C), depending on the Dewar size, a maximum measuring time between 4 h to 8 h can be reached. Beskers et al.[186,187] showed that using an MCT detector improves the $\frac{(S/N)}{\sqrt{t}}$,by a factor of 11, corresponding to a significant decrease in measurement time. For this reason, an MCT detector was used in the development of the Rheo-IR set-up.

3.3 Sampling Methods: Attenuated Total Reflectance (ATR)

In IR spectroscopy, there are many different sampling measurement methods, of which the transmission method is the standard method[174,188]. Since it is possible to penetrate only very thin layer thickness, the sample preparation is time consuming (for example pressed in KBr or foil). Therefore, reflection measurements are becoming more and more common. A distinction is made between external reflection, ie. the sample reflects IR light, which is subsequently detected and called internal reflection, also referred to as the attenuated total reflection (ATR) technique.

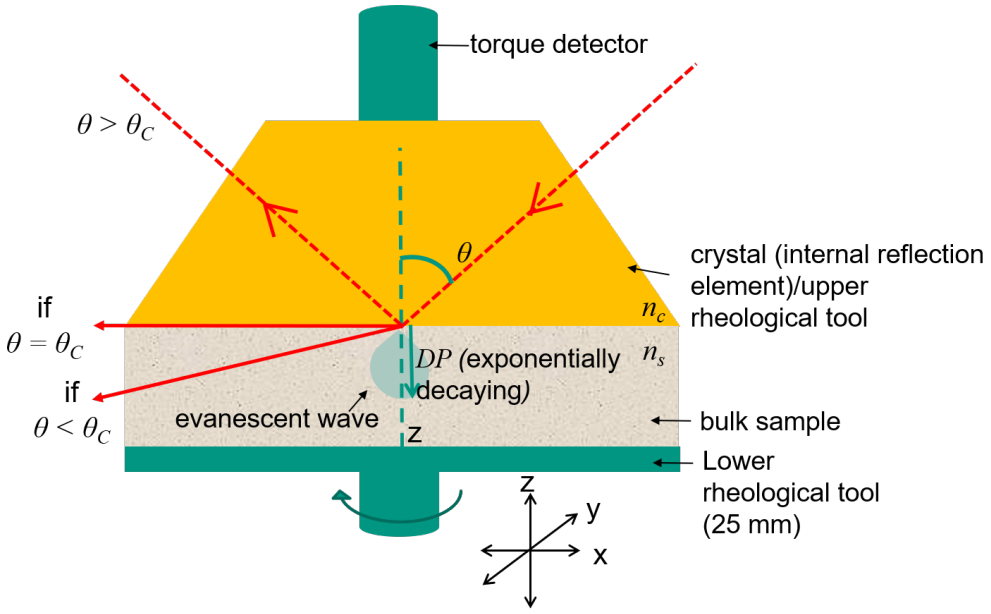

Figure 3.5: ATR crystal with a single reflection. As the angle of incidence is increased the radiation will totally reflect at angles $\geq \theta_c$. Reproduced from Radebe et.al.[189], with the permission of the Society of Rheology. DP refers to depth of penetration, see Equation 4.2.1 and Figure 4.1 in Chapter 4.

In ATR, the sample is placed on a crystal, the so-called internal reflection element (IRE). The infrared light is reflected as shown schematically in Figure 3.5 in a measuring crystal, which is in contact with the sample. An evanescent wave is formed at the interface where the light is internally reflected. The evanescent wave probes the sample within approximately one wavelength. For this reason, good contact between the sample an the crystal is important. Total reflection occurs according to Equation 3.3.1 only below a critical angle θ_c.

$$\theta_c = sin^{-1}(\frac{n_s}{n_c}) \tag{3.3.1}$$

The critical angle depends on the ratio of the refractive indices of the crystal and the sample (n_s, n_c) which are the two media forming the boundary surface. To obtain total internal reflection the IRE must have a larger refractive index (n) than the sample. All refractive index values mentioned from here onwards correspond to a wavelength of

6.6 μm ($\widetilde{\nu} = 1500\ cm^{-1}$). Zinc selenide (ZnSe, $n = 2.43$) and germanium (Ge, $n = 4.01$) are the most commonly used but diamond ($n = 2.40$) is the preferred crystal material due to its high refractive index, chemical and mechanical robustness and durability[176]. However, it is the least used IRE material as it is the most expensive. Both ZnSe and Ge are prone to scratching if improperly used[190], unlike silicon (Si, $n = 3.41$).

3.4 Optimization: Resolution, Signal-to-Noise (S/N) and Measurement Time

This section explores the relationship between spectral quality and analysis time which are critical for efficiency in FTIR. The signal-to-noise ratio (S/N) is a metric used to evaluate the performance efficiency of an IR spectropmeter. and the S/N is proportional to the sensitivity[174].

3.4.1 The origins of noise in an FTIR measurement

Every measurement is accompanied by noise. Noise is by definition the due to fluctuation in the signal, which may have different causes. Thus, e.g. fluctuations in air pressure or temperature have an impact. Discontinuities and the fundamental frequency of 50 Hz (not a fluccuation, so it not defined as noise) in the European electrical mains current are often reflected as unwanted artefacts in measuring signals. Due to the thermal energy, electrons move in electrical conductors causing noise. Movement of people in the lab can cause shocks and are also a source of noise. These are just a few of the countless causes of noise that can never be eliminated. By various measures such a low vibration measurement set-up can substantially reduce noise. In data processing, the signal can be improved by filtering and / or smoothing. In general, noise is unintentional and statistical. It must be distinguished from systematic unwanted and disturbing signals as well as artefacts. The noise, N, is usually described as the standard deviation, σ, of several measurements defined as[178]

$$N = \sigma = \sqrt{\frac{1}{n}\sum_{i=1}^{n}(S_i - \bar{S})^2}, \tag{3.4.1}$$

where n is the number of measurements, S_i is the signals of the individual measurements and $\bar{S}$ is the mean of the signal intensities.

Noise contributions can be minimized in several different ways. These all involve either enhancing the signal by smoothing or using a digital filter, or by modifying the instrumental method. Noise limits detectability but it cannot be completely removed[174]. Each measurement is accompanied by noise and is defined by random fluctuations in the baseline. In practice, a compromise is often made in determining the noise. In spectroscopy, a signal-free region of the spectrum is often used and the fluctuation in the zero signal is calculated as noise. This has considerable drawbacks since; (1) the assumption that the region is free of signals can be wrong, if e.g. low impurities cause signals. Random and systematic signals might not be clearly distinguished in a single measurement. (2) The noise may be frequency dependent. This always increases in FTIR spectrocopy due to the characteristics of the single-channel spectrum. In spectroscopy, a middle ground between the measurement of many spectra and only one spectrum has to be found. Usually two

measurements of the same sample directly after one another and forms the difference, which theoretically only reflects statistical fluctuations, but does not take into account the frequency or intensity dependence. Determining noise values correctly almost always means an increased effort and therefore they are usually determined inaccurately in practice. Since the noise also depends on many various which one can not influence, noise values can only be meaningfully compared if many parameters remain unchanged, i.e. the measurements are carried out as identically as possible. For such direct comparisons, too, a noise value inaccurately determined after the actual definition is sufficient. A figure representing the noise alone is not meaningful, only in relation to the signal intensity results in a meaningful measure, specfically the signal-to-noise ratio.

The maximum path difference (defined in the *Interferometer* section, on page 53) between the two beams limits the resolution of an FTIR instrument. The reciprocal of the pathlength difference (cm) is the limiting resolution in wavenumbers (cm^{-1}). To reach a limiting resolution of 0.1 cm^{-1}, for example, a pathlength difference of 10 cm is necessary. This basic math appears to illustrate that achieving high resolution is straightforward. Unfortunately, this is not the case since with greater pathlength displacements, the accuracy of the optics and mirror movement mechanism becomes more difficult to achieve. Esentially, high-resolution spectra contain more information than low-resolution spectra but are inherently more noisy. However, this is not very important since a resolution of $\Delta\widetilde{\nu} = 4\ cm^{-1}$ is commonly used.

Relationship between measurement time and S/N

The S/N virtually reflects the uncertainty or the measurement error in the signal intensity. A limit value of S/N $\geq$ 3 for the detection of a substance is generally established in spectroscopy and also in chromatography. This defines the limit of detection (LOD). Signals are usually quantified only from a limit value of S/N $\geq$ 10, which corresponds to an uncertainty of 10%. This value defines the limit of quantification (LOQ)[191]. The S/N can be improved by adding up or averaging several measurements, also known as signal averaging[178]6 and defined by

$$S = \sum_{i=1}^{n} S_i \tag{3.4.2}$$

Since the signal intensities of the individual measurements S_i are in theory all the same, the $S = n \cdot S_i$. The signal therefore scales linearly with the number of measurements. The statistical noise, which is calculated as the standard deviation (see Equation 3.4.1),

[6]Infrared measurements are recorded with computers (i.e. digital). For this reason, the measurement determined by the infrared light intensity in the spectrometer is converted into an electrical signal. There is often an electrical voltage that is digitized via an analog-to-digital converter (ADC). The voltage is detected as signal. It must be taken into account how exact such a measurement can be and how large a change must be at least in order to actually be regarded as a signal[174,178].

however, only scales with the square root of the number of added measurements[178] as follows:

$$N = \sqrt{n} \cdot N_i. \tag{3.4.3}$$

For the S/N follows:

$$\frac{S}{N} = \frac{n \cdot S_i}{\sqrt{n} \cdot N_i} = \sqrt{n}(\frac{S}{N})_i. \tag{3.4.4}$$

If the measurement time for each spectra is assumed to be constant, the total measurement time t is proportional to the number of spectra ($t \propto n$). From Equation 3.4.1 and Equation 3.4.4 it follows that with several measurements the S/N scales with the root of the measurement time, as seen in Equation 3.4.5, if the noise is dominant:

$$\frac{S/N}{\sqrt{t}} = constant. \tag{3.4.5}$$

Doubling the number of scans increases the S/N ratio by a factor of approximately $\sqrt{2}$. For this reason it is recommended to calculate the time independent S/N ratio ($\frac{S/N}{\sqrt{t}}$), especially when the set-up is optimized.

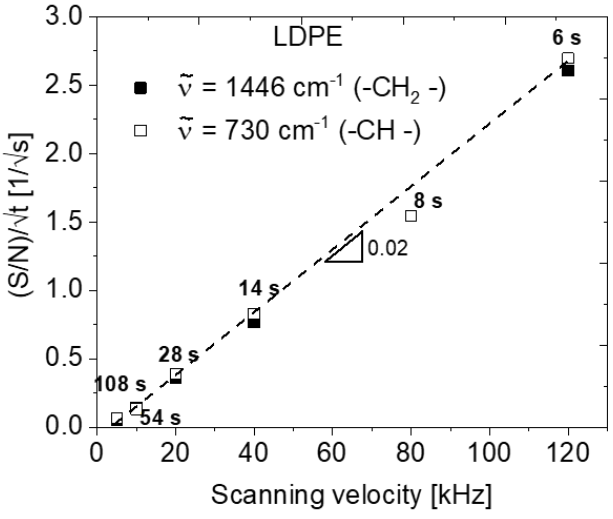

Figure 3.6: Relationship between number of scans, scanning velocity and signal-to-noise ratio using a low density polyethylene (LPDE) film. A total of 64 scans were done and the measurement time was $108, 54, 28, 8$, and 6 s for mirror velocities of $5, 10, 20, 40, 80$, and 120 kHz, respectively. The IR spectrometer used to develop the Rheo-IR set-up is used for these measurements, see Chapter 4.

Using the spectrometer software, the relationship between the number of scans, mirror scanning velocity, and signal-to-noise ratio ($\frac{S/N}{\sqrt{t}}$) was studied as shown in Figure 3.6. Here,

the number of scans is arbitrarily chosen as 64 and the mirror speed is varied between $5 - 120\ kHz$ because any number of scans can be taken based on the desired time it takes to acquire a spectrum. The scan speed is often reported as a frequency rather than the actual physical or optical velocity. When an interferometer scans at a constant velocity, the frequency of each wavelength in the spectrum is different, as follows:

$$f_{\widetilde{\nu}} = 2V'\widetilde{\nu}, \tag{3.4.6}$$

where $f_{\widetilde{\nu}}$ is the frequency of the interferogram corresponding to the radiation of the wavenumber $\widetilde{\nu}$. An optical element is moved so that the optical path difference is changed at a certain rate (optical velocity), V. For the Michelson interferometer, $V = 2V'$. It is simpler to reference the scan velocity to a single wavelength, and the wavelength chosen is usually that of the reference laser, which in this case is a HeNe laser. The wavenumber of a HeNe laser is $\widetilde{\nu} = \ 15,800\ cm^{-1}$ ($\lambda = 632.8\ nm$). A HeNe frequency of 5 kHz generates a physical scan speed of $V' = 0.16\ cm \cdot s^{-1}$ which is an optical speed of $V = 0.32\ cm \cdot s^{-1}$[174].

As expected, an increase in the mirror velocity results in a decrease in the measurement time. The $\frac{(S/N)}{\sqrt{t}}$ increases linearly by 0.02 ($\frac{1}{\sqrt{s} \cdot kHz}$)as the scanning velocity is increased. However, this does not show what the effect will be if the number of scans is increased. This forms part of the method development in this work and will be discussed in Section 4.4, page 71.

3.5 FTIR as Applied to Cementitious Materials

Infrared spectroscopy is a versatile technique that is routinely used for the characterization of chemical structures in biological to composite materials, in varying forms (solids, liquids, and gases). In this section, some examples of ways in which FTIR has been used for cementitious materials is highlighted.

The study of cementitious materials using FTIR spectroscopy dates back to the 5th international symposium on cement chemistry in 1968 (in Tokyo, Japan)[74]. IR spectroscopy has been frequently utilized to analyze cement and hydration products because it is a simple, rapid, and inexpensive analytical technique that can provide a wealth of information on the structure of minerals[192–198]. As opposed to other spectroscopic techniques used in the late 60 s until now, such as nuclear magnetic resonance[128,199,200], X-ray diffraction[201–203], or neutron scattering[204], IR spectroscopy provides unique information about the complex multiphase structure of Ordinary Portland cement (OPC). This includes molecular silicate nanostructures, ettringite formation (aluminate phase), and carbonated phases[194,196,205–207]. FTIR spectroscopy provides resolution for the strongly absorbing hydroxyl bands in the water ($\widetilde{\nu} = 3000 - 3600\ cm^{-1}$), which leads to an understanding of the degree of silicate polymerization occurring. Furthermore, the dynamics of change in the sulfate region ($\widetilde{\nu} = 1100 - 1150\ cm^{-1}$) during hydration reactions can be monitored. Additionally, carbonation resulting from the effect of atmospheric carbon dioxide (CO_2) on hydration can be characterized, as will be in this work in Chapter 6. In previous studies, the sample was made by combining the cement with KBr and pressing the mixture into pellets and performing transmission infrared spectroscopy in earlier research where FTIR was used to analyze the hydration of cement and its components[208,209]. The sample to KBr ratio was generally 1:50 for such studies. However, it is important to mention that most of the studies mentioned do not use FTIR quantitatively to investigate hydration kinetics, specifically when transmission is used as the sampling technique. For this, other sampling techniques are more suited. For example, research from other authors[194,210] used diffuse reflectance Fourier Transform Infrared Spectroscopy, or DR-FTIR. Here, the sample and KBr are ground into a fine powder and the IR beam scatters through the ground powder. It occasionally bounces off the sample and the absorbed sample light directed is by a parabolic mirror to the detector. This method can be used quantitatively as shown by Hughes et al.[210] by performing a concentration series that shows a 10^{-3} deviation in absorbance. Delgado et al.[211] compared DR-FTIR and the KBr pellet technique and found that the spectra produced by the two procedures were identical. The KBr approach has the advantage of providing more defined bands than DR-FTIR, although sample preparation is more time consuming than in ATR. Furthermore, the acquisition of DR-FTIR spectra is still an ex-situ technique which means it cannot be used to study a sample as a function of time without continuously preparing a new sample. On the other hand, the ATR-FTIR method is more useful for such 'in-situ' type of studies and intended to give complementary information.

Conventional IR techniques, however, have a spatial resolution in the order of several μm (discussed in next Chapter) due to the diffraction limit and the wavelength of IR light. For this reason, the direct chemical mapping of the OPC phases at the nanoscale level is prevented. There have been several advances in nanoscale analytic techniques such as the scattering-type scanning near-field optical microscopy (s-SNOM). This methods, also known as nano-FTIR, employs an atomic force microscope (AFM) tip as an antenna, concentrating incident infrared radiation into its apex[212]. By using the s-SNOM/nano-FTIR, de Souza et.al[213] successfully characterized the calcium silicate phases in tricalcium silicate (C_3S) in OPC with spatial point resolution of 20 nm.

To date, in-situ rheological and FTIR investigations for cementitious materials have not been reported to the best of my knowledge. Understanding the effect of the nano/microstructure of cement on the rheological behavior is paramount to its many applications. This will be further explored in subsequent chapters.

3.6 Existing Rheo-IR Set-ups

Since the main topic that underpins this thesis is the development of the Rheo-IR combined technique, only a brief overview of the existing Rheo-IR techniques will be discussed here.

In 2004, Nishikawa et. al[214] realized the concept of coupling mechanical properties to IR through mechanical pulsed compression ATR dynamic infrared step-scan time resolved FTIR. The mechanical pulse generator, which generates soft-pulse waveforms, controls the measurement in this system. A tungsten carbide internal reflection element is used to obtain dynamic compression polarized ATR spectra since the material has a hardness of $>$ 9800 N/mm^2 (9.8×10^9 Pa). The method was used to examine the response of poly(ethylene terephthalate) (PET) and poly(*p*-phenylene biphenyl tetracarboximide) to applied reversible nonlinear mechanical dynamic compression. Monitoring the peak width revealed reversible nonlinear optical dynamic responses in the $C = O$ stretching vibration in the PET. With decreasing compressive strain, nonlinear mechanical responses were reduced[215]. The coupling of IR to a stress-controlled rheometer was realized by Thermofisher Scientific[216–218]. This combined method is commercially known as Rheonaut, and initially coupled through fiber optic cables then later through parabolic mirrors. It has been used to; (1) study the curing reactions of polyurethane (PU) resins[217] and (2) for the investigation of silk protein aggregation kinetics using polarized IR beams[219]. In the first example, samples of two-component PU resins containing a diisocyanate prepolymer and one of two different ester compounds each end-capped with hydroxyl groups were investigated as a function of shear stress (50 Pa) at room temperature over time, using the Rheonaut. As expected, the urethane intensity at $\widetilde{\nu} = 1687\ cm^{-1}$ increased whilst the peak absorbance at $\widetilde{\nu} = 2266\ cm^{-1}$ associated with the isocyanate increased with curing time as did the storage (G') and the loss modulus (G''). The G',G'' crossover was seen 30 minutes later than the inflection points in the IR data[217]. No explanation was given by the authors about trend but as a proof of concept, it showed that acquiring FTIR spectra whilst simultaneously applying mechanical deformation could lead to a correlation between the viscoelastic properties and individual reactive groups of a complex polymer. In the second example, the electric field of the infrared beam was polarized using a motorized zinc selenide holographic wire grid polarizer; s-polarized light only probed vibration modes along the y-axis, the velocity or shearing direction, whereas the p-polarized light selectively probed vibration modes along the x- and z-axes, the vorticity and velocity gradient directions, respectively. The ability to change the position of the probed area by simply moving the rheometer laterally with respect to the infrared sensor is the main benefit of this set-up.

In this work, we show for the first time, to the best of our knowledge, a strain-controlled rheological measurement uniquely coupled with attenuated total reflectance (ATR) infrared spectroscopy through off-axis parabolic (OAP) mirrors and a transparent ATR crystal as a upper rheological plate-plate geometry. In contrast to the Rheonaut, where the ATR crystal is attached to the bottom plate as an accessory in the bottom plate[217], the ATR

crystal in the presented set-up is a rheological top plate. This means that the control of where the spectroscopic measurements takes place is controlled by adjusting the mirrors, in our design, and by moving the ATR crystal in the Rheonaut design.

Chapter 4

Rheo-IR: Method Development and Improvement

The design of an IR transparent upper-plate rheological geometry used as an attenuated total reflectance (ATR) sampling tool, is described in this chapter. Additionally, the technical and methodological adaption of the ATR crystal into an ARES G2 rheometer for combined FTIR and rheological measurements is presented. In this new set-up, a strain-controlled rheometer is combined with an ATR crystal which is used as an upper rheological geometry. The IR beam is guided through two off-axis parabolic mirrors to the quasi-static upper plate of the rheometer to gain maximum IR sensitivity. Thereby, online and directly correlated real-time FTIR spectra can be acquired whilst simultaneously conducting rheological measurements. This allows for in-situ correlation of macroscopic rheological properties with microscopic, molecular chemical changes within a material under controlled conditions having exactly the same sample time evolution for both measurements. Additionally, some of the challenges associated with data acquisition and Fourier transformation (i.e detector nonlinearity) are discussed in detail and solutions are presented[7]*.*

4.1 Overview of Spectrometer Used for the Combined Method

A Bruker Matrix IR spectrometer equipped with an OPUS base package (version 8.1.29) software operating in the mid-infrared spectral range ($4000 - 400\ cm^{-1}$) coupled to an ARES G2 rheometer was used in the development of the Rheo-IR set-up. The spectral range of this spectrometer also covers the fingerprint region ($< 1200\ cm^{-1}$), which is unique for each molecule. The fast signal averaging, high performance, permanently aligned optics, very compact size ($29 \times 31 \times 24\ cm$) and relatively low mass (32 kg) of the the Matrix IR spectrometer is optimized for industrial use. Additionally, an optical high sensitivity quantum detector[174,220] made from a mercury-cadmium-telluride semiconductor material (MCT) was used as the FTIR detector. The detector element is cooled to -196 °C with

[7] The work in Chapter 4 and 5 have been partly published in the Journal of Rheology by Radebe et al.[189]

liquid nitrogen to reduce electronic noise and consequently reaching better S/N. The liquid nitrogen consumption is approximately 0.3 L per 3 to 6 hrs. An MCT detector provides an up to 50 times better sensitivity compared to standard room temperature thermal pyroelectric detector, i.e. deuterated L-alanin doped triglycin sulfate (DTGS)[186,220]. The MCT detector has mirror speeds of up to 160 kHz ($V' = 5\ cm \cdot s^{-1}$, see Equation 3.4.6 on page 62 for frequency to scanning velocity conversion). The spectral range is limited to $4000 - 600\ cm^{-1}$.

4.2 Internal Reflectance Element (IRE) Choice and ATR Crystal Design

In this work, silicon (Si) was chosen due to its mechanical robustness, high refractive index and the ability to be shaped into a rheological geometry. The infrared light is directed into the crystal below a critical angle (θ_c, see Equation 3.3.1). The critical angle is calculated using the refractive indices of the two media as follows[176], see also Figure 3.5.

$$DP = \frac{\lambda}{2\pi n_c \sqrt{sin^2\theta - (\frac{n_s}{n_c})^2}} \tag{4.2.1}$$

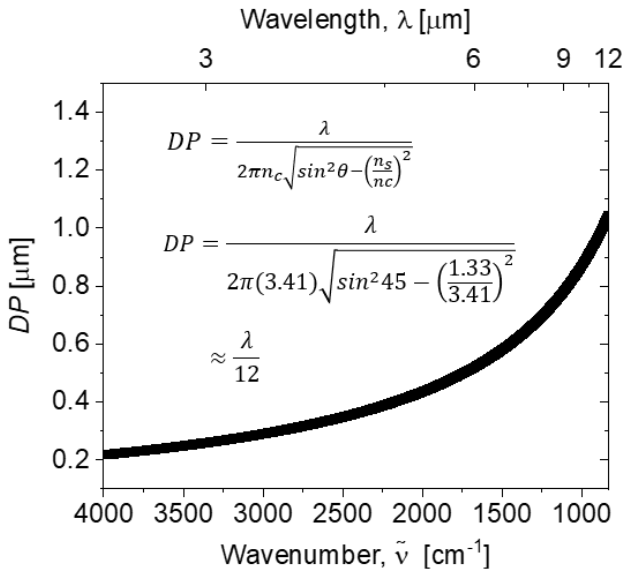

Figure 4.1: Characteristic depth of penetration as a function of wavenumber/wavelength for Si ($n_c = 3.41$) used as the ATR crystal in direct contact with water ($n_s = 1.33$) as the sample, measured at $\theta = 45°$. The critical angle for this example is $\theta_c = 23°$, also see Equation 4.2.1 and Figure 3.5. Reproduced from Radebe et al.[189], with the permission of the Society of Rheology.

Figure 4.1 displays the depth of penetration, DP, over the spectrum. The DP is described by Equation 4.2.1, which is directly proportional to the wavelength divided by some constant. The constant is determined by the angle (θ) at which the light enters the crystal and the refractive index of both the sample (n_s) and the crystal (n_c). Note, the refractive index of both the ATR crystal and the material of interest vary along the wavenumber range

by approximately n = ± 0.4 between 4000 − 700 cm^{-1}. The Si crystal has two functions, within the presented set-up, (1) as an ATR crystal and (2) as an upper plate tool (Figure 3.5). The rheological plate-plate geometry has a diameter of 25 mm. Once the ATR crystal was designed, it had to be attached to the rheometer as a rheological geometry. This was done using a lightweight shaft (Figure 4.2a) with adjustable screws to allow for manual tightening and removal of the ATR crystal (Figure 4.2b)

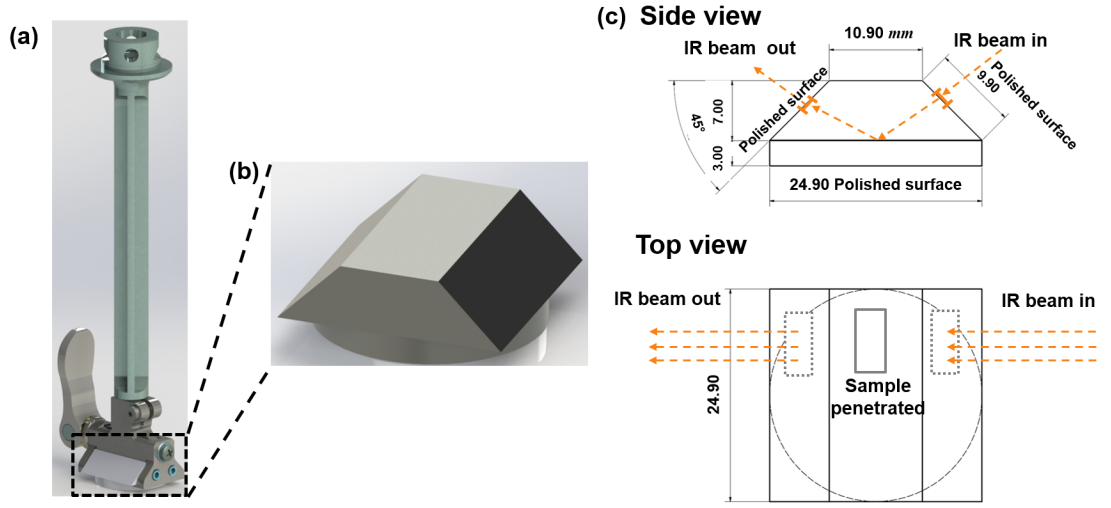

Figure 4.2: **(a)** The shaft for a connection between the rheometer and the ATR crystal made from aluminium, with a length of 160 mm.**(b)** Custom-built single reflectance ATR Si crystal with the black dotted lines representing the side from which the **(c)** dimensions correspond from the side and the top view and are given in mm. The approximate area at which the IR penetrates the sample is highlighted in the solid grey line. Reproduced from Radebe et al.[189], with the permission of the Society of Rheology. For a detailed technical drawing, refer to Appendix 6 on page 155.

The ATR crystal was positioned in such a way that a gap of 1 mm could be achieved between the bottom plate of the lower rheological geometry and the surface of the crystal. Once the crystal was positioned in the rheometer, the IR spectrometer, detector, and parabolic mirrors need to be aligned to reach the ATR crystal at a suitable angle at the interface of the crystal and the sample.

4.3 Infrared Beam Alignment

The focusing and alignment of the IR beam, from the source to the detector, is vital for an optimum S/N ratio in the IR spectrum, since the intensity of light that reaches the sample is increased. The use of off-axis parabolic mirrors is a way of achieving this. A parabolic mirror converges the light that is parallel to the principle axis of the mirror and reflecting it in one point, called the focal point[221]. Each parabolic mirror has its own focal length, depending on the size and parabolic shape. To ensure that the light converges at the position focal point the OAP mirror can be adjusted by using three threads that define a plane and are attached to the back of the mirror.

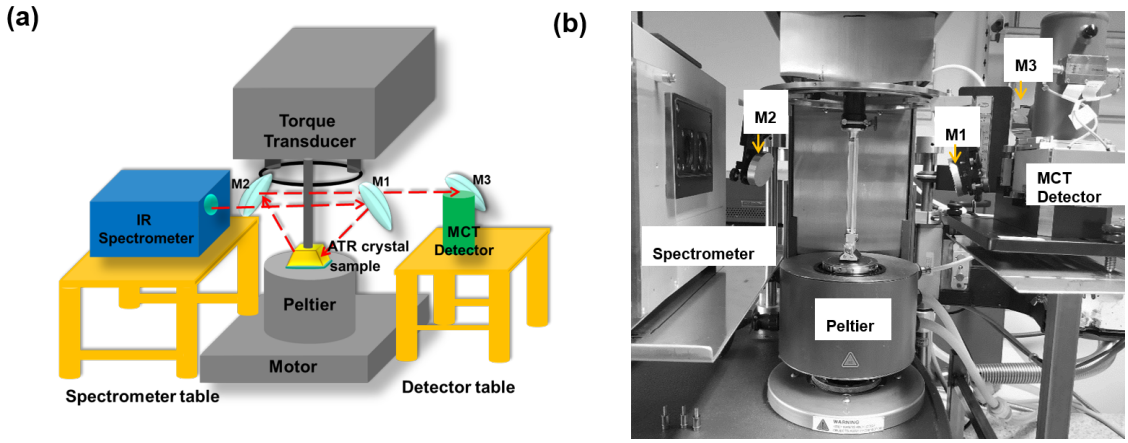

Figure 4.3: **(a)**Schematic overview and **(b)** a photograph of the developed Rheo-IR set-up combining a Matrix IR Spectrometer and an ARES-G2 rheometer. Reproduced from Radebe et al.[189], with the permission of the Society of Rheology.

In addition, the OAP mirrors were mounted onto the rheometer and the height was adjusted by electronically moving the transducer upwards and downwards. Using a laser guide from the spectrometer, the IR beam was focused to the center of the first OAP mirror (M1) (Figure 4.3a) and converges at a focal length of 150 mm, at the interface of the crystal and the sample. The beam first enters perpendicularly the ATR crystal and is reflected at the ATR surface ($\theta > \theta_c$), where the sample is placed. The evanescent field of the total reflectance enters a few μm into the sample, see Figure 3.5. Thereafter, the beam diverges to a second OAP mirror (M2) and is directed towards the detector mirror (M3), and then finally to the detector. The beam path is shown in Figure 4.3a by dotted arrows.

4.4 IR Signal-to-Soise (S/N) and Sensitivity Improvement

4.4.1 Scanning velocity

The measuring time can be limited depending on the system being investigated. For example, if a polymerization process occurs quickly (i.e. in a matter of minutes), the IR measurement period is short, and the parameters should be adjusted to ensure that the appropriate number of scans (s) is completed within the time that the chemical changes occur. If the reaction is slow (hours), more IR scans can be conducted and averaged over a longer period of time. In general, the higher the S/N ratio (S/N $\sim \sqrt{s}$ for stochastic noise[174]), the longer the measurement time or the greater the number of scans taken. The measurement time (t), on the other hand, is directly proportional to number of scans, therefore S/N $\sim \sqrt{t}$. However, the number of scans available for any system that changes over time is limited. As a result, it is critical to strike a balance between measurement time, number of scans, and, ultimately, the signal-to-noise ratio that can be accomplished. The greater the S/N, the better the ability to detect even minor changes in absorbance or absorbencies at lower concentrations. More spectra can be recorded at a given time by increasing the interferometer's moving mirror scanning velocity. The IR spectrometer utilized can capture between 0.6 and 11 spectra per second on average. The measurement time can therefore be between 108 s and 6 s, respectively, for a single IR spectrum consisting of 64 averaged scans (interferograms) combined with a spectral resolution of $\tilde{\nu} = 4\ cm^{-1}$. Since the S/N increases with the square root of the number of scans and the time per scan is considered constant, it is necessary to calculate the time independent signal to noise ratio, $\frac{(S/N)}{\sqrt{t}}$, t in seconds) as the main parameter for quantifying spectrometer sensitivity and being a guide for any optimization.

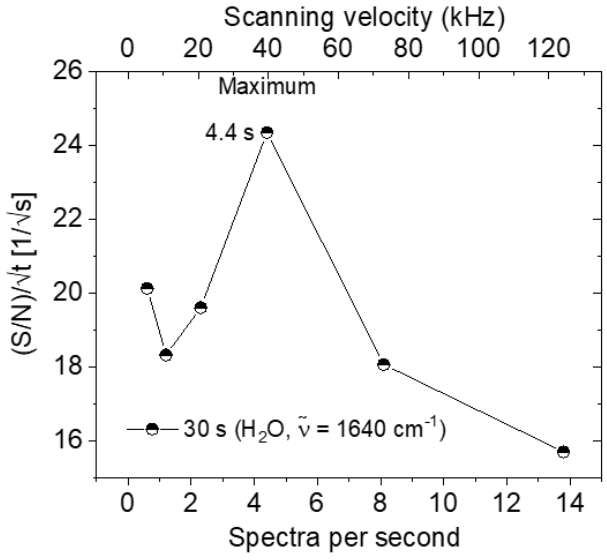

Figure 4.4: The $\frac{(S/N)}{\sqrt{t}}$ at different time intervals for spectral acquisition, for water for after 30 s scanning time. Reproduced from Radebe et al.[189], with the permission of the Society of Rheology.

Water does not change chemically over the measurement time at room temperature. Therefore, it was chosen as test sample to optimize the $\frac{(S/N)}{\sqrt{t}}$ within the time frame in

which chemical changes are expected for other systems (i.e. polymerization).

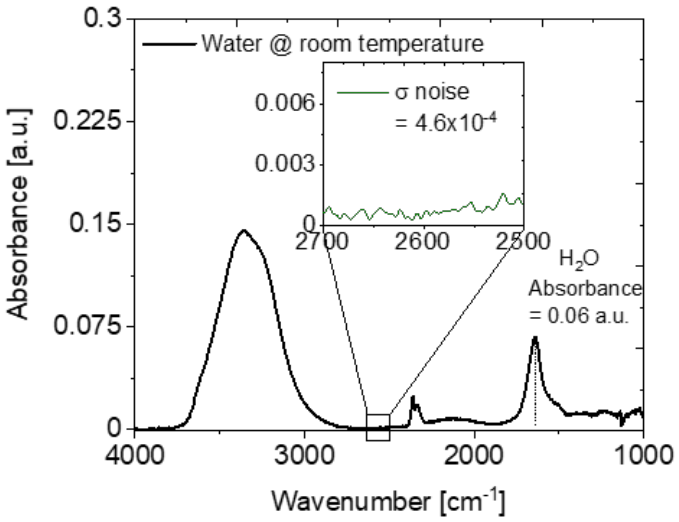

Figure 4.5: Rheo-IR: FTIR spectra ($4000 - 1000\ cm^{-1}$) of water, where the H_2O bending peak vibration at $1640\ cm^{-1}$ was used to calculate the time-independent signal-to-noise, $\frac{(S/N)}{\sqrt{t}}$, after 30 s of measurement time where one spectra took 4.4 s to be obtained. Inset: noise region between 2700 and 2500 cm^{-1}. Reproduced from Radebe et al.[189], with the permission of the Society of Rheology.

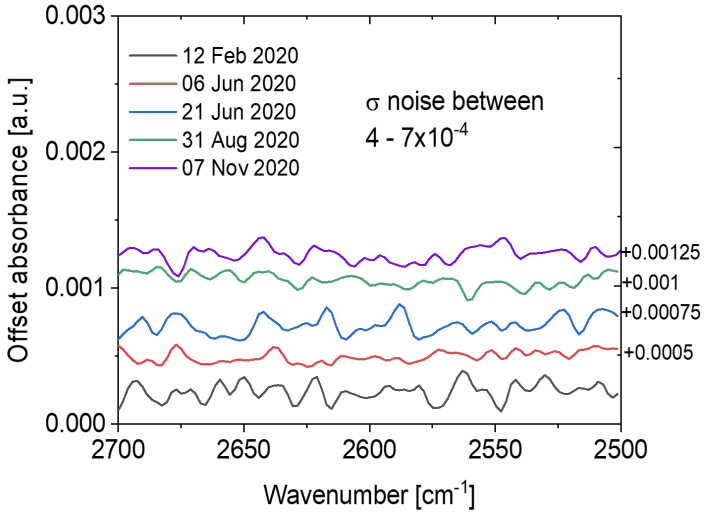

Figure 4.6: Standard deviation (σ) in absorbance of the noise region between 2700 and 2500 cm^{-1} between February and November 2020. The data are horizontally shifted for a clearer visualization. Reproduced from Radebe et al.[189], with the permission of the Society of Rheology.

The $\frac{(S/N)}{\sqrt{t}}$ of the H_2O ($\tilde{\nu} = 1640\ cm^{-1}$) of water is calculated to be 24 $\frac{1}{\sqrt{s}}$ when each spectra was taken within 4.4 s, see Figure 4.5. For all signal-to-noise calculations, the noise region was chosen between $2700 - 2500\ cm^{-1}$, as no IR peaks were expected in this region, as seen in the inlet of Figure 4.5. From Figure 4.4 it is clear that about 4.4 spectra per second, is optimum for the maximum $\frac{(S/N)}{\sqrt{t}}$ for 64 scans taken over 30 s, with the Rheo-IR set-up. Additionally, higher scanner velocities lead to more noise, therefore a lower $\frac{(S/N)}{\sqrt{t}}$. This is perhaps due to mechanical instabilities or mechanical resonances as a

result of the moving mirrors inside the spectrometer. In Figure 4.6, the stability of the IR part of the Rheo-IR set-up is presented as the standard deviation (σ) of the noise within the months of February and November 2020. The noise is relatively stable, with values between $4 - 7 \times 10^{-4}$ a.u..

4.4.2 Relative photon flux (Φ_{rel})

Signal to noise improvement is directly related to an increase in sensitivity. Sensitivity is affected by (1) the number of photons that reach the sample, which are (2) subsequently totally reflected out, (3) detected, (4) analog-to-digital converted (ADC) and given as a count by the OPUS software of the spectrometer used. The photon signals were digitized using a 16-bit ADC. A 16-bit converter allows for 65,535 a.u., which when divided by 2 for the parts of a double-sided interferogram, the count is 32,767 a.u. and would be the absolute maximum value prior detector overload obtained if all photons from the IR sourced were detected. Although the value given by the spectrometer is not the absolute number of photons, it can be used as a relative measure of the photon flux, Φ_{rel} to guide the optimization process.

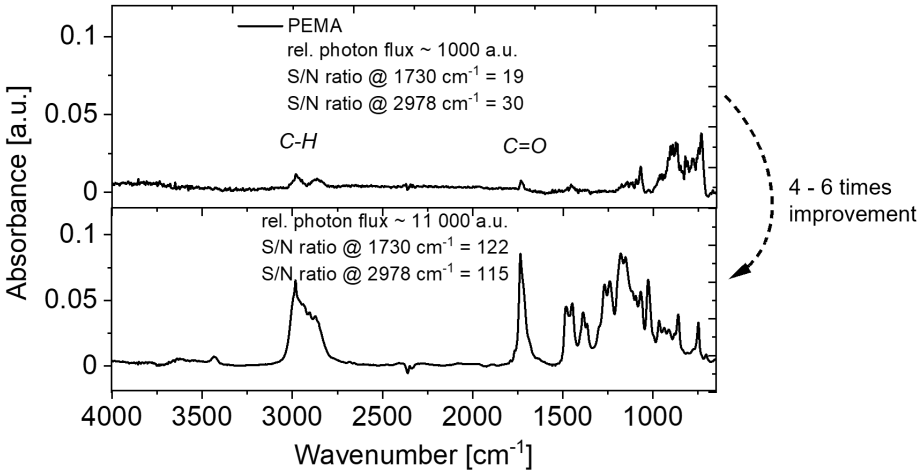

Figure 4.7: Poly(ethyl methacrylate) (PEMA) spectra ($4000 - 750\ cm^{-1}$) measured at a relative photon flux of *(top)*: 100 a.u. and *(bottom)*: 11 000 a.u., showing a signal to noise improvement of between 4 to 6.

In the Rheo-IR set-up, starting with the parabolic mirrors not being correctly aligned, according to the specifications in Section 4.3, and a Si ATR crystal with an unpolished surface (as used first) is placed in the path, the Φ_{rel} is between 500 – 1000 a.u., counts. Correct beam alignment increases the Φ_{rel} to a value between 1000 – 4000 a.u., which improved the S/N by a factor of between 4 and 6 and shown in Figure 4.7. A further improvement was accomplished by reducing the light scattering at the surface of the Si ATR crystal through polishing the geometry. By polishing the surface of the ATR crystal, at the interface of the crystal and the sample, the unwanted scattering was substantially reduced. This resulted an IR increase to relative photon flux of about 8,000 – 16,000 a.u.

This yields a S/N that is 33 times higher than that of the starting set-up, as seen in Figure 4.8. Furthermore, the spectral resolution, when compared to a spectrum taken from a fully optimized research spectrometer (Bruker Vertex 70) is not compromised in the Rheo-IR set-up, as seen in Figure 4.9. The Vertex 70 spectrometer is able to measure up to 58 spectra per second, however the spectral width and resolution is also compromised[186], for these high scanning rates. In Figure 4.9 (top), 2.3 spectra per second (in total 64 scans), at a spectral resolution of 4 cm^{-1}, were taken and a diamond ATR crystal was used. Diamond has a lower refractive index (n = 2.40) than Si (n = 3.41) and therefore diamond has a higher characteristic DP (depth of penetration), 3 μm, compared to 1 μm at $\widetilde{\nu} = 1500\ cm^{-1}$ for the Si material. The longer the characteristic DP at a given wavelength, the longer the pathlength of the light. Therefore, a longer pathlength, l ($\approx DP$) , increases the absorbance as highlighted in Figure 4.9 for the carbonyl peak ($C = O$) peak and the $C - O$ stretching vibration of the carbonyl group in poly(ethyl methacrylate) (PEMA), using the Vertex 70 and the Rheo-IR set-up.

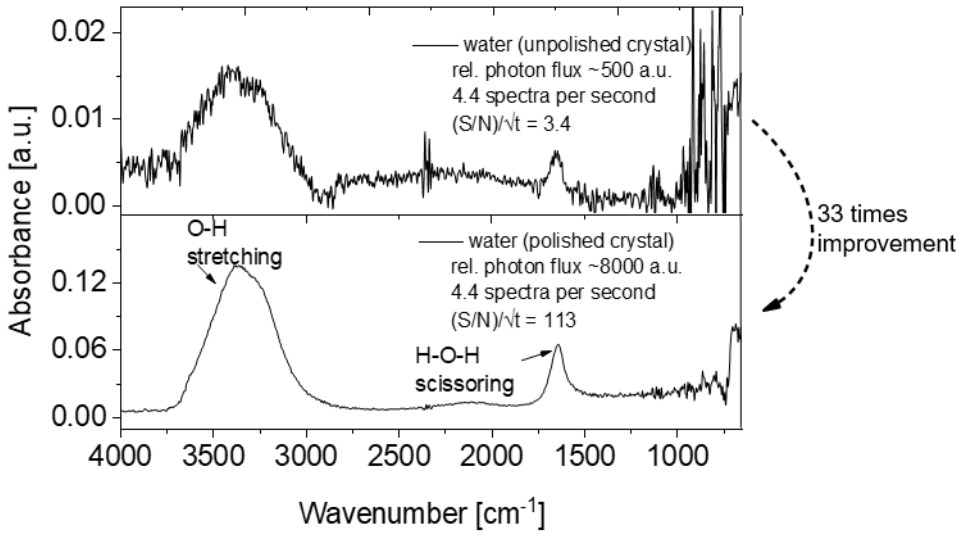

Figure 4.8: Water spectra ($4000 - 750\ cm^{-1}$) measured with a *(top)*: unpolished crystal and *(bottom)*: polished ATR crystal, showing a signal-to-noise improvement of 33. Reproduced from Radebe et al.[189], with the permission of the Society of Rheology.

The improvements made from measurement parameters which includes, the polishing of the Si crystal and the general alignment shown as a product of all improvements as ca. 10^2 times final improvement in the S/N, shown in Table 4.1. The post spectral acquisition data processing applied was 'adjacent averaging' with a boxcar smoothing window of 15 data points ($\Delta\widetilde{\nu} = 10\ cm^{-1}$). Data smoothing improves the sensitivity of a measurement, as it reduced the standard deviation of the noise allowing for a more accurate extraction of absorbance values. For an example see Section 4.5.3.

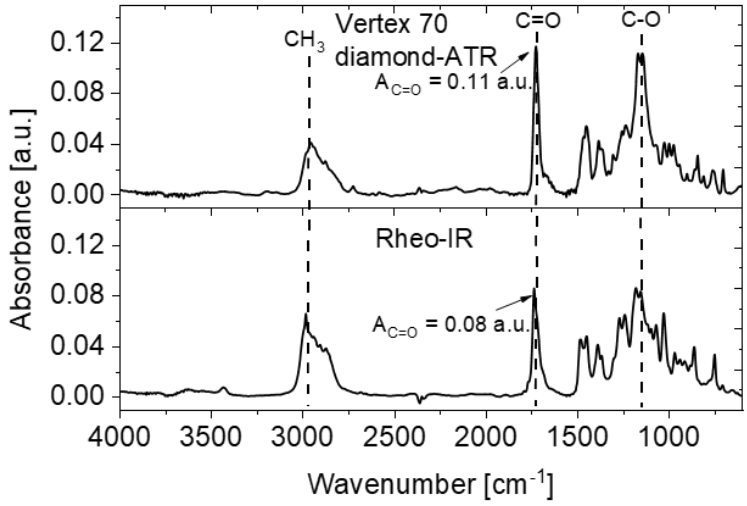

Figure 4.9: Polystyrene (PS) spectra ($4000 - 750\ cm^{-1}$) measured with the (*top*): Vertex 70 commerial spectrometer using a single reflection diamond ATR crystal and (*bottom*): the Rheo-IR set-up. Reproduced from Radebe et al.[189], with the permission of the Society of Rheology.

Table 4.1: A summary of the four parameters used to improve the signal-to-noise by dividing the $\frac{(S/N)}{\sqrt{t}}$ of the start settings with the $\frac{(S/N)}{\sqrt{t}}$ (per second) of the optimized setting.

Parameter	Start	Optimized set-up	S/N improvement factor
FTIR: spectra per second	2.3	4.4	
$\frac{(S/N)}{\sqrt{t}}$	19	24	1.3
FTIR: relative photon flux (a.u.) due to alignment using parabolic mirrors	200 – 500	1,000 – 4,000	
$\frac{(S/N)}{\sqrt{t}}$	30	115	4
FTIR: relative photon flux (a.u.) due to polishing of the surface of crystal	1,000 – 4,000	8,000 – 16,000	
$\frac{(S/N)}{\sqrt{t}}$	3.4	113	33
Post spectral acquisition data processing	Blackman-Harris window function	adjacent averaging-smoothing window of 15 points ($\Delta\widetilde{\nu} = 10\ cm^{-1}$)	1.5
Total improvement			**260**

4.5 Photometric Errors in FTIR Caused by Nonlinear HgCdTe/ MCT Detector Response and Artefacts in time resolved FTIR Spectroscopy

Photoconductive MCT detectors are linear in photometric response when the photon flux (Φ) is below 10^{19} photons $cm^{-2}s^{-1}$, after which a nonlinear behavior is seen where the photoconductivity is proportional to the cube root of the photon flux[222,223]. Additionally, the detector response time at a photon flux above 10^{19} photons $[cm^{-2}s^{-1}]$ decreases from a constant to $\Phi^{-2/3}$[185,223]. Figure 4.10 shows the effect in an interferogram, schematically, in the case if a linear and a nonlinear detector response.

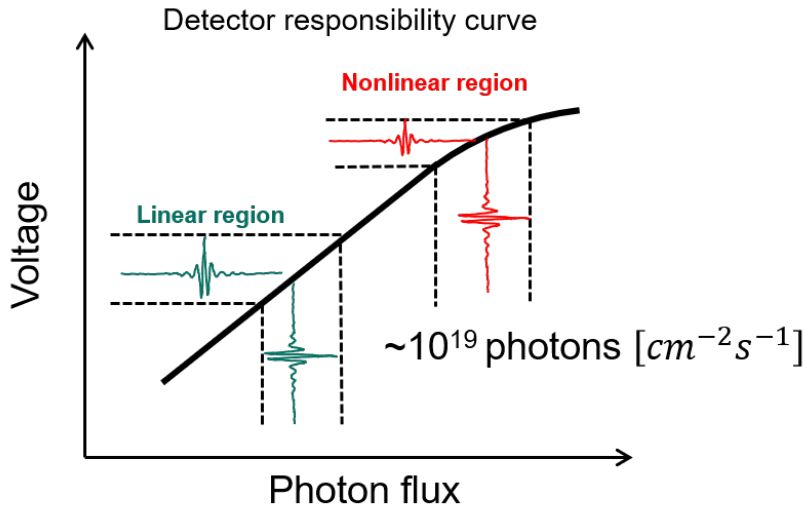

Figure 4.10: Schematic diagram of detector nonlinearity, showing its effect on the measured interferogram and the dependence of nonlinearity on the photon flux (Scheme adapted from[224]).

The detector nonlinearity could either be thermally induced, therefore time dependent, or optically induced. In an IR single channel spectrum, this nonlinearity can be seen by a varying offset or by a non-physical value after the detector cut-off frequency, which is below 600 cm^{-1} for an MCT detector at temperatures of 80 K[174]. There are several ways of correcting the nonlinearity, through photometric or algorithmic corrections[185,224–228]. For the time-dependent Rheo-IR measurements presented in Chapter 5 and 6, the algorithmic solution presented by Shao and Griffiths[185] which corrects the acquired interferogram for nonlinearity, was used.

4.5.1 Data acquisition: Non-physical Value After Detector Cut-off

Nonlinearity in the detector output manifests itself by distorting the resultant spectrum in the wavelength regions where the detector is sensitive and by producing artifacts indicating the presence of energy in wavelengths regions where the detector is insensitive. In the spectrum, this can be evidenced by:

1. Showing a non-physical value after detector cut off and/or

2. a slowly varying off-set in the calculated single channel spectrum (SCS) (Figure 4.11).

This means the measured interferogram is no longer exactly proportional to the incident flux as shown schematically in Figure 4.10.

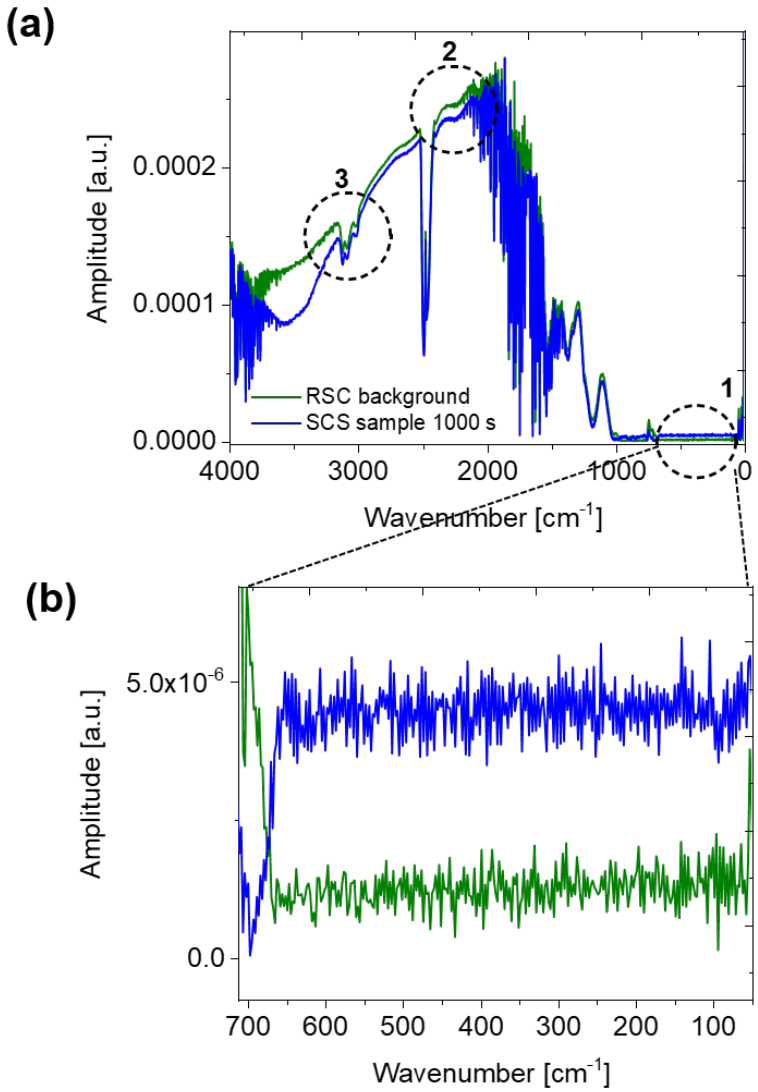

Figure 4.11: **(a)** Reference single channel (RSC) and single channel spectrum (SCS) ($4000-0\ cm^{-1}$) of a precured polyacrylic acid aqueous solution, where the circled region (1) is a non-zero value after the detector cut-off and (2) shows a varying off-set of the SSC to the RSC and (3) are CH, CH_2 and CH_3 peaks that are attributed to hydrocarbons in oils possible present in the spectrometer **(b)** Zoomed in SCS and RSC at the detector cut-off region ($700 - 50\ cm^{-1}$).

4.5.2 Detector Non-linearity Caused by Thermal Expansion

Since many materials undergo a phase change and/or a change in chemistry when exposed to different ranges of temperatures, it is important to know the limits of the Rheo-IR set-up with regards to stability in measurement over a wide range of temperatures. For this reason, a temperature sweep was conducted between 0 and 100 °C on an uncured epoxy resin and the IR part of the Rheo-IR measurement is seen in Figure 4.12. There is a clear

shift in the baseline from 0 to 100 °C and significantly so between 50 and 100 °C. This is caused by the thermal expansion of the aluminium shaft shown in Figure 4.2. Aluminium and its alloys are known to expand $21 - 24 \times 10^{-6}/°C$[229]. Silicon (ATR crystal), on the other hand, expands $3 - 4 \times 10^{-6}/°C$[230]. The combined effects of the expansion of both materials, leads to a total expansion of about 2.4 *mm* which means that the crystal is shifted out of focus of the IR beam, thus changes the baseline.

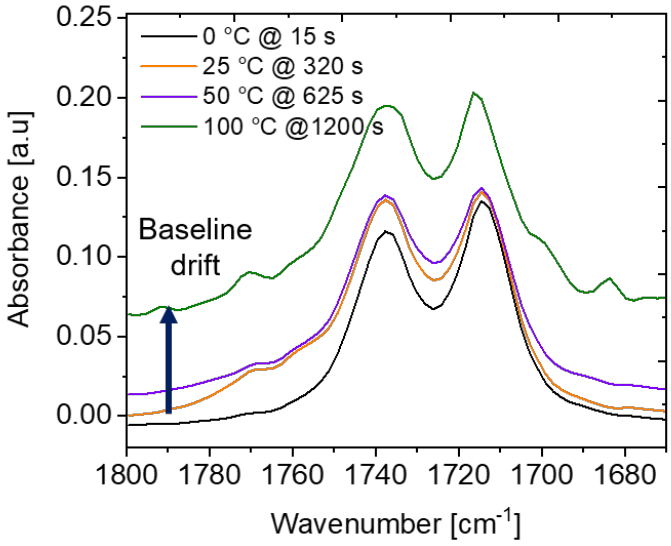

Figure 4.12: Rheo-IR spectrum ($1800-1670\ cm^{-1}$) of a temperature ramp (ramp rate = 5 °C/min) of a commercial uncured epoxy at 0, 25, 50 and 100 °C.

From this, it is recommended that a shaft made from a material with a lower thermal expansion be used like titanium with an almost 3 times lower thermal expansion of $8.5 \times 10^{-6}/°C$[231] be used. This could potentially increase the temperature range to include temperatures above 50 °C, before a baseline shift and peak distortions are seen.

4.5.3 Correction of Photometric Errors

To rectify MCT detector nonlinearity, both software and hardware techniques were applied. A mathematical model is frequently created to replicate the nonlinear interferograms for software correction. Before beginning phase correction, appropriate correction factors are computed and applied to the measured interferogram. A linearizing circuit or voltage-biased MCT detector can be used to do hardware correction. The types of corrections can be subdivided into photometric, electronic or algorithmic corrections. Usually, photometric correction is avoided as it involves using an optical filter to reduce nonlinearity effects, however, the signal-to-noise ratio is lowered to an undesirable fraction. Several investigations[185,224,232–234] revealed that detector nonlinearity predominantly affects a few points around the centerburst, where the largest variation of incident photon flux occur.
Based on this, it is assumed that the observed nonlinearities is ascribed to incorrectly recorded intensities at the centerburst and the two adjacent points. Therefore, the difference

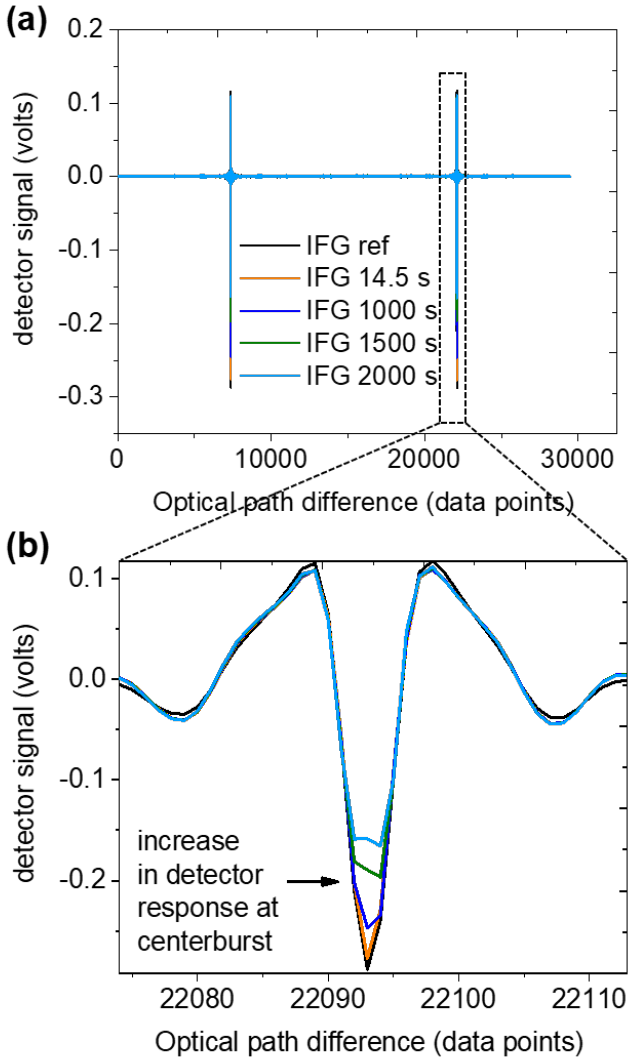

Figure 4.13: **(a)** Double sided interferogram of a reference background (atmosphere) poly acrylic acid sample during gelation at 14.5, 1000, 1500 and 2000 s. **(b)** Zoomed in: centerburst between 22074 and 22112 path difference. This results in a varying off-set n in the SCS (see Figure 4.11) and subsequently a baseline shift with peak distortions in the absorbance spectrum (see Figure 4.15).

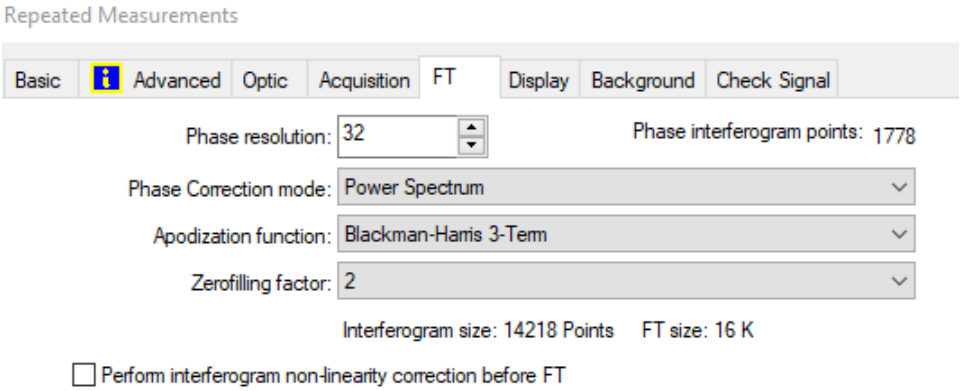

Figure 4.14: Bruker OPUS software interface

between the measured interferogram and the true interferogram is a zero signal except for

two negative voltages at the center burst and the two adjacent points (see Figure 4.13). By replacing the values at the Zero Path Difference (origin of problem) with lower values from background spectrum, the nonlinearity in detector response is resolved. The simple MATLAB code used to do this can be found in Appendix 8 on page 159. However it must be noted that this works best only when the nonlinearity causes a signal distortion around the centerburst of the interferogram and no where else. In fact, replacing only three of the data points at the center turns out to be completely random and based on the data point spacing. For a stronger nonlinear effect, we relay on more complex alogorithm that uses based on two parameters – the cut-off of the detector and the modulation efficiency of the interferogram. The function need to know which part of the 'strongly distored' centerburst comes from nonlineartiy and which part comes from non-perfect modulation efficiency in the acquisition. For this, the Bruker OPUS sofware applied its own patented alogrithim[235] when 'Perform interferogram nonlinearity correction before FT' is selected, see Figure 4.14.

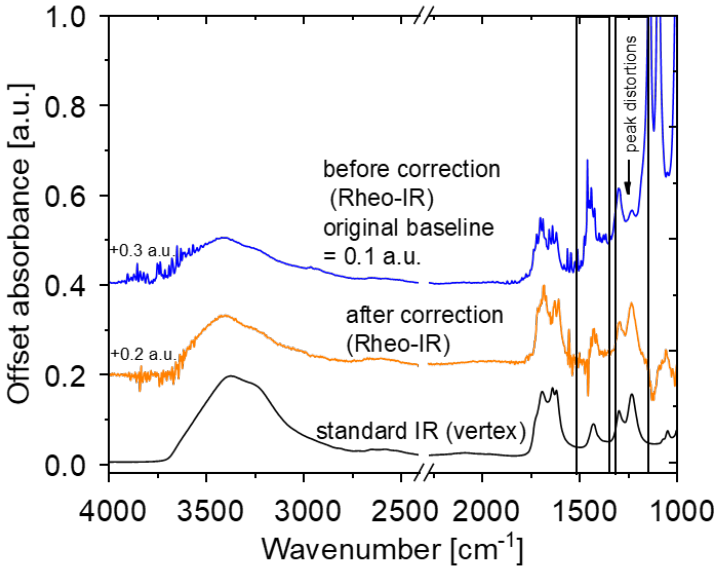

Figure 4.15: An offset (ordinate shifted for visual clarity) absorbance spectrum of acrylic acid from the Vertex 70 (black line) and from the Rheo-IR set-up before (blue line) and after correction (orange line).

Using and algorithmic correction method, where the data point and the centerburst and the two adjacent points are replaced with those of the of the reference spectrum, a significant improvement in the corrected spectrum relative to the uncorrected one is observed in Figure 4.15.

Apodization, zero-filling, and spectral smoothing after correction

There are several operations necessary to convert an interferogram to a spectrum. These include, Fourier transformation, apodization, zero-filling, phase correction and smoothing. In the case where the interferogram and not the spectrum is measured, the above mentioned operations have to be manually done. After the photometric error was corrected, as

discussed in Section 4.5.3, futher mathematical manupulation was done. Before the digital Fourier transformation, zero points are added to the end of the interferogram. This is known as zero filling. Using the same Fourier coefficients, it is the process of interpolating more data points into a spectrum to give the spectral lines a smoother shape and higher digital resolution. By extending the length of an interferogram with a zero straight line, FTIR software automatically provides zero-filling without new information being added to the spectrum. In general, the original interferogram size should be at least doubled by zero filling, i.e. a zero filling factor (ZFF) of two should be (and was) used. In most circumstances, zero-filling is better than polynomial or spline interpolation methods used in the spectrum domain since it does not influence the instrument line-shape. Nowadays, most, if not all commercial spectrometers are equipped with all the above parameters, manually.

Smoothing: Adjacent Averaging

Reducing the noise in a spectrum, often requires smoothing. Smoothing is a signal processing method that is commonly used to eliminate noise in signals. Adjacent Averaging, Savitzky-Golay, percentile filter, FFT filter, LOWESS, LOESS, and the Binomial technique are all commonly used for removing noise[178], while partially lowering spectral resolution.

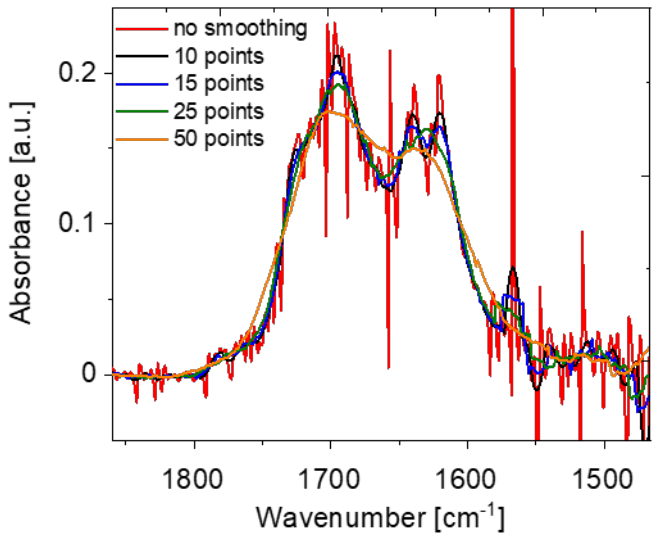

Figure 4.16: Rheo-IR set-up: FTIR spectra of polyacrylic acid ($1860 - 1470\ cm^{-1}$) showing carbonyl group ($C = O$) of the carboxylic acid ($\widetilde{\nu} = 1705\ cm^{-1}$), $C = C$ ($\widetilde{\nu} = 1640\ cm^{-1}$) and the H_2O ($\widetilde{\nu} = 1630 - 1640\ cm^{-1}$). Adjacent averaging using windows of 10, 15, 25 and 50 data points ($\Delta\nu = 7 - 34\ cm^{-1}$).

Depending on the nature of the signal and the amount of noise in the signal, these smoothing algorithms function in different ways. Each approach provides a different performance to highlight the most important components of a result. Figure 4.16 shows 0 to 50 point smoothing effect and smoothing by 50 points no longer reflects the orginal spectrum as seem by the orange line. The percentile filter (especially the 50% percentile filter or median filter) allows elimination of noise with abnormal amplitude. Savitzky-Golay seeks

to preserve peak shapes while adjacent averaging performs wide smoothing. Savitzky-Golay and adjacent averaging are effective solutions for reducing background noise from a signal with regularly distributed noise. As the name implies, adjacent averaging takes the average of a user-specified number of data points around each point in the data and replaces it with the new average value.

4.6 Concluding Remarks

A new combination of an IR spectrometer and a strain-controlled rheometer set-up was presented. A silicon ATR crystal was chosen as a sampling tool and off axis parabolic mirrors were used to focus the IR beam. The developed and optimized combined technique, Rheo-IR, is shown to be suitable to study the time evolution of simultaneous chemical reactions and viscoelastic material properties. The unique combination of rheology and FTIR through off-axis parabolic mirrors was successfully implemented and then used for both qualitative and semi-quantitative measurements. Rheo-IR is a robust and versatile tool and has the flexibility to investigate any molecular structures in a chemically changing material then directly correlate it to its rheological behavior. In the next chapter Rheo-IR will be used to investigate the polymer conversion and hydrogel formation of acrylic acid as a model system to test the new set-up. This newly developed tool can further be used to in rubber curing, food science and construction material (i.e. cement hardening).

Chapter 5

Application of the newly developed Rheo-IR technique on Hydrogel Formation

The newly developed Rheo-IR instrument is used to demonstrate its potential by applying it to study the correlation of the polymer network formation for a free radical co-polymerization of acrylic acid and methylenebis(acrylamide) as a crosslinking agent. This was done by investigating the IR spectra and the respective mechanical properties from rheological measurements, in a dilute solution. Futhermore, the detectivity and sensitivity were tested by preparing an acrylamide (AM) solution in D_2O and H_2O. The resulting spectra were compared the relationship between the storage modulus and the chemical conversion as seen by the absorbance of a the weak CH_2 peak at between $\widetilde{\nu} = 2983 - 2880\ cm^{-1}$.

5.1 Sensitivity: Functional group characterization during the formation of a poly(acrylic acid-co-N,N'-methylenebis (acrylamide)) (PAAc) hydrogel

In this section, the optimized Rheo-IR set-up was used to conduct simultaneous rheological and spectroscopic measurements by following the aqueous free radical crosslinking copolymerization of a diluted acrylic acid (AAc) and N,N'-methylenebis(acrylamide) (MBA). The synthesis procedure for the samples used here can be found in Appendix A.1.4 on page 151. Water is used as the aqueous media as it is known to have efficient heat transfer properties, but also has a high intensity in IR spectroscopy therefore making it difficult to dectect chemical changes with a water solution. The reaction takes place at 44 °C (sample heated using the Peltier element, see Figure 4.3 on page 70) making heat transfer important. For practical performance, a concentrated media (>10 % monomer concentration), a high heat transfer and a reduction in reaction times are required[236]. The AAc mass fraction was chosen to be 50 wt.% while the degree of crosslinking (DC, molar ratio of MBA to

AAc) was kept constant at degree of crosslinking, DC = 0.1 mol %. The water soluble azo initiator 2,2'-Azobis[2-(2-imidazolin-2-yl)propane]dihydrochloride (commercially known as VA-044) with a low decomposition temperature of 44 °C (Figure 5.1) was used to start the free radical polymerization while minimizing water evaporation during network formation. Since the temperature at which the radical decomposes is the preadjusted temperature of the Peltier element, the reaction begins immediately when the sample is placed on the rheological geometery. The free radical crosslinking copolymerization reaction is shown in Figure 5.1.

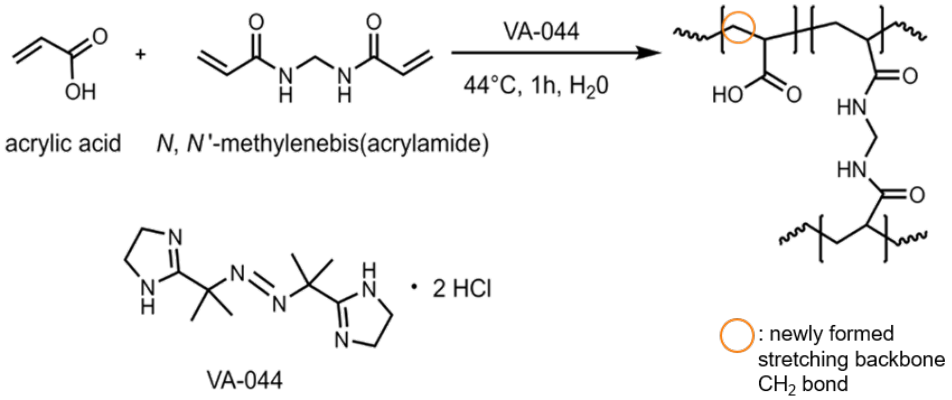

Figure 5.1: Free radical copolymerization of acrylic acid and crosslinking agent N,N'-methylenebis(acrylamide) for the preparation of poly(acrylic acid) hydrogels and azo initiator 2,2'-Azobis[2-(2-imidazolin-2-yl)propane]dihydrochloride (VA-044). The newly formed CH_2 stretching vibration on the polymerized backbone is highlighted by a circle.

The CH_2 stretching bond is rather weak and appears at around 2870 cm^{-1} during gelation and is used to follow the polymerization reaction. IR spectra were taken continuously, the interferograms were preaveraged over 30 s and stored using 64 scans at a final resolution of 4 cm^{-1}. The asymmetric CH_2 stretching bond area at ca. $2983 - 2880$ cm^{-1}[237], is used to monitor the degree of conversion during gel formation. Even though the $O-H$ peak is very pronounced, the asymmetric CH_2 peak evolves distinctively from the shoulder, demonstrating the high sensitivity of the Rheo-IR setup as seen in Figure 5.2 and Figure 5.4a. Additionally, the effect of hydrogen-bonding as evidenced by the broad $O-H$ stretching vibration ($\tilde{\nu} = 3600 - 2850$ cm^{-1})[238,239] could further add to the mechanical response. The effect of crosslinking density on the broadness of the $O-H$ stretching vibration could be comprehensively studied through deconvolution of the peak[239,240]. Other characteristic peak absorbance in acrylic acid are the $C=O$ stretch at 1687 cm^{-1} and 1725 cm^{-1}, a $C=C$ stretching vibration at 1634 cm^{-1} which overlaps with the H_2O vibration, an asymmetric and symmetric stretch of the carboxylate group (COO^-) at 1615 cm^{-1} and 1424 cm^{-1}, respectively[241,242]. The peak for the $C=C$ stretch at 1634 cm^{-1} is expected to decrease as the reaction comes to completion, however in Figure 5.2 we see a shift of this peak. This can be attributed to the H_2O is the atmosphere, since the system is open. In Figure 5.2 (zoomed-in), the sharp peak at 1687 cm^{-1} shifts to a higher wavenumber, whilst, the peak at 1725 cm^{-1} shifts to a lower wavenumber ($\tilde{\nu} = 1705$ cm^{-1}) and is more pronounced, which is indicative of an increase of the hydrogen bonding[239,242]. As an example of the capabilities of the presented Rheo-IR set-up, the relative conversion of the

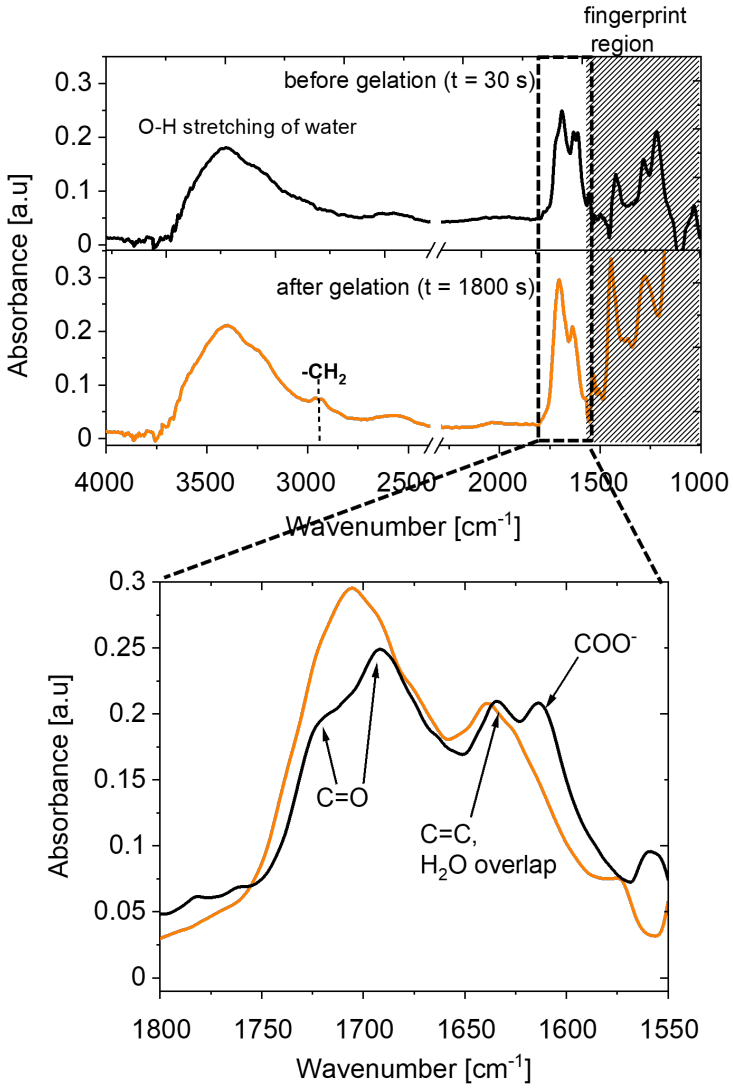

Figure 5.2: Rheo-IR: IR spectra ($4000 - 1000\ cm^{-1}$) before and bottom: after gelation (1800 s) with all relevant bands highlighted. Zoomed-in: IR spectra ($1800 - 1550\ cm^{-1}$) before and after gelation highlighting the carbonyl group ($C = O$), the $C = C$ and the carboxylate group (COO^{-}). Reproduced from Radebe et al.[189], with the permission of the Society of Rheology.

polymerization is considered and is discussed in terms of the kinetics of the CH_2 backbone peak growth and the subsequent rheological properties, in the following section.

5.2 In-situ monitoring of the gel formation

Using a dynamic time sweep the crossover point of the dynamic storage modulus ($G'(t,\omega)$) and loss modulus ($G''(t,\omega)$) development during polymerization is an accepted criteria used to determine the gel point[243–246]. In this work, a strain amplitude of $\gamma_0 = 0.1$ % at $\omega_1/2\pi = 1$ Hz was used for the dynamic oscillatory time sweep. The temperature of the Peltier (temperature range: -40 – 160 °C) was set to 44 °C according to the degradation temperature of the initiator. A gap of 1 mm height was used and the IR background was taken before 0.5 ml of the prepared sample was placed within the 25 mm geometry. Once the sample was added, the combined Rheo-IR measurement was started.

It is understood that the standard time of growth of each individual single chain, during free radical polymerization, is in the order of one second[247,248] which is shorter than the multiple second-to-minute time required to reach gelation as the reaction starts at different points in time due to the slower degradation of the initiator. Therefore, polymer chains are considered to form continuously. This occurs in the form of spatially separated individual coils (sol) in the dilute solution at the beginning of the reaction[247]. In the early stages of polymerization, we observe that G'' is larger than G', indicative of a sample in a viscous sol state and this time period is called the induction period (see Figure 5.2a)). In such a dilute solution, the viscosity is low and the elastic character is difficult to quantify, indicated by the noisy data for G'. The G', G'' crossover time, t_{cross}, is observed for this specific example at 500 s and $G'(t)$ starts to significantly increase, by up to 4 decades, as the polymerized gel network continues to form. The gel transition, t_{gel}, occurs when the sol chains form a critical concentration of interchain bonds spanning through the whole volume of the sample. The period after the t_{cross} where a large increase in G' is observed is the post gel point. The kinetics of this region are observed and quantified by Rheo-IR and will be discussed later.

As experimentally shown by Winter and Chambon[249,250] the t_{cross} is a weak function of frequency in an oscillatory experiment. This means that the t_{cross} is not exactly identical to the gelation time (t_{gel}). For practical reasons the crossover is used as the gel point, which is assumed to be of a similar value (i.e within a factor 2). The obtained rheological time dependance is divided in three phases as seen in Figure 5.2a). The rheological data was normalized using Equation 5.2.1 in analogy to rubber curing experiments[251,252]. The G' , G'_0 and G'_{final} are the storage modulus at time t, the initial storage modulus and the final storage modulus, respectively. As previously mentioned, the CH_2 asymmetric peak area ($2983 - 2880\ cm^{-1}$) is used to quantify the molecular conversion from an aqueous system to a gel. This microstructural polymer chain development is indicated in Figure 5.4a, with the appearance of the CH_2 peak at 2870 cm^{-1} over time. After baseline correction, the integral of the peak was normalized, θ_{IR}, as seen in Equation 5.2.2 The α_t, α_0 and α_{final} are the area at time t, the initial area (0.75 a.u.) and the final are (1.65 a.u), respectively.

$$\theta_{rheo} = \frac{G'_t - G'_0}{G'_{final} - G'_0} \tag{5.2.1}$$

$$\theta_{IR} = \frac{\alpha_t - \alpha_0}{\alpha_{final} - \alpha_0} \tag{5.2.2}$$

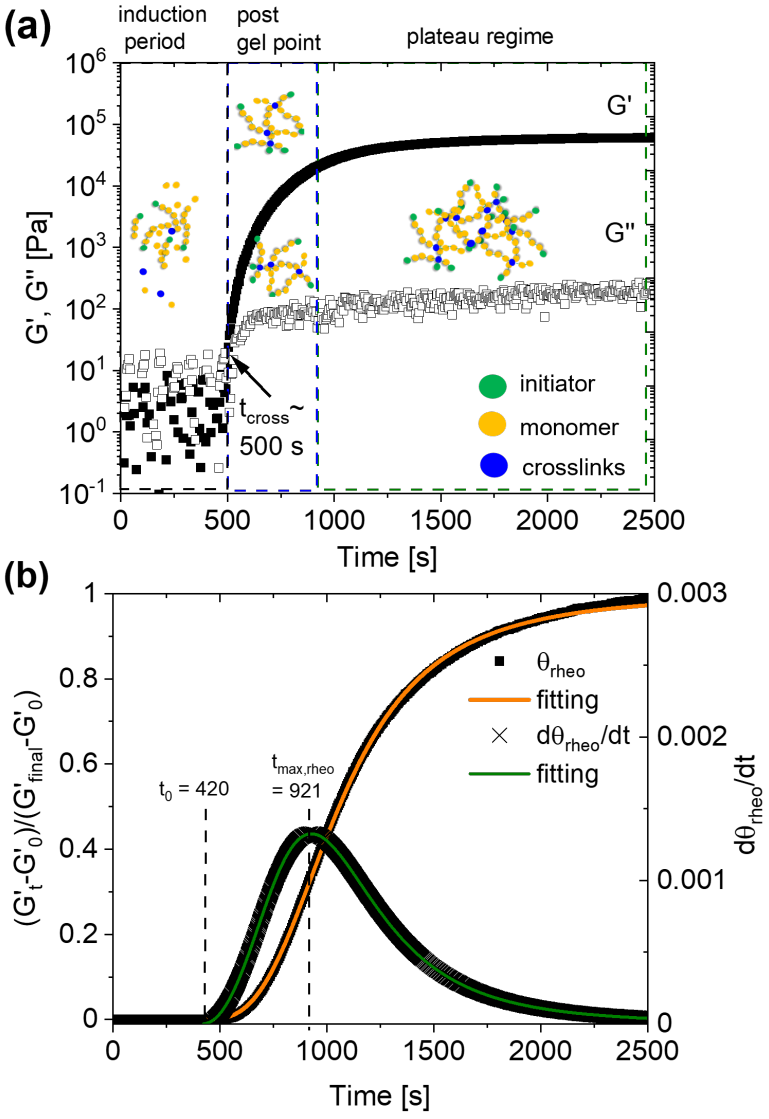

Figure 5.3: **(a)** Schematic and rheological representation of different regions within a time sweep measurement of the PAAc hydrogel formation. Induction period: No distinct increase of G′ is observed. The propagation of short non-crosslinked chains is progressing. Post gel point: Regime starts at the gel point where interchain crosslinking of polymer chains form a macroscopic network as G′ increases. Plateau regime: G′ and G″ levels off at the maximum and the moduli remain relatively stable and the reaction is complete[250]. **(b)** Normalized storage modulus as a function of polymerization time and fitted with Equation 5.2.3 (fitting parameters are found in Table 5.1.) and the first derivation, taken from the modelled Equation 5.2.3 data points, of the normalized storage modulus as a function of polymerization time. Reproduced from Radebe et al.[189], with the permission of the Society of Rheology.

The normalized storage modulus and absorbance were fitted empirically with the Equation 5.2.3[253,254]. This model is also used for isothermal rubber curing[252]. Here k, r and t_0 are the gelation rate, kinetic order of the reaction, and the onset (e.g. induction period) of the increase in the chemical (absorbance area, a.u) or mechanical response ($G'(t)$, $G''(t)$) respectively. The first derivative of Equation 5.2.3 is Equation 5.2.4 used to fit the normalized first derivative of the normalized modulus, $d\theta_{rheo}$ and normalized absorbance area, $d\theta_{IR}$. The mathematical derivation of Equation 5.2.4 from Equation 5.2.3 can be found in Appendix A.1.1 on page 147.

$$\theta = \frac{(k(t-t_0))^r}{1+(k(t-t_0))^r} \tag{5.2.3}$$

$$\frac{d\theta}{dt} = \frac{r(k(t-t_0))^r}{(t-t_0)(1+(k(t-t_0))^r)^2} \tag{5.2.4}$$

Table 5.1: Kinetic parameters obtained from fitting the normalized storage modulus (rheo) and normalized absorbance (IR) experimental as function with of Equation 5.2.3 and the extrapolated t_{cross} and t_{max} (see Figure 5.2 and Figure 5.4 on page 89 and page 90, respectively) values.

	k [s^{-1}]	r	t_{cross}[s]	t_0[s]	t_{max}[s]	R^2 (Equation 5.2.3)
Rheo	0.0016 ± $1.50\times^{-5}$	3.02 ± 0.025	500 (see Figure 5.2a)	420 ± 5.70	921	0.999
IR	0.0027 ± $3.09\times^{-4}$	2.96 ± 0.296	-	144 ± 38.4	430	0.994

The first derivative of the storage modulus with time, $d\theta_{rheo}/dt$ (Figure 5.2b), and the first derivative of the relative degree of conversion, $d\theta_{IR}/dt$ (Figure 5.2b), yielded a peak corresponding to the rate post gelation kinetics, as also deduced by Equation 5.2.4. Table 5.1 shows the he maximum growth rate of the storage modulus increase is slower ($k = 0.0016\ s^{-1}$) than that of the relative degree conversion ($k = 0.0027\ s^{-1}$), however both increase with the power law exponent of 3. Furthermore the start of the increase occurs at approximately 420 s for the storage modulus and almost immediately (144 s) for the relative degree of conversion, which is expected considering the mechanism of free radical copolymerization crosslinking, explained earlier. The t_{max} is taken as the time value of the definitive peak height of the derivative functions of the normalized storage modulus and the peak area from the IR absorbance peak. The t_{max} from the rheological measurement, $t_{max,rheo}$ was 921 s which corresponds to approximately 90 % relative conversion, at which point the gelation process can be considered complete. The t_{max} from the IR relative absorbance area, $t_{max,IR}$, was 430 s (30 % relative conversion), which can be correlated to the gelation point because the t_{cross} (crossover time of $G'(t, \omega)$ and $G''(t, \omega)$) occurs at approximately 70 s later and is followed by a sharp increase in the storage modulus, associated with the post gel point kinetics (see Figure 5.2a). The

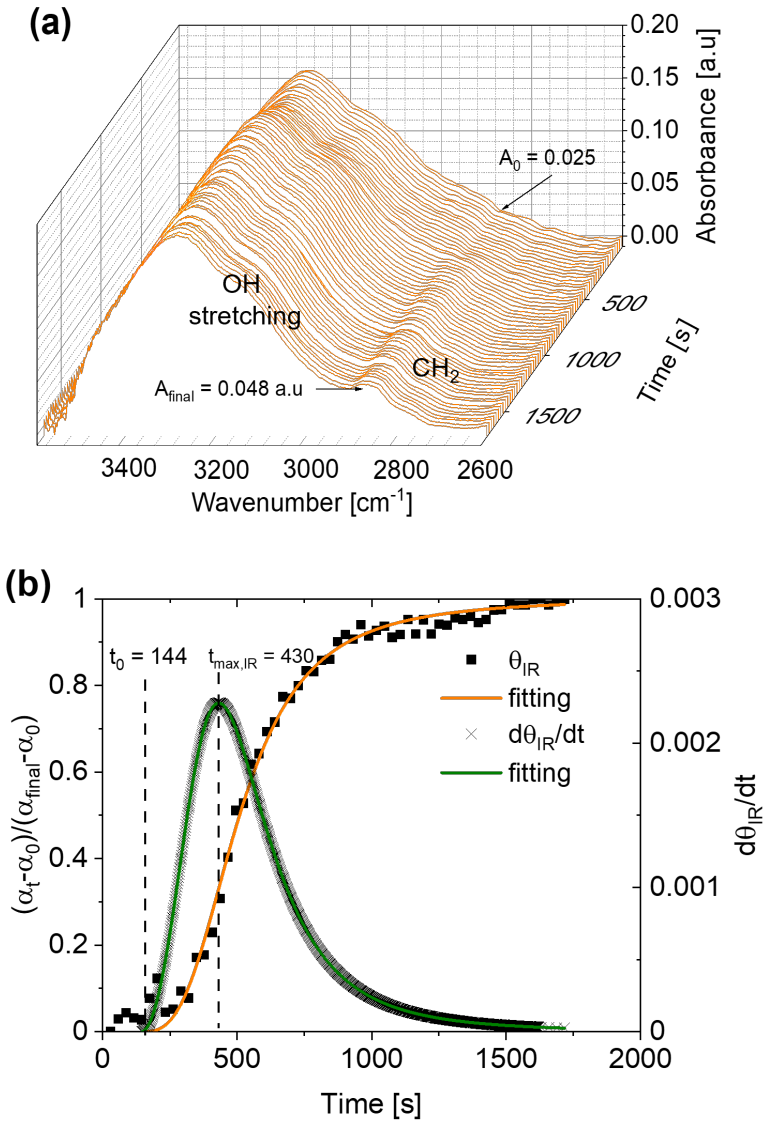

Figure 5.4: **(a)** FTIR spectra ($3600 - 2600\ cm^{-1}$) during the time sweep of the copolymerization with the initial and final absorbance (A_0 and A_{final} respectively) as well as the initial and final absolute area (α_0 and α_{final}, respectively) of the CH_2 asymmetric peak ($2983 - 2880\ cm^{-1}$). **(b)** Normalized peak area, θ_{IR}, as a function of polymerization time fitted with Equation 5.2.2 (fitting parameters are found in Table 5.1.) of the polymerization obtained from the area of the CH_2 asymmetric peak ($2983 - 2880\ cm^{-1}$) and the first derivation, taken from the modelled Equation 5.2.3 data points, of the CH_2 asymmetric peak as a function of polymerization time. Reproduced from Radebe et al.[189], with the permission of the Society of Rheology.

different time values seen in Table 5.1 indicate that chemistry occurs before any significant change in the modulus can be observed. By using Rheo-IR, we were able to follow the kinetics of monomer conversion during the gelation process including the sol formation and the gelation whilst simultaneously measuring the mechanical response. It is important to note that in this work, the absolute conversion is not of interest, rather the conversion kinetics and thus theories that predict the monomer conversion of polymeric system, such as the Flory-Stockmayer mean field theory (F-S theory)[255,256], are not considered.

The relationship between the mechanical behavior and the polymerization degree is shown

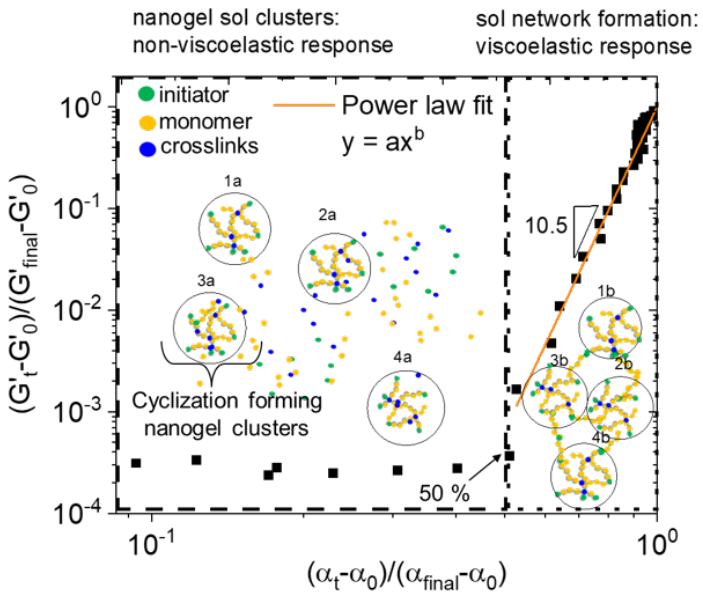

Figure 5.5: Evolution of the normalized storage modulus, θ_{rheo}, as a function of normalized CH_2 peak area, θ_{IR}, where the relationship is observed. The illustrations labelled 1a, 2a, 3a and 4a represent the forming nanogel clusters during the induction period (see Figure 5.2a), where a non-viscoelastic mechanical response is observed. The illustrations labelled 1b, 2b, 3b and 4b represent a heterogeneous polymer network gel[248,257]. Reproduced from Radebe et al.[189], with the permission of the Society of Rheology.

in Figure 5.5. Approximately 50 % relative chemical conversion is required to reach the onset of gelation observed in rheometry by a storage modulus of about 10 Pa (10^{-3} normalized final modulus), thus making t_{cross} (500 s) the gel point, for the given system. After 50 % relative conversion, the system continues to rapidly cure (post gel point kinetics) as seen in Figure 5.2a through a further chain-growth and crosslinking in a free-radical copolymerization of monomers and crosslinker. Crosslinkers such as the one used, N,N'-methylenebis(acrylamide) (MBA), are known to be more reactive than acrylic acid[258]. Consequently, it is assumed that the crosslinker is consumed faster than the monomer during the early stage of the reaction, leading to cyclization and multiple intramolecular crosslinking within the growing polymer chains[247,258] as illustrated in Figure 5.5, where a non-viscoelastic response is observed. This leads to the formation and growth of locally isolated nanogel clusters where the low concentration of radicals preferentially consumes the crosslinker at the beginning of the reaction, before the gel point conversion[257], as also illustrated in Figure 5.5. Later in the reaction, after approximately 500 s for this system, these clusters are covalently interconnected to form a space-filling network (gel) exhibits an increased viscoelastic response with the power law exponent of 10.5. The final factor 2 in polymerization (50 % to 100 % relative conversion) gives an increase of a factor 1000 in modulus. This data set and correlation can be uniquely determined through the combined method of Rheo-IR. The above hypothesis, is consistent with the experimental data from the Rheo-IR measurement. Previous studies have additionally shown, a noticeable degree of spatial inhomogeneity[259], which would not be detectable with set-up. As shown, Rheo-IR is very useful in systematic studies of gel formation as function of monomer concentration, crosslinker density or reaction temperature. Rheo-IR allows the study of the interplay

between chemical conversion and mechanical parameters, specifically $G'(t, \omega)$ and $G''(t, \omega)$ in hydrogels.

5.3 Resolution and sensitivity: Functional group characterization in H_2O vs D_2O

In the previous section, the sensitivity of the newly developed Rheo-IR technique was shown by monitoring and quantifying a CH_2 asymmetric peak on the shoulder of a broad water peak in the region $\tilde{\nu} = 3600 - 2600\ cm^{-1}$. To isolate the CH_2 peak, water (H_2O) can be replaced with deuterated water (D_2O), which has a $O-D$ peak at ca. $\tilde{\nu} = 2600\ cm^{-1}$ (a factor $\sqrt{2}$ lower than the $O-H$ peak) and $D-O-D$ absorbance peak at ca. $\tilde{\nu} = 1200\ cm^{-1}$. In the previous section, AAc was used as a proof of concept (also has industrial relevance). However, AAc has a carboxylic acid group, which undergoes $H-D$ exchange. Therefore, it is not as ideal as acrylamide (AM) in D_2O for a comparative study. For this, two acrylamide (AM) solutions were prepared (see Appendix A.1.5)[8], one in H_2O and another in D_2O.

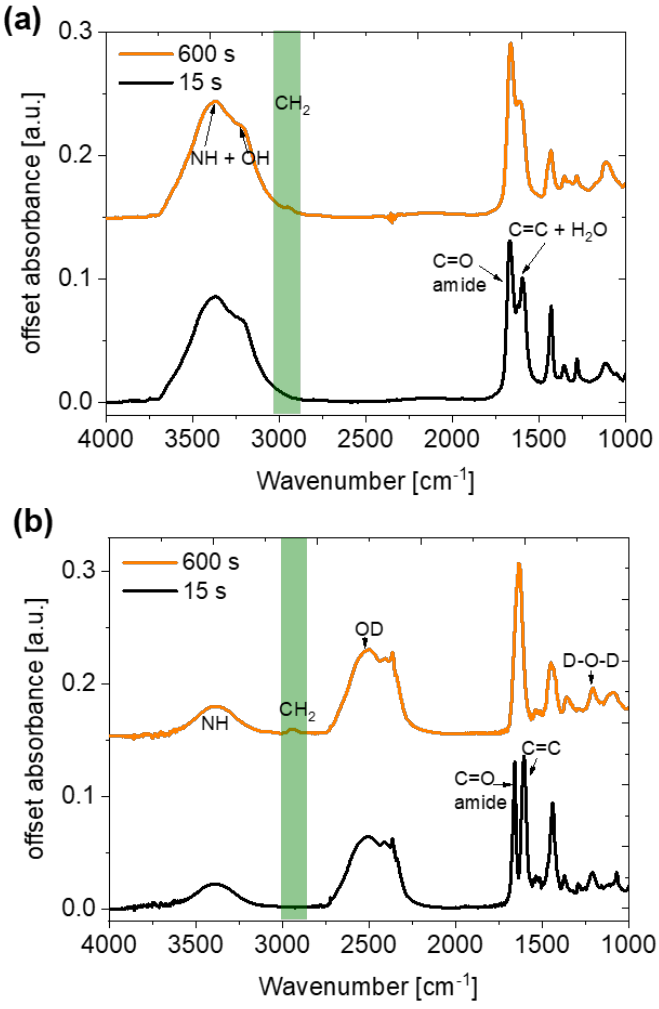

Figure 5.6: Rheo-IR:**(a)** FTIR spectrum ($4000 - 1000\ cm^{-1}$) of acrylamide, before (15s – black line) and after polymerization (600 s – orange line) in H_2O **(b)** FTIR spectrum ($4000 - 1000\ cm^{-1}$) of acrylamide, before (15 s – black line) and after polymerization (600 s – orange line) in D_2O.

The same rheological parameters as used for the acrylic acid (AA) polymerization in Section

[8]These samples were kindly prepared by Christian Fengler as a part of his PhD work on hydrogels.

5.1 were used for the AM solutions. Figure 5.6a and b show the FTIR spectra from the Rheo-IR after 15 s on a 40°C Peltier plate and after 600 s (10 mins). As highlighted by the green box, at 15 s there is no CH_2 peak as polymerization has not been completed and after 600 s both solutions have polymerized as evidenced by the appearance of the CH_2 peak. The amide (NH) stretching vibration also overlaps with the OH from the water as does the $C = C$ and the H_2O peak as seen in Figure 5.6a.

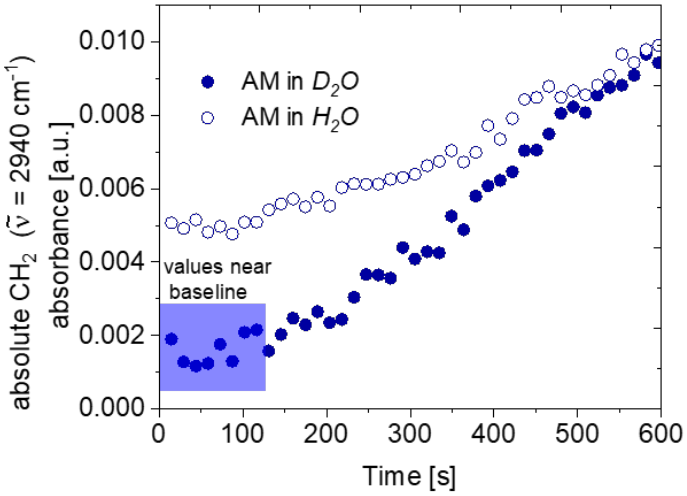

Figure 5.7: Evolution of the absolute peak aborbance of CH_2 polyacrlyamide at $\widetilde{\nu} = 2940\ cm^{-1}$ as a function of time in D_2O and H_2O.

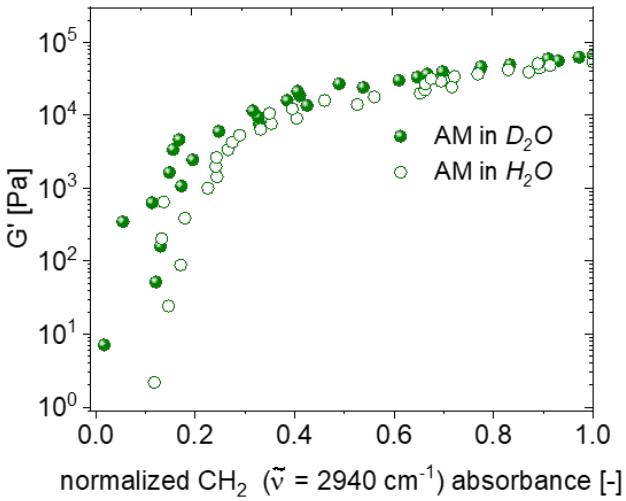

Figure 5.8: Evolution of the storage modulus (G'[Pa]) as a function of the normalized CH_2 polyacrlyamide peak absorbance.

Similarly, the $C = O$ ($\widetilde{\nu} = 1651\ cm^{-1}$) from the amide also slightly overlaps with the $C = C$ and H_2O peak as also seen in Figure 5.2 for the AA polymerization. The OD and $D - O - D$ peaks, from the deuterated water, absorb at 2500 cm^{-1} and 1250 cm^{-1}, respectively, as shown in Figure 5.6b and do not overlap with any of the characteristic peaks of interest allowing for better sensitivity (i.e. detectability). By definition, as explained

in Chapter 3, sensitivity in FTIR is the smallest change in the peak intensity that can be detected while resolution is the smallest portion of $\Delta\tilde{\nu}$ deviation of the peak that can be qualified. In terms of absolute absorbance values, the CH_2 peak in H_2O is expected to appear to have higher absorbencies because of the combination (additive absorbances) with the OH absorbances.

This is clearly illustrated in Figure 5.7 by the open symbols. The closed symbols used to represent the polymerization in D_2O are near the baseline values with the first minute and a half, and could be regarded as noise. In order to compare the sensitivity of a Rheo-IR polymerization experiment done in H_2O and D_2O, the dependency of the storage modulus on the normalized CH_2 peak absorbance, as per Equation 5.2.2, is investigated. Figure 5.8 shows that the polymerization in both D_2O and H_2O have the same relationship since both plots overlap. However the polymerization in D_2O shows a slight delay in the low absorbance $(0 - 0.3)$. The first few data points can be regarded as noise since they correspond the liquid material properties. The rheometer is not sensitive to enough to viscosities (Pa.s) and moduli below 10 Pa, at the chosen experimental conditions. In conclusion, polymerization in D_2O, for this kind of sample, does not enhance the normalized sensitivity. However, if the chemical changes are expected to be see immediately when the Rheo-IR measurements is started, the sensitivity would be affected and D_2O could be a useful alternative to H_2O.

5.4 Concluding remarks

In this chapter, FTIR spectroscopy combined with rheology proved to be a sensitive method for monitoring chemical bond formation and assigning of characteristic changes occurring during the aqueous crosslinking copolymerization of acrylic acid and N,N'-methylenebis(acrylamide), as a model system. Specifically, a rather weak asymmetric CH_2 stretch growing peak could be monitored as an indication of network formation and correlated to the rheological evolution through the storage modulus. The combined technique provides a unique insight into molecular changes during gelation which can be further utilized to obtain a fundamental understanding of the complex interplay between chemical conversion and mechanical properties. Additionally, the reproducibility and resolution of the FTIR was monitored in a polymeric gel solution of acrylamide in water and deuterated water. As expected, both solutions showed the same overall relationship between the storage modulus and the normalized absorbance of the weak CH_2 peak, further demonstrating the sensitivity capabilities of the newly developed Rheo-IR set-up.

Chapter 6

Application of FT-Rheology and Rheo-Combined Methods on Cement Paste

The linear and nonlinear oscillatory shear rheology of fresh cement paste was investigated in this study. The main focus was on the deformation and flow processes of fresh cement paste on the basis of microscale processes during early hydration. By applying FT-rheology, the intensity at higher harmonics that are normalized to the fundamental intensity and a model with a quadratic scaling in the strain amplitude is used to predict two critical strains, associated with the solid and mobile parts of cement paste. The lower strain amplitude of 0.01% *is used as the linear oscillatory strain and the higher strain amplitude of* 0.3% *is used as the criticcal strain. Both strains are used to investigate their effect on the molecular dynamics via Rheo-NMR and Rheo-Dielectrics. Additionally, offline and online (Rheo-IR) are compared and used for a qualitative and qunatitative description of hydrate formation as a function of storage modulus.*

6.1 Determining the critical strain, γ_c, for cement using SAOS

6.1.1 Material and sample preparation

Ordinary Portland cement (OPC) type CEM I 42,5 R was used in all cement paste mixes, in this chapter. For a detailed analysis of the material, see reference[76]. Distilled water was used for all measurements. The mixing ratios used are found in Table 6.1. The cement paste was mixed by an IKA mixer with a four-blade propeller for 1 min at 500 revolutions per minute (rpm), rested for 2 mins then placed on the plate geometry.

Table 6.1: Cement paste water to cement ratios (w/c) and solid volume fractions (ϕ) used in this work, based on cement density (ρ_{cement}) of 3.15 g/ml and water density ρ_{water} of 1 g/ml.

cement, c (g)	water, w (ml)	w/c	solid volume fraction (ϕ)
10	2.9	0.29	0.52
10	3.4	0.34	0.48
10	4	0.4	0.44
10	5	0.5	0.39
10	6	0.6	0.35

6.1.2 Experimental protocol: Rheology and FT-Rheology

A strain-controlled rheometer (ARES G2, TA Instruments) was used to perform all rheological measurements. The temperature was controlled at 23 °C ± 0.1 °C by using a Peltier system.

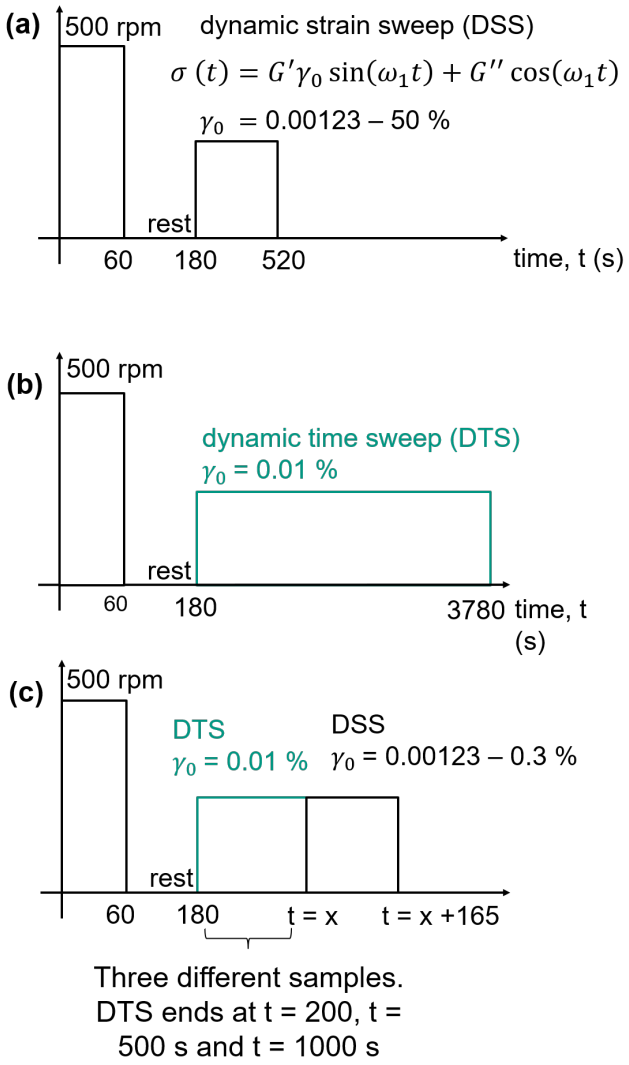

Figure 6.1: Mixing and rheological protocol used to measure evolution of the cement paste in both LVE and NVE region as function of strain amplitude and time (unless otherwise stated) where **(a)** is the mixing and rheological protocol for the DSS **(b)**is is the mixing and rheological protocal for the DTS and **(c)** is is the mixing and rheological protocol for the DSS and DTS measurements.

Dynamic strain sweep (DSS) and dynamic frequency sweep (DFS)

A parallel-plate stainless steel geometry (d = 25 mm), with a roughed surface was used. The plate-plate gap was kept in the range of 1 mm. DSS test were conducted by changing the strain amplitude, $\gamma_0 = 0.0025\%$ to 50% at a fixed frequency $\omega/2\pi$= 1 Hz. DFS test were conducted by sweeping the material frequency from $\omega/2\pi = 0.1$ to 100 Hz at a fixed strain amplitude, $\gamma_0 = 0.01\%$, which has experimentally been proven before on these samples to be in the LVE regime.

Fourier Transform (FT) rheology

To acquire the stress signal, the ARES-G2 rheometer was set in the transient mode for 1 minute (60 cycles of 1 Hz). The FT spectra was obtained by Fourier transforming the stress signal from the time domain to the frequency domain and the intensity was normalized by the absolute intensity at the basic excitation frequency. These harmonics are described as peak intensities at the frequency domain (i.e., I_3 is the intensity of the harmonic at 3 Hz). All the rheological protocols are used are shown schematically in Figure 6.1.

6.1.3 FT-rheology: characterizing the inhomogeneity of networks in the cement paste

In rheology, a dynamic strain sweep is when a range of strain amplitudes (normally from low to high) is applied on a material whilst keeping the frequency of oscillatory deformation constant. The onset of the decrease of the storage modulus (G′) is often referred to as the critical strain, γ_c[113,260,261]. Physically, this means that the material is perturbed, and the applied strain affects the stress response of the material. The nonlinear mechanical behaviours of cement paste under oscillatory shear have been studied and are typically presented in terms of Lissajous-Bowditch curves[33]. Figure 6.2 illustrates the response of linear rheological properties to the strain amplitudes from $\gamma_0 = 0.0025\%$ to 50% at 23 °C and oscillatory frequency $\omega_1/2\pi = 1$ Hz. The storage moduli G′ and the loss moduli G″ of four cement pastes with different solid volume fractions are compared in Figure 6.2a and Figure 6.2b, respectively. The G′ and the G″ values for solid volume fractions lower than 0.52 have very similar values. This may be expected for relatively low solid volume fractions (i.e. 0.35 and 0.39) but not necessarily for solid volume fractions above 0.4. Figure 6.3 shows a sample that is prepared as described under *Material and sample preparation* and follows the rheological protocol from Figure 6.1b. Here it is observed that the time frame in which the strain sweeps takes place is within a time when the viscous properties are possibly still present, whereas the work by Schultz et al.[113] takes place at a time when the material is more elastic (10 minutes hydration), as seen by the area marked with a dotted circle and the number 2 in Figure 6.3. However, since the geometry type is plate-plate, the material is prone to sedimentation and formation of an aqueous layer. The actual presence and thickness of this layer within the strain sweep experimental time frame ($\sim$ 6 min measurement time) is unknown but is in the order of ($< 1\mu m$)[96]. This aqueous layer is superimposed upon the strain area within the rest of the material.

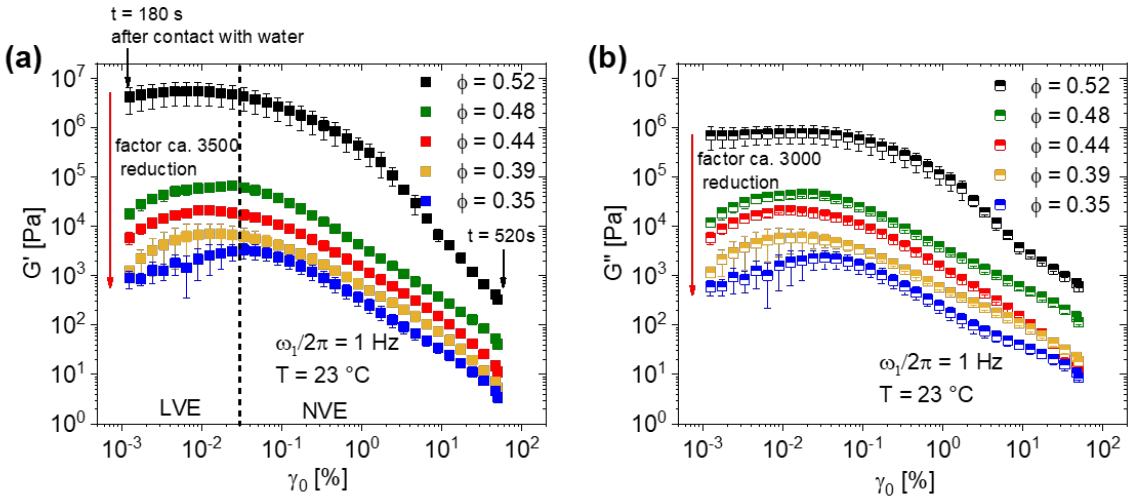

Figure 6.2: Oscillatory strain sweep of four fresh cement pastes at $\omega_1/2\pi = 1Hz$ at 23 °C, conducted over 6 minutes for each sweep **(a)** storage modulus as a function of γ_0 and time, t, ($G'(\gamma_0, t)$) **(b)** loss modulus as a function of γ_0 and t ($G''(\gamma_0, t)$) at different solid fractions. See Table 6.1 for mixing ratios.

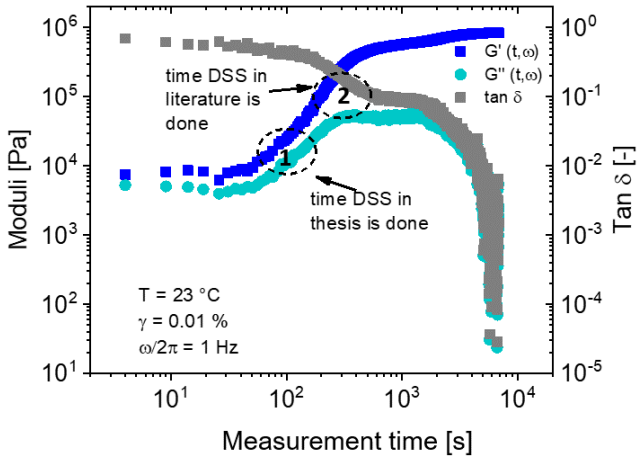

Figure 6.3: Dynamic time sweep (G′, G″ and tan δ) of cement paste with water to cement ratio (0.4, $\phi = 0.42$) at $\omega_1/2\pi = 1Hz$ at 23 °C.

The result is an underestimate of the stiffness/elasticity of the sample[262]. At very low strain amplitudes as the ones used here (0.01 %) the slippage from this layer is not always present. Figure 6.3, for example, shows no slippage effects whereas Figure 6.18b (see Section 6.3, page 118) shows slippage for a strain amplitude of 0.3%. Therefore, either the material is really not stiff within this time frame as suggested by Figure 6.3 or the aqueous layer has a 10 times decrease effect in the storage/elastic modulus. Nevertheless, this can be avoided and better quantified in future work by using roughened geometry surfaces. However, the development of the Rheo-IR limits the use of roughened geometries,

especially as a top geometry because the optimized signal to noise is only possible with a smooth, polished surface (see Figure 4.8 in on page 74).

An overview of the effect of time and strain on the stress response and particularly the storage modulus is presented in Figure 6.4. It is expected that the storage modulus increases by at least 3 decades[35,261] within an hour of hydration, based on point data (open squares). The sinusoidal applied strain and stress response data was acquired by setting the ARES-G2 rheometer to transient mode. In Figure 6.4, the stress clearly changes between 200 and 3600 s. From here $G'(\gamma_0, t)$ and $G''(\gamma_0, t)$ can be better visualized. As expected, the overall $G'(\gamma_0, t)$ and the $G''(\gamma_0, t)$ decrease as the solid content decreases, seen in Figure 6.4. The materials behave more viscous than elastic at solid fractions lower than 0.52. Furthermore, two distinct regions are observed and separated in the linear viscoelastic region (LVE), indicated by a dashed border in Figure 6.2, and nonlinear viscoelastic (NVE) region. Here, the LVE region is defined as the end when the G' and the G'' deviate by 10 % or more from the plateau. However, since cement paste is chemically active, the effect of time must also be considered and thus deviation is expected to be higher. In order to understand where the LVE region ends and the NVE starts, the time and strain evolution of the higher harmonics were investigated. Therefore, the importance of determining a linear viscoelastic region and how a small change in strain can affect the structural build up is shown. Since the end of the LVE cannot be precisely determined for a material with an asymptotic deviation in the moduli, investigation into the appearance of higher harmonics can provide a clearer indication. However, depending on the data acquisition and therefore the noise in baseline of an FT magnitude spectrum, higher harmonics in the 0.01-5% range may not be seen. Generally, the noise in the spectrum can be reduced by averaging over many cycles, but this is not recommended for cementitious materials, as they are constantly changing over time. For this reason, we use 1% appearance of the 3rd higher harmonic as a threshold for when nonlinear behavior begins. At a small γ_0, noise from the rheometer dominate in the FT spectra. For the same experimental system, i.e. identical rheometer under the same torque level for the force transducer, the noise level of I_3 in Equation 6.1.1 should be a constant[61]. The Fourier intensity at the excitation frequency, I_1, increases linearly with strain amplitude according to the first term in Equation 6.1.1; therefore, at small strain amplitudes where $I_1 \sim \gamma_0$ and $I_3 \sim$ noise, then:

$$I_{3/1}\,(at\ small\ \gamma_0) \equiv \frac{I_3}{I_1} \propto \frac{constant\ noise}{\gamma_0} \tag{6.1.1}$$

After FT of the stress signals from Figure 6.4a,c and e, an FT spectrum is obtained such as the ones shown in Figure 6.5. Figure 6.5a shows the FT spectra of cement from a linear stress response. This is seen through the appearance of only the principle harmonic I_1.

An important observation from these spectra is that only odd higher harmonics are observed due to symmetry[263] of the waveform, which is commonly observed in FT-rheology. At a

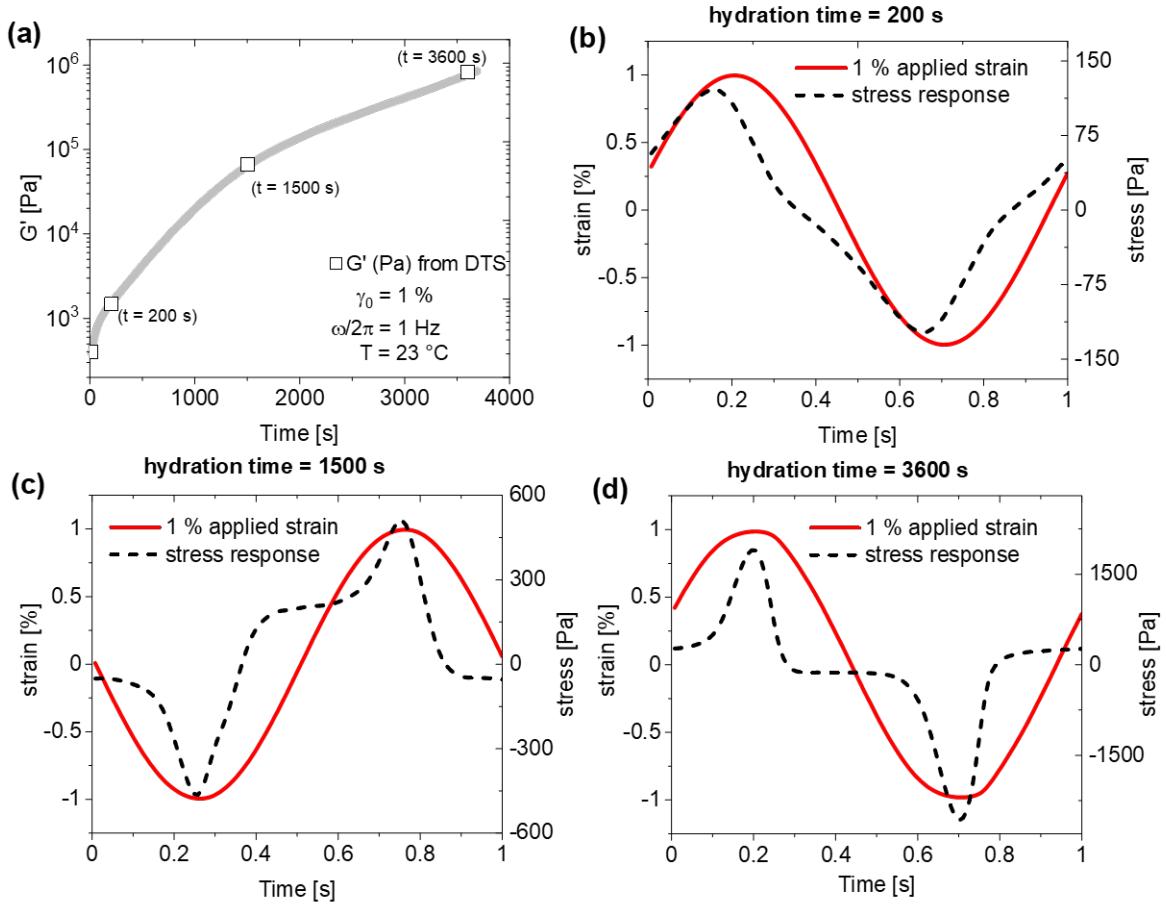

Figure 6.4: **(a)** Storage modulus, G′, as a function of hydration time and stain amplitude $\gamma_0 = 1$ %, $\omega_1/2\pi = 1Hz$, and T = 23 °C. The stress responses of the cement paste at **(b)** t = 200 s, **(c)** 1000s and **(d)** 3600 s.

$\gamma_0 = 0.05\%$, the FT spectrum shows the appearance of two odd higher harmonics, I_3 and I_5 as seen in Figure 6.5b. From the stress response, in the inlet, the output is visually seen as linear, which could be misleadingly considered as a linear response. Upon FT of this $\sigma(t)$, the nonlinearity can be displayed by a spectrum in the frequency domain, which is more observable with the intensities of higher harmonics. The stress response of Figure 6.5c is noisy and tilted. Therefore, the FT spectra is expected to show higher relative intensity of the higher harmonics. In this case $I_{3/1}$, $I_{5/1}$ and $I_{7/1}$ are all more obvious than the $\sigma(t)$ at smaller γ_0. Theoretically, the maximum intensity of $I_{3/1}$ is expected to be 0.33[61], when the raw signal in the time domain is close to a square shape waveform. The $I_{3/1}$= 0.176 indicates that the material shows a stronger nonlinearity when a strain amplitude of 0.1% is applied. At $\gamma_0 = 0.3\%$, the stress waveform is more tilted as seen in the inlet of Figure 6.5d. More obvious odd higher harmonic appeared in the FT spectra. The intensity of $I_{3/1}$is 0.357, which is higher than the theoretical value, in the simplifies theory. This indicates that there could be other factors that are influencing the material besides the applied strain.

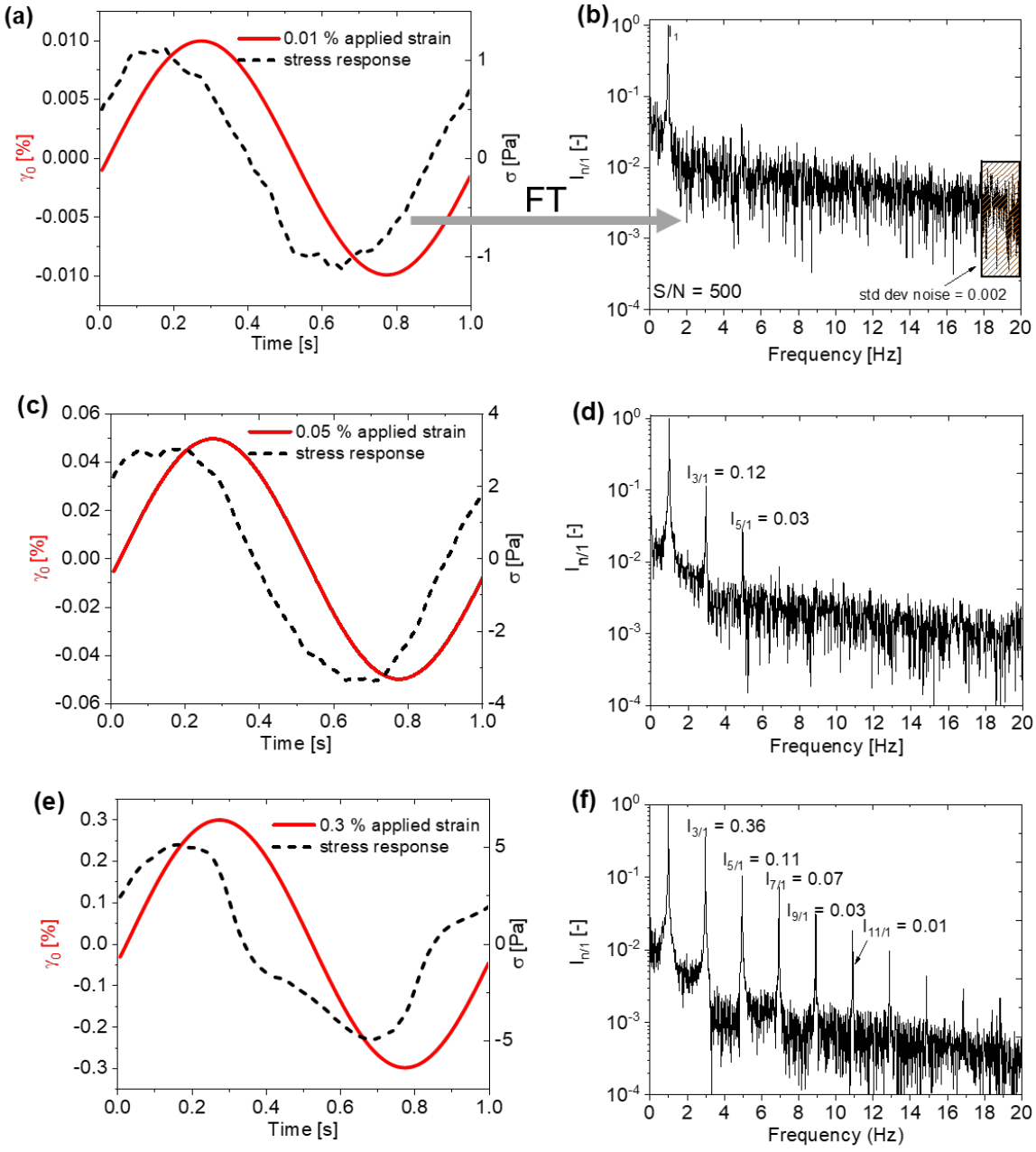

Figure 6.5: Stress responses of the cement paste to the strain amplitude of **(a)** $\gamma_0 = 0.01$ %, **(c)** $\gamma_0 = 0.05$ %, **(e)** $\gamma_0 = 0.3$ % and their corresponding FT spectra in the frequency domain **(b)**, **(d)** and **(d)** where the intensity of the higher harmonics is on a logarithmic y-scale, $\omega_1/2\pi$ =1 Hz at a $\phi = 0.44$.

Fitting function of $I_{3/1}(\gamma_0)$

According to Roussel et al.[112] from a rheological study, fresh cement pastes have two intrinsic critical strain amplitudes, with the large one in the range of $\gamma_l = 2.5\%$ and the small one in the range $\gamma_s = 0.05\%$, where subscript l and s mean large and small. The large critical strain amplitude is obtained through a yield stress measurement and is associated with the colloidal network between two particles. It is also described as onset of flow. The small critical strain amplitude is obtained through a dynamic strain sweep measurement

and is related to the hydrates at the early stage, which in the absence of superplasticizers is formed preferably at the contact points of cement particles. At γ_s, the system does not begin to flow.

In this work, the $\gamma_c$is also of interest (γ_s, in Roussel et al.[112]), specifically the physical changes in the material that govern the non-linear response.

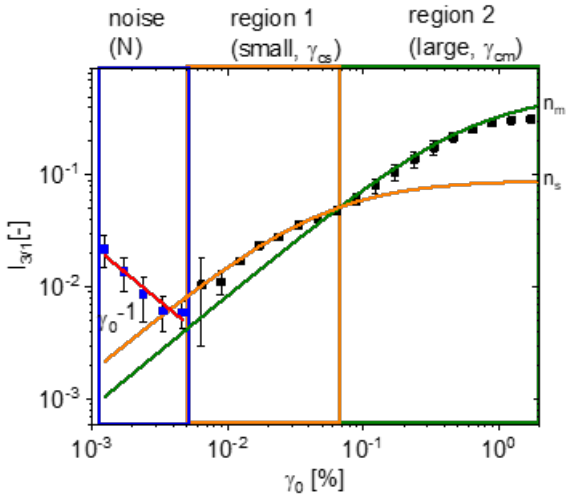

Figure 6.6: The relative intensity of third harmonics, $I_{3/1}$, acquired from FT-rheology, as a function of strain amplitude of cement paste with three regions highlighted corresponding to Equation 6.1.1, for $\phi = 0.44$. The red line represents the noise where the slope is -1. The orange line is the $I_{3/1}(\gamma_0)$ corresponding to the more small strain amplitude (γ_{cs}) and the green line is the $I_{3/1}(\gamma_0)$ corresponding to the larger strain amplitude (γ_{cm}).

By considering the data behavior of $I_{3/1}(\gamma_0)$ as shown in Figure 6.6, three distinct regions are observed at different strain amplitudes. These regions are highlighted in Figure 6.6 and described as the noise (γ^{-1}), small, and large strain region. Considering a quadratic growth function, which is sensitive to the strain amplitude and reaches a plateau at infinitely high strain, a quantitative function to describe $I_{3/1}(\gamma_c)$ was proposed for materials with mixed networks at different length scales[264].

$$I_{3/1(\gamma_0)} = \underbrace{\frac{N}{\gamma_0}}_{noise\ dominated} + n_s * \underbrace{\frac{(\gamma_0/\gamma_{cs})^2}{1+(\gamma_0/\gamma_{cs})^2}}_{region\ 1} + n_m * \underbrace{\frac{(\gamma_0/\gamma_{cm})^2}{1+(\gamma_0/\gamma_{cm})^2}}_{region\ 2} \tag{6.1.2}$$

From this function, two critical strains are deduced. The smaller critical strain amplitude, γ_{cs}, is associated with the solid phases where "s" stands for the solid, including both hydrated and unhydrated networks. Where n_s or n_m stands for the utmost rheological nonlinearity. The larger critical strain amplitude, γ_{cm}, is assigned to the more mobile "m" network in the cement paste which is formed by the colloids with more mobile water molecules network. The two types of networks build up nonlinearity near their critical strain amplitude, and reach the limitation denoted as n_s and n_m, respectively. This model

is used to fit the $I_{3/1}(\gamma_0)$ of cement pastes of different solid fractions, shown in Figure 6.7 a anb b. The increase of $I_{3/1}(\gamma_0)$ for the highest and lowest solid fractions ($\phi = 0.52$ and $\phi = 0.35$, respectively) is not quadratic anymore but rather grows with a smaller growth power order. A modified, non-quadratic, model was used to fit the solid region of the $I_{3/1}(\gamma_0)$ for $\phi = 0.52$ and 0.35 as follows:

$$I_{3/1}(\gamma_0) = \frac{N}{\gamma_0} + n_s * \frac{(\gamma_0/\gamma_{cs})^k}{1 + (\gamma_0/\gamma_{cs})^k} + n_m * \frac{(\gamma_0/\gamma_{cm})^2}{1 + (\gamma_0/\gamma_{cm})^2} \tag{6.1.3}$$

$$\text{and } 1 < k < 2$$

where k is the power law of the $I_{3/1}(\gamma_0)$ of the more solid part of the material. Figure 6.7c shows that a k value of 1.1 ± 0.12 for both samples fits better.

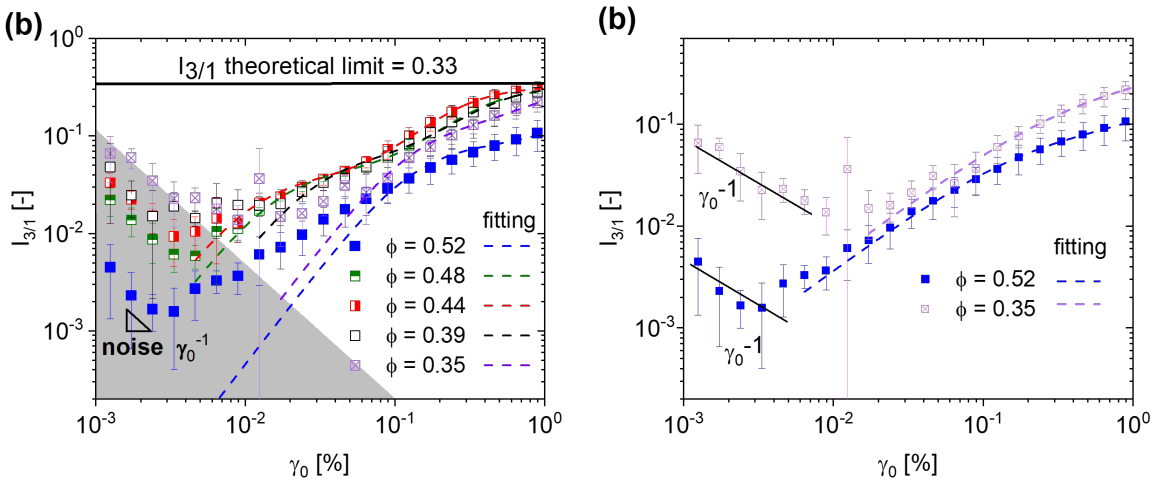

Figure 6.7: **(a)** The sum of the overall fit for region 1 and 2 for different solid fractions, without the term for noise, at T = 23 °C and $\omega_1/2\pi = 1Hz$. **(b)** Equation 6.1.3 fitting on experimental $I_{3/1}(\gamma_0)$ data for $\phi = 0.52$ and 0.35.

This could imply that under oscillatory shear, the mobility of the cement grains for very high solid fractions (i.e. 0.52) are hindered because the maximum packing fraction has been reached, therefore rheological nonlinearity started to build up at lower strain amplitudes.

Effect of hydration time on the non-linearity (γ_c)

At room temperature, the set retarder of OPC, which is typically a blend of gypsum, hemi-hydrate and anhydrite, is normally adjusted that setting of cement paste without admixtures occurs roughly between $180 - 240$ min, according to different sources[194,260,265]. The critical strain can be loosely defined as the strain at which a network rupture in particle suspension occurs[112]. However, considering that cement paste is dominated by drastic dissolution and precipitation processes which are dominant within the first few minutes and continue at significantly lower rate during the induction period[80,266,267].

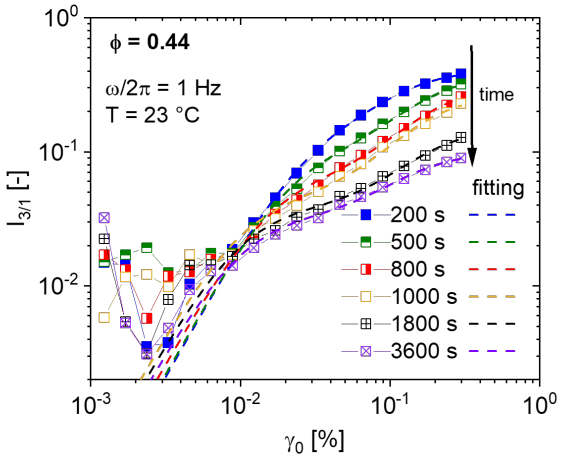

Figure 6.8: Fitting of Equation 6.1.2 to the experimental $I_{3/1}(\gamma_0)$ data of a cement paste ($\phi = 0.44$), without the noise term (N), after 200, 500, 800, 1000, 1800 and 3600 s of hydration time. For fitting parameters, see Equation 6.9.

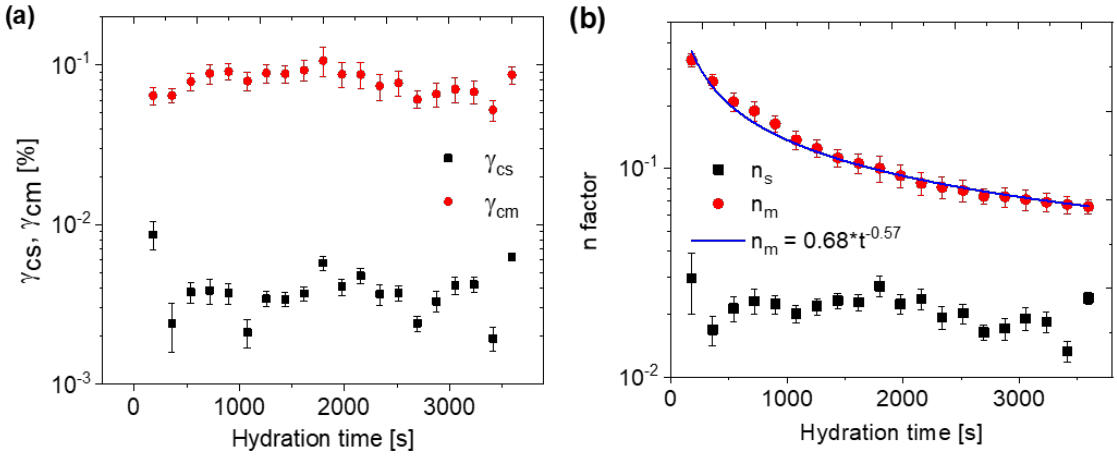

Figure 6.9: **(a)** Critical strains (γ_{cs} and γ_{cm}) as a function of hydration time, **(b)** n factors limitation or maximum of nonlinearity of the corresponding networks ($\phi = 0.44$), deduced from Equation 6.1.2.

This changes the morphology, chemistry and particle interaction permanently, the assumption is that the critical strain is not constant as a function of time. To know the extent of

these early cement hydration effects on the critical strain over time, two sets of experiments were conducted.

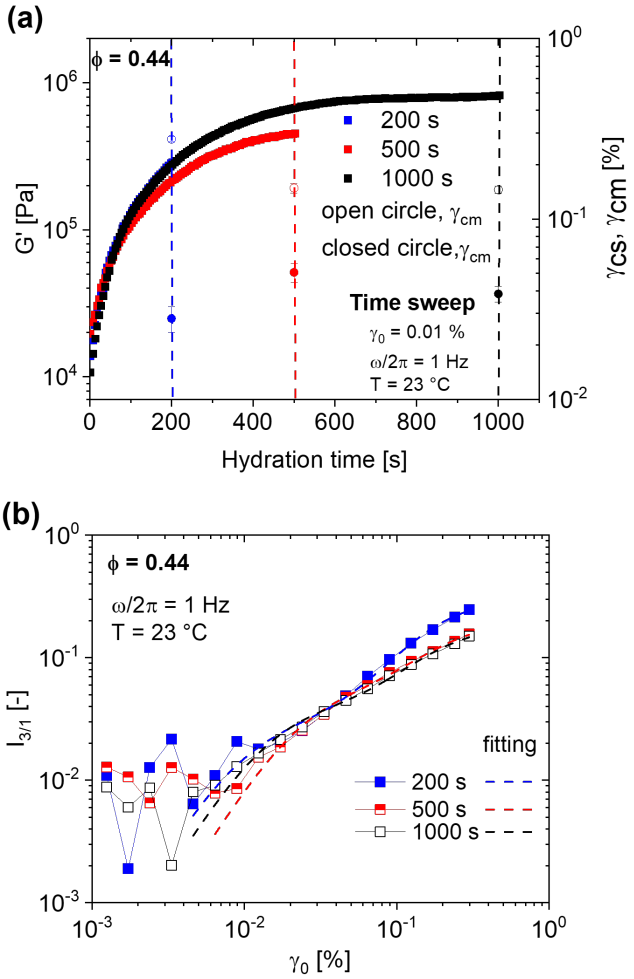

Figure 6.10: **(a)** Build-up of G′(t) after different hydration periods of 200, 500, and 1000 s, low critical strain ($\gamma_0 = 0.01\%$) and the critical strain amplitudes γ_{cs} and γ_{cm} as a function of hydration time. **(b)** Fitting of Equation 6.1.2 on the experimental $I_{3/1}(\gamma_0)$ data of three cement pastes, without the noise term (N) after 200, 500 and 1000 s of hydration.

In the first set of experiments, DSS experiments were continuously done over an hour on the same sample, and the FT-rheological data of the stress signal was fitted with Equation 6.1.2 to determine the critical strain γ_c. The overall fit at t = 200, 500, 800, 1000, 1800 and 3600 s is shown in Figure 6.8. Figure 6.9a shows that both the γ_{cs} and the γ_{cm} remained relatively constant over 3600 s. Figure 6.9b shows shows a decreasing polynomial fit function of that the maximum nonlinearity reflecting the mobile part of the materials, n_m, as function of time. This is expected because hydration reduces the content of water molecules in the mobile phase. However, the rapid decrease could also be attributed to sedimentation. Sedimentation typically occurs when there is a difference in density between the disperse phase particles (cement) and the medium (water). For particles with radii R that are large ($> 1\ \mu m$), the Brownian diffusion is no longer sufficient to overcome the gravitational force[55]. In the case of the cement used in this work, the

particle size distribution is between $0.1 - 100\ \mu m$[76], therefore the effect of sedimentation is overwhelmingly present. If the fitted exponent is the rate of the decay, it can also be used as a rate of loss of water thus subsequently a rate of sedimentation.

In the second set of offline rheological experiments, after mixing (t = 3 minutes), a time sweep was conducted for a set duration (200, 500, 1000 s) at the end of which a DSS test was applied. Thereafter, Equation 6.1.2 was used to determine the critical strain γ_c. Figure 6.10 shows the increase of the storage modulus over time. An increase of 2 decades in storage modulus is observed for all samples, yet the critical strain values, regardless of the oscillatory measurement, remains constant. This phenomenon that can either be explained by the sedimentation effects, or the formation of more hydrates in the liquid phase than assumed, which would possibly not affect the critical strain but have effect on the G'. It is possible that the topology of the structure does not change much, but the strength of the structure due to physical forces, changes more.

6.2 Correlating microscale chemistry to rheology of hydrating cement paste: offline FTIR and online Rheo-IR

Based on the aforementioned theories behind structuration and rigidification, it is valuable to study cement paste at different length scales to obtain more insight into the mechanisms. Infrared spectroscopy measures vibrations in chemical bonds and is therefore sensitive at a nm length scale with a spatial resolution of 1 μm. In this section, offline IR spectroscopy and Rheo-IR will be used to monitor the chemical changes that influence structrual build-up of cement paste.

6.2.1 Experimental protocol: Offline FTIR and online Rheo-IR

Offline FTIR

The Vertex 70 (Bruker, Ettlingen, Germany) FTIR spectrometer installed with a diamond ATR crystal was used to collect FTIR spectra of hydrating cement. A cement paste of water to cement ratio of 0.40 ($\phi = 0.44$) was hand mixed for 2 minutes before being placed on the ATR crystal. Once the sample was placed on to the crystal for measurement, it was covered with a small plastic cup, to prevent evaporation. The measurement was started 3 minutes after water and cement contact. A total of 2.2 scans per second were recorded at averaged over 8 s to produce one spectrum for the both the background and the sample. A resolution of 4 cm^{-1} was used. All samples were measured within the mid-IR ($4000 - 600\ cm^{-1}$) spectral range. The measurements were conducted at room temperature. No temperature control was possible as the Vertex 70 does not have a temperature control unit.

Rheo-IR

The newly developed Rheo-IR[189] was used to monitor the hydrate formation as a function of strain (γ_0). The unique coupling of the Matrix IR spectrometer coupled with the ARES G2 rheometer, allows for in-situ rheological (macroscopic mechanical) and spectroscopic (microscopic chemistry) measurements. A 25 mm plate-plate geometry was used with the bottom plate being sand blasted to avoid slippage. All samples were measured within the mid-IR ($4000 - 600\ cm^{-1}$) spectral range. Attenuated total reflectance (ATR) FTIR is the sampling technique used in the Rheo-IR set-up. Silicon (Si) is used as the ATR crystal. The background and sample spectra were measured by collecting 4.4 scans per second over 14.55 s. The resolution of 4 cm^{-1} was used. A cement paste of water to cement ratio of 0.40 ($\phi = 0.44$) was hand mixed for 2 minutes before being placed on the bottom plate stainless steel geometry. The measurement was started 3 minutes after water and cement contact. The rheological measurement was done using a dynamic time sweep conducted at $\omega_1/2\pi = 1$ Hz and a strain amplitude of $\gamma_0 = 0.05$ %. For the Rheo-IR measurement a Peltier element could be used for temperature control. The experiments were conducted at 23 °C.

Table 6.2: Classification of characteristic wavenumber ranges for IR bands associated with different hydrates and cement paste components from different at room temperature, over $0-24$ hours. The data is acquired from literature[194,195,268–271].

Characteristic component	Wavenumber range $[cm^{-1}]$
O-H stretch mode in portlandite	3650
O-H in H_2O	3000 −3600
H_2O bending vibration	1650
Wagging vibration $CaCO_3$	1481−1414
S-O stretching vibration of ettringite	$[SO_4]^{-2}$ 1150 −1200 own measurement (refer to Appendix 1, page 149)
Asymmetric stretching vibrations of SiO_4 tetrahedral	900−1100

6.2.2 Functional Group Characterization and Structural Build-up of Cement Paste

The length scale of a rheological measurement is between $(0.1-100\ mm)$. The depth of penetration of attenuated total reflectance (ATR) IR is approximately 1 μm (see Figure 4.1 on page 68) within the mid-IR range $(2.5-10\ \mu m)$.

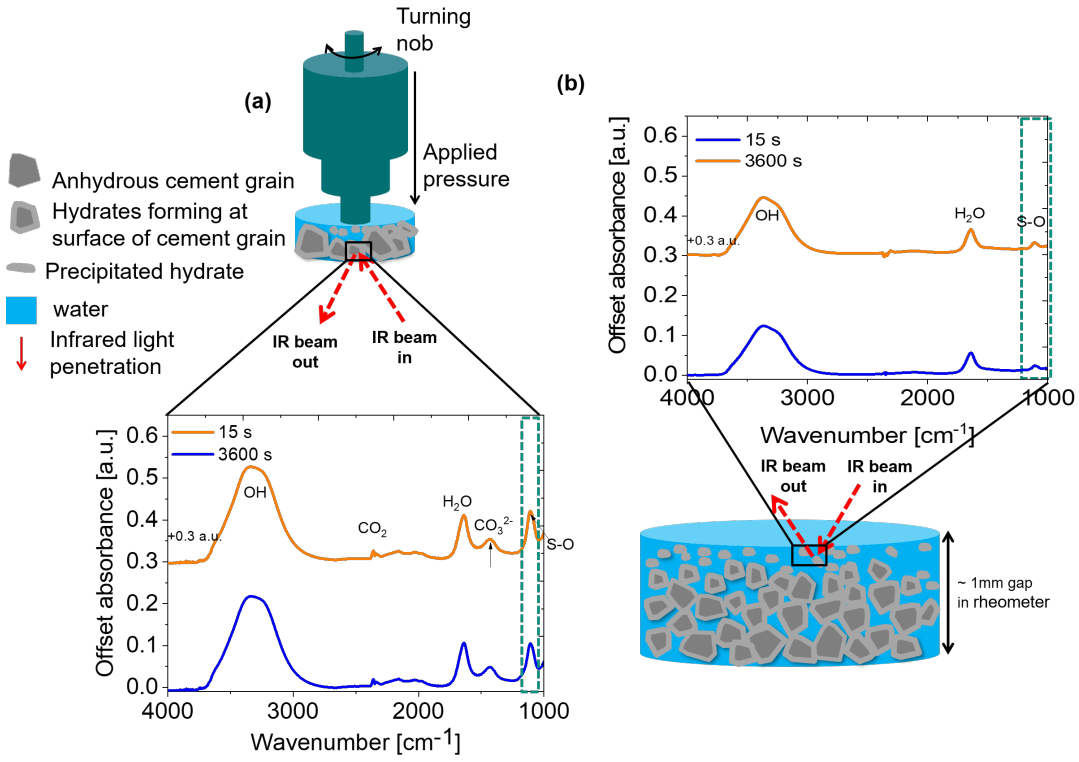

Figure 6.11: Schematic overview of **(a)** the offline FTIR method where a pressure using an adaptable pressure clamp is applied from the top and the measurement takes place at the bottom of the sample. **(b)** of the length scales at which the online Rheo-IR measurement takes place in relation to cement paste. The inserts in **(a)** and **(b)** FTIR spectra $(4000-1000\ cm^{-1})$ after mixing at $t=\ 15\ s$ and $t=\ 3600\ s$.

Therefore, the IR part of Rheo-IR is useful for the study of the aqueous medium rather than

the cement ($10 - 100\ \mu m$). Figure 6.11 shows the different parts of the sample measured by the online and offline FTIR spectrometers. It is clear from Figure 6.11b, that due to sedimentation that cannot be avoided, it is probable that the aqueous phase is being measured instead of the surface of the solid phase. The effect of drying would not be seen directly on the FTIR measurement due to the depth of penetration (DP): the DP approximately 1 micrometer and the measure in not on the drying edges of the sample where drying is more dominant. Therefore, only the rheological measurement would show this effect.

The formation of new species can be observed, the characteristic wavenumbers of which are presented in Table 6.2 and indicated in Figure 6.11 and 6.12 as a waterfall plot.

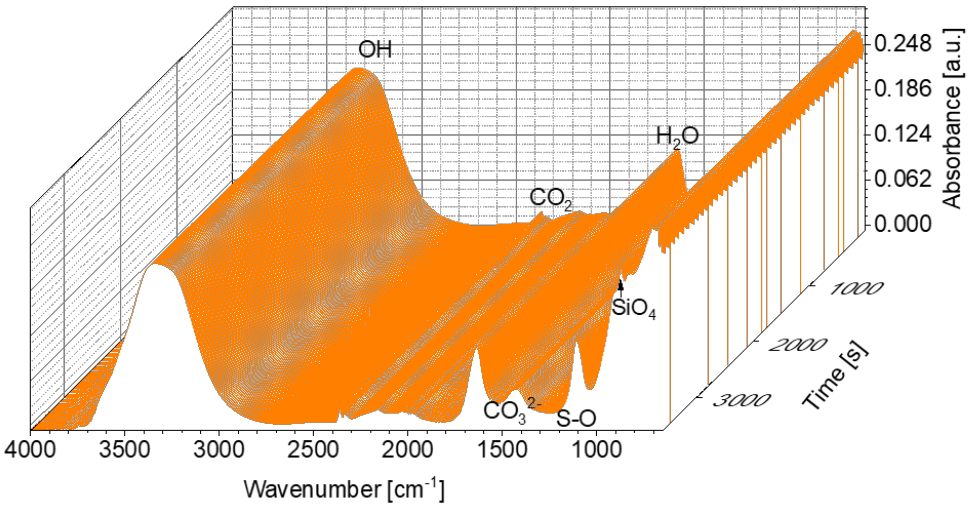

Figure 6.12: Offline FTIR spectra ($4000 - 650\ cm^{-1}$) over 3600 s, no obvious changes in the IR bands H_2O, CO_3^{2-}, SiO_4, $[SO_4]^{2-}$, and OH associated with water, calcium carbonate ($CaCO_3$), *C-S-H*, ettringite (AFt) or portlandite ($Ca(OH)_2$), respectively, are observed.

The bands in the range of $1481 - 1414\ cm^{-1}$ correspond to the asymmetric stretching (υ_3) of CO_3^{2-}. The presence of calcium carbonate is inevitable since the CO_2 is incorporated if the sample is exposed to air. Even though the sample is covered with a plastic cup to prevent evaporation, some air still seeps through. The peak band observed at $1640\ cm^{-1}$ is due to *H-O-H* bending vibration of molecular H_2O and the broad band at $2900 - 3600\ cm^{-1}$ corresponds to the stretching vibrations of *O-H* groups in H_2O and/or any hydroxyls groups associated with a wide range of hydrogen-bond strengths. From Figure 6.11b, it appears that the *S-O* functional group appears as per Table 6.2 does appear when conducting a Rheo-IR measurement.

However, due to the fact that the sample contact in the Rheo-IR set-up is limited by a gap of 1 mm because of the beam alignment, the sample contact cannot be altered by changing the gap or applying pressure through a pressure clamp as it can be with

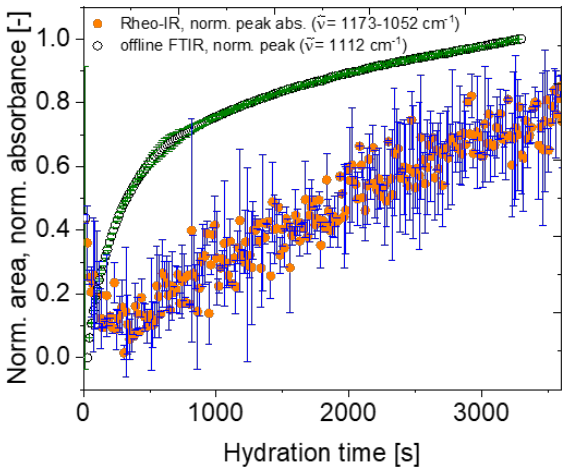

Figure 6.13: The normalized peak area, $\widetilde{\nu} = 1173 - 1052\ cm^{-1}$, averaged for three online Rheo-IR measurements and the normalized peak absorbance $\widetilde{\nu} = 1112\ cm^{-1}$ of three averaged offline FTIR measurements. The standard deviation is shown as blue bars for the Rheo-IR and green bars for the offline FTIR measurements.

the offline (Vertex) spectrometer. Moreover, decreasing the gap in Rheo-IR for cement to ensure sufficient sample contact, not only misaligns the beam but also changes the water to cement ratio by squeezing out the water. Applying pressure on the Vertex also introduces a change in the water to cement ratio. Unfortunately, the pressure clamp is not digitally connected to the spectrometer, which means that the user is unable to know exactly how much pressure is being applied on the sample. This introduces the question; how reproducible are the kinetics as investigated by the change in absorbance bands over time? Figure 6.13 shows the standard deviation of the normalized peak area, $\widetilde{\nu} = 1173 - 1052\ cm^{-1}$, from the three Rheo-IR measurements. The same figure shows the normalized peak absorbance $\widetilde{\nu} = 1112\ cm^{-1}$ of the offline FTIR measurements. The peak area was used for the Rheo-IR in order to reduce the noise. However, it could be more valuable to fit a Gaussian/Lorenzian peak and then calculate the area or the full width at half maximum. Nevertheless, Figure 6.13 shows that the relative concentration and rate of ettringite (*S-O*) formation is measured to be different for offline FTIR and Rheo-IR, for the samples prepared the same way. This could also serve as further evidence that the Rheo-IR method measures the water layer that is most probably in contact with the Si ATR crystal as shown in Figure 6.11. Since the offline FTIR measurements prove to have significantly lower standard deviation, absorbance values were correlated to the rheological data were a strain amplitude of 0.05% (SAOS region) was used to investigate the time dependent behavior of cement paste.

In Figure 6.14a, the presence and continual formation of both ettringite, *C-S-H* and portlandite is seen. The change in the storage modulus as function of time is seen in Figure 6.14b. A rapid increase in the storage modulus is seen within the first 1000 s, after which the growth slows down. The overall change within the first 1 hour of hydration is 10^3 decades but is expected to slow down and remain more constant whilst in the

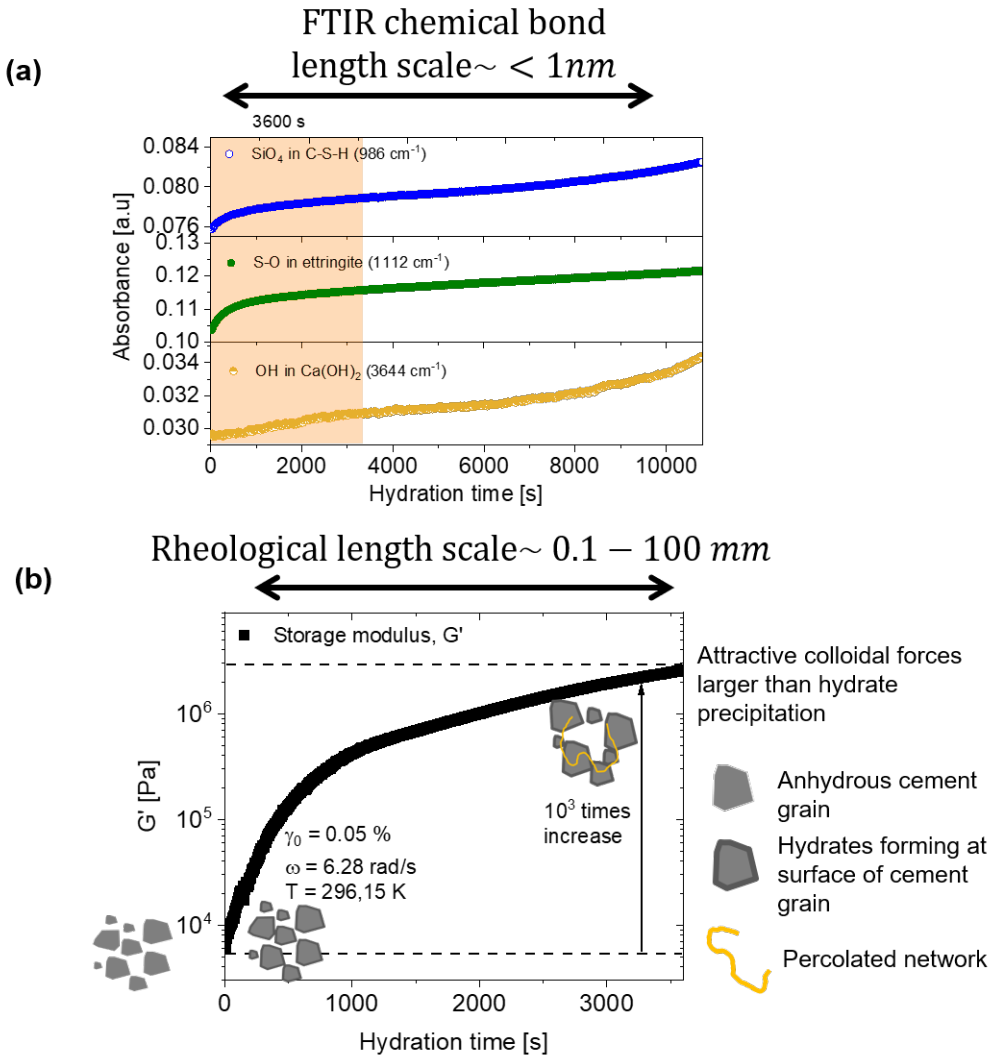

Figure 6.14: **(a)** Offline FTIR: IR spectral bands that are associated with the hydrates *C-S-H*, Aft, and $Ca(OH)_2$ as a function of time. **(b)** storage modulus as a function of time.

induction period [272]. According to Ylmen et al.[194] rapid re-crystallization of sulphates in etrringite is observed during the first 15 s, which appears to be complete after $\sim$ 30 min. Only after $\sim$ 60 min there are absorbance peaks that correspond to polymeric silica ($1011 - 1080\ cm^{-1}$) as well as a corresponding increase in the water bending vibration bands ($1500 - 1700\ cm^{-1}$), which implies the formation of *C-S-H*. Using SEM, the authors observed time dependent morphological changes after $\sim$ 60 min of hydration that correlate and corresponding to the *C-S-H* peak absorbances from DR-FTIR. In all the work from Ylmen et al. referred to in this thesis are based on DR-FTIR (Diffuse Reflectance Fourier Transform Infrared Spectroscopy). The measurements were conducted on 200 g of cement after 15 s contact with water[194]. Most published work on FTIR spectroscopy either no kinetic studies but rather to study the structure-chemistry relationship, independent of time effects[205,210,273] or the time intervals are far larger than the ones of interest in this work (i.e. 2 to 24 hours between each measurement)[195,268].

If we consider that the absorbance (A) is directly proportional to the concentration (c)

via the Bouguer-Lambert-Beer law [177,179], where ε is the extinction coefficient and l is the pathlength through the crystal (Equation 3.1.9, Chapter 3), then the approximate concentration of ettringite based on the molar extinction coefficient of calcium sulfate ($\varepsilon_{1000cm^{-1}} = 0.167\ Lmol^{-1}cm^{-1}$) [274] and $l \sim 0.1\ cm$, is 6 mol/L. Although the concentration may differ depending on where on the sample the measurement takes place, the approximation still gives an indication that the ettringite contribution is rather small. A value in the same range is expected for the *C-S-H* contribution but the concentration is not reflective of the volume fraction of these hydrates. For the this, the crystal structure would have to be determined by X-ray diffraction (XRD) analysis. The portlandite peak appears on the shoulder of the broad OH peak, therefore its presence can only be seen once the concentration is relatively high as seen in Figure 6.14a after 3 hours of hydration.

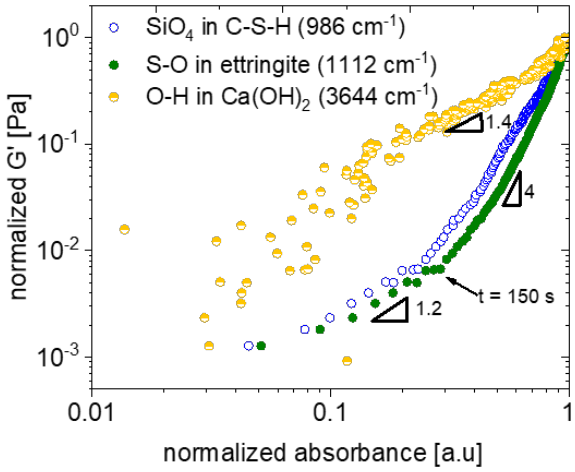

Figure 6.15: Evolution of the storage modulus as a function of the SiO_4 absorbance associated with *C-S-H,* the *S-O* of $[SO_4]^{2-}$ in ettringite and the *O-H* associated with $Ca(OH)_2$.

In addition to directly calculating the concentration from the Bouguer-Lambert-Beer law, an indirect correlation between the modulus and the peak absorbance can be made. In Figure 6.15, the relationship between the modulus and chemistry is shown for the IR bands associated with *C-S-H*, ettringite and portlandite. Although each data set is from two independent measurements of rheology and FTIR, both measurements are done within the linear regime and can therefore be indirectly correlated. Figure 6.15 shows that storage modulus increases at an almost 1:1 ratio with portlandite, which means that the overall rate of structural build up and portlandite formation is the same. A similar behavior is seen for the change in the modulus as a function of the *S-O* associated with ettringite and SiO_4, associated with *C-S-H*, within the first 3 minutes of the experiment. Thereafter, both the ettringite and the *C-S-H* formation contributes to a 4 times increase in the modulus. From this, it is clearer that the ettringite and the *C-S-H* play a more vital role than portlandite in the rigidification process. Similar results can been seen in Appendix 2 for $\phi = 0.39$. The mechanism behind rigidification is not related to effects directly resulting from the growth of cementitious hydration products. It has been shown, by obtaining diffraction

patterns within a time resolution of 1 s through synchrotron XRD[275], that ettringite growth takes place continuously right after water addition, and that the hydration location without the presence of superplasticizers is predominantly around the particle surfaces. This observation had already been reported by Winnefeld et al.[92] before. However, cement paste hardening within 1–2 hours after contact with water is likely due to a combination of the following factors:

- Colloidal percolation and flocculation due to colloidal attractive forces[34,114,276,277]. Van der Waals attractive forces are dominant increasing the storage modulus in the absence of hydration products.
- Formation of small *C-S-H* bridges, described as 'pseudo contact forces' between particles[112].
- Recrystallisation of ettringite during the dormant period. According to Locher et al.[278,279], the ettringite significantly affects the early workability by recrystallizing to larger needles that bridge particles although no significant new amounts of ettringite are being formed. The important aspect of ettringite formation in the early rheological changes has been also reported by Schmidt et al.[280], Stroh et al.[275] and more recently by Jakob et al.[281].

In this work it is observed that both *C-S-H* and ettringite are present in cement paste during very early hydration (1 hour). All the above mentioned possible reactions have an impact on the structural build-up, seen in Figure 6.14b, however, as mentioned the spectroscopic and the rheological measurement are a factor $10^2 - 10^3$ in length scale apart and thus can only be indirectly correlated. Based on the approximate concentration of ettringite and *C-S-H*, it can be concluded that physical interactions such as colloidal interactions leading to a percolated network are mostly likely more dominant than chemical factors in the first few minutes to the first hour of hydration.

In future work, in-situ Rheo-IR[189] and Rheo-NMR[17] measurements will be conducted for a more precise and direct correlation of the mechanical and the molecular properties, even beyond the rheological linear regime.

6.3 Correlating molecular relaxation to rheology of hydrating cement paste

6.3.1 Experimental protocol: Rheo-NMR

The microstructure of the cement during hydration and its rheological response were determined by NMR and rheological experiments in parallel via a combined Rheo-NMR set-up[17] as seen in Figure 6.16 (also see Figure 2.19 in Chapter 2).

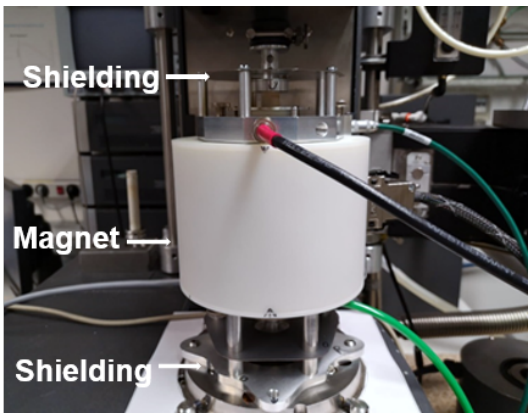

Figure 6.16: Picture of Rheo-NMR set-up used.

The lab-made magnet possesses a static magnetic field of $B_0 = 0.59$ Tesla, i.e. 25 MHz for protons. The pulse length is $\tau_{90} = 2.7\ \mu s$ and $\tau_{180} = 5.1\ \mu$s. The magnet temperature was stabilized as 40 °C during the measurement to supress the drifting of magnetization signals. A Bruker Minispec spectrometer equipped with a 25 mm solenoid resonator coil, was used to acquire all raw data of the NMR part. Rheo-NMR samples were placed in a coaxial small gap cylinder cell, composed of a Polychlorotrifluoroethylene (PCTFE) cup and vane rotor (see Appendix 7, page 156). The outer and inner radii of the shear cell were $R_0 = 6\ mm$ and $R_i = 4\ mm$, respectively, resulting in a fluid gap of 2 mm and a radius ratio ($\tau = R_i/R_0$) of 0.67. It is not recommended to control the sample temperature with gas flow since it will accelerate the evaporation of water in the cement. Therefore, the temperature of the sample is adjusted through a recirculating chiller. In order to acquire the T_2 distribution, longitudinal proton magnetization decays because of the NMR signal relaxation were measured by means of a combined MSE-CPMG pulse sequence[132] (see Figure 2.18 on page 42). The analysis of the raw data from NMR was performed using the Bruker Dynamic Center. The MSE pulse can refocus the initial magnetization signal of the whole sample over the dead time of the NMR probe after a 90° pulse[132]. The initial intensity of magnetization from MSE pulse, I_{mse} (t = 0), can give an information about the total amount of protons remaining in the sample as hydration products or confined water. The CPMG refocus the relatively mobile protons in the sample. The acquired relaxation curve was evaluated regarding the relative intensity of the MSE and CPMG decay curve.

6.3.2 Rheo-NMR: molecular mobility

The in-situ combination of rheological measurements with solid-state NMR as a second characterization method is used to gain unique information about molecular dynamics and structure of time-dependent phenomena (i.e. hydration). This study aims to show the application of low field benchtop ^{1}H NMR relaxometry combined with rheology to investigate the hydration and hydration kinetics of cement pastes. Here the relationship between the storage modulus, G′ and transverse, T_2, ^{1}H-NMR relaxation rates in different water environments that exist during early hydration of cement paste at different water to cement ratios is presented. In Table 6.3, the characteristic T_2 times (in ms) for the different proton environments present in hydrating and hydrated cement paste are found. Additionally, Figure 2.17 on page 40 shows a schematic overview of the characteristic regions of the different T_2 relaxation times. The MSE part of the MSE-CPMG FID was fitted with a Gaussian-exponential as seen in Equation 6.3.1 For this, a bi-exponential (Equation 6.3.2) decay function was used for the intensity and spin-spin relaxation times of the CPMG. The interlayer, gel pore, capillary pore and interhydrate intensities and T_2 times are represented by I, G, C, and H, respectively.

$$I_{MSE}(t) = I_I^{\left(-\frac{t-t_0}{T_{2,I}}\right)^2} - I_G^{-t/T_{2,G}} \tag{6.3.1}$$

$$I_{cpmg}(t) = I_C^{-t/T_{2,C}} + I_H^{-t/T_{2,H}} \tag{6.3.2}$$

Table 6.3: Classification of characteristic T_2 relaxation times of the protons from different sources in the cement paste during hydration at 20−40 °C, data are acquired from literature[126–129].

Proton environment	Description	Characteristic T_2 $[ms]$
C-S-H	solid hydrate phases	<0.01
Interlayer	spaces between the backbone of *C-S-H* sheets	0.02-0.12
Gel pores	pores on the agglomerates (stacks or globules) of the *C-S-H* sheets, as intrinsic part of the *C-S-H* gel	0.35-0.5
Interhydrate pores	pores between the *C-S-H* needles, larger than the above	0.9-2
Capillary pores	pores between the *C-S-H* needles, larger pores remained after consumption of water	12-100

The MSE relative signal intensity as seen in Figure 6.17 is indicative of the total amount of protons within the sample. It decreases by approximately by 25 % for the sample measured with $\gamma_0 = 0.3\%$. This indicates that there is a loss in protons due to evaporation. The NMR signal is processed and interpreted such that there are 2 populations of water, whereas there are usually 5 in a fully hydrated sample[282]. The MSE part of the MSE-CPMG FID was fitted with a Gaussian-exponential (Equation 6.3.1). Usually for a sample measured after initial setting, the Gaussian part spin-spin relaxation time in the order of

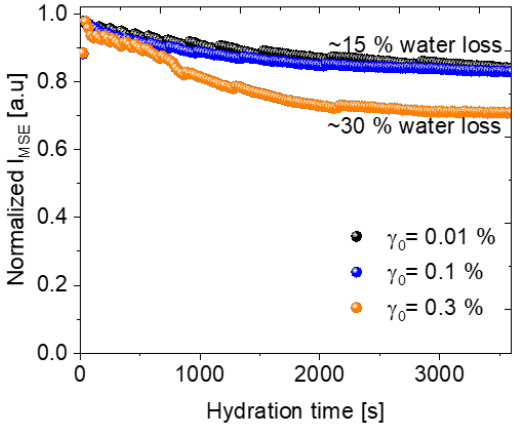

Figure 6.17: Evolution of MSE intensity over time as function of different strain amplitudes of cement pastes (w/c = 0.40) under different strain amplitudes ($\gamma_0 = 0.01, 0.1$ and 0.3%).

0.01 ms[128]. However, within the time frame of the measurement the as the values are scattered indicating that *C-S-H* hydrate phases have not yet formed, or have not formed in a detectable amount.

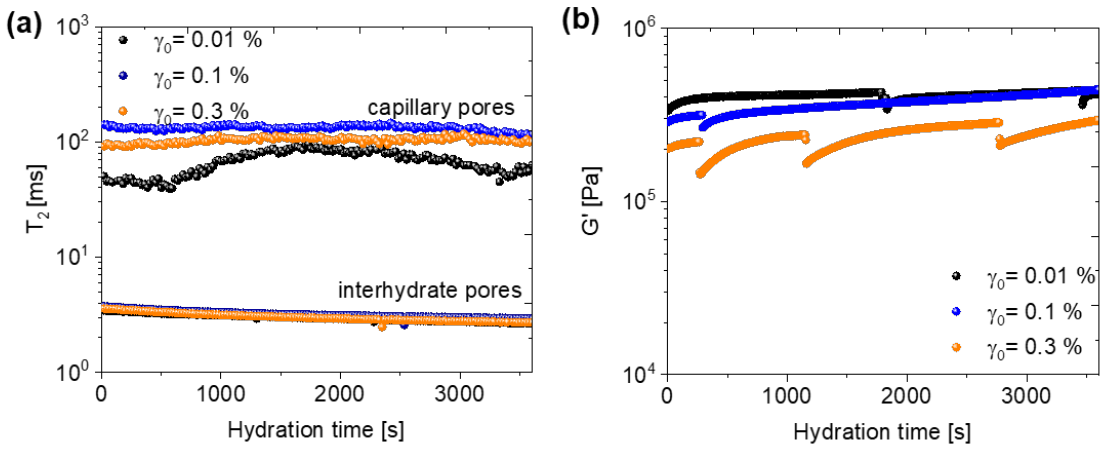

Figure 6.18: **(a)** Evolution of the T_2, the longest T_2, of the protons in capillary pores and the inter-hydrate pores, shortest recorded T_2, as a function of hydration time. **(b)** An overlay of the G′ development at $\gamma_0 = 0.01$ %, 0.1% and 0.3% (b) G' development at 40 °C (temperature of the magnet).

The rapid drops in modulus seen in Figure 6.18b, page 118 is attributed to either the slippage between the sample and the geometry, or to the sudden break down of agglomerated networks in the sample. In addition, due to evaporation, observed in the next section of NMR results, the drop in G′(t) can also be attributed to shrinkage. This phenomenon is not observed in Figure 6.14b since a stricter temperature control can be managed for offline rheological experiments than online Rheo-NMR experiments.

Since the T_2 relaxation times associated with the *C-S-H* layers is not yet measurable after 3600 s, it is useful to use the intensities as a measure of the relative degree of hydration,

D_h. This is consitant with what is known from literature[78] which is that less than 1 % of the hydrates have formed at the end of induction period ($0 - 2\ hrs$ from water-cement contact). For every point in the experimental time (t_{exp}), CPMG intensities, $I_{CPMG}\ (t_{exp})$, are back extrapolated to $t_{NMR} = 0\ ms$ and compared with the total intensity $I_{total}(t_{exp})$ at $t_{NMR} = 0\ ms$ of all protons as captured by the MSE:

$$D_{h,direct}\ (t_{exp}) = 1 - \frac{c \times I_{cpmg}(t_{exp})}{I_{total}(t_{exp})} \tag{6.3.3}$$

This direct method (see Equation 6.3.3) has been used in crystallization of polymers, however, errors in the detection of I_{total} limit the reliability of this method[283]. The indirect method, as seen in Equation 6.3.4, is a normalization of the CMPG intensity. Figure 6.19b is the inverse of Figure 6.17. This method is not useful in determining the degree of hydration since intensity of the CPMG FID is not linked to hydration.

$$D_{h,indirect}\ (t_{exp}) = 1 - \frac{I_{cpmg}(t_{exp})}{I_{CPMG}(t_{exp} = 0)} \tag{6.3.4}$$

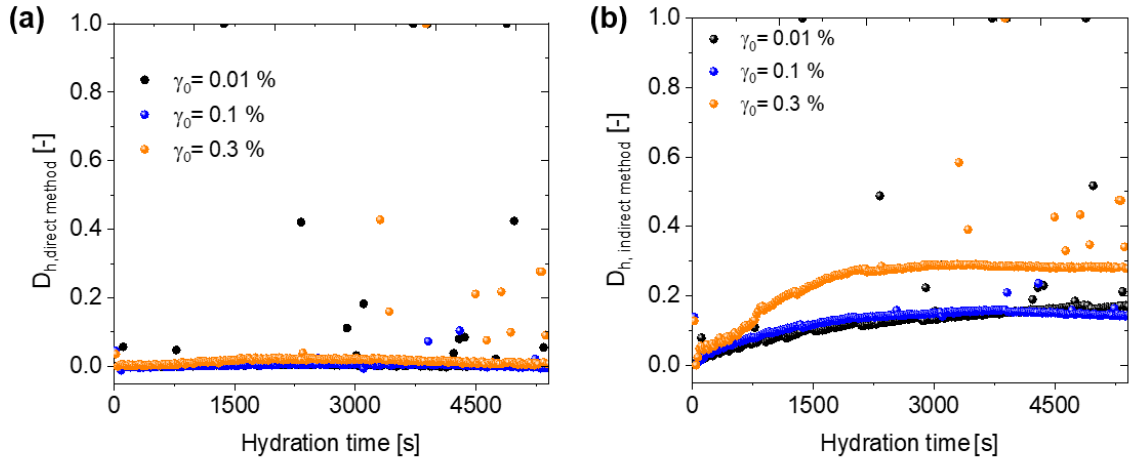

Figure 6.19: Influence of the shear strain amplitude on the solidification process of cement paste using the **(a)** direct method (see Equation 6.3.4) and the **(b)** indirect method (see Equation 6.3.3). The solidification factor, Dh, is calculated from NMR data with oscillatory shear in parallel at γ_0 = 0.01/0.1/0.3% (final Dh = 14/17/28%).

Figure 6.19 is unique to Rheo-NMR as the degree of hydration is shown as function of strain amplitude. At a strain amplitude of 0.01% and 0.1% the relative degree of hydration goes from 0 to approximately 0.005%. At a higher strain amplitude of 0.3% (NVE) the relative degree of hydration increases to 0.02% after 3600 s. Within this time frame of the Rheo-NMR measurements, structure has been built but an insignificant amount of hydration (chemistry) has occurred.

Rheo-Dielectrics

6.3.3 Experimental protocol: Rheo-Dielectrics

A sensitive Rheo-Dielectrics set-up was designed and built by combining an ARES G2 rheometer (TA instruments) and a dielectric ALPHA-Analyzer (Novocontrol Technologies)[9], as seen schematically in Figure 2.20 in Chapter 2, page 47. By using the ALPHA-Analyzer, 12 orders of magnitude of frequency range (3×10^{-5} to 1×10^{7} Hz), 15 orders of capacity range (10^{-15} to 1 F) as well as 16 orders of impedance range (10^{-2} to 10^{14} [-]) are able to be measured. PCTFE was used as an insulating material for the bottom strainless steel measuring plate. In this work, a sample plate of 25 mm in diameter was connected to the electronic wire with a bolt, and the other end of the wire is connected with a BNC connector. The design of the plate was adapted to fit onto a Peltier element bottom plate and covered with a solvent trap to prevent evaporation of any solvent, as seen in Figure 6.20.

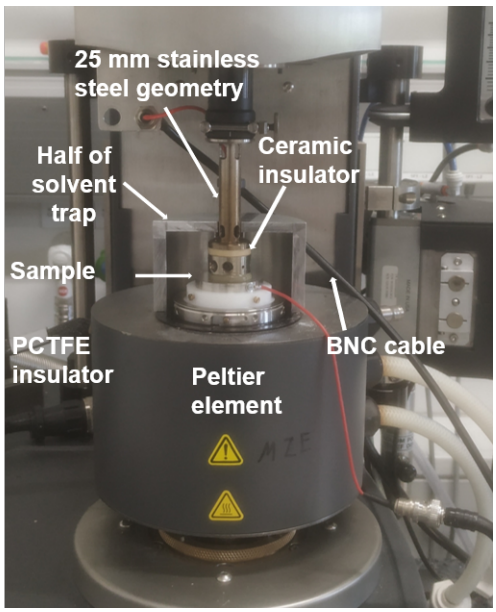

Figure 6.20: Picture of Rheo-Dielectrics set-up used, which is attached to a Peltier element for temperature control and a solvent trap to reduce evaporation.

The set-up was used to measure the complex dielectric function:

$$\varepsilon^*(\omega) = \varepsilon'(\omega) - i\varepsilon''(\omega), \tag{6.3.5}$$

where $\omega = 2\pi v$, in the frequency (v) range from $v = 10^{-1}$ Hz to $v = 10^{6}$ Hz. The samples were placed between parallel gold-plated electrodes with a diameter of 25 mm and the thickness was about 1 mm. Frequency scans recording $\varepsilon^*(\omega)$ were performed throughout the aforementioned range at 23°C. Sample temperature was controlled by a Peltier element with stability better than ± 0.1 K.

6.3.4 Dc-conductivity and Permittivity During Early Hydration

The interaction between an external electric field and the permanent molecular dipoles within the material of interest is measured in a dielectric experiment[284]. Complex permittivity measurements may be used to investigate the dynamics of dipolar species as well as charge transport. Water molecules and hydroxyl groups are expected to contribute to the dielectric signal in the case of Portland cement. Between frequencies of $10^{-1} - 10^{8}$ Hz, at least 3 different relaxation processes are expected to be observed as function of time. The dc-conductivity, on the other hand is determined mainly by the amount of interconnected capillary pores in the cement matrix. The main conducting phase in cement paste is the capillary water. The dc-conductivity is proportional to the diffusion of water molecules in the cement structure. The reaction products that block the pores cause a reduction of the conductivity (Figure 6.21a). The decrease in conductivity is therefore not linearly related with the volume of capillary water. In other words, the decrease of connectivity of the pores results in a sharp decrease in the conductivity. The connectivity can thus be determined from the dielectric measurements. All samples presented two broad time-dependent dielectric processes (see arrows in Figure 6.21b).

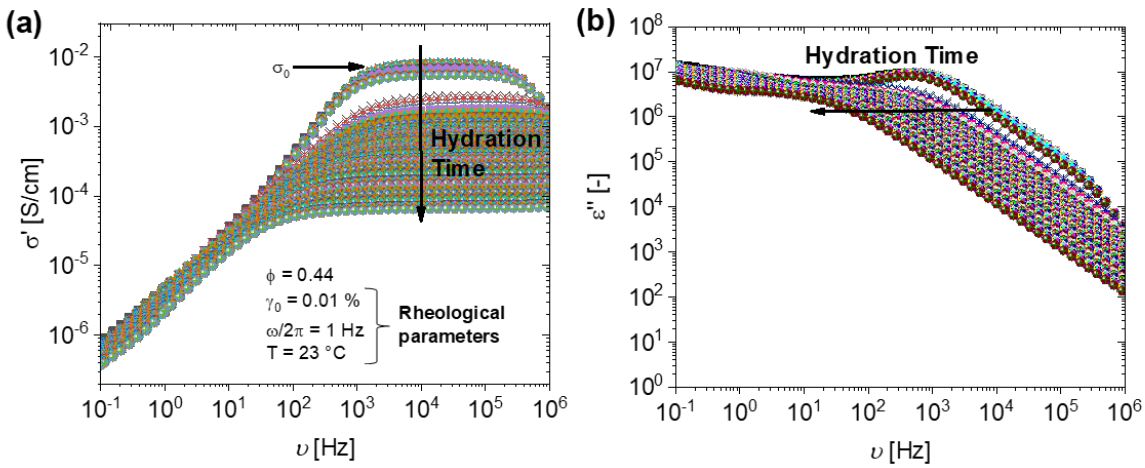

Figure 6.21: **(a)** Real part of complex conductivity function $\sigma^*(\omega, T) = i\varepsilon_0\omega\varepsilon^*(\omega, T)$, implying that $\sigma''(\omega, T) = \varepsilon\omega\epsilon'$ and $\sigma'(\omega, T) = \varepsilon_0\omega\varepsilon''$, ε_0 being the vacuum, $\sigma_0(T)$ is dc- conductivity, and **(b)** imaginary part (ε'') of the complex permittivity function) after 5.5 hours as a function of frequency, at 23 °C. The strain amplitde as applied by the rheometer was 0.01% for this sample and the $\phi = 0.44$.

The different dielectric processes shift to lower frequencies with increasing time. Standard fit functions can be used to characterize the dielectric response. The Havilliak-Negami (HN) function (Equation 6.3.6) is able to describe the data in the wide frequency range and thus requires several parameters to describe isolatd relaxtion regions;

$$\varepsilon^*(\omega) = \varepsilon_\infty + \frac{\Delta\varepsilon}{(1 + (i\omega\tau_{HN})^z)^k}, \tag{6.3.6}$$

here, τ_{HN} is the postion of the maximal loss, described $1/\omega_{HN}$. The frequency of maximal

loss v_p is related to a characteristic relaxation rate $\omega_{HN} = 2\pi v_p$[22]. The imaginary part is fitted using:

$$r(\omega)sin[k\psi(\omega)] \tag{6.3.7}$$

where,

$$r(\omega) = [1 + 2(\omega\tau_{HN})^z cos(\frac{z\pi}{2}) + (\omega\tau_{HN})^{2z}]^{-k/2} \tag{6.3.8}$$

and

$$\psi(\omega) = \ acrtan\ [\frac{sin(\frac{z\pi}{2})}{(\omega\tau_{HN})^{-z} + cos(\frac{z\pi}{2})}]. \tag{6.3.9}$$

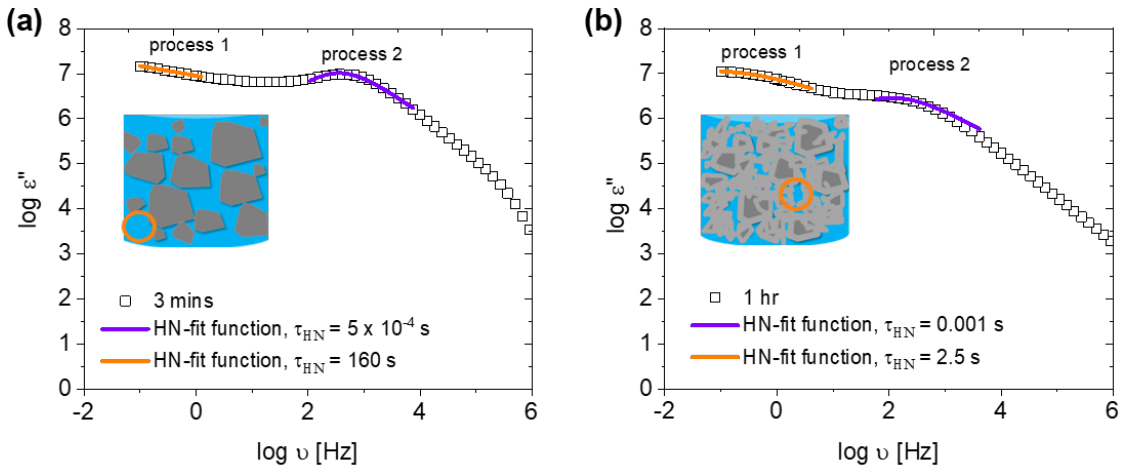

Figure 6.22: Imaginary part: ε'' of the complex permittivity function after **(a)** 3 minutes, and **(b)** after 1 hour of hydration. The solid line is the best fit according to Equation 6.3.6. The dotted lines show the contribution of the low frequency and high frequency relaxtion to the total spectrum. Raw data taken from Figure 6.21b.

Figure 6.22 shows that the dielectric relaxation mechanism in the low-frequency (1 Hz - process 1) increases over time, with the τ_{HN} decreasing from 10^2 to 10^1 s after one hour of hydration. Conversely, the higher frequency (10^3 Hz - process 2) relaxation mechanism decreases with hydration time with the τ_{HN} increasing from 10^{-4} to 10^{-3} s. The increase in the relaxation frequency for process 1 could be indicative of 'free' unbound water that incorporates into the gel pore structure and pictorially indicated in Figure 6.22a and b. It is not clear what process 2 is representative of, since a decrease in the frequency implies an increase in the pore size or larger water clusters that are less bound to hydrate or unreacted cement surfaces.

Interestingly, an increase in the modulus by four decades is seen without a decrease in the conductivity, see Figure 6.23a. This could mean that although structure is being

built, water is still able to move freely within the pores through capillary channels. The conductivity only begins to decrease significantly after 3 hours (see Figure 6.23b) which is the general setting time for cement paste without admixtures (i.e. superplasticizers, or accelerators).

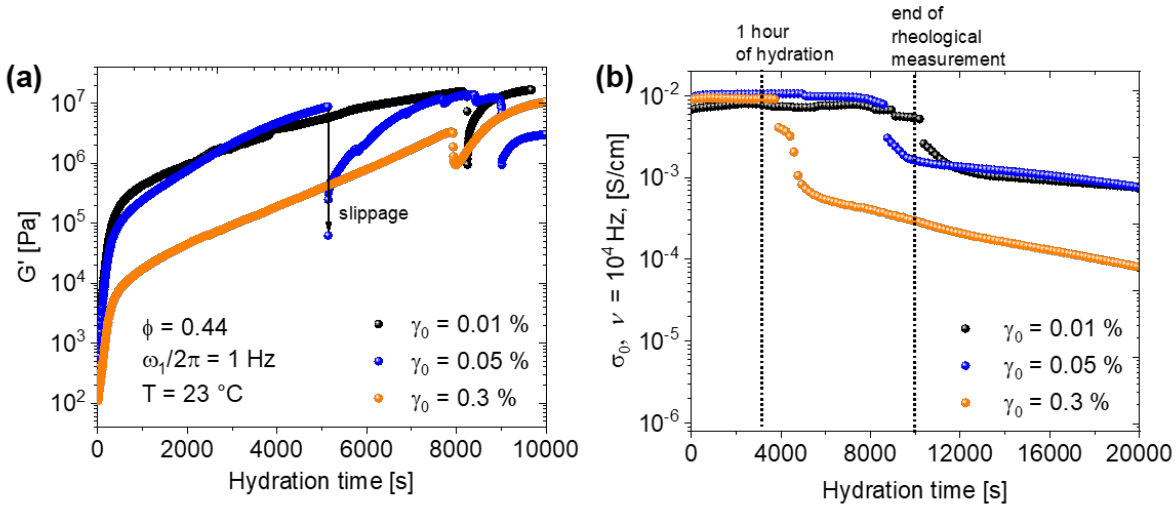

Figure 6.23: **(a)** dc-conductiviy as a function of time, for cement paste ($\phi = 0.44$) at $\gamma_0 = 0.01, 0.05$ and 0.3% **(b)** Storage modulus, G′ development within one hour of water and cement contact.

Furthermore, a similar behvavior seen in Figure 6.19a as in Figure 6.23b. Both the degree of hydration ($D_{h,directmethod}$) and dc-conductivity show no distinct evolution as function of applied strain within the first hour of hydration. Even though the Rheo-NMR experiments were conducted at an elevated temperature of 40 °C (unavoidable due to magnet temperature and gas flow remained turned off, see experimental protocol) compared to the 23 °C in Rheo-Dielectrics, the results were still comparable. This leads to the hypothesis that, the temperature with a certain range, does not affect effect the hydration behavior as observed by the T_2 times and dc-conductivity during very early hydration. However, this does not predict how the behavior will be affected at a later stage (i.e. after setting). For this, a temperature dependence study using both Rheo-NMR and Rheo-Dielectrics would be more appropriate and will form part of future studies.

Chapter 7

Conclusion and Outlook

Cement paste is a heterogeneous material, therefore characterizing it is complex. The combination of rheological measurements with a second characterization method (i.e. NMR, dielectric spectroscopy and FTIR) is addressed in order to gain unique information about molecular dynamics, and the structure of time and shear dependent phenomena. The importance of determining a linear viscoelastic region and the effect of a small change in strain can affect the structural build up, was demonstrated. In order to determine where the LVE region ends and the NVE starts, higher harmonics were investigated. The effect of the strain amplitude is of significance when it is above or close to the critical strain. The critical strain can be determined via FT-rheology using a dynamic strain sweep test. There are two critical strains that can be associated with either the mobile phase (colloid with mobile water molecules) or the growing solid phase (cement and/or hydrates) in the cement paste. Remaining at or below the critical strain allows for a non-destructive monitoring of the transient behavior as a function of time. The effect of hydration time has minimal relevance on the critical strains. However, the higher harmonics and the stress response from the applied sinusoidal excitation show an obvious deviation throughout the hydration time. The evolution of the microstructure seen through the mechanical evolution is influenced by the formation of hydrates, as seen spectroscopically through FTIR. Hydration is a relatively slow process therefore the strain sweep time frame is not relevant, γ_{cs} (10^{-2}) and γ_{cm} (10^{-1}) remain within the same range. Additionally, increasing the initial solid fraction, ϕ, does not have a significant effect on these critical strains. This is unexpected as there are particle volume effects, but it is known that segregation is dominant in the mixtures with lower solid fractions.

By using rheology combined with FTIR, NMR and dielectric spectroscopy, the influence of the microstructure on the macrostructure during early hydration was determined. It is observed that the structural build-up is dominated my physical effects rather than the early formation of hydrate. Although, the hydration products (i.e ettringite) do form within the first hour of hydration, the relative amount is not the main contributing factor to structural build up. Similarly, the T_2 relaxation times from NMR that can be associated with the capillary pores (100 ms) and interhydrate pores (5 ms), remain constant during the first hour, regardless of the strain amplitude applied. The dc-conductivity, also remained

unchanged during the first hour of hydration but later drastically decreased by a factor between $100 - 1000$ during to setting. The dc-conductivity of cement paste is sensitive to the applied strain amplitude. When γ_0 is within the linear regime, the decrease in the conductivity occurs later than when $\gamma_0 (< 0.3\%)$ is in the nonlinear $\gamma_c (\geq 0.3\%)$. By investigating the relaxation peaks shown by the permittivity, two relaxation processes, similar to those in NMR could be deduced. The increase in the relaxation frequency at lower frequencies was associated with the incorporation of unbound water into the gel pore structure. To conclude, physical interactions such as colloidal interactions are more dominant than chemical factors in the first few minutes to the first hour of cement paste hydration.

The newly developed Rheo-IR technique presents opportunities for a deeper understanding of the kinetics of early cement hydration, even in the presence of adsorbing admixtures (i.e. superplasticizers). Under optimized conditions, all mentioned combined Rheo-techniques are both quantitative and qualitative. This means that direct correlated insights to mechanism of hydration and structural build-up can be gained for cementitious materials. The use of these combined techniques on cementitious materials will lead to a better understanding of the mechanisms behind different rheological behaviors influenced by e.g. polymeric materials used as admixtures. Thus, a complete knowledge of basic kinetic mechanisms of hydration will aid towards the understanding of novel cement types and the influence of polymers on the rheological and chemical behavior. These novel cement types (e.g. LC^3, Limestone Calcined Clay Cement) are currently and will continue to be developed in order to reduce the carbon emissions that contribute to global warming.

However, the limitation of the current Rheo-IR setup is that the resolution is within the 1 μm range, whereas the species of interest are in the nm range. A large deviation in the results was seen which is attributed to the change in the axial force therefore sample contact in the rheometer as a function of hydration time. This can be avoided in an offline FTIR measurement by applying a constant force using a pressure clamp. Although the combined techniques used in this work are limited by design to particles that are contained in cement paste, and does not extend into mortars and concrete, the information gained at the micro level can aid in understanding some of the processes that take place at a macro level. Additionally, if we consider that cement paste is a time dependent material, there is a time limit after which experiments on the material are no longer physically possible (i.e. upper torque limit of rheometer, 0.2 Nm).

In general, the combination of rheological testing and spectroscopy on hydrating cement pastes is a promising tool to investigate the relation between macroscopic structure formation and the underlying physico-chemical processes leading to changes in the water mobility on a broad timescale, dc-conductivity and hydrate formation. Future work will focus on further increase of the sensitivity (signal-to-noise ratio) of the IR spectroscopy measurement in the Rheo-IR set-up with respect to measuring molecular changes during chemical reactions (i.e. hydration). By incorporating polarization of the IR beam into the

set-up, the orientation of hydrates formed during cement hydration could be determined, which will further aid in understanding the effects of different forms of hydrate phases on the structural build-up. In addition to increasing the sensitivity, an automated data evaluation method will be implemented for the Rheo-IR measurements. Furthermore, experimental protocols that include more dynamic rheological parameters such as shear rate and/or temperature dependent measurements will be explored. Since the ARES G2 is a strain-controlled rheometer, development of the intensity of the higher harmonics as a function of chemistry is possible and will allow for the quantification and prediction of material orientation. Even through this thesis presents extensive investigations of cement paste, the methods used are versatile and applicable to a larger variety of materials such as hydrogels, epoxy resins and potentially emulsions.

References

[1] H. A. Barnes, J. F. Hutton, K. Walters, *An Introduction to Rheology*, 3rd ed., Elsevier Science Publishers B.V, **1993**.

[2] R. Larson, *The structure and rheology of complex fluids*, Oxford University Press, **1999**.

[3] C. W. Macosko, *Rheology Principles , Measurements , and Applications*, Wiley-VCH, New York, **1994**.

[4] M. Boulet-Audet, F. Vollrath, C. Holland, *Physical Chemistry Chemical Physics* **2011**, *13*, 3979–3984.

[5] T. O. M. Scherzer, *Journal of Applied Polymer Science* **1998**, *70*, 247–259.

[6] M. Kempf, B. Dippel, O. Arnolds in Annual Transactions - Nordic Rheology Society, *Vol. 25*, **2017**.

[7] A. P. Kotula, M. W. Meyer, F. De Vito, J. Plog, A. R. Hight Walker, K. B. Migler, *Review of Scientific Instruments* **2016**, *87*, DOI 10.1063/1.4963746.

[8] J. P. Plog, M. Meyer, *Thermo Fisher Scientific* **2018**.

[9] K. Hyun, S. Höfl, S. Kahle, M. Wilhelm, *Journal of Non-Newtonian Fluid Mechanics* **2009**, *160*, 93–103.

[10] Y. Peng, L.-S. Turng, H. Li, Z. Cui, *Journal of Rheology* **2011**, *55*, 301–311.

[11] H. Watanabe, Y. Matsumiya, K. Horio, Y. Masubuchi, T. Uneyama in *Non-equilibrium Soft Matter Physics*, **2012**, pp. 37–87.

[12] H. Watanabe, Y. Matsumiya, T. Inoue, *Journal of Physics: Condensed Matter* **2003**, *15*, S909–S921.

[13] T. Meins, K. Hyun, N. Dingenouts, M. Fotouhi Ardakani, B. Struth, M. Wilhelm, *Macromolecules* **2012**, *45*, 455–472.

[14] B. Struth, K. Hyun, E. Kats, T. Meins, M. Walther, M. Wilhelm, G. Grübel, *Langmuir* **2011**, *27*, 2880–2887.

[15] R. N. Al-kaby, J. S. Jayaratne, T. I. Brox, S. L. Codd, J. D. Seymour, J. R. Brown, *Journal of Rheology* **2018**, *62*, 1125–1134.

[16] P. T. Callaghan, *eMagRes* **2012**, *1*, 155–168.

[17] K.-F. Ratzsch, C. Friedrich, M. Wilhelm, *Journal of Rheology* **2017**, *61*, 905–917.

[18] C. Schmidt in *Modern Magnetic Resonance*, (Ed.: G. A. Webb), Springer Netherlands, Dordrecht, **2006**, pp. 1515–1521.

[19] J. Calero, J. P. Murtha, S. P. Wu, C. Pope, S. L. Chuang, *Journal of Lightwave Technology* **1994**, *12*, 1081–1091.

[20] C. O. Klein, P. Venema, L. Sagis, D. van Dusschoten, M. Wilhelm, H. W. Spiess, E. van der Linden, S. S. Rogers, A. M. Donald, *Applied Rheology* **2008**, *17*, 45210–45217.

[21] M. Shibayama, H. Kawada, T. Kume, T. Matsunaga, H. Iwai, T. Sano, N. Osaka, S. Miyazaki, S. Okabe, H. Endo, *Journal of Chemical Physics* **2007**, *127*, DOI 10.1063/1.2790900.

[22] F. Kremer, A. Schönhals, *Broadband dielectric spectroscopy*, Springer Berlin Heidelberg, **2003**.

[23] W. H. Stockmayer, J. J. Burke, *Macromolecules* **1969**, *2*, 647–650.

[24] H. Watanabe, *Macromolecular Rapid Communications* **2001**, *22*, 127–175.

[25] S. Kiewiet, V. Janssens, H. E. Miltner, G. Van Assche, P. Van Puyvelde, B. Van Mele, *Review of Scientific Instruments* **2008**, *79*, DOI 10.1063/1.2838585.

[26] S. Jovanović, S. Samaržija-Jovanović, G. Marković, V. Jovanović, T. Adamović, M. Marinović-Cincović, *Composites Part B: Engineering* **2016**, *98*, 126–133.

[27] L. Li, Q. Wu, S. Li, P. Wu, *Appl. Spectrosc.* **2008**, *62*, 1129–1136.

[28] K. L. Scrivener, V. M. John, E. M. Gartner, *Cement and Concrete Research* **2018**, *114*, 2–26.

[29] W. Schmidt, M. Commeh, K. Olonade, G. L. Schiewer, D. Dodoo-Arhin, R. Dauda, S. Fataei, A. T. Tawiah, F. Mohamed, M. Thiedeitz, N. W. Radebe, A. Rogge, *Developments in the Built Environment* **2021**, *6*, 100047.

[30] R. Maddalena, J. J. Roberts, A. Hamilton, *Journal of Cleaner Production* **2018**, *186*, 933–942.

[31] S. Sprung in *Cement*, Wiley-VCH, Weinheim, **2012**, pp. 399–460.

[32] L. Barcelo, J. Kline, G. Walenta, E. Gartner, *Materials and Structures/Materiaux et Constructions* **2014**, *47*, 1055–1065.

[33] T. Conte, M. Chaouche, *Cement and Concrete Research* **2016**, *89*, 332–344.

[34] A. M. Mostafa, A. Yahia, *Cement and Concrete Research* **2017**, *97*, 11–27.

[35] Q. Yuan, D. Zhou, K. H. Khayat, D. Feys, C. Shi, *Cement and Concrete Research* **2017**, *99*, 183–189.

[36] D. Feys, R. Verhoeven, G. De Schutter, *Applied Rheology* **2007**, *17*, 1–10.

[37] J. W. Bullard, H. M. Jennings, R. A. Livingston, A. Nonat, G. W. Scherer, J. S. Schweitzer, K. L. Scrivener, J. J. Thomas, *Cement and Concrete Research* **2011**, *41*, 1208–1223.

[38] N. W. Radebe, K. F. Ratzsch, C. O. Klein, M. Wilhelm in *RILEM Bookseries*, *Vol. 23*, **2020**, pp. 256–265.

[39] D. M. Kirby, J. J. Biernacki, *Cement and Concrete Research* **2012**, *42*, 1147–1156.

[40] J. Cheung, A. Jeknavorian, L. Roberts, D. Silva, *Cement and Concrete Research* **2011**, *41*, 1289–1309.

[41] M. Kalra, G. Mehmood, *IOP Conference Series: Materials Science and Engineering* **2018**, *431*, DOI 10.1088/1757-899X/431/8/082001.

[42] D. Tarangini, B. Radha Kiranmaye, P. Sravana, Naveen, *International Journal of Civil Engineering and Technology* **2019**, *10*, 914–921.

[43] J. E. Wallevik, *Cement and Concrete Research* **2009**, *39*, 14–29.

[44] M. Fladvad, A. Ulvik, *Bulletin of Engineering Geology and the Environment* **2019**, DOI 10.1007/s10064-019-01683-z.

[45] J. Dong, Y. Ozaki, K. Nakashima, *Journal of Polymer Science Part B: Polymer Physics* **1997**, *35*, 507–515.

[46] J. Dong, Y. Ozaki, K. Nakashima, *Macromolecules* **1997**, *30*, 1111–1117.

[47] M. Todica, R. Stefan, C. V. Pop, L. Olar, *Acta Physica Polonica A* **2015**, *128*, 128–135.

[48] M. Reiner, *Physics Today* **1964**, *17*, 62.

[49] G. Scott Blair, *Jonrnal of Texture Studies* **1969**, *1*, 14–18.

[50] Samuel, Nathan, Gad in *Old Testament Bible, Judges 5*, pp. 2–31.

[51] J. M. Dealy, R. G. Larson, *Structure and Rheology of Molten Polymers*, First Edit, Carl Hanser Verlag GmbH & Co. KG, **2006**, pp. I–XIV.

[52] J. M. Dealy, J. Wang, *Melt Rheology and its Application in the Plastics Industry*, *Vol. 16*, **2013**.

[53] J. Mewis, N. Wagner, *Colloidal Suspension Rheology*, Cambridge University Press, New York, **2012**.

[54] M. T. Shaw, *Introduction to Polymer Rheology*, John Wiley & Sons, Ltd, **2012**.

[55] T. F. Tadros, *Rheology of Dispersions: Principles and Applications*, Wiley-VCH, **2010**.

[56] R. Hooke, *De Potentia Restitutiva, or of Spring. Explaining the Power of Springing Bodies*, London, **1678**.

[57] A. Y. Malkin, A. Isayev, *Rheology - Concept, Methods, and Applications*, Toronto, **2017**, p. 500.

[58] G. I. Taylor, *Philosophical Transactions of the Royal Society of London* **1923**, *223*, 289–343.

[59] K. Hyun, M. Wilhelm, *Macromolecules* **2009**, *42*, 411–422.

[60] R. H. Ewoldt, A. E. Hosoi, G. H. McKinley, *Journal of Rheology* **2008**, *52*, 1427–1458.

[61] K. Hyun, M. Wilhelm, C. O. Klein, K. S. Cho, J. G. Nam, K. H. Ahn, S. J. Lee, R. H. Ewoldt, G. H. McKinley, *Progress in Polymer Science* **2011**, *36*, 1697–1753.

[62] M. Wilhelm, *Rheologica Acta* **1998**, *37*, 399–405.

[63] M. Wilhelm, *Macromolecular Materials and Engineering* **2002**, 83–105.

[64] S. Nie, J. Lacayo-Pineda, N. Willenbacher, M. Wilhelm, *Polymer* **2019**, *181*, 121804.

[65] M. A. Cziep, M. Abbasi, M. Heck, L. Arens, M. Wilhelm, *Macromolecules* **2016**, *49*, 3566–3579.

[66] D. Ahirwal, H. Palza, G. Schlatter, M. Wilhelm, *Korea Australia Rheology Journal* **2014**, *26*, 319–326.

[67] L. Schwab, N. Hojdis, J. Lacayo, M. Wilhelm, *Macromolecular Materials and Engineering* **2016**, *301*, 457–468.

[68] P. Hou, J. Shi, S. Prabakar, X. Cheng, K. Wang, X. Zhou, S. P. Shah, *Construction and Building Materials* **2020**, *263*, 120226.

[69] B. Felekoğlu, S. Türkel, B. Baradan, *Building and Environment* **2007**, *42*, 1795–1802.

[70] L. Chen, G. Ma, G. Liu, Z. Liu, *Construction and Building Materials* **2019**, *225*, 311–323.

[71] R. G. Burg, *(No. R&D Bulletin RD113T) Portland Cement Association* **1996**, 18.

[72] S. Mindess, J. F. Young, D. Darwin, *Concrete*, Prentice Hall, Englewood, **1981**.

[73] S. Brunauer, D. L. Kantro, L. E. Copeland, *Journal of the American Chemical Society* **1958**, *80*, 761–767.

[74] H. Taylor, *Cement Chemistry*, Academic Press, London, **1990**.

[75] J. Stroh, T. Feiler, N. Zafar Ali, M. E. Minas da Piedade, F. Emmerling, *ChemistryOpen* **2019**, *8*, 1012–1019.

[76] Z. C. Lu, M. Haist, D. Ivanov, C. Jakob, D. Jansen, S. Leinitz, J. Link, V. Mechtcherine, J. Neubauer, J. Plank, W. Schmidt, C. Schilde, C. Schröfl, T. Sowoidnich, D. Stephan, *Data in Brief* **2019**, *27*, DOI `10.1016/j.dib.2019.104699`.

[77] E. M. Gartner, H. M. Jennings, *Journal of the American Ceramic Society* **1987**, *70*, 743–749.

[78] J. W. Bullard, R. J. Flatt, *Journal of the American Ceramic Society* **2010**, *93*, 1894–1903.

[79] P.-C. Aïtcin, R. J. Flatt, *Science and Technology of Concrete Admixtures*, Woodhead Publishing, Amsterdam, **2016**, pp. 129–146.

[80] P. Juilland, E. Gallucci, R. Flatt, K. Scrivener, *Cement and Concrete Research* **2010**, *40*, 831–844.

[81] J. D. Birchall, A. J. Howard, D. D. Double, *Cement and Concrete Research* **1980**, *10*, 145–155.

[82] H. N. Stein, J. M. Stevels, *Journal of Applied Chemistry* **1964**, *14*, 338–346.

[83] I. Odler, H. Dörr, *Cement and Concrete Research* **1979**, *9*, 277–284.

[84] S. Garrault, A. Nonat, *Journal of Crystal Growth* **1999**, *200*, 565–574.

[85] S. Garrault, E. Finot, E. Lesniewska, A. Nonat, *Materials and Structures* **2005**, *38*, 435–442.

[86] M. Tadros, J. Skalny, R. Kalyoncu, *Journal of American Ceramic Society* **1976**, *59*, 344–347.

[87] B. Derjaguin, *Acta Phys. Chim* **1939**, *10*, 333–346.

[88] H. Uchikawa, S. Hanehara, D. Sawaki, *Cement and Concrete Research* **1997**, *27*, 37–50.

[89] W. Kurdowski, *Cement and concrete chemistry*, *Vol. 9789400779*, **2014**, pp. 1–700.

[90] J. N. Israelachvili, *Intermolecular and Surface Forces*, 3rd ed., Academic Press, Amsterdam, **2011**.

[91] J. Plank, C. Hirsch, *Cement and Concrete Research* **2007**, *37*, 537–542.

[92] F. Winnefeld, A. Zingg, L. Holzer, J. Pakusch, S. Becker in 9th ACI International Conference on Superplasticizers and Other Chemical Admixtures, **2009**.

[93] N. Ukrainczyk, M. Thiedeitz, T. Kränkel, E. Koenders, C. Gehlen, *Materials* **2020**, *13*, 1–17.

[94] J. Mewis, N. J. Wagner, *Advances in Colloid and Interface Science* **2009**, *147-148*, 214–227.

[95] G. Tattersall, *Workability and Quality Control of Concrete*, Taylor & Francis, London, **1991**.

[96] G. Tattersall, P. Banfill, *The Rheology of Fresh Concrete*, Pitman Books Limited, Great Britain, **1983**.

[97] P. L. J. Domone, X. Yongmo, P. F. G. Banfill, *Magazine of Concrete Research* **1999**, *51*, 171–179.

[98] G. H. Tattersall, S. J. Bloomer, *Magazine of Concrete Research* **1979**, *31*, 202–210.

[99] M. Haist, J. Link, D. Nicia, S. Leinitz, C. Baumert, T. von Bronk, D. Cotardo, M. Eslami Pirharati, S. Fataei, H. Garrecht, C. Gehlen, I. Hauschildt, I. Ivanova, S. Jesinghausen, C. Klein, H. W. Krauss, L. Lohaus, D. Lowke, O. Mazanec, S. Pawelczyk, U. Pott, N. W. Radebe, J. J. Riedmiller, H. J. Schmid, W. Schmidt, E. Secrieru, D. Stephan, M. Thiedeitz, M. Wilhelm, V. Mechtcherine, *Materials and Structures/Materiaux et Constructions* **2020**, *53*, DOI `10.1617/s11527-020-01477-w`.

[100] D. Feys, J. E. Wallevik, A. Yahia, K. H. Khayat, O. H. Wallevik, *Materials and Structures/Materiaux et Constructions* **2013**, *46*, 289–311.

[101] D. Feys, R. Verhoeven, G. De Schutter, *Cement and Concrete Research* **2008**, *38*, 920–929.

[102] D. Feys, R. Verhoeven, G. De Schutter, *Cement and Concrete Research* **2009**, *39*, 510–523.

[103] A. Yahia, *Cement and Concrete Research* **2011**, *41*, 230–235.

[104] A. Yahia, K. H. Khayat, *Cement and Concrete Research* **2001**, *31*, 731–738.

[105] D. Feys, G. Heirman, G. De Schutter, R. Verhoeven, L. Vandewalle, D. Van Gemert, *5th Int. RILEM Symposium on Self-Compacting Concrete* **2007**, 1–6.

[106] H. A. Barnes, *Journal of Non-Newtonian Fluid Mechanics* **1999**, *81*, 133–178.

[107] O. Esping, *Early age properties of self-compacting concrete*, **2007**, pp. 1–204.

[108] N. Roussel, A. Lemaître, R. J. Flatt, P. Coussot, *Cement and Concrete Research* **2010**, *40*, 77–84.

[109] C. F. Zukoski, *Chemical Engineering Science* **1995**, *50*, 4073–4079.

[110] S. Hutzler, D. Weaire, F. Bolton, *Philosophical Magazine B: Physics of Condensed Matter; Statistical Mechanics Electronic Optical and Magnetic Properties* **1995**, *71*, 277–289.

[111] D. J. Durian, *Physical Review E* **1997**, *55*, 1739–1752.

[112] N. Roussel, G. Ovarlez, S. Garrault, C. Brumaud, *Cement and Concrete Research* **2012**, *42*, 148–157.

[113] M. A. Schultz, L. J. Struble, *Cement and Concrete Research* **1993**, *23*, 273–282.

[114] A. M. Mostafa, A. Yahia, *Cement and Concrete Research* **2016**, *85*, 174–182.

[115] P. Coussot, *Rheometry of Pastes, Suspensions, and Granular Materials: Applications in Industry and Environment*, Wiley, **2005**, pp. 41–78.

[116] C. Slichter, *Principles of Magnetic Resonace*, Springer, Berlin Heidelberg, **1978**.

[117] A. Abragam, *The Principles of Nuclear Magnetism*, Oxford University Press, Oxford, **1961**.

[118] R. R. Ernst, G. Bodenhausen, A. Wokaun, A. G. Redfield, *Principles of Nuclear Magnetic Resonance in One and Two Dimensions*, Clarendon Press, Oxford, **1987**.

[119] R. K. Harris, *Nuclear Magnetic Resonance Spectroscopy*, Pitman Publishing Inc, Marshfield, MA, **1983**.

[120] B. Blümich, *Essential NMR: For scientists and engineers*, Springer, Switzerland, **2018**.

[121] K. Schmidt-Rohr, H. W. Spiess, *Multidimensional Solid-State NMR and Polymers*, Academic Press, London, **1994**.

[122] F. Bloch, *Physical Review* **1946**, *70*, 460–474.

[123] E. L. Hahn, *Physical Review* **1950**, *80*, 580–594.

[124] P. J. McDonald, A. M. Gajewicz, R. Morrell, *Measurement Good Practice Guide* **2016**, *144*.

[125] N. Bloembergen, E. M. Purcell, R. V. Pound, *Physical Review* **1948**, *73*, 679–712.

[126] W. P. Halperin, J.-Y. Jehng, Y.-Q. Song, *Magnetic Resonance Imaging* **1994**, *12*, 169–173.

[127] M. Wyrzykowski, P. J. McDonald, K. L. Scrivener, P. Lura, *Journal of Physical Chemistry C* **2017**, *121*, 27950–27962.

[128] A. C. A. Muller, K. L. Scrivener, A. M. Gajewicz, P. J. McDonald, *Microporous and Mesoporous Materials* **2013**, *178*, 99–103.

[129] A. C. A. Muller, K. L. Scrivener, A. M. Gajewicz, P. J. McDonald, *Journal of Physical Chemistry C* **2013**, *117*, 403–412.

[130] S. Meiboom, D. Gill, *Review of Scientific Instruments* **1958**, *29*, 688–691.

[131] H. Y. Carr, E. M. Purcell, *Physical Review* **1954**, *94*, 630–638.

[132] A. Maus, C. Hertlein, K. Saalwächter, *Macromolecular Chemistry and Physics* **2006**, *207*, 1150–1158.

[133] P. E. Kristiansen, E. W. Hansen, B. Pedersen, *Journal of Physical Chemistry B* **1999**, *103*, 3552–3558.

[134] R. Blinc, M. Burgar, G. Lahajhar, M. Rozmarin, V. Rutar, I. Kocuvan, J. Ursic, *Journal of the American Ceramic Society* **1978**, *61*, 35–37.

[135] K. R. Brownstein, C. E. Tarr, *Journal of Magnetic Resonance* **1977**, *26*, 17–24.

[136] J. Greener, H. Peemoeller, C. Choi, R. Holly, E. J. Reardon, C. M. Hansson, M. M. Pintar, *Journal of the American Ceramic Society* **2000**, *83*, 623–627.

[137] K. Friedemann, F. Stallmach, J. Kärger, *Cement and Concrete Research* **2006**, *36*, 817–826.

[138] P. F. De, A. E. Marble, B. J. Balcom, J. C. García, I. V. Masthikin, M. D. A. Thomas, T. W. Bremner, *Cement and Concrete Research* **2009**, *39*, 324–328.

[139] M. Wyrzykowski, A. M. Gajewicz-Jaromin, P. J. McDonald, D. J. Dunstan, K. L. Scrivener, P. Lura, *Journal of Physical Chemistry C* **2019**, *123*, 16153–16163.

[140] V. Räntzsch, M. B. Özen, K. F. Ratzsch, E. Stellamanns, M. Sprung, G. Guthausen, M. Wilhelm, *Macromolecular Materials and Engineering* **2019**, *304*, 1–14.

[141] F. Rebry, A. Declerck, K. F. Ratzsch, M. Wilhelm, K. Dewettinck, P. Van der Meeren, *Current Research in Food Science* **2021**, *4*, 414–420.

[142] N. G. McCrum, B. E. Read, G. Williams, *Anelastic and dielectric effects in polymeric solids*, John Wiley & Sons, Ltd, New York, **1967**.

[143] V. I. Gaiduk, *Dielectric Relaxation and Dynamics of Polar Molecules*, World Scientific Publishing, Singapore, **1999**.

[144] V. Raicu, Y. Feldman, *Dielectric Relaxation in Biological Systems: Physical Principles, Methods, and Applications*, Oxford University Press, Oxford, **2015**, p. 464.

[145] G. Polizos, E. Tuncer, V. Tomer, I. Sauers, C. Randall, E. Manias in *Nanoscale Spectroscopy with Applications*, CRC Press Taylor & Francis Group, **2014**, pp. 93–130.

[146] N. E. Hager, R. C. Domszy, *Journal of Applied Physics* **2004**, *96*, 5117–5128.

[147] C. Tsonos, I. Stavrakas, C. Anastasiadis, A. Kyriazopoulos, A. Kanapitsas, D. Triantis, *Journal of Physics and Chemistry of Solids* **2009**, *70*, 576–583.

[148] S. Cerveny, S. Arrese-Igor, J. S. Dolado, J. J. Gaitero, A. Alegra, J. Colmenero, *Journal of Chemical Physics* **2011**, *134*, DOI 10.1063/1.3521481.

[149] G. Goracci, M. Monasterio, H. Jansson, S. Cerveny, *Scientific Reports* **2017**, *7*, 1–10.

[150] M. Monasterio, H. Jansson, J. J. Gaitero, J. S. Dolado, S. Cerveny, *Journal of Chemical Physics* **2013**, *139*, 1–8.

[151] F. Abe, A. Nishi, H. Saito, M. Asano, S. Watanabe, R. Kita, N. Shinyashiki, S. Yagihara, M. Fukuzaki, S. Sudo, Y. Suzuki, *Measurement Science and Technology* **2017**, *28*, DOI 10.1088/1361-6501/aa5c65.

[152] Y. Suzuki, H. Duran, M. Steinhart, M. Kappl, H. J. Butt, G. Floudas, *Nano Letters* **2015**, *15*, 1987–1992.

[153] M. Bittelli, M. Flury, K. Roth, *Water Resources Research* **2004**, *40*, 1–11.

[154] N. Miura, N. Shinyashiki, S. Yagihara, M. Shiotsubo, *Journal of the American Ceramic Society* **1998**, *81*, 213–216.

[155] Y. El Hafiane, A. Smith, P. Abelard, J. P. Bonnet, P. Blanchart, *Ceramics - Silikaty* **1999**, *43*, 48–51.

[156] Y. El Hafiane, A. Smith, J. Pierre Bonnet, P. Abelard, P. Blanchart, *Cement and Concrete Research* **2000**, *30*, 1057–1062.

[157] P. Debye, *Polar Molecules*, Chemcial Catalogue Company, New York, **1929**.

[158] K. S. Cole, R. H. Cole, *Journal of Chemical Physics* **1941**, *9*, 341–351.

[159] R. R. Nigmatullin, Y. E. Ryabov, *Physics of the Solid State* **1997**, *39*, 87–90.

[160] S. Havriliak, S. Negami, *Journal of Polymer Science: Part C* **1966**, *14*, 99–117.

[161] S. Khodadadi, S. Pawlus, A. P. Sokolov, *Journal of Physical Chemistry B* **2008**, *112*, 14273–14280.

[162] W. Doster, S. Busch, A. M. Gaspar, M. S. Appavou, J. Wuttke, H. Scheer, *Physical Review Letters* **2010**, *104*, 1–4.

[163] M. Vogel, *Physical Review Letters* **2008**, *101*, 1–4.

[164] R.-J. Roe, *Methods of X-Ray and Neutron Scattering in Polymer Science*, Oxford University Press, New York, **2000**.

[165] G. G. Fuller, *Optical Rheometry of Complex Fluids*, Oxford University Press, New York, **1995**.

[166] H. Watanabe, T. Sato, M. Hirose, K. Osaki, M. L. Yao, *Rheologica Acta* **1998**, *37*, 519–527.

[167] H. Watanabe, T. Sato, Y. Matsumiya, T. Inoue, K. Osaki, *Nihon Reoroji Gakkaishi* **1999**, *27*, 121–125.

[168] J. Diani, K. Gall, *Polymer Engineering and Science* **2006**, *60*, 1–10.

[169] S. Capaccioli, D. Prevosto, A. Best, A. Hanewald, T. Pakula, *Journal of Non-Crystalline Solids* **2007**, *353*, 4267–4272.

[170] K. Horio, T. Uneyama, Y. Matsumiya, Y. Masubuchi, H. Watanabe, *Macromolecules* **2014**, *47*, 246–255.

[171] J. Knapik-Kowalczuk, K. Jurkiewicz, A. Kocot, M. Paluch, *Journal of Molecular Liquids* **2020**, *302*, 112494.

[172] M. Born, E. Wolf, *Principles of Optics*, Seventh, Cambridge University Press#, **1998**.

[173] J. D. Jackson, *Classical Electrodynamics*, Third, John Wiley & Sons, Ltd, New Jersey, **1999**.

[174] P. R. Griffiths, J. A. de Haseth, *Fourier Transform Infrared Spectrometry*, *Vol. 42*, 2nd, John Wiley & Sons: New Jersey, New Jersey, **2007**, pp. 3–13.

[175] M. R. Derrick, D. Stulik, J. M. Landry, *Infrared spectroscopy in Conservation Science*, Los Angeles, **1999**, pp. 4–15.

[176] B. C. Smith, *Fundementals of Fourier Transform Infrared Specroscopy*, 2nd, CRC Press : Florida, United States, **2011**.

[177] B. H. Stuart, *Infrared Spectroscopy: Fundamentals and Applications*, *Vol. 8*, John Wiley & Sons, Ltd, **2004**, p. 224.

[178] D. A. Skoog, J. F. Holler, S. R. Crouch, F. J. Holler, S. R. Crouch, *Principles of Instrumental Analysis*, 7th, Cengage Learning: Boston, **2006**.

[179] T. G. Mayerhöfer, J. Popp, *ChemPhysChem* **2019**, *20*, 511–515.

[180] P. J. Larkin, *Infrared and Raman Spectroscopy - Principles and Spectral Interpretation*, **2011**, pp. 1–239.

[181] G. Ramer, B. Lendl, *Attenuated Total Reflection Fourier Transform Infrared Spectroscopy*, John Wiley & Sons, Ltd, **2013**.

[182] J. N. Ollagnier, T. Tassaing, S. Harrisson, M. Destarac, *Reaction Chemistry and Engineering* **2016**, *1*, 372–378.

[183] T. Scherzer, U. Decker, *Polymer* **2000**, *41*, 7681–7690.

[184] B. S. Chiou, S. A. Khan, *Macromolecules* **1997**, *30*, 7322–7328.

[185] L. Shao, P. R. Griffiths, *Analytical Chemistry* **2008**, *80*, 5219–5224.

[186] T. F. Beskers, T. Hofe, M. Wilhelm, *Macromolecular Rapid Communications* **2012**, *33*, 1747–1752.

[187] T. F. Beskers, T. Hofe, M. Wilhelm, *Polymer Chemistry* **2015**, *6*, 128–142.

[188] J. M. Chalmers, *Handbook of Vibrational Spectroscopy* **2006**, DOI 10.1002/0470027320.s3101.

[189] N. W. Radebe, C. Fengler, C. O. Klein, R. Figuli, M. Wilhelm, *Journal of Rheology* **2021**, 681–693.

[190] A. R. Hind, S. K. Bhargava, *Advances in Colloid and Interface Science* **2001**, *93*, 91–114.

[191] R. M. McCormick, B. L. Karger, *Analytical Chemistry* **1980**, *52*, 2242–2249.

[192] S. N. Ghosh, S. K. Handoo, *Cement and Concrete Research* **1980**, *10*, 771–782.

[193] T. Liang, Y. Nanru, *Cement and Concrete Research* **1994**, *24*, 150–158.

[194] R. Ylmén, U. Jäglid, B. M. Steenari, I. Panas, *Cement and Concrete Research* **2009**, *39*, 433–439.

[195] R. Ylmén, U. Jäglid, I. Panas, *Journal of the American Ceramic Society* **2014**, *97*, 3669–3675.

[196] S. Puligilla, P. Mondal, *Cement and Concrete Research* **2015**, *70*, 39–49.

[197] I. García Lodeiro, D. E. Macphee, A. Palomo, A. Fernández-Jiménez, *Cement and Concrete Research* **2009**, *39*, 147–153.

[198] S. J. Barnett, D. E. Macphee, E. E. Lachowski, N. J. Crammond, *Cement and Concrete Research* **2002**, *32*, 719–730.

[199] P. F. Faure, S. Caré, J. Magat, T. Chaussadent, *Construction and Building Materials* **2012**, *29*, 496–503.

[200] E. Pustovgar, R. P. Sangodkar, A. S. Andreev, M. Palacios, B. F. Chmelka, R. J. Flatt, J. B. D'Espinose De Lacaillerie, *Nature Communications* **2016**, *7*, 1–9.

[201] Y. Renhe, L. Baoyuan, W. Zhongwei, *Cement and Concrete Research* **1990**, *20*, 385–393.

[202] K. L. Scrivener, T. Füllmann, E. Gallucci, G. Walenta, E. Bermejo, *Cement and Concrete Research* **2004**, *34*, 1541–1547.

[203] N. A. Voglis, G. T. Kakali, S. G. Tsivilis, *Mikrochimica Acta* **2001**, *136*, 181–183.

[204] A. J. Allen, J. J. Thomas, H. M. Jennings, *Nature Materials* **2007**, *6*, 311–316.

[205] X. Ren, W. Zhang, J. Ye, *Cement and Concrete Research* **2017**, *99*, 129–136.

[206] M. Yousuf, A. Mollah, T. R. Hess, Y. N. Tsai, D. L. Cocke, *Cement and Concrete Research* **1993**, *23*, 773–784.

[207] P. Yu, R. J. Kirkpatrick, B. Poe, P. F. McMillan, X. Cong, *Journal of the American Ceramic Society* **2004**, *82*, 742–748.

[208] M. Y. Mollah, W. Yu, R. Schennach, D. L. Cocke, *Cement and Concrete Research* **2000**, *30*, 267–273.

[209] M. Y. Mollah, M. Kesmez, D. L. Cocke, *Science of the Total Environment* **2004**, *325*, 255–262.

[210] T. L. Hughes, C. M. Methven, T. G. Jones, S. E. Pelham, P. Fletcher, C. Hall, *Advanced Cement Based Materials* **1995**, *7355*, 91–104.

[211] A. H. Delgado, R. M. Paroli, J. J. Beaudoin, *Applied Spectroscopy* **1996**, *50*, 970–976.

[212] P. Alonso-González, P. Albella, F. Neubrech, C. Huck, J. Chen, F. Golmar, F. Casanova, L. E. Hueso, A. Pucci, J. Aizpurua, R. Hillenbrand, *Physical Review Letters* **2013**, *110*, 1–6.

[213] F. Basquiroto de Souza, C. Zheng, S. Chen, Y. Liu, K. Sagoe-Crentsil, W. Duan, *Cement and Concrete Research* **2021**, *147*, 106525.

[214] Y. Nishikawa, T. Nakano, H. Miyauchi, K. Nishikida, E. Y. Jiang, *Applied Spectroscopy* **2004**, *58*, 958–968.

[215] Y. Nishikawa, T. Nakano, I. Noda, *Applied Spectroscopy* **2012**, *66*, 312–318.

[216] C. Küchenmeister-Lehrheuer, J. P. Plog, F. Meyer, *Thermo Fisher Scientific* **2016**, 3–4.

[217] M. Feustel, C. Küchenmeister, J. Philip Plog, *Thermo Fisher Scientific* **2010**, 1–4.

[218] K. Sugimoto, F. Soergel, M. Feustel, *Thermo Fisher Scientific* **2012**, 2–5.

[219] M. Boulet-Audet, A. E. Terry, F. Vollrath, C. Holland, *Acta Biomaterialia* **2014**, *10*, 776–784.

[220] R. A. Spragg in *Encyclopedia of Spectroscopy and Spectrometry*, **2016**, pp. 419–427.

[221] C. L. Chakrabarti, *Spectrochimica Acta Part A: Molecular and Biomolecular Spectroscopy* **1999**, *33*, 58–75.

[222] D. A. Neamen, *Semiconductor Physics and Devices*, McGraw-Hill, **2003**.

[223] H. E. Ruda, N. Matsuura, *Handboook of Electronic and Photonic Materials*, **2017**, p. 1.

[224] L. Fiedler, S. Newman, S. Bakan, *Applied Optics* **2005**, *44*, 5332–5340.

[225] M. C. Abrams, G. C. Toon, R. A. Schindler, *Applied Optics* **1994**, *33*, 6307.

[226] Z. M. Zhang, C. J. Zhu, L. M. Hanssen, *Applied Spectroscopy* **1997**, *51*, 576–579.

[227] C. Yao, H. Mei, Y. Xiao, A. Shahsafi, W. Derdeyn, J. L. King, C. Wan, R. O. Scarlat, M. H. Anderson, M. A. Kats, Correcting thermal-emission-induced detector saturation in infrared spectroscopy, tech. rep., Cornell University, **2020**, pp. 1–15.

[228] R. L. Richardson, H. Yang, P. R. Griffiths in Fourier Transform Spectroscopy: 11 th International Conference, **1998**, pp. 428–431.

[229] P. Hidnert, H. Krider, *Journal of Research of the National Bureau of Standards* **1952**, *48*, 209.

[230] Y. Okada, Y. Tokumaru, *Journal of Applied Physics* **1984**, *56*, 314–320.

[231] P. Hidnert, *Journal of Research of the National Bureau of Standards* **1943**, *30*, 101.

[232] D. B. Chase, *Applied Spectroscopy* **1984**, *38*, 491–494.

[233] B. T. Bowie, P. R. Griffiths, *Applied Spectroscopy* **2000**, *54*, 1192–1202.

[234] P. Jeseck, C. Camy-Peyret, S. Payan, T. Hawat, *Applied Optics* **1998**, *37*, 6544.

[235] A. Keens, A. Simon, United States Patent, **1990**.

[236] J. Diani, K. Gall, *Polymer Engineering and Science* **2013**, 96–104.

[237] W. J. Walczak, D. A. Hoagland, S. L. Hsu, *Macromolecules* **1996**, *29*, 7514–7520.

[238] G. I. Andrade, E. F. Barbosa-Stancioli, A. A. Mansur, W. L. Vasconcelos, H. S. Mansur, *Journal of Materials Science* **2008**, *43*, 450–463.

[239] D. L. Pavia, G. M. Lampman, G. S. Kriz, J. R. Vyvyan, *Introduction to Spectroscopy*, 4th, Brooks/Cole, Cengage Learning, New York, **2009**.

[240] H. S. Mansur, C. M. Sadahira, A. N. Souza, A. A. P. Mansur, *Materials Science and Engineering C* **2008**, *28*, 539–548.

[241] M. Klokkenburg, J. Hilhorst, B. H. Erné, *Vibrational Spectroscopy* **2007**, *43*, 243–248.

[242] J. J. Max, C. Chapados, *Journal of Physical Chemistry A* **2002**, *106*, 6452–6461.

[243] S. Migliozzi, P. Angeli, L. Mazzei, *Colloids and Surfaces A: Physicochemical and Engineering Aspects* **2019**, *577*, 84–95.

[244] H. De Paz, A. Chemtob, C. Croutxé-Barghorn, D. Le Nouen, S. Rigolet, *Journal of Physical Chemistry B* **2012**, *116*, 5260–5268.

[245] E. Rudé Payró, J. Llorens Llacuna, *Journal of Non-Crystalline Solids* **2006**, *352*, 2220–2225.

[246] H. H. Winter, M. Mours, *Advances in Polymer Science* **1997**, *134*, 164–234.

[247] N. Orakdogen, M. Y. Kizilay, O. Okay, *Polymer* **2005**, *46*, 11407–11415.

[248] S. Seiffert, *Polymer Chemistry* **2017**, *8*, 4472–4487.

[249] F. Chambon, H. H. Winter, *Journal of Rheology* **1987**, *31*, 683–697.

[250] H. H. Winter, F. Chambon, *Journal of Rheology* **1986**, *30*, 367–382.

[251] A. J. Marzocca, S. Cerveny, J. M. Méndez, *Polymer International* **2000**, *49*, 216–222.

[252] A. J. Marzocca, M. A. Mansilla, *Journal of Applied Polymer Science* **2006**, *101*, 35–41.

[253] V. Adibnia, R. J. Hill, *Journal of Rheology* **2016**, *60*, 541–548.

[254] A. V. Hill, *Biochemical Journal* **1913**, *7*, 471–480.

[255] P. J. Flory, *Principles of Polymer Chemistry*, Cornell University Press: Ithaca, NY, **1953**, p. 357.

[256] W. H. Stockmayer, *The Journal of Chemical Physics* **1943**, *11*, 45–55.

[257] A. Matsumoto, Y. Miwa, S. Inoue, T. Enomoto, H. Aota, *Macromolecules* **2010**, *43*, 6834–6842.

[258] C. Sayil, O. Okay, *Polymer* **2001**, *42*, 7639–7652.

[259] J. Nie, B. Du, W. Oppermann, *Macromolecules* **2004**, *37*, 6558–6564.

[260] A. Bogner, J. Link, M. Baum, M. Mahlbacher, T. Gil-Diaz, J. Lützenkirchen, T. Sowoidnich, F. Heberling, T. Schäfer, H. M. Ludwig, F. Dehn, H. S. Müller, M. Haist, *Cement and Concrete Research* **2020**, *130*, 105977.

[261] Q. Yuan, X. Lu, K. H. Khayat, D. Feys, C. Shi, *Materials and Structures* **2017**, *50*, 112.

[262] H. A. Barnes, *Journal of Non-Newtonian Fluid Mechanics* **1995**, *56*, 221–251.

[263] D. Merger, M. Abbasi, J. Merger, A. J. Giacomin, C. Saengow, M. Wilhelm, *Applied Rheology* **2016**, *26*, 1–15.

[264] S. Nie, J. Lacayo-Pineda, M. Wilhelm, *Soft Materials* **2018**, *17*, 1–15.

[265] J. J. Zheng, J. Zhang, G. W. Scherer, *Cement and Concrete Research* **2012**, *42*, 1280–1285.

[266] H. Minard, S. Garrault, L. Regnaud, A. Nonat, *Cement and Concrete Research* **2007**, *37*, 1418–1426.

[267] K. L. Scrivener, A. Nonat, *Cement and Concrete Research* **2011**, *41*, 651–665.

[268] R. Ylmén, L. Wadsö, I. Panas, *Cement and Concrete Research* **2010**, *40*, 1541–1546.

[269] N. Y. Mostafa, E. A. Kishar, S. A. Abo-El-Enein, *Journal of Alloys and Compounds* **2009**, *473*, 538–542.

[270] Y. Guo, T. Zhang, W. Tian, J. Wei, Q. Yu, *Journal of Materials Science* **2019**, *54*, 2152–2169.

[271] M. Horgnies, J. J. Chen, C. Bouillon, *WIT Transactions on Engineering Sciences* **2013**, *77*, 251–262.

[272] T. Huang, Q. Yuan, S. Zuo, B. Li, Q. Wu, Y. Xie, *Cement and Concrete Research* **2021**, *149*, 106556.

[273] A. H. López, J. L. G. Calvo, J. G. Olmo, S. Petit, M. C. Alonso, *Journal of the American Ceramic Society* **2008**, *91*, 1258–1265.

[274] M. R. Querry, Optical constants of minerals and other materials from the millimeter to the ultraviolet, tech. rep., Contractor Report CRDEC-CR-88009, **1987**.

[275] J. Stroh, M. C. Schlegel, W. Schmidt, Y. Nguyen Thi, B. Meng, F. Emmerling, *Construction and Building Materials* **2016**, *106*, 18–26.

[276] A. Boumiz, *Advanced Cement Based Materials* **1996**, *3*, 94–106.

[277] A. Prabhu, J. C. Gimel, A. Ayuela, S. Arrese-Igor, J. J. Gaitero, J. S. Dolado, *Nature* **2018**, *8*, 1–11.

[278] F. W. Locher, W. Richartz, S. Sprung, *Zement-Kalk-Gips International* **1980**, 271–277.

[279] F. W. Locher, W. Richartz, S. Sprung, *Zement-Kalk-Gips International* **1976**, 435–442.

[280] W. Schmidt, H. J. H. Brouwers, H. C. Kühne, B. Meng, *Cement and Concrete Composites* **2014**, *49*, 111–126.

[281] C. Jakob, D. Jansen, N. Ukrainczyk, E. Koenders, U. Pott, D. Stephan, J. Neubauer, *Materials* **2019**, *12*, DOI 10.3390/ma12182957.

[282] V. Bortolotti, P. Fantazzini, R. Mongiorgi, S. Sauro, S. Zanna, *Cement and Concrete Research* **2012**, *42*, 577–582.

[283] V. Räntzsch, M. Haas, M. B. Özen, K. F. Ratzsch, K. Riazi, S. Kauffmann-Weiss, J. K. Palacios, A. J. Müller, I. Vittorias, G. Guthausen, M. Wilhelm, *Polymer* **2018**, *145*, 162–173.

[284] L. J. Parrott, M. Geiker, W. A. Gutteridge, D. Killoh, *Cement and Concrete Research* **1990**, *20*, 919–926.

List of Figures

List of Tables

Acknowledgements

I am grateful to have had very supportive colleagues, some of which became my friends. A special thank you goes to

- My supervisor, **Prof. Dr. Manfred Wilhelm** for his intellectual stimulation and for his confidence that I will see this project through.
- I would like to thank and acknowledge **Deutsche Forschungsgemeinschaft (DFG)** under the grant WI 1911/25-1, within the DFG priority programme 2005 "Opus Fluidum Futurum—Rheology of reactive, multiscale, multiphase construction materials." Project number 386871659, for funding me from April 2018 to date. The project has also played a vital role in my transferable skills development through all the soft skills workshops that were offered. Thank you!
- Within the SPP2005, I have had the privilege to work with some incredible people including **Wolfram Schmidt** who not only proof read my work but has more importantly has been instrumental in my scientific, professional and personal growth. From the beginning of out journey in Nairobi (2019) to now with our new FALCONESS project, it has been really awesome encountering someone with so much passion for sustainable development and building long last networks between researchers in Africa and researchers in Europe.
- I would like to thank **Christopher Klein** for his mentorship and being an awesome travel companion to all the SPP2005 meetings around Germany. To **Roxana Figuli**, thank you for ensuring that I was well equipped at the start of my PhD. To both of you, thank you for proofreading my work.
- I would also like to extend gratitude to my colleagues who became friends, for creating a productive yet homely working environment. To **Christos**, **Shouliang** and **Christian**, thank you for your input and fruitful/fun discussions (even on weekends) and to **Carlo** for your encouragement, bringing a little bit of the South African flavour into the office and for proof reading parts of my work. Thank you to **Lorenz** for being a really great desk buddy and for keeping all my secrets.
- Thank you to **Dr. Albrecht Rager** from Bruker Optik GmbH with his endless assistance in acquiring the spectrometer used in this work and for being open to address the questions I had. I wish you a very happy retirement! I would also like to

thank **Mathias Keßler**, from Bruker Optik GmbH for always being willing to help with the OPUS software or MATRIX spectrometer related questions.

- A huge thank you goes to **Frau. Sabine Weiland** for her patience with my admin related questions and for arranging all my business travels with no hassle, especially my trips to Kenya, South Africa and most recently to Ghana.
- Thank you to **Maxi** and **Karl** for proofreading my dielectrics and NMR sections, respectively.
- I would like to thank my friends, both in Mzansi and Deutschland for constantly reminding me of how capable I am!
- Thank you to **Timo Beskers** for making me your third South African import into Germany and for sharing with me about travel grant opportunities, specifically the one from the Karlsruhe House of Young Scientists (KHYS). Receiving this grant opened up so many opportunities and networks for me and I am truly grateful to have connected with you at Stellenbosch University.
- Last but certainly not least, without my prayer warrior - my mother **Brenda Radebe** - my sisters, my brother, uncles, cousins, and my ancestors this journey would have not been possible. Ngiyanithanda futhi ngiyanibonga kakhulu bo Bhungane nabo Tau ♡

Ubuntu-I am because you are

Appendix

A.1 Equations, figures and additional text

A.1.1 Mathematical first derivative of Equation 5.2.3

$$\frac{d}{dt}\left[\frac{(k(t-t_0))^r}{1+(k(t-t_0))^r}\right]$$

$$=\frac{\frac{d}{dt}[(k(t-t_0))^r]\cdot((k(t-t_0))^r+1)-(k(t-t_0))^r\cdot\frac{d}{dt}[(k(t-t_0))^r+1]}{((k(t-t_0))^r+1)^2}$$

$$=\frac{r(k(t-t_0))^{r-1}\cdot\frac{d}{dt}[k(t-t_0]\cdot((k(t-t_0))^r+1)\ -(k(t-t_0))^r(\frac{d}{dt}[(k(t-t_0))^r]\ +\frac{d}{dt}[1])}{((k(t-t_0))^r+1)^2}$$

$$=\frac{r(k(t-t_0))^{r-1}\cdot k(\frac{d}{dt}[t]+\frac{d}{dt}[-t_0])\cdot((k(t-t_0))^r+1)-(k(t-t_0))^r(r(k(t-t_0))^{r-1}\cdot\frac{d}{dt}[k(t-t_0]+0)}{((k(t-t_0))^r+1)^2}$$

$$=\frac{rk(k(t-t_0))^{r-1}(1+0)((k(t-t_0))^r+1)-k(\frac{d}{dt}[t]+\frac{d}{dt}[-t_0])\cdot\ r(k(t-t_0))^{2r-1}}{((k(t-t_0))^r+1)^2}$$

$$=\frac{rk(k(t-t_0))^{r-1}((k(t-t_0))^r+1)-(1+0)\cdot rk(k(t-t_0))^{2r-1}}{((k(t-t_0))^r+1)^2}$$

$$=\frac{k(k(t-t_0))^{r-1}((k(t-t_0))^r+1)-rk(k(t-t_0))^{2r-1}}{((k(t-t_0))^r+1)^2}$$

$$=\frac{r(k(t-t_0))^r}{(t-t_0)((k(t-t_0))^r+1)}-\frac{r(k(t-t_0))^{2r}}{(t-t_0)((k(t-t_0))^r+1)^2}$$

Simplified

$$=\frac{r(k(t-t_0))^r}{(t-t_0)(1+(k(t-t_0))^r)^2}$$

A.1.2 IR spectrum of water and Casul (Ettringite) in water

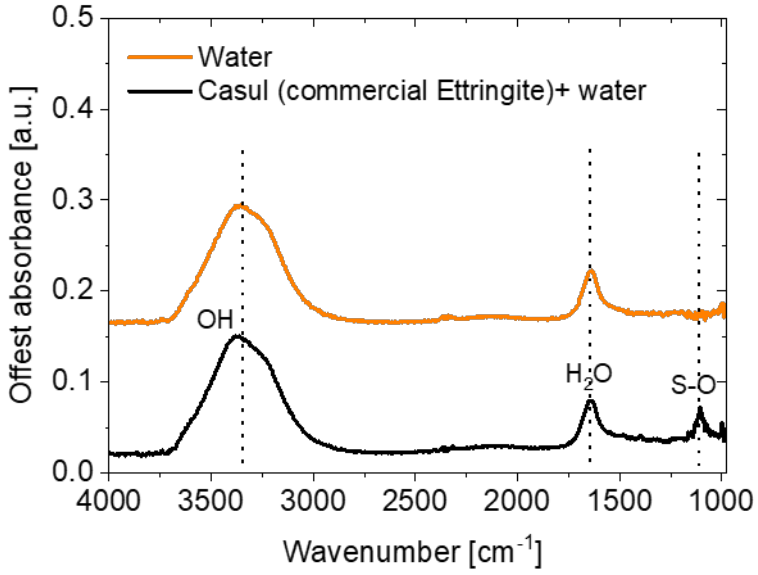

Figure 1: Rheo-IR:IR spectrum ($4000 - 1000\ cm^{-1}$) commercial ettringite (Casul) in water (water to Casul ratio = 0.7). Note that the Casul does not quite dissolve in water, the water is used to disperse the Casul in order to try increase contact with the Si-ATR crystal.

A.1.3 Offline FTIR, dynamic time sweep and correlated FTIR and rheology of cement paste ($\phi = 0.39$)

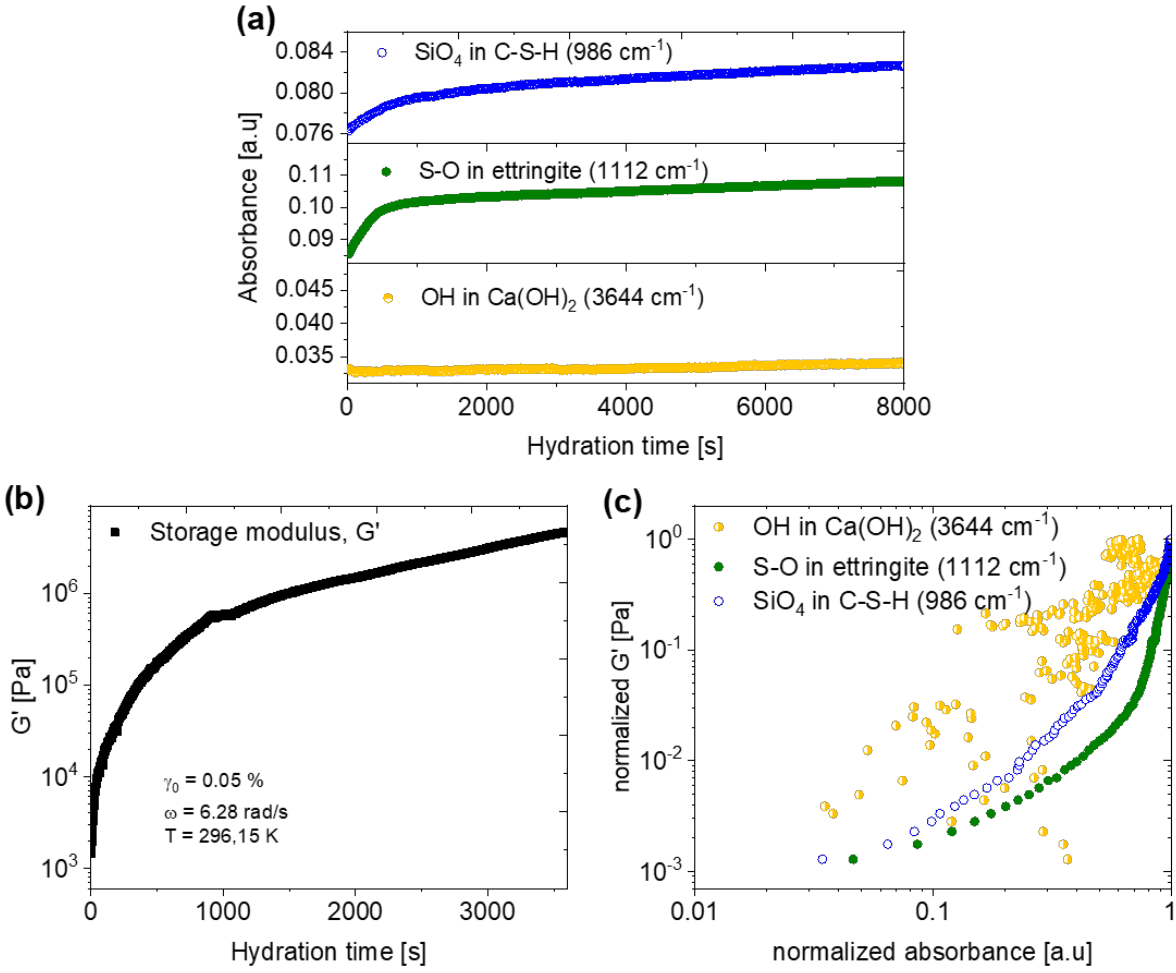

Figure 2: (a) Offline FTIR: IR spectral bands that are associated with the hydrates *C-S-H*, *Aft*, and $Ca(OH)_2$ as a function of time (b) storage modulus as a function of time and (c) evolution of the storage modulus as a function of the SiO_4 absorbance associated with *C-S-H*, the *S-O* of $[SO_4]^2$ in ettringite and the *O-H*associated with $Ca(OH)_2$ for $\phi = 0.39$.

A.1.4 PAAc hydrogel synthesis procedure

Materials

N,N'-methylenebis(acrylamide) (MBA, 99 %, Sigma-Aldrich) and 2,2'-Azobis[2-(2-imidazolin-2-yl)propane]dihydrochloride (VA-044, 95 %, FUJIFILM Wako Pure Chemical) were used as received. Acrylic acid (AAc, >99 %, Merck) was freshly distilled at reduced pressure prior to the synthesis.

Preparation of acrylic acid pre-gel solution

Poly(acrylic acid) hydrogels are synthesized by aqueous free radical copolymerization of acrylic acid (AAc) and N,N'-methylenebis(acrylamide) (MBA) as bifunctional crosslinking agent. The sample was prepared with a monomer weight fraction of 50 wt.% and a degree of crosslinking (molar ratio of MBA to AAc) of DC = 0.1 mol%. The weight ratio of the initiator 2,2'-azobis[2-(2-imidazolin-2-yl)propane]dihydrochloride (VA-044) to AAc was fixed to 0.5 wt.%. The preparation procedure of the sample was as follows: (1) MBA (7.7 mg, 0.050 mmol) was dissolved in deionized water (2.57 g). (2) Freshly distilled AAc (3.6 g, 0.05 mol) was added to the mixture. (3) The initiator VA-044 (0.018 g, 0.056 mmol) was dissolved in 1 g deionized water and added to the mixture. (4) The pre-gel solution was stirred vigorously for 1 min and then 1 ml of the solution was placed on the lower Ares G2 plate geometry.

A.1.5 Acrylamide gelation synthesis procedure

To prepare the 40 wt% acrylamide (AM) pre-gel solution, 3.6 g AM (50.6 mmol) were dissolved in either 5.38 g H_2O or 5.38 g D_2O. Then, 18 mg (0.06 mmol) VA-044 photoinitiator was added to the mixture. The pre-gel solution was stirred vigorously for 1 min and then 1 mL of the solution were poured onto the lower plate geometry.

B.2 Technical Drawings and Matlab Code

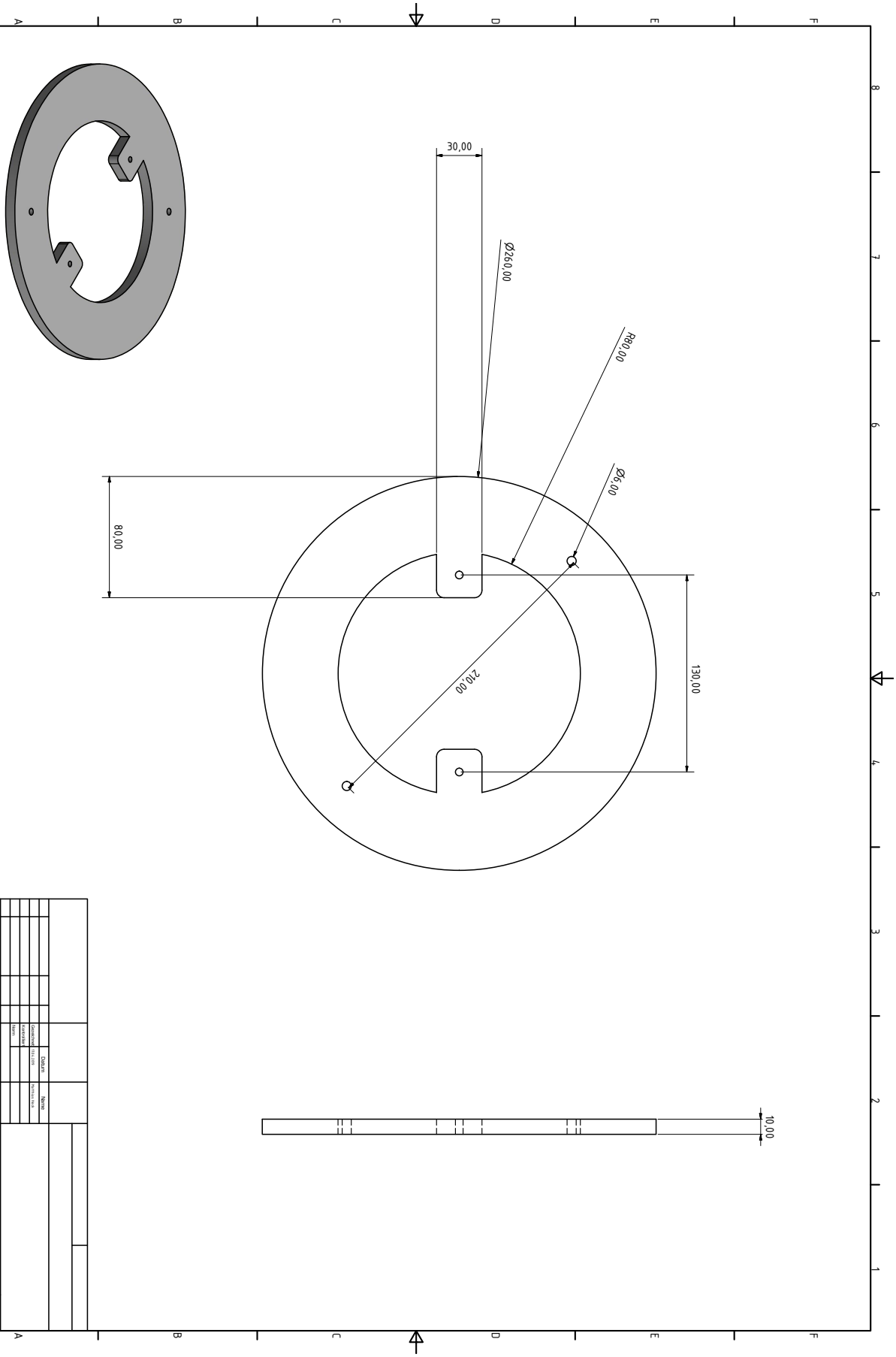

Figure 3: Rheo-IR: Mirror mounting with no movable parts. Credit to Dr. Matthias Heck

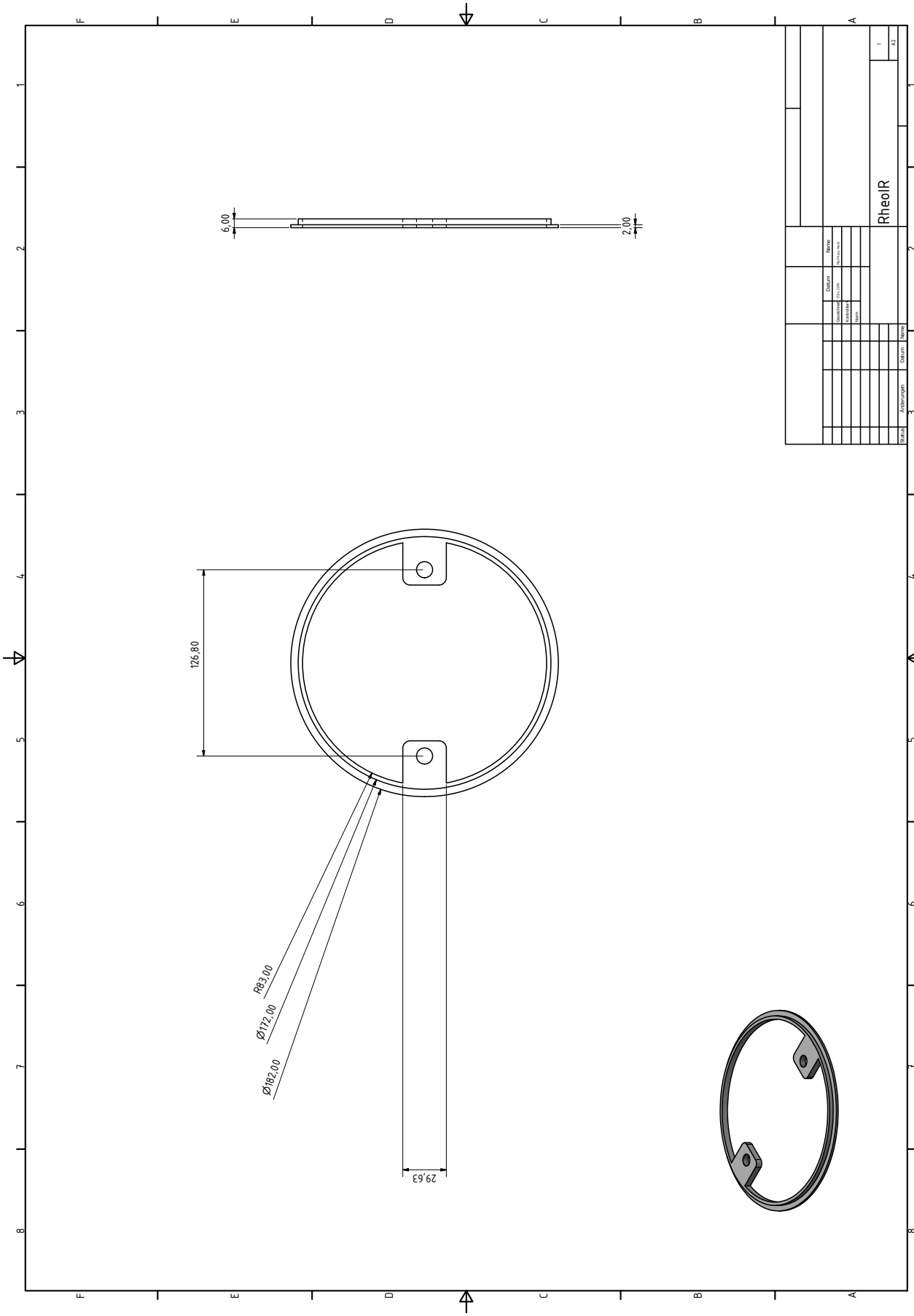

Figure 4: Rheo-IR: Mirror mounting attached directly to the transducer, Part 1 of the mounting. Credit to Dr. Matthias Heck

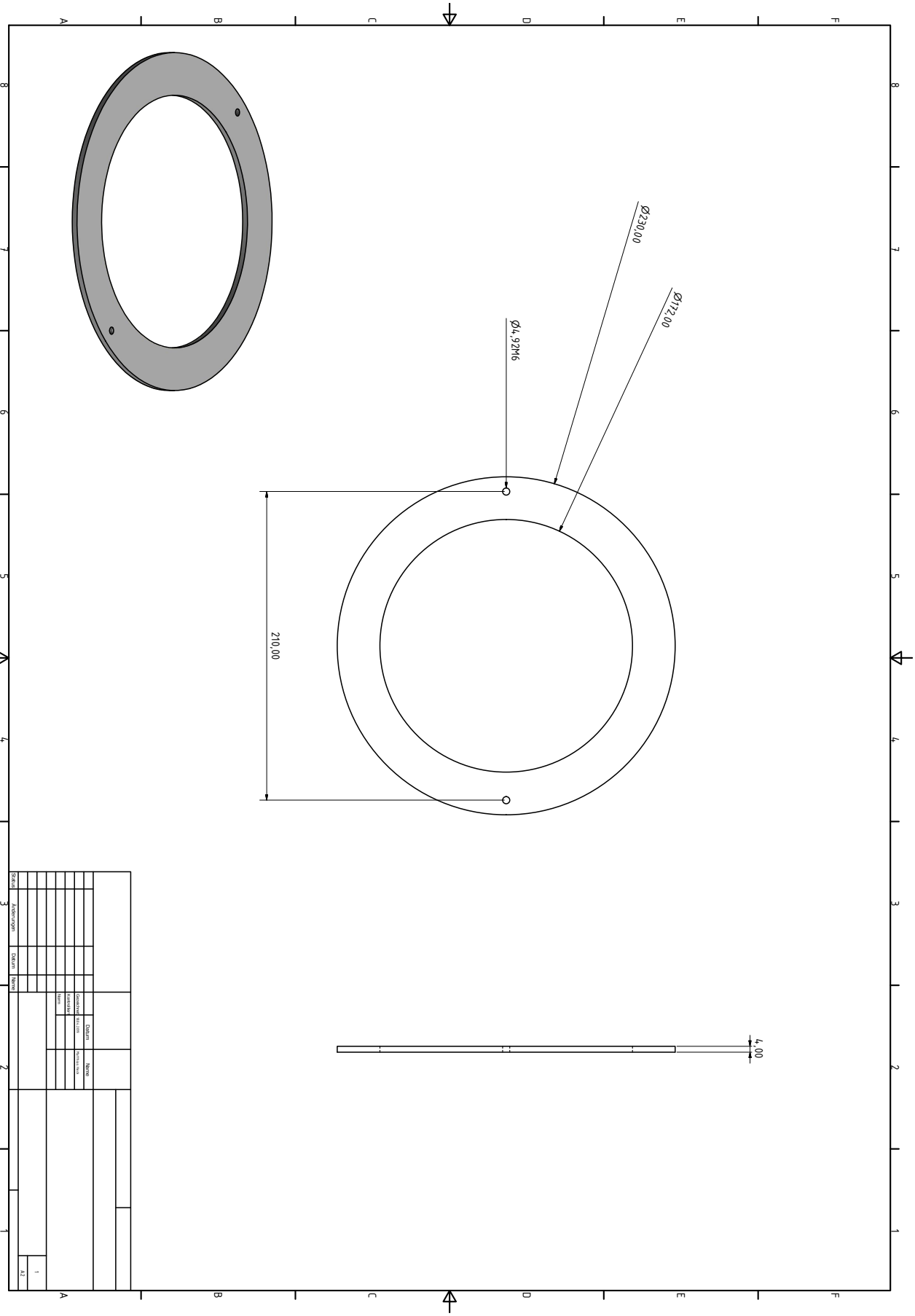

Figure 5: Rheo-IR: Part 2 (moveable) attached to Part 1 of the mounting Credit to Dr. Matthias Heck

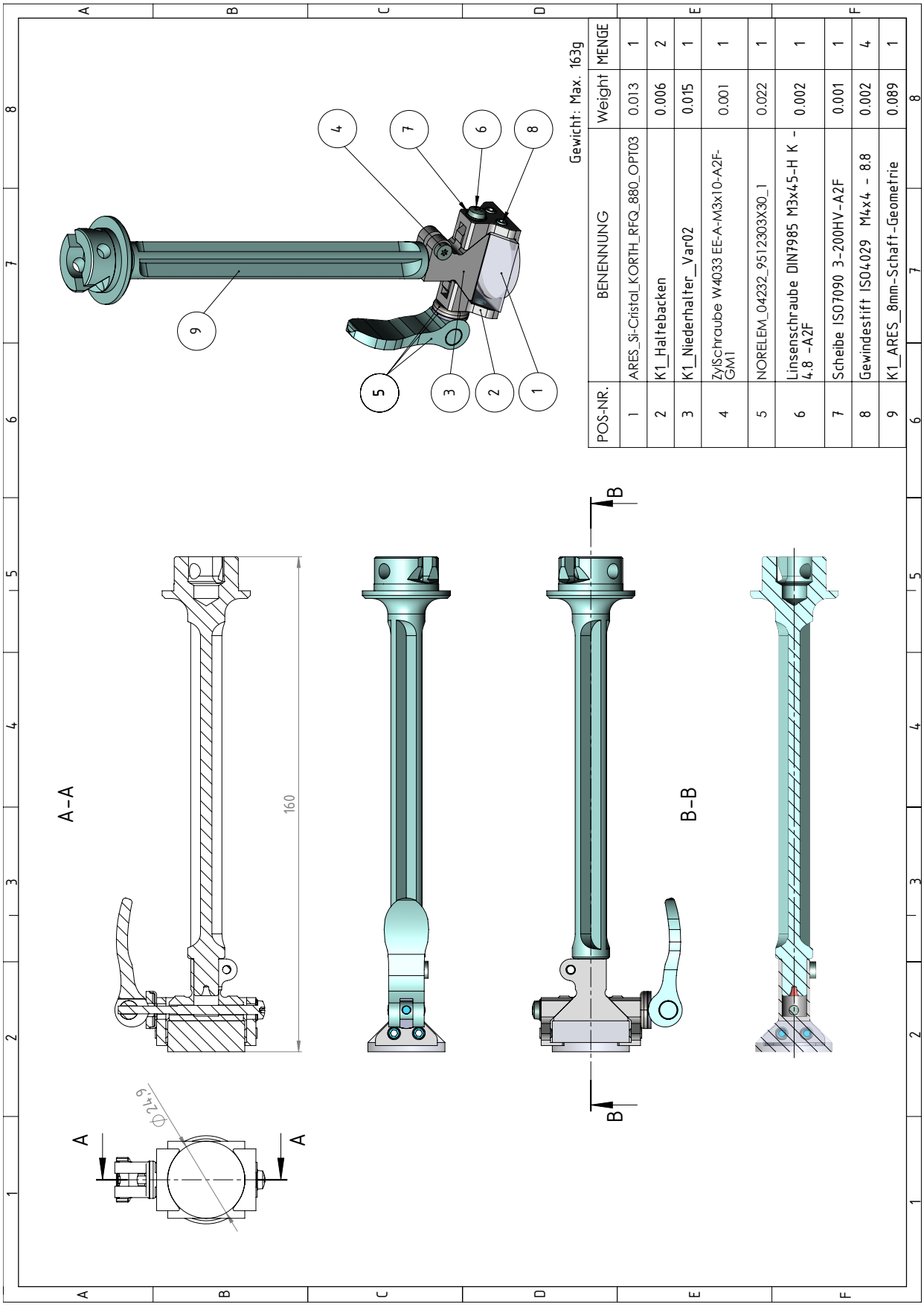

Figure 6: Rheo-IR: modified shaft design for a connection between the rheometer and the ATR crystal made from aluminium, with a length of 160 *mm*. Credit to Dr. Roxana Figuli

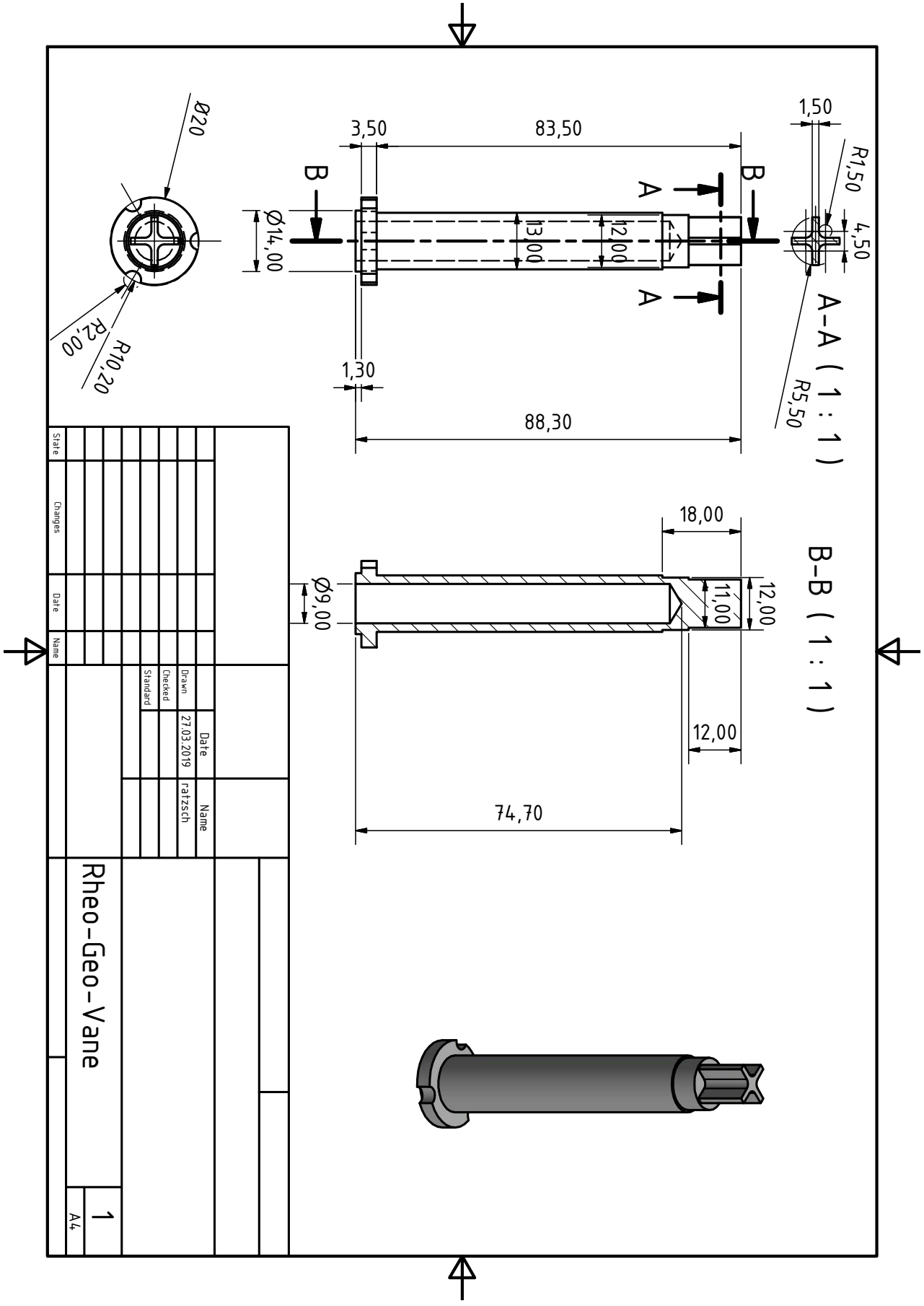

Figure 7: Rheo-NMR: Technical drawing of vane geometry. Material used: Polytetrafluoroethylene (PTFE) Credit to Dr. Karl Ratzsch

7/23/21 11:43 AM D:\My documents\IFG CO...\IFG_to_spec.m

```
%==========code for IFG to spectrum=========%
%=====By Nonkululeko Radebe July 2020=====%

SamY = PAAcDC0150wt05ini (1:end, 1:3: end); %find and replace file name
Ref = PAAcDC0150wt05ini (1:end,1:2);
%Ref_bfg = refIFGwater (1:14730,1:2);
%bkg = refIFGwater (1:14730,[1 3]);

%zero padding and windowing
ZerosRef = cat (1,Ref,zeros(14730,2));
ZerosSamY =cat (1,SamY,zeros(14730,46));
%ZerosRef_bkg = cat(1,Ref_bfg,zeros(14730,2));
%Zerosbkg = cat(1,bkg,zeros(14730,2));

ZerosRef = ZerosRef.*hanning (length(ZerosRef));
ZerosSamY = ZerosSamY.*hanning (length(ZerosSamY));
%ZerosRef_bkg = ZerosRef_bkg.*hanning (length(ZerosRef_bkg));
%Zerosbkg = Zerosbkg.*hanning (length(Zerosbkg));

OPD = ZerosRef (1:14730,1);
IREF = ZerosRef (1:14730,2);

figure(1);
subplot (2,2,1),
    plot (Ref);
    ylim ([-0.4 0.2]);
    xlim ([0 14729]);

% find and replace three lowest values
[pks, locs] = mink(IREF,3);
SamYnew = zeros (size (14730:1));
SamYnew (7361:7363,1) = pks;

SamYnewc = repmat (SamYnew,1,46);
ZerosSamY (7361:7363,1:end) = SamYnewc (7361:7363,1:end);

% FFT reference/background
FFTRef = fft(ZerosRef);
AbsFFTRef = abs(FFTRef);
AbsFFTRefy = AbsFFTRef (1:end,2);
AbsFFTRefys = repmat (AbsFFTRefy,1,46);

subplot (2,2,2),
     plot (real(FFTRef));
     ylim ([-2 2]);
     xlim ([0 14729]);

subplot (2,2,3),
     plot (imag(FFTRef));
```

7/23/21 11:43 AM D:\My documents\IFG CO...\IFG_to_spec.m

```
     ylim ([-2 2]);
     xlim ([0 14729]);

subplot (2,2,4),
    plot (abs (FFTRef));
    xlim ([1 4000]);
    ylim ([0 2.5]);
    xlabel ('wavenumber [cm^-1]');
    ylabel ('amplitude [a.u]');

%FFT 'solvent'
%FFTbkg = fft(Zerosbkg);
%AbsFFTbkg = abs(FFTbkg);
%AbsFFTbkgy = AbsFFTbkg (1:14730,2);

%FFTRef_bkg = fft (ZerosRef_bkg);
%AbsFFTRef_bkg = abs (FFTRef_bkg);

% figure (2)
% %subplot (2,1,1), plot (abs(FFTbkg))
%  xlim ([1 4000]);
%  ylim ([0 2.5]);
%  xlabel ('wavenumber [cm^-1]');
%  ylabel ('amplitude [a.u]');
% subplot (2,1,2), plot (abs (FFTRef_bkg));
%  xlim ([1 4000]);
%  ylim ([0 2.5]);
%  xlabel ('wavenumber [cm^-1]');
%  ylabel ('amplitude [a.u]');


  %FFT of all sample interferograms
FFTSamY_PAAcDC0150wt05ini = fft(ZerosSamY);
AbsFFTSamY_PAAcDC0150wt05ini = abs(FFTSamY_PAAcDC0150wt05ini);

%Use PSD to filter out noise, find all freqs with large power
figure (3)
    plot(abs(FFTSamY_PAAcDC0150wt05ini));
    xlim ([1 4000]);
    ylim ([0 2.5]);
    xlabel ('wavenumber [cm^-1]');
    ylabel ('amplitude [a.u]');


 % divide FFt
% Trans_bkg = AbsFFTbkg./AbsFFTRef_bkg;
% Abs_bkg = -log (Trans_bkg);
% Abs_bkgy = Abs_bkg (1:end,2);
% Abs_bkgys = repmat (Abs_bkgy,1,64);
```

7/23/21 11:43 AM D:\My documents\IFG CO...\IFG_to_spec.m

```
Trans = AbsFFTSamY_PAAcDC0150wt05ini./AbsFFTRefys;
% figure (4)
% subplot (2,2,1), plot (Abs_bkg);
%     xlim ([1000 4000]);
%     ylim ([-0.1 0.6]);
% subplot (2,2,2), plot (Trans_bkg);
%     xlim ([1000 4000]);
%     ylim ([0.6 1]);

%plot absorbance spectra
% Abs_firstY_PAAcDC0150wt05ini = -log(Trans_bkg);
Abs_PAAcDC0150wt05ini = -log(Trans);

%subtract

%sub_PAAcDC0150wt05ini = Abs_bkgys-Abs_PAAcDC0150wt05ini;

subplot (2,2,3); plot (Abs_PAAcDC0150wt05ini)
    xlim ([1000 4000]);
    ylim ([-0.1 0.6]);

% subplot (2,2,4), plot (sub_PAAcDC0150wt05ini);
%     xlim ([1000 4000]);
%     ylim ([-0.1 0.6]);

% Smooth data
% Abs_smoothed_PAAcDC0150wt05ini = smoothdata (Abs_PAAcDC0150wt05ini);

% plot (Abs_smoothed_PAAcDC0150wt05ini);
% export data

writematrix (Abs_PAAcDC0150wt05ini);
% writematrix (Abs_smoothed_PAAcDC0150wt05ini);
```

Publications

Journal Articles

Radebe N. W., Nie S., Schmidt W., Klein C.O., Figuli R., Wilhelm M., Cement paste hydration and structuration during early hydration as investigated by FT-Rheology and FTIR to understand the relationship between the macro and microscale, *in preparation*

Radebe N.W., Fengler C., Klein C.O., Figuli R., Wilhelm M., Rheo-IR: A combined setup for correlating chemical changes via FTIR spectroscopy and rheological properties in a strain-controlled rheometer spectroscopy and rheological properties in a strain-controlled rheometer, J. Rheol. 681 (2021). https://doi.org/10.1122/8.0000251

Schmidt W., Commeh M., Olonade K., Schiewer G.L., Dodoo-Arhin D., Dauda R., Fataei S., Tawiah A.T., Mohamed F., Thiedeitz M., **Radebe N.W.**, Rogge A., Sustainable circular value chains: From rural waste to feasible urban construction materials solutions, Dev. Built Environ. 6 (2021) 100047. https://doi.org/10.1016/j.dibe.2021.100047

Haist M., Link J., Nicia D., Leinitz S., Baumert C., von Bronk T., Cotardo D., Eslami Pirharati M., Fataei S., Garrecht H., Gehlen C., Hauschildt I., Ivanova I., Jesinghausen S., Klein C., Krauss H.W., Lohaus L., Lowke D., Mazanec O., Pawelczyk S., Pott U., **Radebe N.W.**, J.J. Riedmiller, H.J. Schmid, W. Schmidt, Secrieru E., Stephan D., Thiedeitz M., Wilhelm M., Mechtcherine V., Interlaboratory study on rheological properties of cement pastes and reference substances: comparability of measurements performed with different rheometers and measurement geometries, Mater. Struct. Constr. 53 (2020). https://doi.org/10.1617/s11527-020-01477-w

Schmidt W., Otieno M., Olonade K., **Radebe N.W.**, Van-Damme H., Tunji-Olayeni P., Kenai S., Tetteh Tawiah A., Manful K., Akinwale A., Mbugua R., Rogge A., Innovation potentials for construction materials with specific focus on the challenges in Africa", RILEM Technical Letters, 50, pp. 63-74 (2020).

Radebe N.W., Beskers T. Greyling G. Pasch H., Online coupling of thermal field-flow fractionation and Fourier transform infrared spectroscopy as a powerful tool for polymer characterization, J. Chromatogr. A 1587 (2018), https://doi.org/10.1016/j.chroma.2018.12.012

Conference proceedings (Orals Presentations/Peer-reviewed papers)

Schmidt W., Olonade K., **Radebe N.W**., Zando F., and Ssekamatte V., "Rural employment perspectives from sustainable, green construction materials for urban development -" Rural 21, no. 2/20, 2020.

Schmidt, W., **Radebe, N.**, Otieno, M., Olonade, K., Fataei, S., Mohamed, F.,Schiewer, G.L., Thiedeitz, M., Tawiah, A.T., Dauda, R., Bassioni, G., Rogge, A. (2020, March). Challenges, opportunities and potential solution strategies for environmentally and socially responsible urban development of megacities in Africa. In RILEM Spring Convention and Conference (pp. 119-132). Springer, Cham.

Radebe N.W., Ratzsch KF., Klein C.O., Wilhelm M. (2020), Use of Combined Rheo-NMR to Investigate the Relationship Between the Molecular and Mechanical Properties of Early Cement Paste Hydration. In: Mechtcherine V., Khayat K., Secrieru E. (eds) Rheology and Processing of Construction Materials. RheoCon 2019, SCC 2019. RILEM Bookseries, vol 23. Springer, Cham

Radebe N.W., Klein C.O., Lei L., Wilhelm M. (2020), Effect of Different Molecular Weights and Chemical Composition of Superplasticizers on the Structural Build-up of Cement Paste Using Dynamic Oscillatory Rheology. In: Boshoff W., Combrinck R., Mechtcherine V., Wyrzykowski M. (eds) 3rd International Conference on the Application of Superabsorbent Polymers (SAP) and Other New Admixtures Towards Smart Concrete. SAP 2019. RILEM Bookseries, vol 24. Springer, Cham

FALCONESS (Female Academic Leadership Network for Conscious Engineering and Science towards Sustainable Urbanisation) kick-off workshop, Accra (2021) http://falconess.org/

Poster Presentations

ISEE (Innovation, Science, Engineering and Education) Africa workshop coordinator. The workshop focused on global research and education requirements in civil engineering. http://isee-africa.com/

Poster: 'Combined rheo-spectroscopy methods to monitor the transient kinetics of early cement paste hydration' presented at the Annual European Rheology Conference AERC 2019, European Society of Rheology https://rheology-esr.org/aerc-2019/welcome/